CRANFIELD UNIVERSITY

SCHOOL OF ENGINEERING

PhD THESIS

MANUEL QUERO GARCÍA

ANALYTICAL AND EXPERIMENTAL INVESTIGATION INTO THE THERMAL ASPECTS OF DROPLET IMPINGEMENT

Supervisor David Hammond

March 2006

This thesis is submitted in partial fulfilment of the requirements for the degree of Master of Science

Abstract.

The mechanics and heat transfer of droplet impact is studied in the range of parameters interest for Super-cooled Large Droplet icing. The investigation explores the development of the splash produced experimental and numerically.

A Navier-Stokes solver has been developed in order to compare experiments and modelling.

Heat transfer is included in the simulations making possible the analysis of the thermal history during the impact of a Super-cooled droplet into a warm and running thin water film.

Also a theoretical and numerical study has been undertaken in order to simulate the first stages of ice formation on the critical surfaces of aircraft during the droplet impact under freezing conditions due to super-cooled icing.

The parameters considered experimental and numerically are:

- Droplet size: 100-700μm.
- Droplet impact velocity: 18-80m/s.
- Angles of impact: 70°, 45° and 20°.
- Airflow (droplet) temperature: 20°C and -10°C.
- Water film thicknesses: 150μm and 50μm.
- Water film temperature: 15°C and 10°C.
- Water film velocity: 5m/s.

The simulations are compared to the experiments run under the same conditions. Results for the parameters at the early stages of the splash agree well but as the splash process continues there are more differences between the two sets of results.

INDEX.

List of Figures.

List of Graphs and Tables.

List of Equations.

List of Symbols.

D Droplet diameter and water film thickness.

F Fraction of volume of the cell occupied by fluid.

Fh Fraction of volume of the cell occupied by ice.

Fcc Fraction of volume of the cell occupied by fluid from droplet and layer.

f1 Fraction of volume of the cell occupied by fluid from the droplet.

g_x Acceleration for the horizontal axes.

g_y Acceleration for the vertical axes.

h Height of the oblate droplet.

$\hat{h}_0$ Position of the ice – liquid interface (dimensional form).

h_0 Position of the ice – liquid interface (non - dimensional form).

$\hat{h}_1$ Position of the layer - droplet interface (dimensional form).

$\hat{h}(\hat{t})$ Distance thickness of the solid ice for time $\hat{t}$ (dimensional form).

L Latent Heat.

$m_{i,j}$ Normal exterior vector.

$\vec{n}$ Normal unit exterior vector.

$P_{i,j}$ Pressure field at the computational cell.

p Pressure.

T Temperature.

$T_{droplet}$ Initial temperature at the droplet.

T_{layer} Initial temperature at the layer.

T^n Temperature at time step n.

$\hat{T}_t$ Derivative of the temperature respect the time (dimensional form).

$\hat{T}_z$ Derivative of the temperature respect the z direction (dimensional form).

$\hat{T}^l$ Temperature in the liquid (dimensional form).

$\hat{T}^s$ Temperature in the solid (dimensional form).

T_t Temperature derivative respect time.

T_x Temperature derivative respect horizontal axes.

T_y Temperature derivative respect vertical axes.

T_z Temperature derivative respect z.

$\hat{T}_l(\hat{z})$ Temperature above the melting temperature (dimensional form).

$T_l(z)$ Temperature above the melting temperature (non - dimensional form).

$\hat{T}_m$ Melting temperature (dimensional form).

T_m Melting temperature (non - dimensional form).

$\hat{T}_\infty$ Temperature far away from the interface ice – liquid (dimensional form).

T_∞ Temperature in the droplet or layer (non - dimensional form).

t Time.

t_n Time step n.

$U_{i,j}$ Velocity field for the horizontal component at the computational cell.

$V_{i,j}$ Velocity field for the vertical component at the computational cell.

u Component x of the velocity vector.

V Velocity.

V_n Velocity of the ice – liquid interface.

v Component y of the velocity vector.

w Width of the oblate droplet.

x Horizontal axes component.

y Vertical axes component.

δ_x Dimension of the cell for the horizontal axes.

δ_y Dimension of the cell for the vertical axes.

k Thermal Diffusivity.

k^l Thermal Diffusivity in the liquid.

k_c Thermal Conductivity.

μ Dynamic viscosity.

ν Kynematic viscosity.

ρ Density.

ρ^s Density in the solid.

ρ^l Density in the liquid.

σ Surface Tension.

θ Temperature(non-dimensional form).

$a = \frac{1}{\mathrm{Pr} \cdot \mathrm{Re}}$ Dimensionless number used for the Thermal Diffusivity.

$Cp = \frac{k_c}{\rho \cdot k}$	Specific Heat.
$\mathrm{Pr} = \frac{Cp \cdot \mu}{k_c}$	Prandtl number.
$\mathrm{Re} = \frac{V \cdot D}{\nu}$	Reynolds number.
$\Delta\hat{T} = \hat{T}_m - \hat{T}_\infty$	Temperature difference (dimensional form).
$VED = \sqrt[3]{w^2 \cdot h}$	Volume Equivalent Diameter.
$We = \frac{V^2 D \rho}{\sigma}$	Weber number.

Introduction.

When aircraft fly through clouds at temperatures below freezing point, ice accretion is often observed on a number of critical surfaces. These sensitive areas include the leading edge of wings, tail, around the engine inlets and on the rotor blades of a helicopter. The resultant ice can have serious consequences with large increases in drag and decrease in lift, leading to a severe reduction on the stability, control and safety of an aircraft.

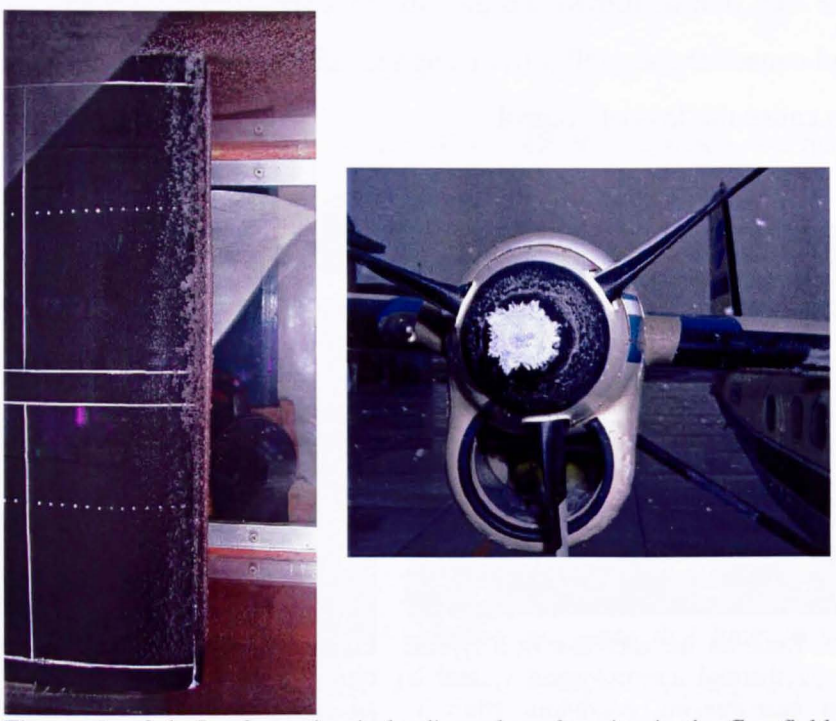

Figures 1 a & b. Ice formation in leading edge of a wing in the Cranfield University Icing Tunnel and in the engine inlet and rotor of an aircraft (NASA Glenn).

Until the ATR-72 accident in October 1994 that cost 68 lives which was accepted to have occurred as a result of freezing rain/drizzle conditions, most understanding about aircraft icing had been related to freezing fog and clouds.

The difference between freezing rain/drizzle and freezing fog and cloud is based on the diameter assumed for the different droplets. Thus, for freezing fog and cloud droplet diameters are considered to be generally lower than 50μm, freezing drizzle are between 50 and 500μm and freezing rain, from 500μm to 2mm. Icing conditions due

to impacts of droplets over 50μm are known as Super-cooled Large Droplet (or SLD) icing.

When a large droplet impacts into a thin water layer at high speed it will splash ejecting secondary droplets back into the air-stream. Some of these will escape completely while others will re-impinge further aft down the wing. Also something different happens with SLD. Larger droplets impinge in a wider area than the small droplets which can include unprotected surfaces and helps the ice formation. It was this accumulation of an ice ridge on the upper surface of the wing aft of the de-icing facilities the one that disturbed the airflow over the aileron surfaces in the ATR-72 accident and caused the autopilot to disengage, after which the ailerons uncontrollably deflected to cause the loss of control.

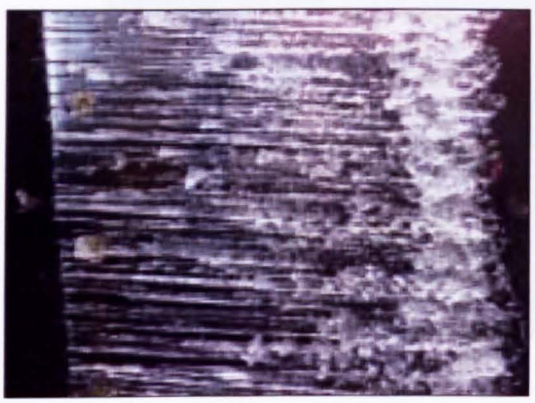

Figure 2a. Runback ice accretion of a typical business jet thermal ice protection system is shown at near-freezing conditions (flow is from right to left). (Aerospace America, AIAA 2005.)

Figure 2b. Runback ice accretion of a typical business jet thermal ice protection system is shown at colder conditions (flow is from right to left). (Aerospace America, AIAA 2005.)

Airlines and aircraft manufacturers are continually searching for better methods to protect aircraft from ice build-up during flight. One method is to draw hot air from the engine to heat the leading edges of critical surfaces evaporating the water on the heated portion of the protected areas. However, this reduces engine efficiency, and therefore increasing costs of operating the aircraft. Another method is electrical heating which also place a power requirement on the engine.

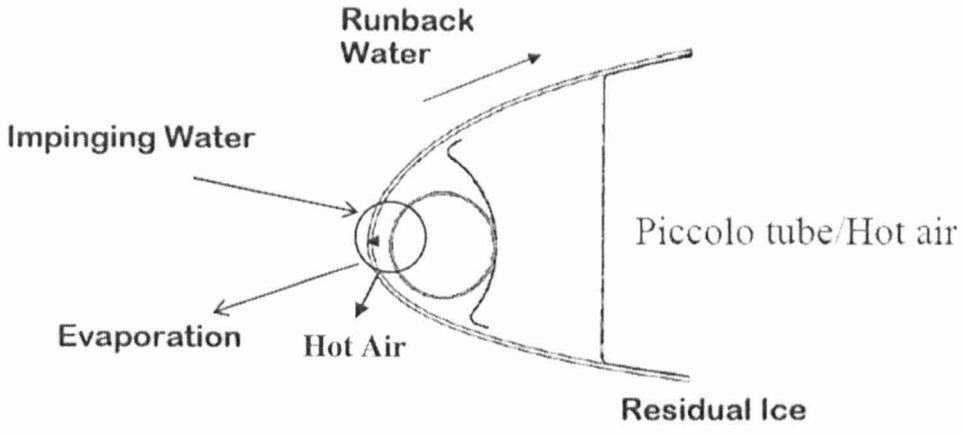

Figure 3. Cross section of Piccolo tube (NASA Glenn).

One of the sponsor's businesses of this project, GKN Aerospace, is a manufacture of ice protection systems. Therefore, this project is motivated by the following objective: to reduce as much as possible the effect of the ice protection system in the engine efficiency. Thus, this investigation seeks the understanding of what is happening during the immediate stages after the super-cooled water droplets suspended in the cloud impact upon the aircraft, including corona development and temperature of the involved fluids during the splash.

In order to reduce the chance of further accidents due to SLD, a roadmap has been designed and includes three different key technology areas that have to be tackled: SLD Environment Characterisation, SLD Certification Development and SLD Engineering Tool Development. This last area involves experimental and computational work including experiment in tunnels and code development taking also into account droplet splashing (Miller, 2000).

This research explores experimental and numerically how Super-cooled Large Droplets impact into a thin water film that simulates the water that previously has been deposited on the critical surfaces of the aircraft. The splash produced after the impact forms a corona which can be studied in size, velocity of growth and the time they need to develop and reach the maximum size. The break-up or collapse of the coronas is the responsible of the ejection of secondary droplets that may re-impinge

further aft down the wing where there is not ice protection. The experiments and the simulations were run under similar conditions in order to be compared.

The investigation also presents, through numerical work, the heat transfer between the super-cooled droplet and the warmer water film. The study of the heat transfer gives additional insight into super-cooled large droplet impact, particularly when it comes to considering the heat taken away with splashed fluid and gives a new vision of what is really happening. A numerical investigation is also presented of when and how the super-cooled droplets start to freeze after the impact into a thin water film with an ice rough set in the bottom.

Both experiments and modelling give a good approximation to the reality and they facilitate the understanding of the droplet impact problem, the subsequent splash and the early stages of the building up of ice. However they present certain limitations.

The experiments were carried out in the Cranfield University High Speed Vertical Tunnel. A wide range of impacts is studied including droplets sizes that go from 100μm to 700μm and air flow velocities in a range between 18m/s to 90m/s. The temperatures considered are between -10°C to ambient temperatures which are assumed to be at 20°C. The angles of impact taken into account are 70°, 45° and 20°. The limitations of the experiments are based on the lack of data obtained for some of the impacts. Thus, there are only a small number of cases recorded at cold temperatures and when the angle is 45° or 20°. This restriction affects the nature and depth of the analysis comparison between the different conditions of relevance.

The main limitations of the modelling resides in the fact that the simulations are made in two dimensions and also in absence of any airflow, i.e., in a void. The consequences of a model in 2D are that the splashes will not form a corona but two different jets coming off the water film. The effect of the lack of airflow is that the splash is not distorted or forced to break up in the same way. Therefore the comparison with the experiments is most direct only for early stages of this splash.

The Vertical Tunnel was conceived to accelerate and cool droplets down without breaking them up and to impact them into a thin water film supported on a hard

surface in order to study the splash produced. This is recorded with a high speed camera. The obtained results are a series of images that allow the measurement of the different parameters considered in the corona. The Vertical Tunnel design is a join project with Wichita State University in the U.S. (Tan, 2002).

Thus, this work is presented with the aim of achieving three main objectives:

- To explore experimental and numerically how SLD impact into a thin water film.
- To study of the heat transfer between SLD and water film during splash.
- To give an outline of a Solidification Model: When and how the SLD starts to freeze after the impact into a thin water film with an ice rough set in the bottom.

Overview.

It can be said that the average temperature for the most hazardous environment for SLD icing covers a narrow range from -5.5°C to -9.4°C (Politovich). However this range can be extended if parameters such as the altitude are taken into account. According to many researchers, icing occurs most frequently at temperatures between -2°C and -12°C. Under this conditions glaze ice is formed. This ice builds up on surfaces as a tightly bonded, clear, hard and dense glasslike coating. This type of icing is the most serious threat to aircraft because of its density and the alteration of the airfoil geometry.

Complicated ice shapes can be formed under these conditions when SLD are hit by the plane and they immediately begin to freeze. Figure 4 shows a picture of the typical double horn shape obtained experimentally in the NASA Glenn icing tunnel. Figure 5 shows a cross section of the double horn shape on an airfoil.

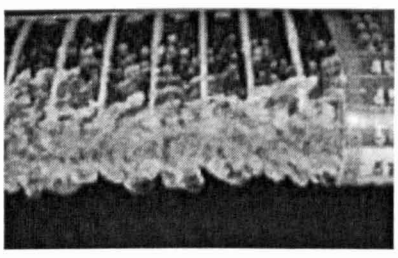

Figure 4. Ice forming a double horn shape. (NASA Glenn.)

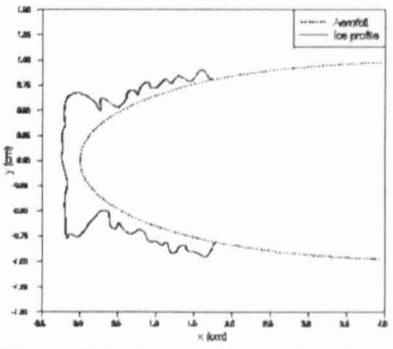

Figure 5. Scheme of a double horn ice profile on an airfoil (Gent, 2003).

During a flight in a cloud a water film appears on the stagnation points of the airfoil. The thickness and temperature of it influences on the development of the corona during the splash and on the resultant temperature of the corona.

The depth of the water layer is in a range between 60μm (Morency *et al.*) and 154μm (Feo et al. 2002). The first case is presented in graph 1. Two different experimental works are compared, CANICE and Al-Khalil. The results show the

thickness against the position in the airfoil. The second case is also experimental and shows in table 1 the water film thickness regarding the air velocity.

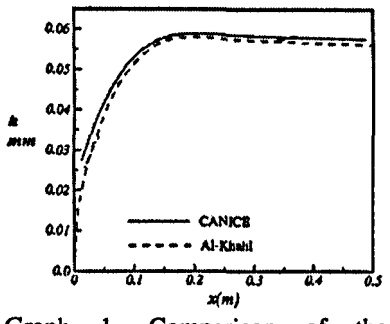

Graph 1. Comparison of the CANICE and Al-Khalil model for the measurement of the water film thickness h on an airfoil (Morency)

V, m/s	h, μm
55	106
30	118
20	154

Table 1. Water film thickness h on a stagnation point in a simulated cloud when varying the velocity (Feo *et al.* 2002)

When considering as anti-icing a hot air region inside the wing of the aircraft, the temperature distribution of the water film is assumed to be between 16 and 2°C when moving upward from the stagnation point (Morency *et al.*). Graph 2 shows the temperature distribution obtained with CANICE and Al-Khalil models.

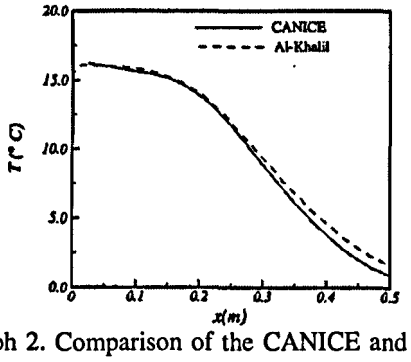

Graph 2. Comparison of the CANICE and Al-Khalil model for the calculation of temperature distribution of the water film on an airfoil (Morency)

This investigation studies the impact and subsequent splash, the temperature and droplet size in range mentioned previously. The droplets impact into a water film at 10°C and 15°C and two different thicknesses, 50 and 150μm.

There is much interest in what happens as the droplet first makes contact with the aircraft (or other structure). This focus has increased with the acceptance that droplet

size may be a significant factor beyond the consideration of the trajectory of droplets around the aircraft.

Thoroddsen (2002) reports on an experimental study of single droplet impacts onto undisturbed water films. His experiments cover droplet Reynolds numbers of up to 4000. This is an order of magnitude lower than the situation under investigation here but he has given the field a valuable range of data including jet velocities as a function of droplet size and speed for normal impact and the influence of viscosity. In particular Thoroddsen provides evidence of the formation of a fast moving horizontal jet in the early stages of the impact which was to prove supportive to work on modelling droplet impact.

Weiss and Yarin (1999) provide a numerical study of a single water droplet impact onto a film of the same liquid. They consider surface tension and gravity but not viscosity or compressibility. The results provide information of the velocity of the jets emanating from the contact area of the droplet with the film at low Weber numbers and at low droplet velocities. Their results agree well with the experimental work by Thoroddsen suggesting that in this range of Weber number and speed and in the case the droplet properties are the same as layer properties, viscous and compressibility effects may be neglected. Further background is provided by Howison *et al.* (2004) with an analytical study of the high speed droplet impact on a shallow water layer giving special emphasis to the solution at very short timescales. They only consider the case when $\varepsilon = H/R$ is small and u is very large where H is water film thickness, R the droplet diameter and u the velocity.

Josserand *el al.* (2003) pursues a similar line but looks at intermediate time scales giving results on the form of the jets as they begin to project upwards away from the surface of the water layer/target. Their results show the influence of the Reynolds number on the form of the jet.

The current investigation follows on from the work of Purvis *et al.* (2004). He studies droplet impact onto an undisturbed water layer and addresses the parameter range associated with SLD icing. Surface tension, viscosity, gravity and the influence of pre-existing air flow are neglected. The work provides and discusses solutions for

the flow over intermediate timescales for different angles of impact varying droplet sizes, velocities and layer depth. He also starts to consider methods of quantifying the amount of fluid displaced from the surface. Purvis' work has been expanded upon in this study by a number of refinements including the ability to ascribe different properties to the droplet and the layer. In particular, some of the physical properties are made to be dependent on temperature and a thermal model is included. In this way variations in local fluid properties may be accounted for. The model also provides for the freezing and the development of ice roughness elements on the target surface.

PART I: NUMERICAL WORK

CHAPTER 1. Volume of Fluid (VOF) and Marker and Cell (MAC) Methods.

The numerical method on which the work is based is a technique that describes numerically the solution of a problem that involves time dependent flow of an incompressible and viscous fluid in two-dimensional Cartesian coordinates (F.H. Harlow *et al.*, 1965). Because a set of marked particles move with this fluid, the technique is called a *marker and cell method.* The solution for the method is achieved by solving the Navier-Stokes equations making use of finite-differences approximations applied in space and time. The primary variables are the pressure and the velocity.

In order to do these calculations, the velocity field must be known at the beginning of every cycle. This must be known either from a previous cycle or from initial conditions. The corresponding field of pressures is calculated assuming that the rate of change of the velocity divergence vanishes everywhere. Therefore the equation for mass conservation has to be satisfied and this is done by an iterative process. The marker particles are moved according to the velocity components of the neighbouring cells, and finally some adjustments are made to allow the marker particles to cross the cell boundaries. These marker particles introduced into the incompressible flow calculation are for the purpose of indicating which cells contain fluid and especially which cells contain a free surface.

The starting point of the derivation of the finite difference relation is the Navier-Stokes equation for viscous and incompressible fluid in two-dimensional Cartesian coordinates. Thus, for mass and momentum conservation, the differential form is:

$$\frac{\partial u}{\partial x}+\frac{\partial v}{\partial y}=0, \tag{1}$$

$$\frac{\partial u}{\partial t}+u\frac{\partial u}{\partial x}+v\frac{\partial u}{\partial y}=-\frac{1}{\rho}\frac{\partial p}{\partial x}+g_x+\nu\left[\frac{\partial^2 u}{\partial x^2}+\frac{\partial^2 u}{\partial y^2}\right], \tag{2}$$

$$\frac{\partial v}{\partial t}+u\frac{\partial v}{\partial x}+v\frac{\partial v}{\partial y}=-\frac{1}{\rho}\frac{\partial p}{\partial y}+g_y+\nu\left[\frac{\partial^2 v}{\partial x^2}+\frac{\partial^2 v}{\partial y^2}\right]. \tag{3}$$

The x and y coordinate axes are horizontal and vertical respectively. Also t denotes time. The corresponding components of the velocity are u and v and p is the pressure. The kinematic viscosity coefficient is designated by v and the acceleration components are g_x, g_y. The finite difference approximation to the equations corresponds to an Eulerian mesh of cells covering the computational region. For each cell the local field variable is centred as shown in figure 6. The dimensions of the rectangular cells are δx for the horizontal axis and δy for the vertical.

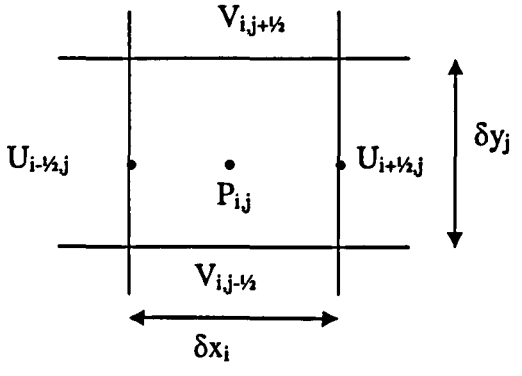

Figure 6. Field variable value placement at a computational cell

In order to determine the pressures, equation (1) must be satisfied. If superscript n+1 represents the value of each parameter at the time $t = (n + 1)\,\delta t$, and

$$D_{i,j}^{n+1} = \frac{\left(u_{i+\frac{1}{2},j}^{n+1} - u_{i-\frac{1}{2},j}^{n+1}\right)}{\partial x_i} + \frac{\left(v_{i,j+\frac{1}{2}}^{n+1} - v_{i,j-\frac{1}{2}}^{n+1}\right)}{\partial y_j}, \qquad (4)$$

then the finite difference form for (1) is $D_{ij} = 0$.

Once the pressure and velocity fields are calculated, the tracking of the surface cells must be performed. The surface position must be calculated and following of trajectories is required because, initially, marker particles are placed in cells containing fluid and they are moved with the local velocity. In order to impose this, a linear interpolation is performed and so the velocity at which the particle should move is calculated. A cell with no marker particles is assumed to have no fluid. A cell with marker particles that has a neighbouring cell empty is

considered as a surface cell and all other cells with particles are assumed to be totally filled with fluid.

Boundary conditions are applied to the rigid walls and to the free surface. Regarding the rigid walls, these can be two types, no-slip or free-slip depending on whether they represent a true wall (no-slip), characterised because the velocity is tangential to this wall and the others are considered zero or, on the other hand, a plane of symmetry (free-slip) which allows fluid to pass through the wall. The boundary conditions at a free surface are divided into conditions for the velocity and for the pressure. The conditions for the calculation of the velocity field are based on the requirement that $D = 0$ for surface cells. The conditions for the calculation of the pressures are derived from the fact that the normal stress component has to be zero at these cells.

VOF for the dynamics of free boundaries, NASA-VOF2D and SOLA-VOF

Based on the previous VOF and MAC method, different algorithms which have developed in order to calculate the solution of two-dimensional transient fluid flow with free boundaries give the foundation of the numerical work of the research. These methods (Hirt *et al.* 1981, Torrey *et al.* 1985 and Nichols *et al.* 1981) consider free boundaries as the free surfaces or material interfaces and the fluid may be treated as incompressible or having limited compressibility.

Instead of using Lagrangian formulations for fluid dynamics problems, these algorithms use Eulerian calculations. Therefore it is necessary to compute the flow of fluid through the mesh. This flow requires an averaging of the flow properties of all fluid elements that are found in a given mesh cell after some period of time.

The basis of the (Solution Algorithm) SOLA-VOF method is the fractional volume of fluid scheme for tracking free boundaries. In this technique, a function $F(x, y, t)$ is defined

over every cell of the computational mesh. The value of F in a cell is equal to the fraction of volume of the cell occupied by the fluid. Therefore:

- $F(x, y, t) = 1$ if the cell is completely full of fluid.
- $F(x, y, t) = 0$ if the cell has no fluid.
- $F(x, y, t) \in (0, 1)$ if the cell contains a boundary.

A cell is considered to be a boundary cell if it has at least one neighbouring cell with $F = 0$.

These cells are rectangular and have variable sizes δx_i for the horizontal axis and δy_j for the vertical one.

The fluid equations to be solved are the Navier-Stokes equations (same as (2) and (3)):

$$\frac{\partial u}{\partial t}+u\frac{\partial u}{\partial x}+v\frac{\partial u}{\partial y}=-\frac{1}{\rho}\frac{\partial p}{\partial x}+g_x+\nu\left[\frac{\partial^2 u}{\partial x^2}+\frac{\partial^2 u}{\partial y^2}\right], \tag{5}$$

$$\frac{\partial v}{\partial t}+u\frac{\partial v}{\partial x}+v\frac{\partial v}{\partial y}=-\frac{1}{\rho}\frac{\partial p}{\partial y}+g_y+\nu\left[\frac{\partial^2 v}{\partial x^2}+\frac{\partial^2 v}{\partial y^2}\right]. \tag{6}$$

Velocity components (u, v) are in Cartesian coordinates (x, y). The acceleration is denoted by (g_x, g_y), $p(x, y)$ is the pressure field, ν is the kinematic viscosity and ρ is the fluid density.

The continuity equation is defined by:

$$\frac{\partial u}{\partial x}+\frac{\partial v}{\partial y}=0. \tag{7}$$

Discrete values of the dependent variables are placed at cell positions shown in Figure 7.

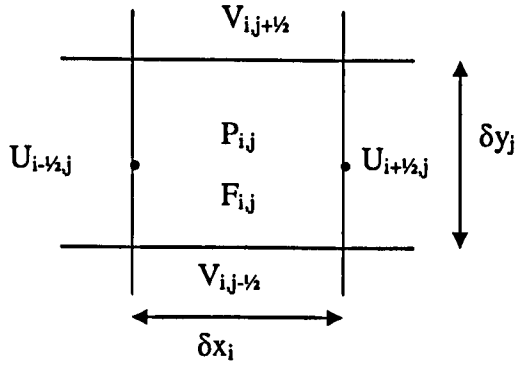

Figure 7. Location of variables in a typical mesh cell.

In order to solve equations (1) and (2), a generic finite difference approximation is made leading to, for the horizontal direction,

$$u^{n+1}(i,j)=u^{n}(i,j)+\delta t\left[\frac{-\left(p^{n+1}(i+1,j)-p^{n+1}(i,j)\right)}{\rho\delta x}+g_x+FUX+FUY+VISX\right] \qquad (8)$$

where FUX and FUY are the advective fluxes of u in the x and y-direction.

$$\text{FUX}=\left(\frac{u_{i+1/2,j}}{2\cdot\delta x}\right)\left[\delta x_{i+1}DUL+\delta x_i DUR+\alpha\,\text{sgn}(u)\left(\delta x_{i+1}DUL-\delta x_i DUR\right)\right] \qquad (9)$$

where

$$\text{DUL}=\frac{u_{i+1/2,j}-u_{i-1/2,j}}{\delta x_i},$$

$$\text{DUR}=\frac{u_{i+3/2,j}-u_{i+1/2,j}}{\delta x_{i+1}}$$

and sgn(u) means the sign of $u_{i+1/2,j}$. If $\alpha = 0$ it will be a full centred difference approximation and if $\alpha = 1$ it will be a full donor difference.

VISX is the term referring to the viscosity in the x-direction:

$$\text{VISX}=\nu\left[\frac{\partial^2 u}{\partial x^2}+\frac{\partial^2 u}{\partial y^2}\right]. \qquad (10)$$

The generic finite difference approximation for the vertical cases is made in the same way.

Once the velocities are computed, they must satisfy the continuity equation (1). In order to obtain this, the pressures and velocities must be adjusted in each computational cell occupied by fluid. Therefore the pressure change needed to satisfy (1) will become defined by:

$$P_{i,j} = P_{i,j} + \delta p, \tag{11}$$

$$\delta p = -\frac{S}{\frac{\partial S}{\partial p}}, \tag{12}$$

where S will change depending on the type of fluid cell. For a cell containing a free surface it is

$$S = (1-\eta)p_N + \eta p_s - p_{i,j} \tag{13}$$

This represents a linear interpolation between the pressure required at the surface (p_s) and the pressure inside the fluid (p_N).

For a cell full of fluid:

$$S = \frac{\left(p_{i,j}^{n+1} - p_{i,j}^{n}\right)}{\rho \delta t} + D_{i,j}^{n+1}, \tag{14}$$

$$D_{i,j}^{n+1} = \frac{\left(u_{i+\frac{1}{2},j}^{n+1} - u_{i-\frac{1}{2},j}^{n+1}\right)}{\partial x_i} + \frac{\left(v_{i,j+\frac{1}{2}}^{n+1} - v_{i,j-\frac{1}{2}}^{n+1}\right)}{\partial y_j}. \tag{15}$$

Therefore the new estimation for the velocities is:

$$u_{i+\frac{1}{2},j} = u_{i+\frac{1}{2},j} + \delta\Omega \frac{\delta p}{\rho \delta x_{i+1/2}}. \tag{16}$$

This example is presented for the x axis and the right side of the cell. For the left side and the y axis the situation is analogous.

In the above, Ω is a function of $\delta t/\delta x$ but in particular, for purely incompressibility reasons, Ω will always be set to unity.

A complete iteration is performed until the velocities and pressures are adjusted in all the cells occupied by fluid. Convergence of the iteration is achieved when all cells have S values a number which typically is of order 10^{-3}.

The advance of F in time is computed by the use of Donor-Acceptor flux approximation (Hirt *et al.* 1981, Torrey *et al.* 1985 and Nichols *et al.* 1981). The essential idea is to use the information about F downstream as well as upstream of a face boundary to establish a crude interface shape and then to use this shape for computing the flux. It is basic to know the amount of F fluxed across the cell face in one time step from the donor to the acceptor cell and in which direction it will travel. This is δF times the face cross sectional area which is the amount of F that is going to be fluxed, where

$$\delta F = \text{MIN} \{F_{AD} |V_x| + CF, F_D \delta x_D\}, \tag{17}$$

$$CF = \text{MAX} \{(1 - F_{AD}) |V_x| - (1 - F_D) \delta x_D, 0\} \tag{18}$$

and

$$V_x = u\delta t. \tag{19}$$

Single subscripts denote the acceptor (A) and donor (D) cells. The double subscript, AD, refers to either A or D, depending on the orientation of the interface relative to the direction of flow.

The direction is given by the sign of the normal velocity at the cell face. Once the amount of F that is going to flux is calculated, this is moved from the donor cell to the acceptor.

SOLA-VOF also includes Surface Tension (force per unit length). This coefficient is denoted by σ. It is included by computing a local curvature in each boundary cell and evaluating the surface pressure by means of:

$$P_S = - \sigma K, \tag{20}$$

K being the curvature.

Also, some boundary conditions have to be set at all mesh boundaries. Considering for instance, for every j and on the bottom of the mesh, the conditions are:

$$\begin{aligned} v_{1,j} &= v_{2,j}, \\ P_{1,j} &= P_{2,j}, \\ F_{1,j} &= F_{2,j}. \end{aligned} \tag{21}$$

However, for the term u of the velocity the boundary conditions will depend on, whether there is a free slip wall, in which case the condition is:

$$u_{1,j} = 0 \tag{21a}$$

which means that there is no tangential velocity component but only normal ones, or whether what is needed is a prescription that permits fluid to flow out of the mesh with minimum upstream influence, in which case the condition will be:

$$u_{1,j} = u_{2,j}. \tag{21b}$$

CHAPTER 2. The Method of Richard Purvis.

As an application of the SOLA-VOF method (Nichols *et al.*, 1981), Richard Purvis developed at University College London a model which simulates the impact of a single droplet onto a non-moving film in a void.

The model considers initially a droplet moving towards a film at a steady velocity. Both are fluids with the same density, and gravitational forces are not considered. Therefore the term (g_x, g_y) as seen in the previous chapter is considered to be (0, 0). Figure 8 shows this first position on the computational mesh, which is formed by cells all of the same size. In this case, the droplet diameter has the same size as the film thickness.

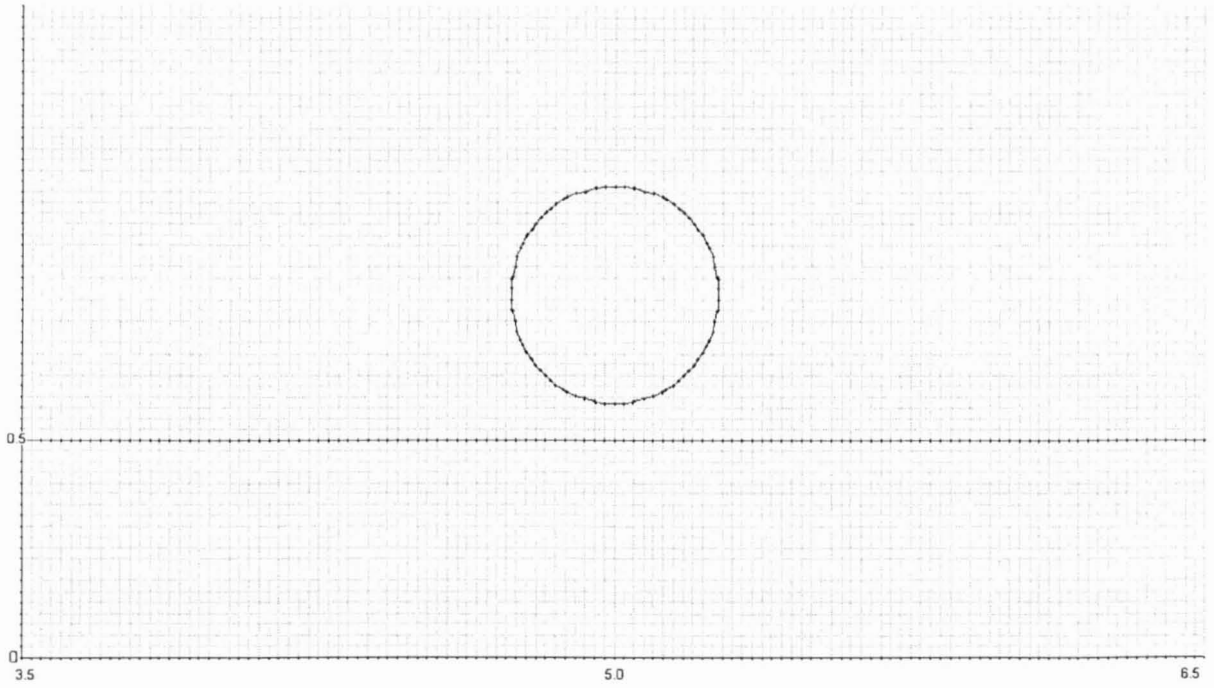

Figure 8. Mesh at first time step. The approximate circle represents the droplet and the straight line the surface of the layer at the bottom.

The impact can be studied for different droplet sizes, film thicknesses and different velocities, which allow the study of impact at different angles by applying to

the droplet a horizontal velocity. Also the fluid density and the number of cells and their size can be changed.

It should be mentioned that the initial Purvis method does not consider the viscosity term. Thus the equation that is solved is:

$$u^{n+1}(i,j) = u^{n}(i,j) + \delta t\left[\frac{-\left(p^{n+1}(i+1,j) - p^{n+1}(i,j)\right)}{\rho \delta x} + FUX + FUY\right]. \qquad (22)$$

The terms FUX and FUY are the same as have been defined in the previous section.

Purvis's model simulates the impingement of the droplet and subsequent splash, which is represented by the two jets (right and left) that come off from the film surface while the droplet continues to enter the film. Also the simulations included a detachment of very little droplets from the jet and expelled to the void.

Figures 9a, b, c, and d give an idea of how the model simulates the impact. First the droplet is about to touch the layer. In this case only the droplet is affected by a vertical velocity that makes the drop approach the film in the normal direction.

In figure 9b the droplet has just touched the layer and, according to the literature (Thoroddsen, 2001 and Howison *et al.*, 2005), thin and symmetric jets arise at very high speeds in comparison with the impact velocity. Figure 9c shows the moment when the jets are developing and the first satellite droplets are detaching. At this time, the jets have decreased their velocity. To finish, in figure 9d the jets are totally developed. There are plenty of satellite droplets coming off the jets and at the bottom it is possible to see some little peaks produced once the splash is totally formed.

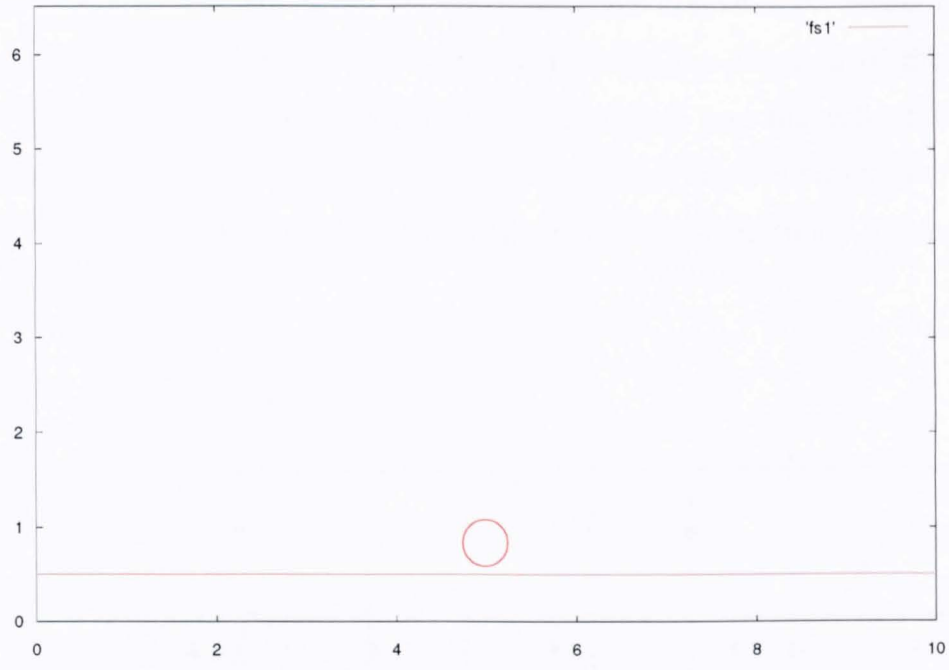

Figure 9a. The droplet approaches the film.

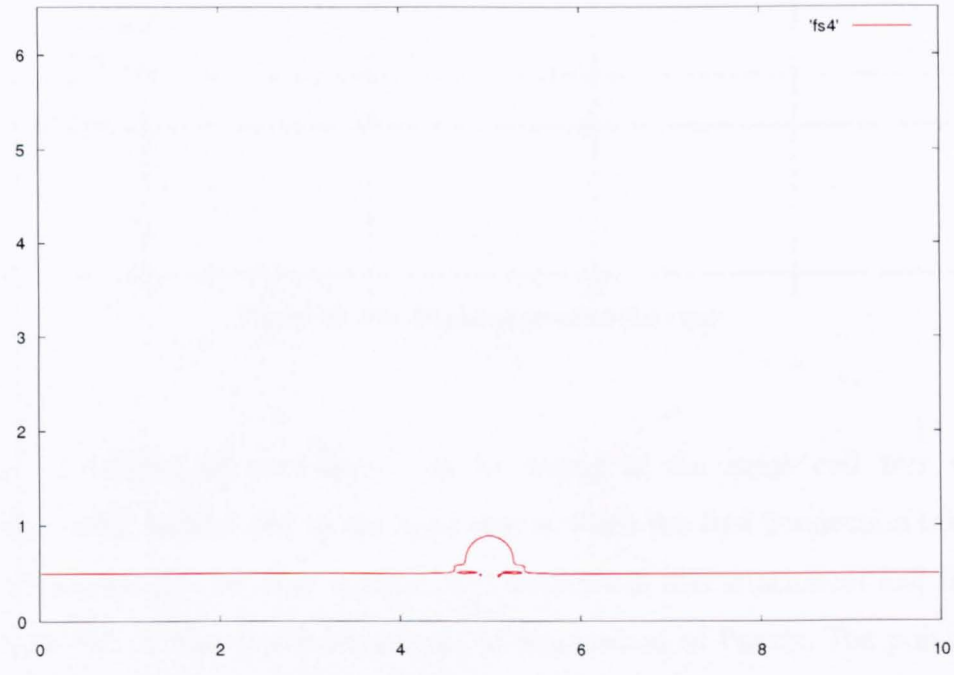

Figure 9b. Early stages of the impact.

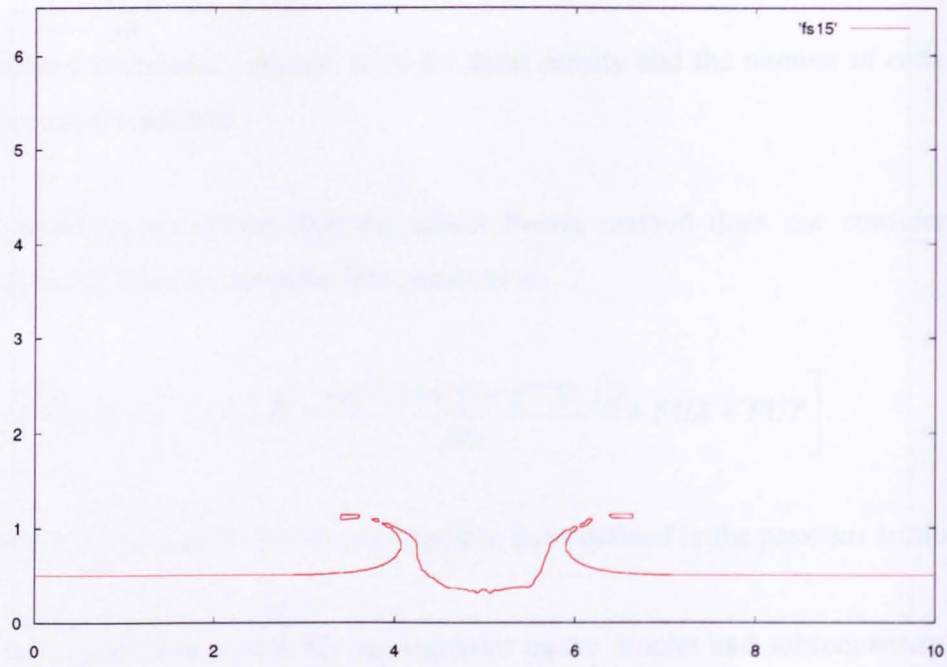

Figure 9c. First satellite droplets detaching.

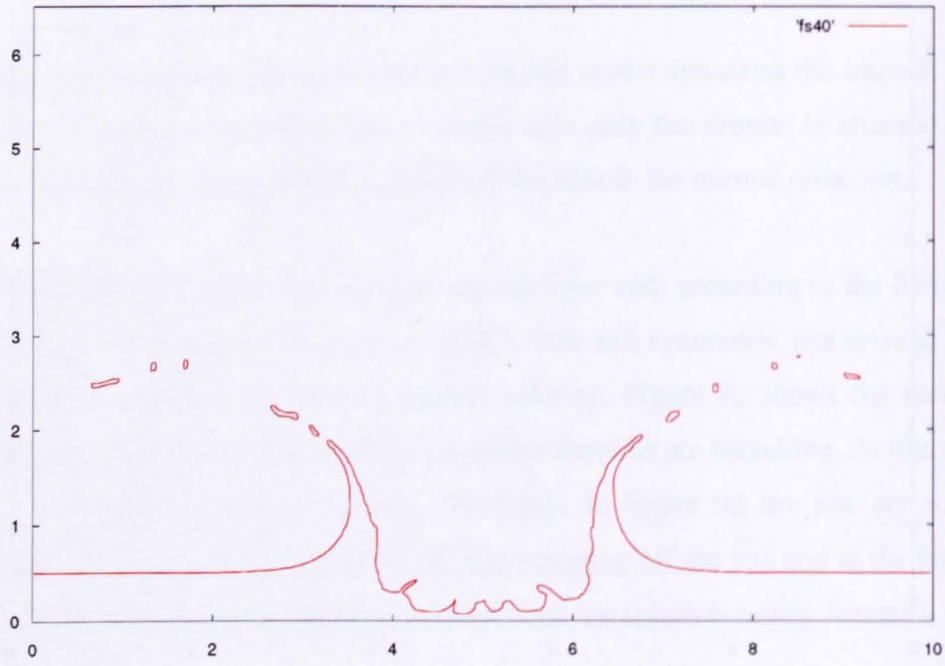

Figure 9d. Jets are well developed.

The way the fluid flows is explained with a simple but clear example, as follows. An extract of the mesh is considered. This example shows the free boundary moving in the void and the approach and attachment to another surface.

Figure 10 shows the free boundary representing the droplet approaching the film. Some of the velocity fields are also included pointing the direction of the droplet motion. The horizontal straight line is the film surface and the cells bellow are assumed to be filled with fluid. The lines forming a half circle represent the droplet surface. The cells over these lines are also filled with the same fluid. The remaining cells are taken to be void.

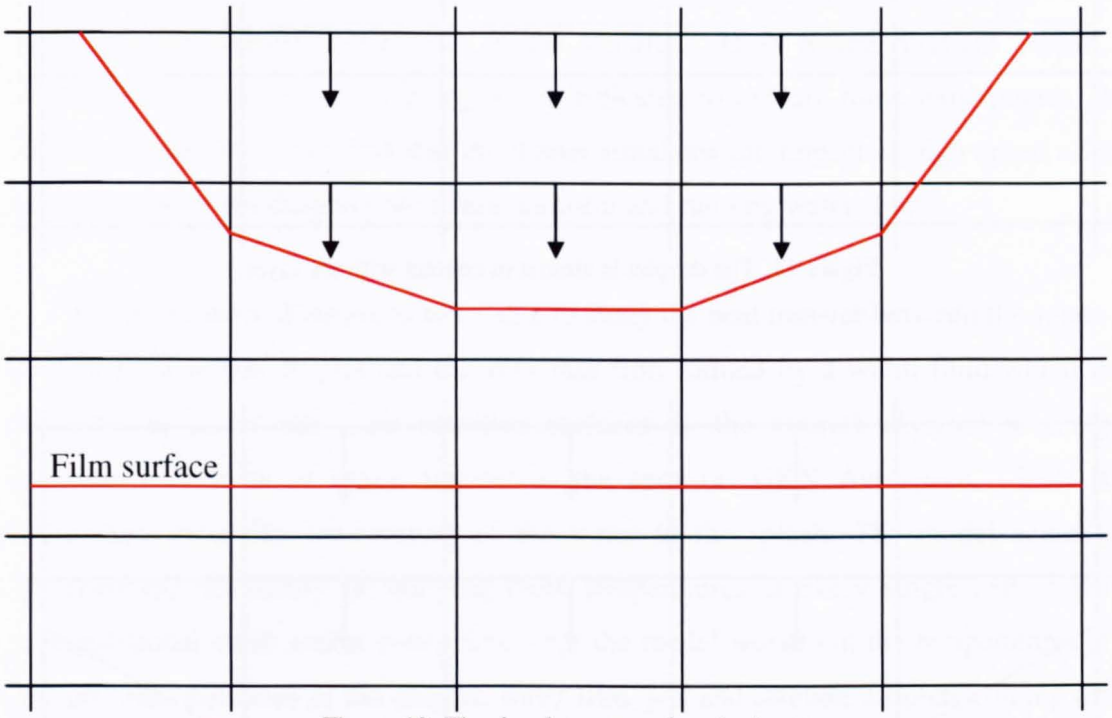

Figure 10. The droplet approaches the layer.

After a number of time-steps, can be found in the same cell free surfaces belonging to the droplet and to the layer that is when the first connection takes part. Figure 11 shows how the free surfaces will be without this attachment and figure 12 gives the detail of how it actually works in the method of Purvis. The pointed lines show how the situation would be without the reconnection. Also the model simulates the thin sheet that is ejected at high speed emanating horizontally from the neck region connecting the two liquids as is found on the literature (Weiss *et al.* 1999, Josserand *et al.* 2000, Thoroddsen, 2002).

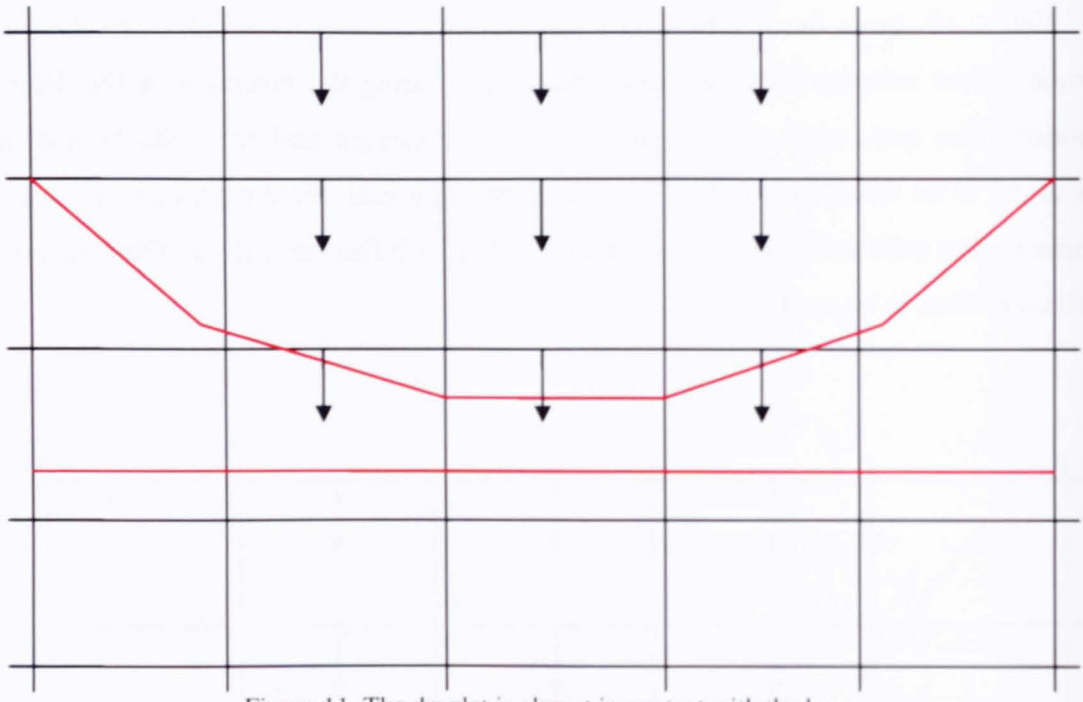

Figure 11. The droplet is almost in contact with the layer.

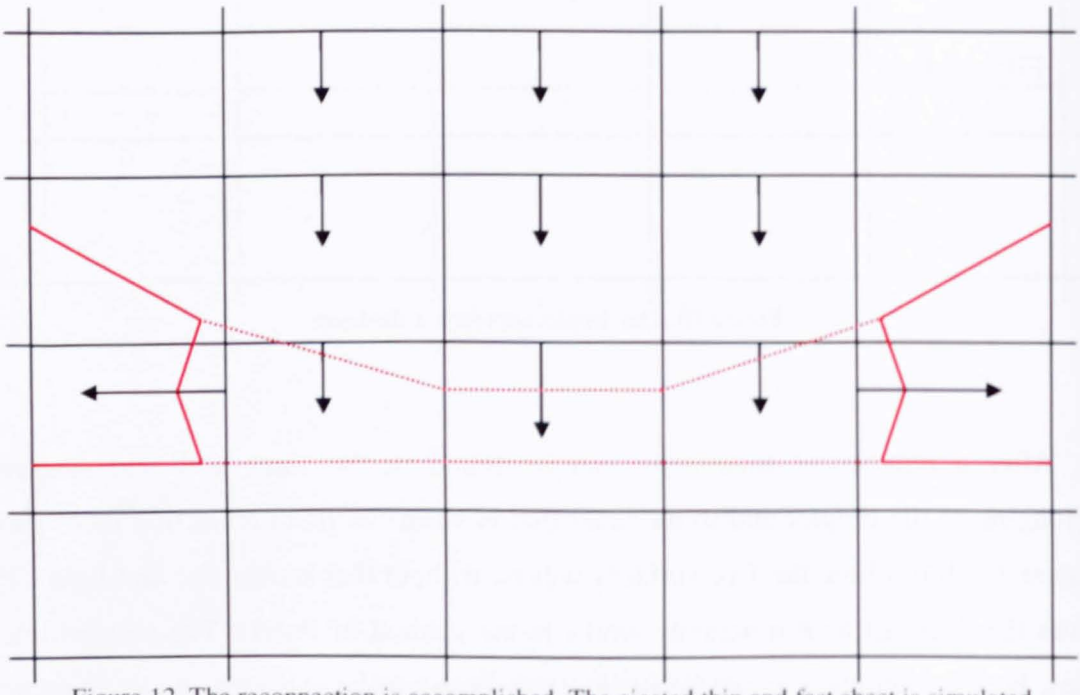

Figure 12. The reconnection is accomplished. The ejected thin and fast sheet is simulated.

Numerical model for the investigation into the thermal aspects of droplet impingement.

The initial Purvis model accurately simulates the free surface deformation during the impact of a droplet onto a water film. Both fluids are considered incompressible and inviscid. Making use of this, a new model is now built. The goals that are pursued are based on achieving two main objectives. One is to make possible a comparison with the experiments carried out in the Cranfield High Speed Vertical Tunnel. Although a whole section is going to be dedicated to explain these experiments, it should at least be mentioned that the tunnel simulates the impact at high speed of a super-cooled water droplet onto a thin, uniform and running water film.

The other main objective is to be able to study the heat transfer between the super-cooled fluid of the droplet and the very thin film formed by a warm fluid which is assumed to cover the most sensitive surfaces of the aircraft exposed to icing conditions. This is of major interest to the sponsor, GKN Aerospace, which is concerned about the temperature of the water in the splash. The model actually provides the possibility of studying these temperatures at every single cell of the computational mesh and at every time-step; the model works out the temperatures at the different positions of the droplet, water film, jets and satellite droplets coming off that water film during all the stages of the impact and later splash.

The development of the new model involves some enrichment and enlargement of the original method.

The new approach is focused on dealing with two different fluids, droplet and water film, whose mechanical behaviour and physical properties affect and are going to be affected by each other. Also it includes a consideration of temperature and several new parameters, some of them linked to temperature, in order to perform the heat transfer study and to give more realism to the simulations. Some of the parameters included in the initial Purvis model are to be linked to the temperature also.

Apart from these changes, other new variables were also incorporated once the experiments started to yield results. One of these new parameters is a tangential velocity that has been applied to the layer; so the model is able to simulate the thin running water film covering the target where the droplets are going to impact in the experiments. Another parameter arises because, as has been observed in the experiments, the droplets as they approach the target are affected by decelerating forces and subsequently they are flattened, depending on their velocity. Therefore the faster the droplet travels the more flattened it will to be. Thus it is possible in this model to use an oblate droplet depending on the velocity of impact, as exactly happens during the experiments.

Two Different Fluids.

Because one of the objectives is to compare the model with the experiments, a distinction between the fluids should be considered. This is motivated by the fact that the two liquids, super-cooled water droplet and layer, are initially at very different temperatures which can differ by as much as 30°C. This makes some of the physical properties have very different values in the different fluids. Therefore it is interesting to observe the effect that those changes have in the model.

To identify these new parameters in the computational mesh, the functions defining the volume of fluid in the cells have to be designated with different names depending on whether they are found in the droplet or in the layer. These new functions are:

- $F(x, y, t)$ is the function representing the volume of fluid in the layer.
- $f1(x, y, t)$ defines the volume in the droplet.
- $Fcc(x, y, t) = F(x, y, t) + f1(x, y, t)$ is the function defining the total fluid in the cell.

The pressures and velocities refer to the $Fcc(x, y, t)$ function and they are set in every cell in the same way as was shown in figure 7. Therefore at the initial point of

the simulation there are two kinds of cells in the computational mesh depending on whether they are in the droplet or the layer, as figures 13 and 14 illustrate. They give the location of the variables depending on the fluid in which they are placed.

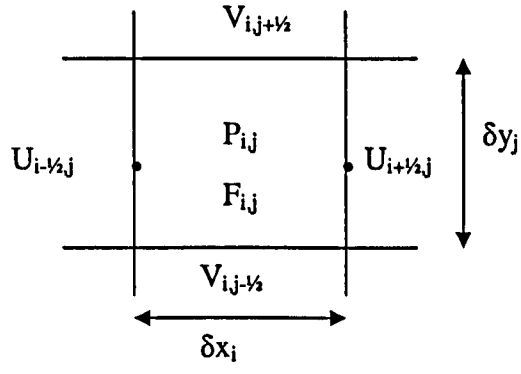

Figure 13. Location of variables in a layer cell.

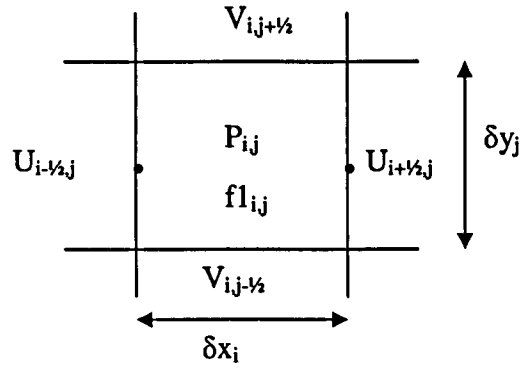

Figure 14. Location of variables in a droplet cell.

For the cases where there is only fluid from one liquid, the value of the variables for the Fcc(x, y, t) function will be the same as for the one with the fluid.

The velocities and the pressures are not related to the kind of fluid that is involved in the cell. These two parameters are related to the cell Fcc.

The velocity calculations are done using the finite difference approximation (equation (8)) method and based on Purvis's calculations. The changes that have been introduced are mainly related to the problem created by the increase in the number of

parameters considered including the different physical properties and the velocity applied in order to have a running water film.

The calculations needed for the adjustment of pressures and velocities are based also on Purvis's method and explained in the MAC section. The changes that have been introduced here are related mainly to the identification of the surface cells in order to improve the convergence and therefore to satisfy the continuity equation (1) but also to allow the calculations to be done for the Fcc function.

Once the velocities and pressures are calculated and adjusted, the progress of the droplet and film has to be computed taking into account their influence on each other. That is, once the droplet strikes the layer both free surfaces are going to change their initial shape. The droplet will "push" the film and this will produce two jets together with the drop. Also however each of them has different properties that, due to the changes in temperature and in the free surface during the process, will modify their values.

This advance in time is done independently for every function representing the two fluids, that is, the advancing in time for F representing the water of the layer and for f1 representing the water of the droplet. The temporal advance of the function Fcc is calculated assuming that its volume is the addition of the volume found in F and that in f1.

According to the SOLA-VOF method, occasionally some new values for the functions that represent the amount of fluid in the cells can be slightly less than zero or slightly more than unity. In order to accommodate this, once the advance has been calculated, one more adjustment has to be done. Specifically, a cell is defined to be empty when the values for the function meaning are less that 10^{-6}, and completely full of fluid if these values are greater than $1 - 10^{-6}$.

This fill factor adjustment is done independently for F and f1 and also for Fcc. The reason is that assuming $Fcc(x, y, t) = F(x, y, t) + f1(x, y, t)$ is not sufficient to prevent values for this function becoming less than zero or greater than one.

Thus the model gives three different kinds of free surfaces: one represents the surface and how this is pushed by the droplet to the bottom and to the sides, forming the jets; the second is the droplet and how this is deformed and distributed when impacting the surface; and the third one is the surface of the droplet and layer together.

The results obtained using this fluid "separation" for a 70 degrees impact are as follows.

Figure 15 shows the layer represented by function F(x, y, t) for the first time-step. No forces or velocities are disturbing it. The arrow indicates the direction of the impact. The horizontal and vertical axes illustrate the coordinates in millimetres.

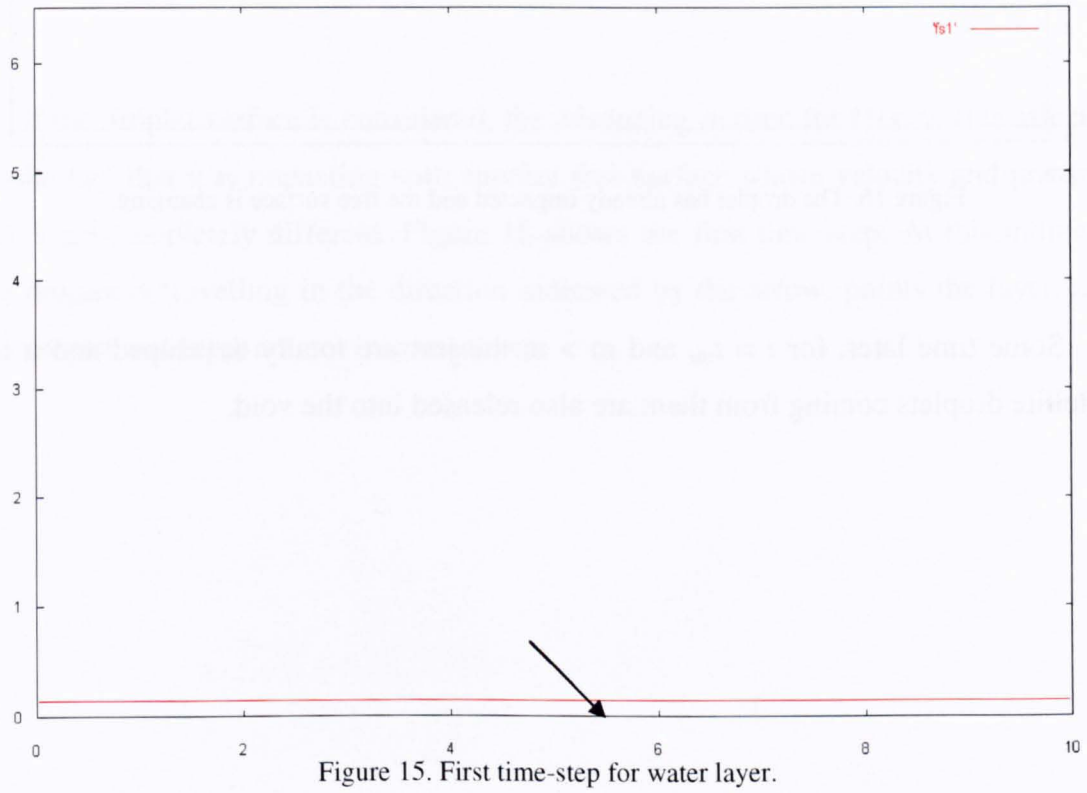

Figure 15. First time-step for water layer.

After a number of time-steps, the droplet strikes the film and begins to affect the film velocities. Prior to the impact, the values for $u(x, y)$ and $v(x, y)$ are zero. Following the droplet impact, they are changed and allow the layer to advance and to

change the shape of the free surface, changing also the values for $F(x, y, t_n)$ for the subsequent time step t_n.

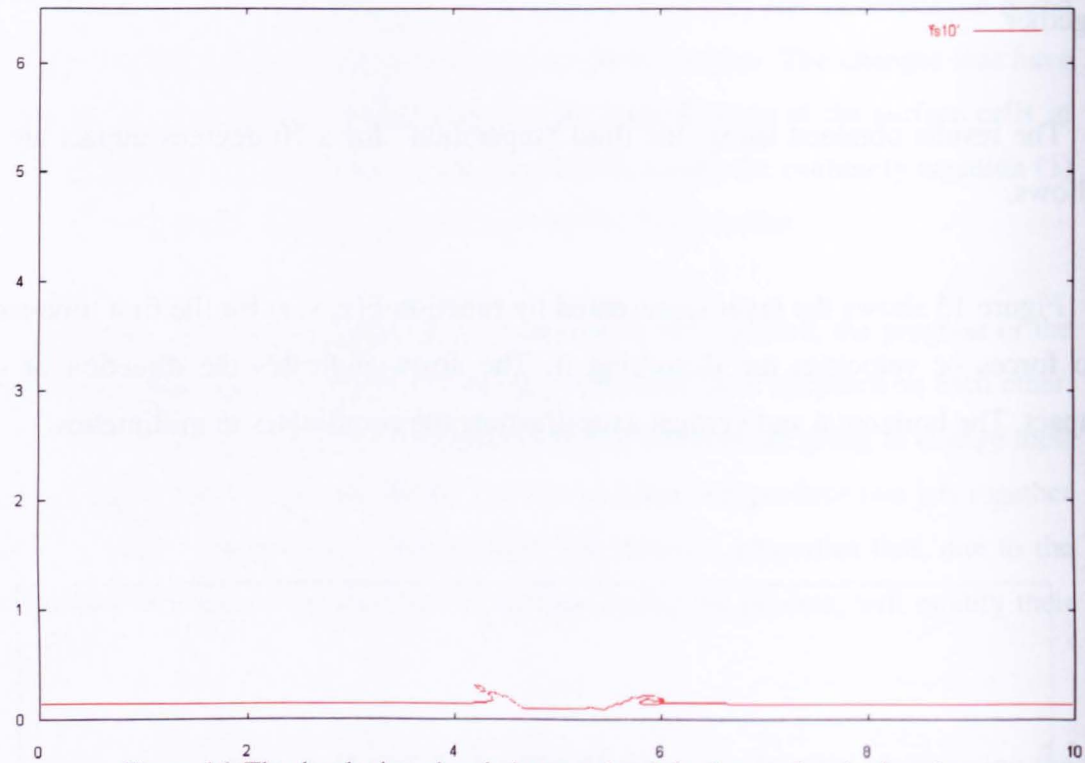

Figure 16. The droplet has already impacted and the free surface is changing.

Some time later, for $t = t_m$, and m > n, the jets are totally developed and a few satellite droplets coming from them are also released into the void.

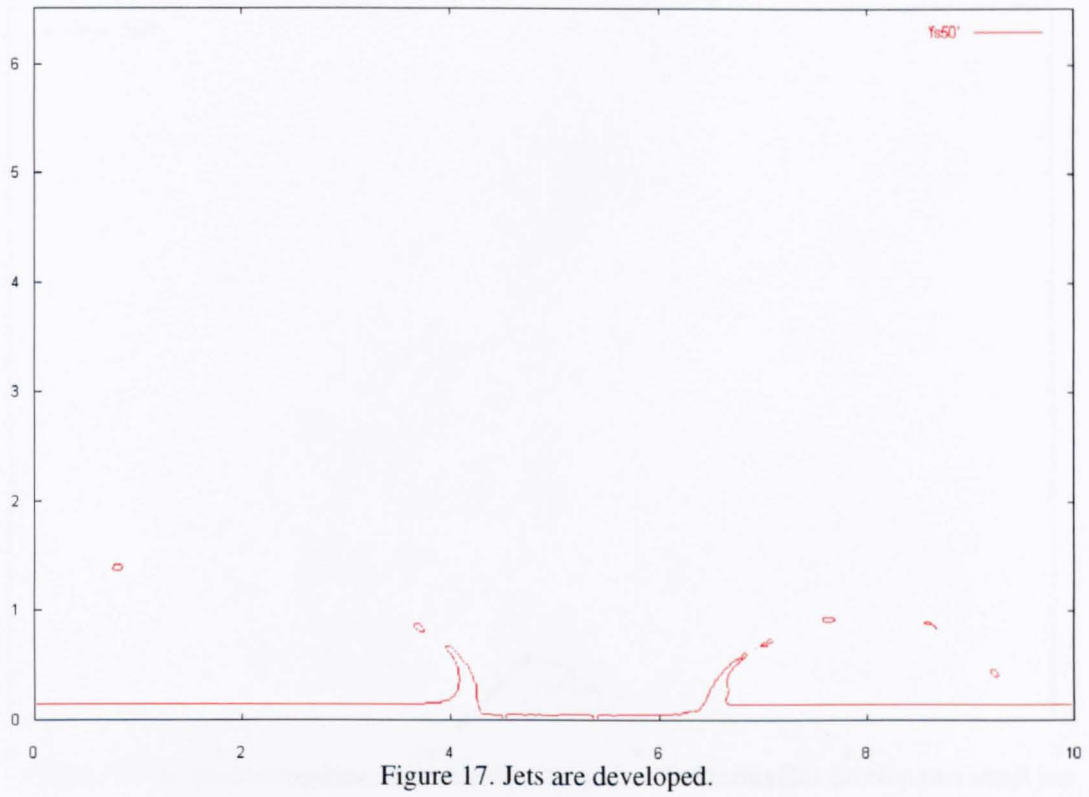

Figure 17. Jets are developed.

If the droplet surface is considered, the advancing in time for f1(x, y, t) is affected by the fact that it is impacting with another free surface whose velocity and pressure fields are completely different. Figure 18 shows the first time-step. At this moment, the droplet is travelling in the direction indicated by the arrow, points the layer, and the droplet and layer are not in contact yet.

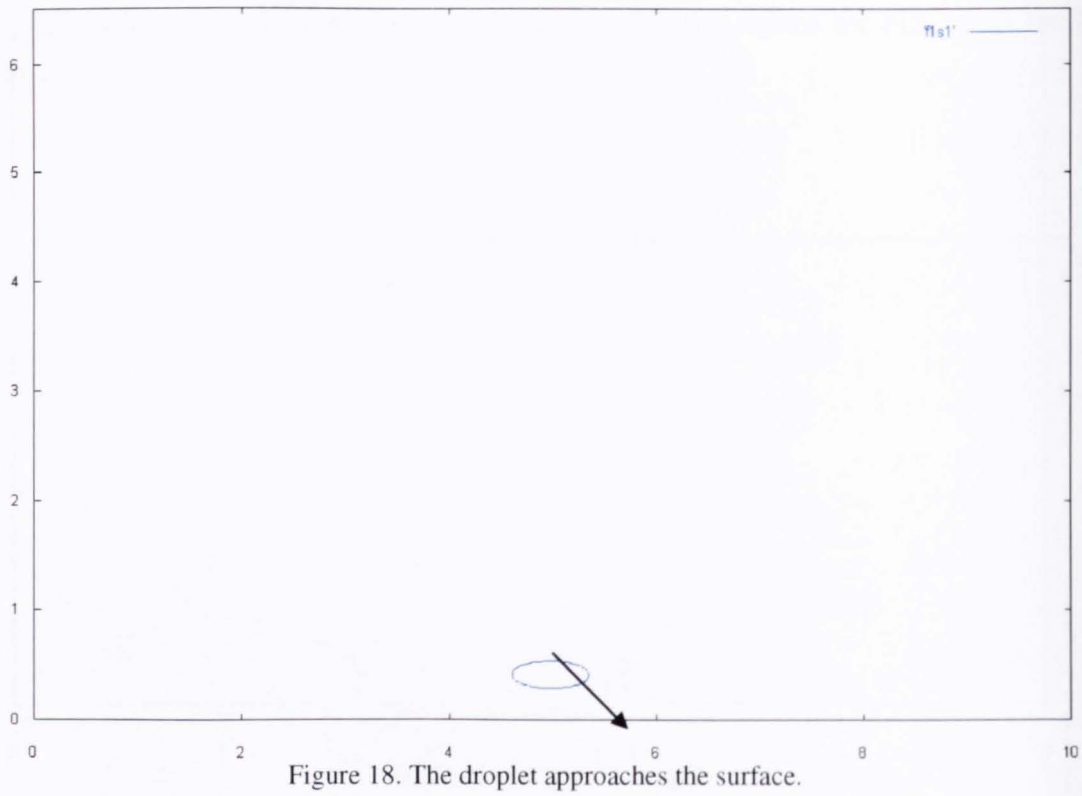

Figure 18. The droplet approaches the surface.

After a number of time-steps, the droplet impacts with the film and starts to change its surface according to the velocities and the different adjustments calculated. The values for $f1(x, y, t_n)$ change considering that there are neighbouring cells $F(x, y, t_n)$ greater zero or even, there are cells where both $F(x, y, t_n)$ and $f1(x, y, t_n)$ are greater than zero.

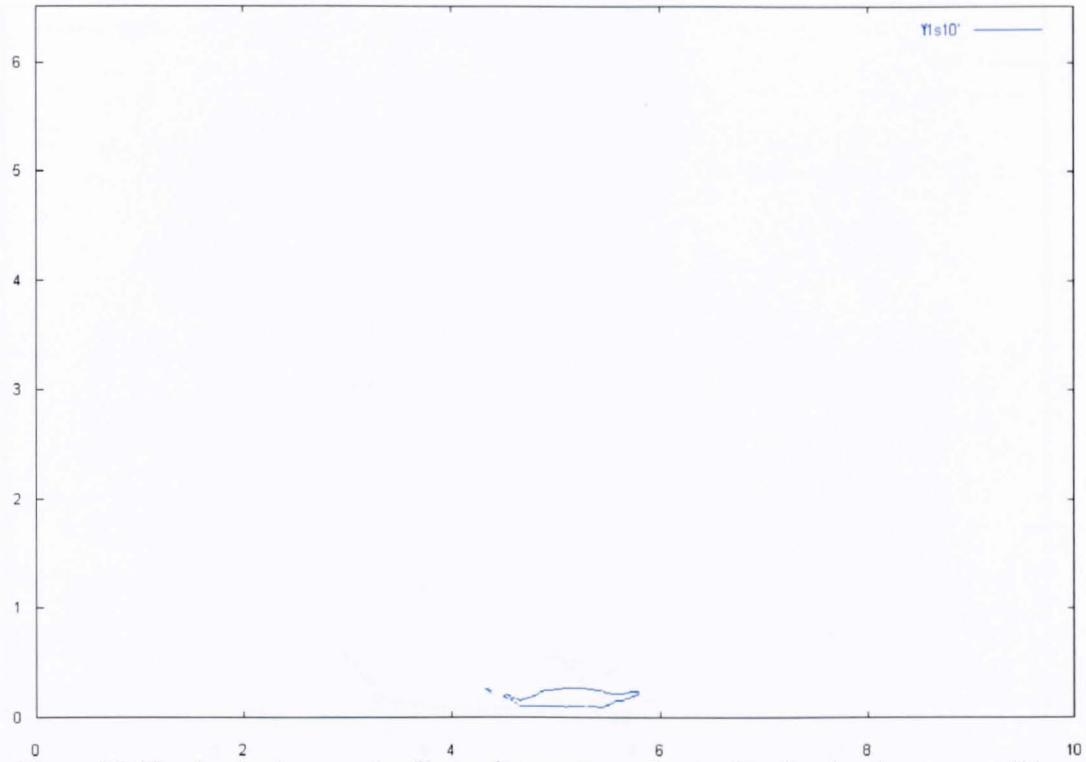

Figure 19. The droplet impacts the film and starts to get flattened and to develop two small jets.

For time-step t_m (m > n), figure 17 shows that the jets are totally developed. As can be seen in this figure, the droplet also contributes some fluid to the jets. This can be seen positioned more to the right side of the impact area. This is caused by the oblique angle of the impingement.

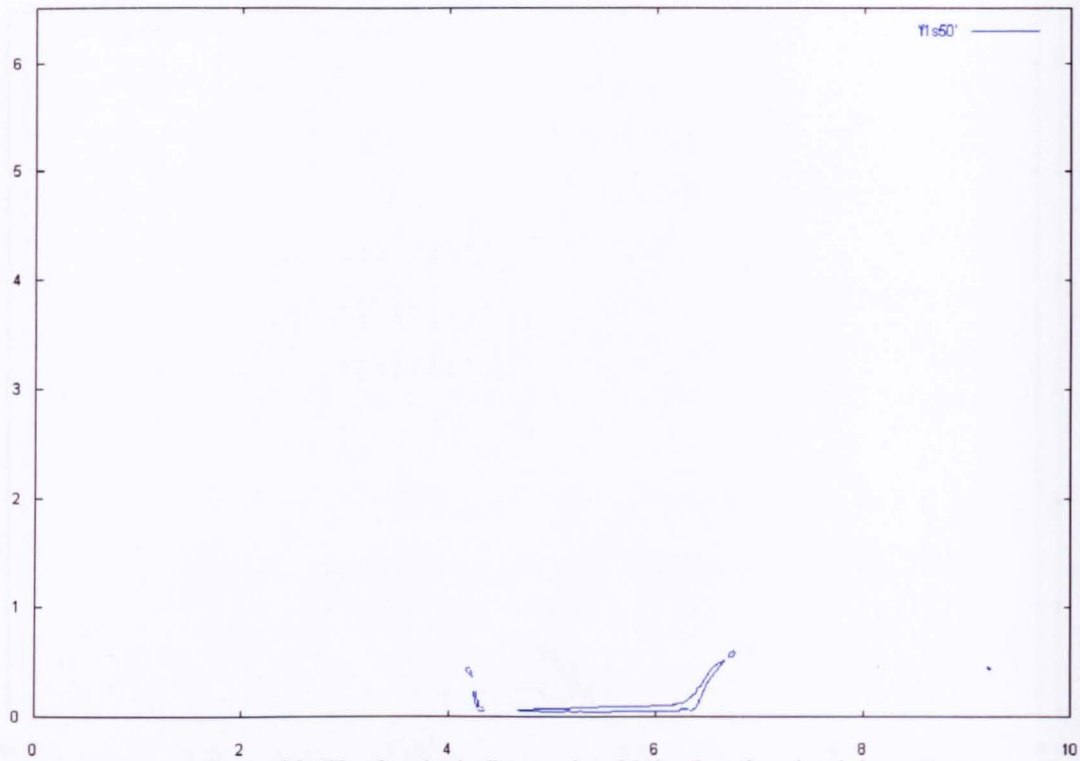

Figure 20. The droplet is flattened and it is placed to the right.

Finally, considering the three functions F, f1, and Fcc, a result giving the actual simulation of the droplet impacting at 70 degrees, at a velocity of 66 m/s, with 757μm width and 243μm height against a 150μm thickness film, can be seen in figures 21, 22 and 23 for the same time-steps as for the previous examples.

Figure 21 shows the first time-step. At this time, Fcc = f1 in the droplet and Fcc = F in the layer.

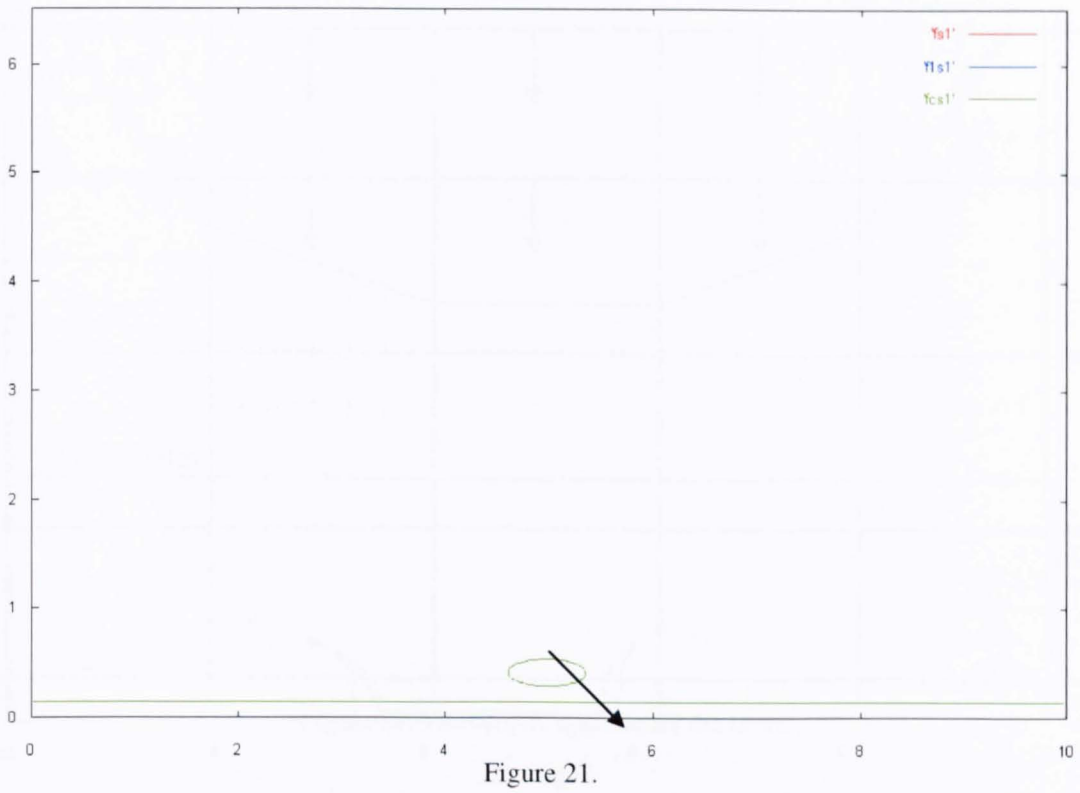

Figure 21.

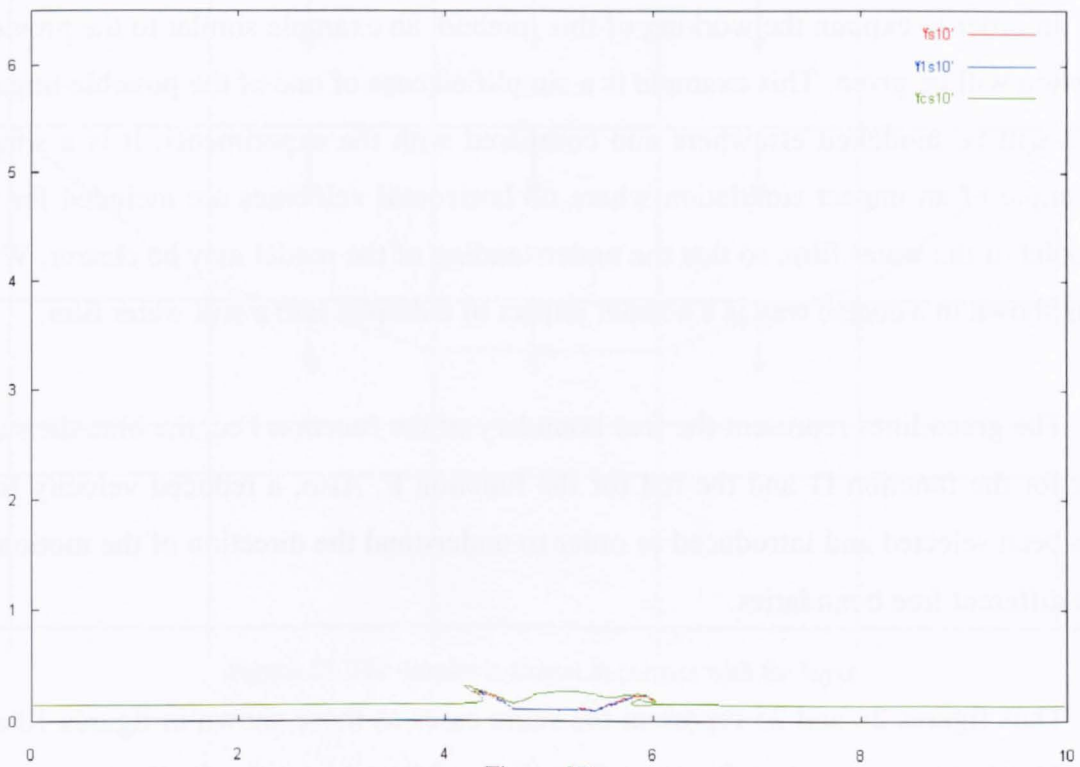

Figure 22.

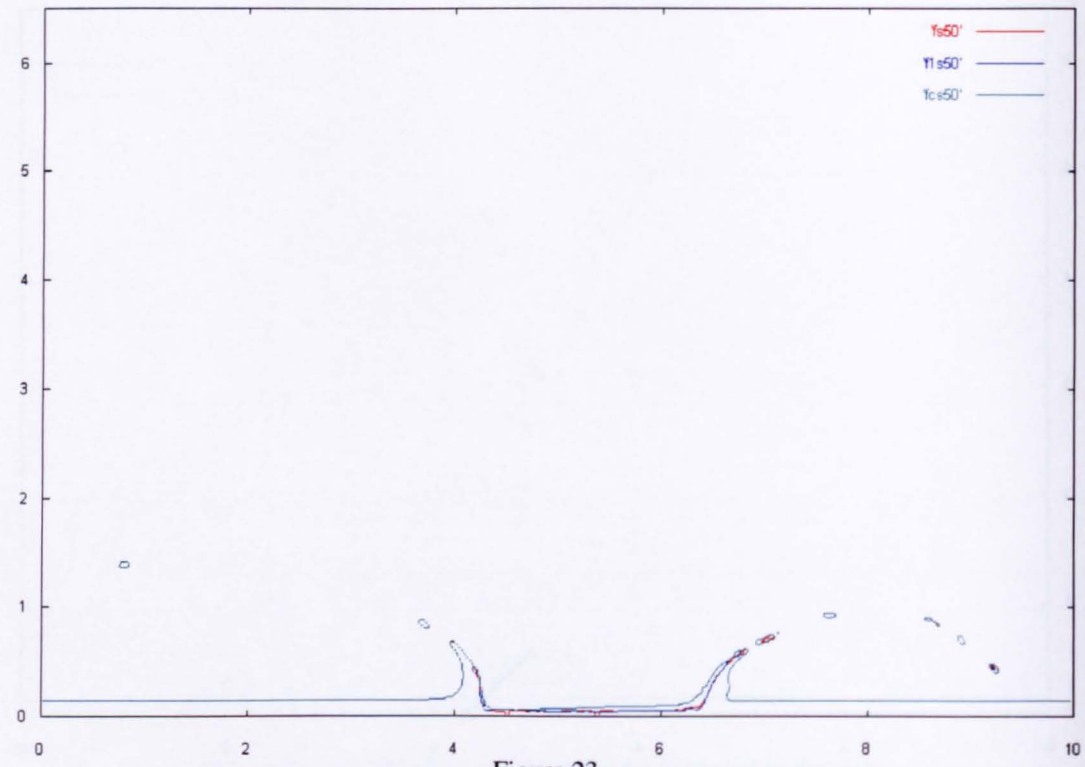

Figure 23.

In order to explain the working of this method, an example similar to the previous section will be given. This example is a simplified case of one of the possible impacts that will be modelled elsewhere and compared with the experiments. It is a simple example of an impact simulation where no horizontal velocities are included for the droplet or the water film, so that the understanding of the model may be clearer. What it is shown in a coarse way is a normal impact of a droplet into a still water film.

The green lines represent the free boundary of the function Fcc, the blue the same but for the function f1 and the red for the function F. Also, a reduced velocity field has been selected and introduced in order to understand the direction of the motion of the different free boundaries.

Thus figures 24 and 25 represent the same cases as those shown in figures 10 and 11. The droplet approaches the water film (figure 24) and later the droplet is almost in contact with the layer (figure 25).

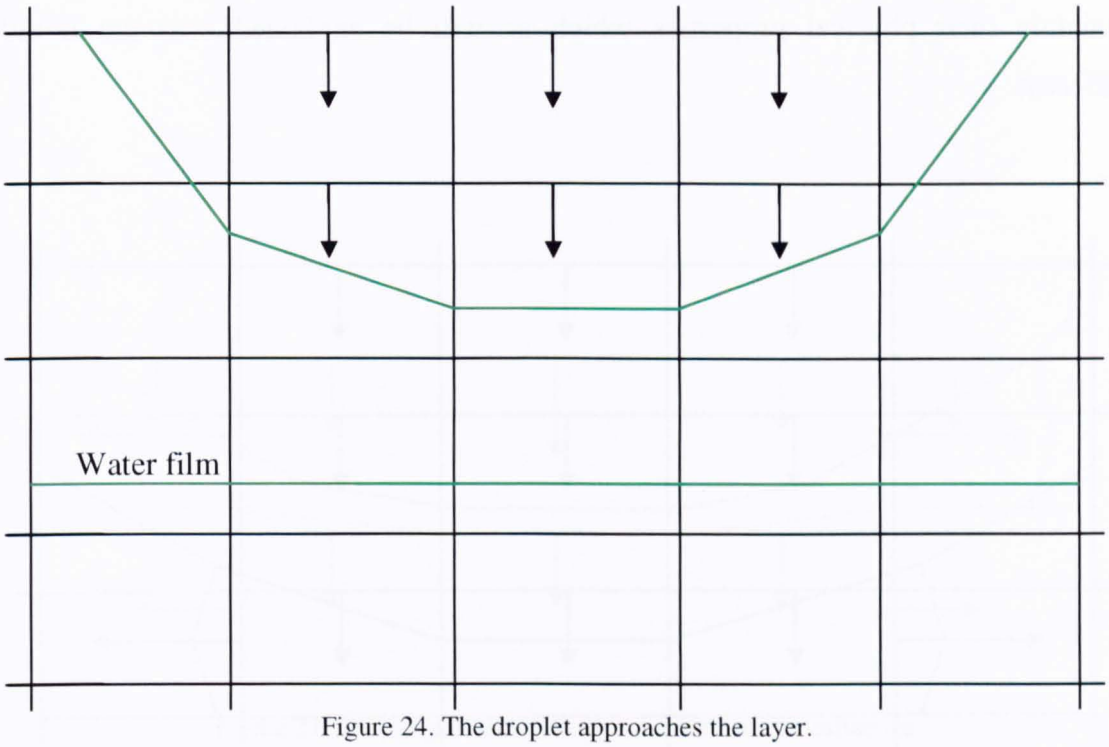

Figure 24. The droplet approaches the layer.

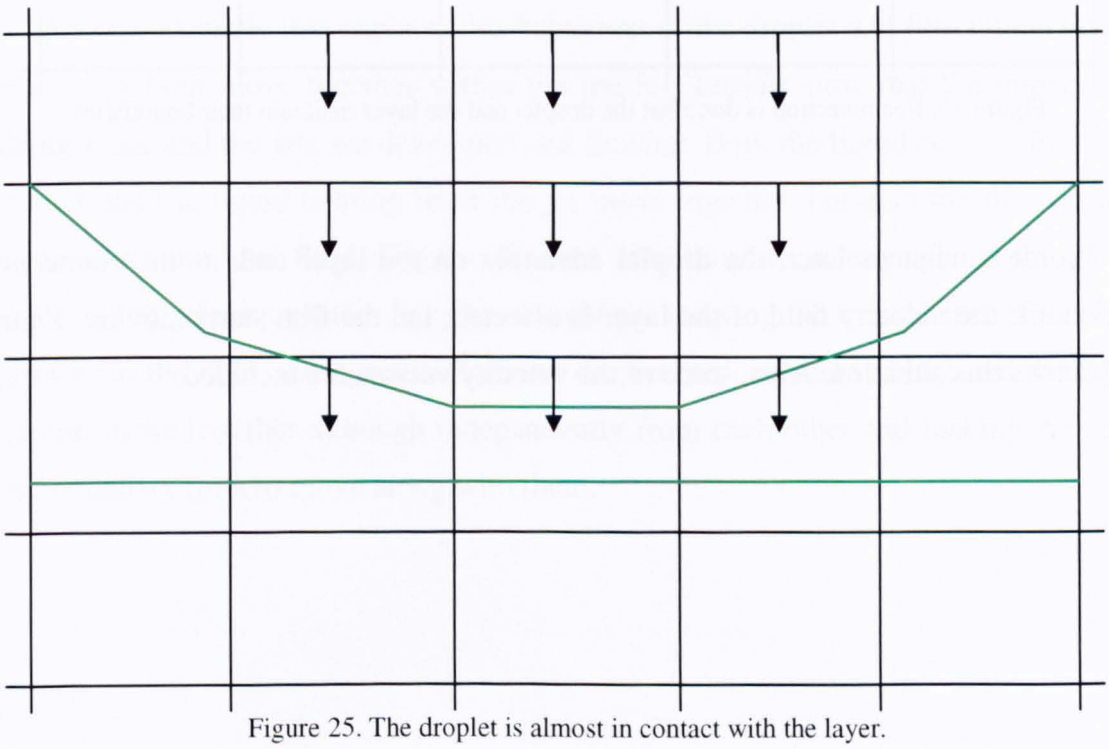

Figure 25. The droplet is almost in contact with the layer.

The differences start to show up during the first contact. The advance in time for function Fcc, representing the addition of F (layer) and f1 (droplet), gives a solution that is similar to the one found in figure 12. However the free surfaces representing the droplet and the layer remain in the computational mesh, allowing both liquids to

maintain their physical properties which as will be explained later are initially different.

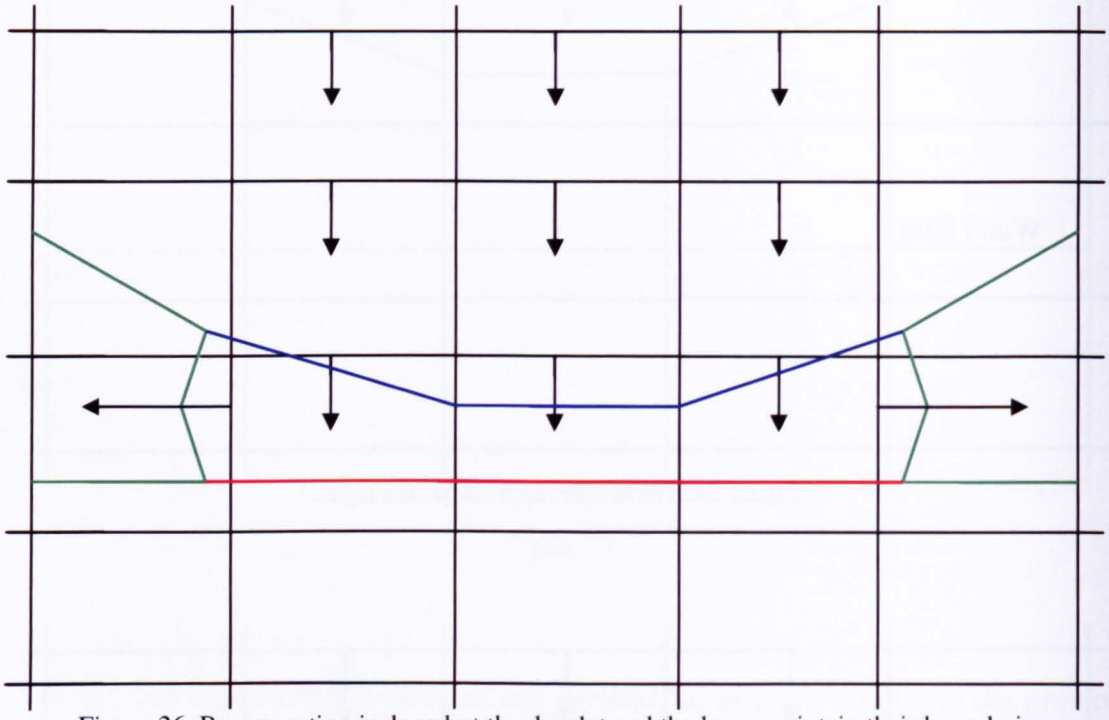

Figure 26. Reconnection is done but the droplet and the layer maintain their boundaries.

Some time-steps later, the droplet advances on the layer and, as the connection develops, the velocity field of the layer is affected, i.e. the film starts moving. Figure 27 shows this situation. Also, some of the velocity vectors are included.

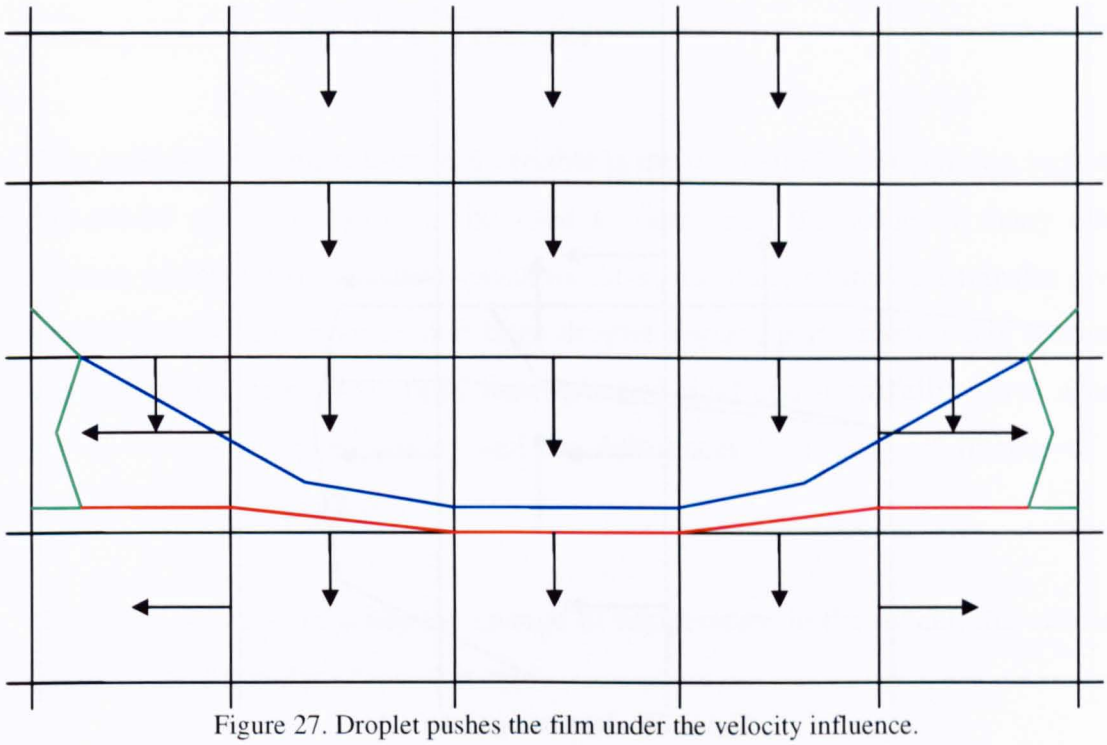

Figure 27. Droplet pushes the film under the velocity influence.

Another example that explains this behaviour of the droplet and film interaction is when they both move together within the mesh. Consider now that the impact has taking place and the jets are developed and flowing. Both the liquid coming from the droplet and the liquid coming from the jet move together, but also the free surface representing the total fluid. Figures 28a and 28b illustrate an example of this flow. Some of the velocity vectors have been included showing the movements of the free surfaces to the right and upward. Both the droplet (represented in blue) and the layer (in red) move together although independently from each other and making the total free boundary (green) move along with them.

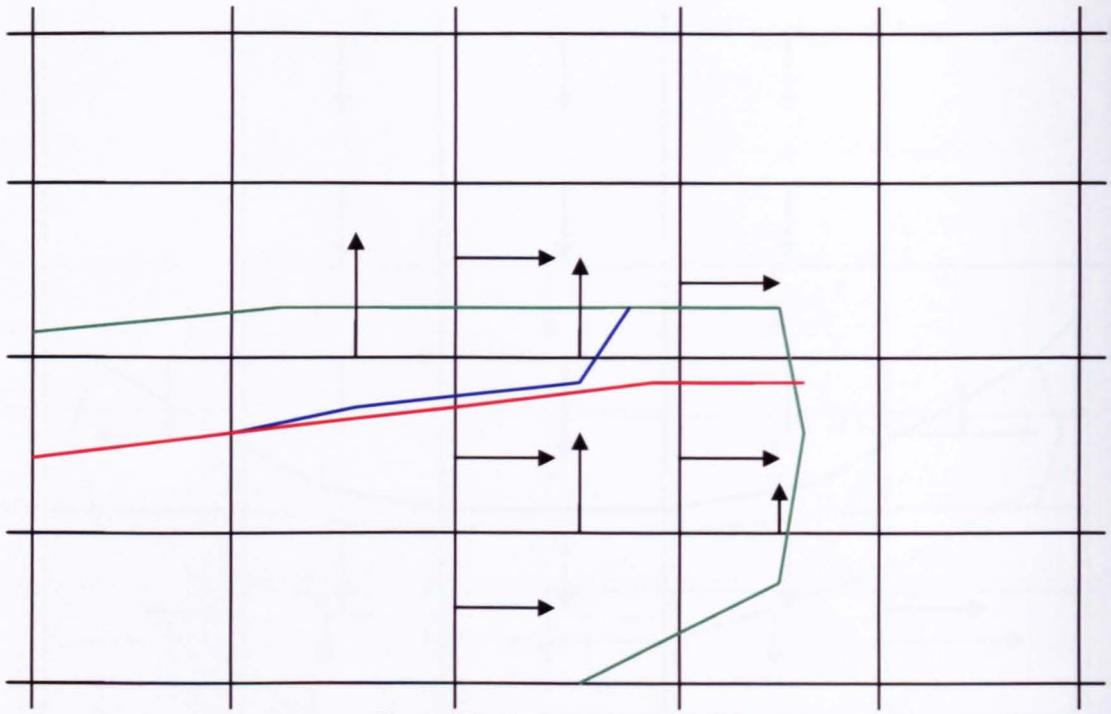

Figure 28a. Jet moving to the right.

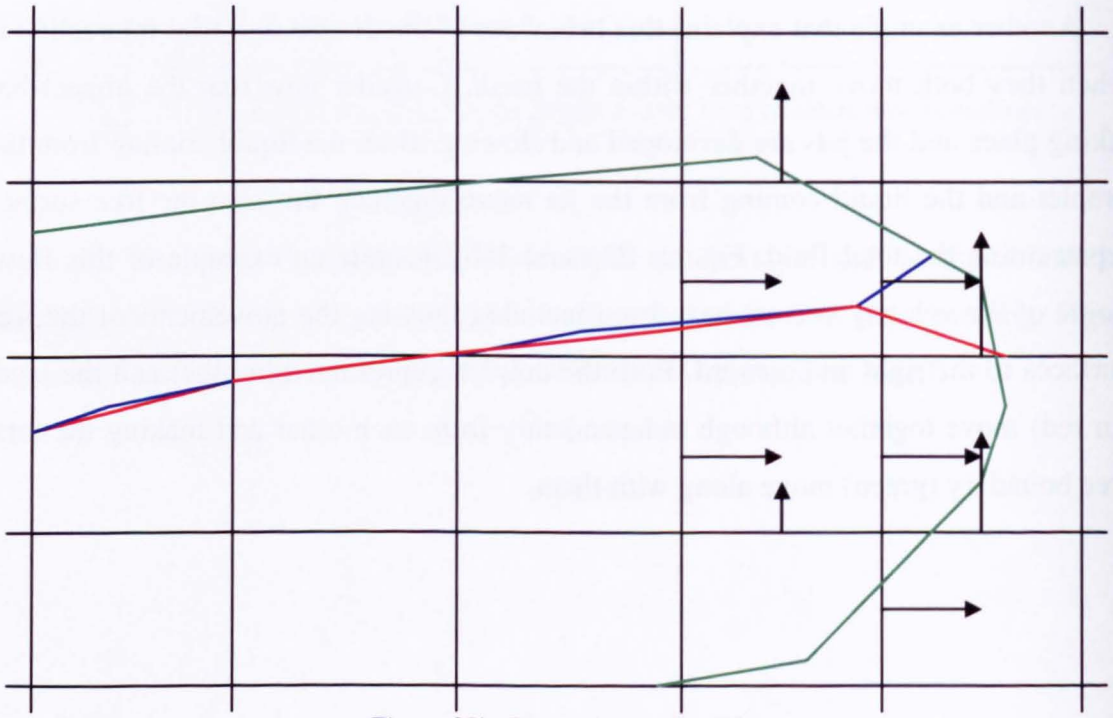

Figure 28b. Jet moving to the right.

Temperature and Heat Transfer.

The inclusion of temperature as a variable is the most significant addition included in the model and it is going to be used to determine the value of many other parameters which are temperature-sensitive. Also, the study of the heat transfer gives additional insight into super-cooled large droplet impact, particularly when it comes to considering the heat taken away with splashed fluid and (hopefully) gives a new vision of what is really happening and the differences from the performance of an impact at ambient temperature.

In order to be able to study the change of temperature in the model, the classical equation for heat transfer (23) is solved,

$$T_t + \vec{u} \cdot \nabla T = k(T_{xx} + T_{yy}) . \tag{23}$$

The result gives the value for the function temperature $T(x, y, t)$ depending on position and time. Hera again $\vec{u}$ is the velocity vector and k is the thermal diffusivity.

The equation has an imposed boundary condition (24) that has to be satisfied,

$$\frac{\partial T}{\partial \vec{n}} = 0 . \tag{24}$$

This condition indicates that there cannot be heat transfer between the fluid and the cell pointing in the direction of $\vec{n}$, the normal exterior vector to the liquid surface. Figure 29 shows an example of what this boundary condition indicates. The first time step is considered in the picture; therefore for this case heat cannot be released from either fluid (droplet or layer) to the void. Thus this heat flows only between fluids.

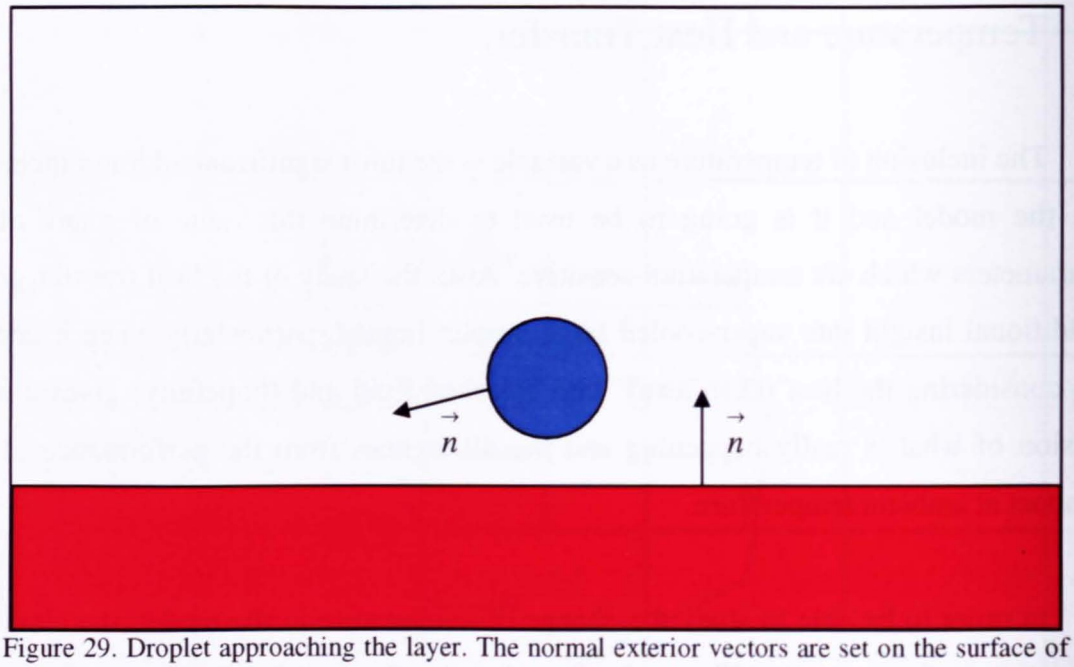

Figure 29. Droplet approaching the layer. The normal exterior vectors are set on the surface of the droplet and the film. Is in that direction where there is not going to be heat transfer.

Lastly, as already mentioned, there is the two-liquids condition that is imposed on the equation in order to distinguish between droplet and layer. Initially different temperatures are given to each fluid. This initial condition means that, from the beginning, the droplet and the layer have almost all their parameters with different values since as has been mentioned earlier they depend on the temperature.

Therefore, the equations to be solved in the model are:

$$\begin{aligned} &T_t + \vec{u}\cdot\nabla T = k(T_{xx} + T_{yy}), \\ &\frac{\partial T}{\partial \vec{n}} = 0, \\ &T_{Layer} = \text{Initial layer temperature}, \\ &T_{Droplet} = \text{Initial droplet temperature}. \end{aligned} \tag{25}$$

To solve the equation, finite-differences approximations are used. Therefore in order to obtain the temperature under these conditions, the following are defined:

$$T_t \cong \frac{T^{n+1}(i,j) - T^n(i,j)}{\delta t}, \tag{26}$$

$$T_{xx} \cong \frac{T^n(i+1,j)-2\cdot T^n(i,j)+T^n(i-1,j)}{(\delta x)^2}, \tag{27}$$

$$T_{yy} \cong \frac{T^n(i,j+1)-2\cdot T^n(i,j)+T^n(i,j-1)}{(\delta y)^2}, \tag{28}$$

$$T_x \cong \frac{T^n(i,j)-T^n(i-1,j)}{\delta x} \text{ If } u(x,y) > 0, \tag{29}$$

$$T_x \cong \frac{T^n(i+1,j)-T^n(i,j)}{\delta x} \text{ If } u(x,y) < 0, \tag{30}$$

$$T_y \cong \frac{T^n(i,j)-T^n(i,j-1)}{\delta y} \text{ If } v(x,y) > 0, \tag{31}$$

$$T_y \cong \frac{T^n(i,j+1)-T^n(i,j)}{\delta y} \text{ If } v(x,y) < 0. \tag{32}$$

So the temperature is given by:

$$T^{n+1} = T^n + \delta t\left(-uT_x^n - vT_y^n + k\left(T_{xx}^n + T_{yy}^n\right)\right) \tag{33}$$

Hence the equation gives the value of the function T in a giving cell for the next time step.

In order to keep the model dimensionless the parameter k is not used directly in the equation. Instead, the dimensionless number

$$a = \frac{1}{\mathrm{Pr}\cdot\mathrm{Re}} \tag{34}$$

is used. Here Pr is the Prandtl number which is defined as

$$\mathrm{Pr} = \frac{Cp\cdot\mu}{k_c}, \tag{35}$$

where Cp is the specific heat, v is the dynamic viscosity and k_c is the thermal conductivity.

Also Re is the Reynolds number defined by:

$$\mathrm{Re} = \frac{V \cdot D}{\nu}. \tag{36}$$

Here V is the velocity and D the diameter of the droplet or the thickness of the water film.

All these new parameters are also included in the model and their values are related to the temperature. This point will be explained in more detail below.

The fact that the temperature is set in one whole cell, and does not refer to the amount of fluid in it, means that certain considerations are necessary in some specific cases, particularly in those where the cell contains a free boundary. Thus the temperature calculations are not always done in the same way.

Two main cases are distinguished:

- T.1: Temperature calculation for a cell full of fluid.
- T.2: Temperature calculation for a surface cell.

It is assumed that for empty cells the temperature is always zero.

T.1 *Temperature calculation for cell full of fluid.*

For this case, the calculations are based strictly on solving the heat transfer equation, so (33) is used. Two different examples for temperature calculation in cells full of fluid are illustrated in figures 30a and 30b. The first one shows a cell (i, j) full of the same fluid; in this case the liquid comes from the layer. In order to find the temperature inside, the temperatures on the neighbouring cells are taken into account as set by the finite-difference approximation. Hence this (i, j) cell is affected by the temperature in cell $(i, j+1)$. If there is the situation where all the neighbouring cells have the same temperature, as can happen in the layer and in the water before impact,

the temperature is affected only by the velocities which are affected by the viscosity (see eq (4) in SOLA VOF) and the thermal diffusivity.

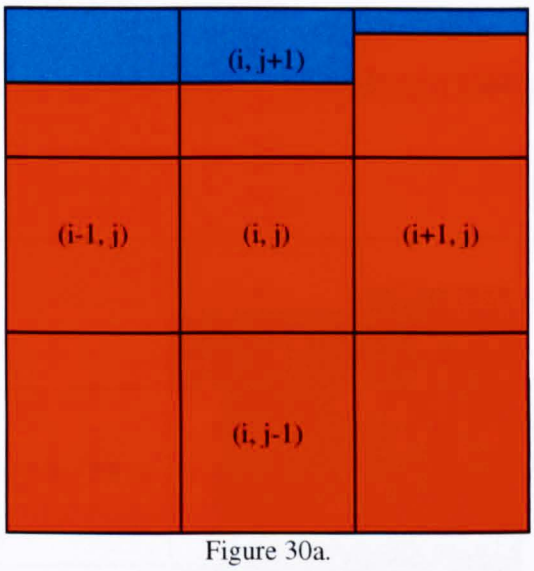

Figure 30a.

The other case of cells full of fluid is represented in an example in figure 30b. Here the cell is partially filled by fluid from the layer and partially with fluid from the droplet. The way the temperature is calculated is the same as for the previous case, that is, from solving the heat transfer equation. The temperature at cell (i, j) is affected also by all the different temperatures that are found in the neighbouring cells.

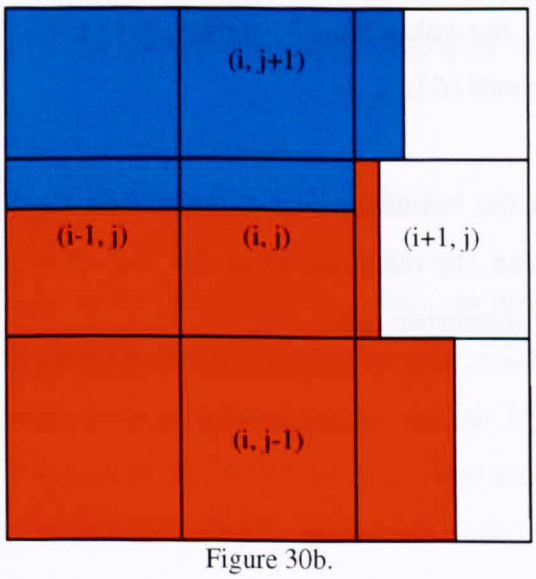

Figure 30b.

T.2 *Temperature calculation for surface cell.*

At this point it is necessary to distinguish two different cases. One is when the boundary cell is filled with only one liquid (figure 31) and the other when the boundary cell contains fluid from both the droplet and the layer as shown in figure 32.

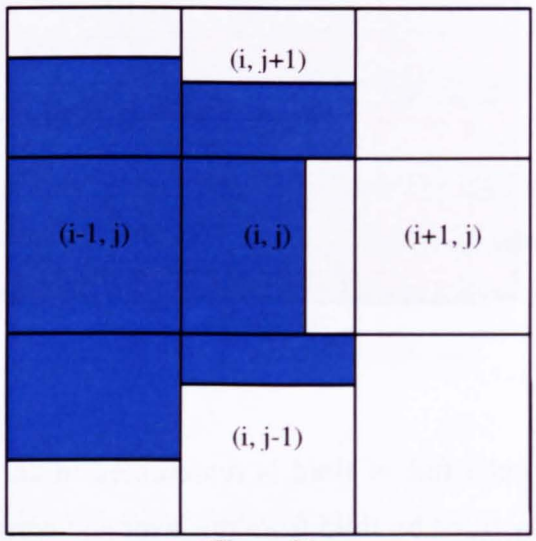

Figure 31.

For the first situation, the temperature in the boundary cell (i, j) is not calculated according to the heat transfer equation. What is done instead is that the cell is given the value of the temperature of the neighbouring cell filled with more fluid. Therefore, according to figure 31, the value that the temperature takes in cell (i, j) is the value that this variable has in cell $(i\text{-}1, j)$.

For the case when the boundary cell contains two fluids equation (33) is again used. As can be observed, the temperature in this cell takes into account the different temperatures of the neighbouring cells.

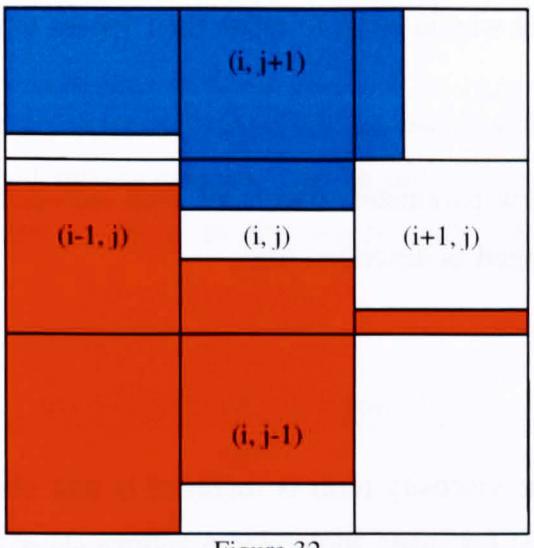

Figure 32

Once the temperature is calculated in every cell the values that the parameters for the fluids take are related to the value of the temperature. Thus these variables are different depending on the cell of the computational mesh where they are found.

Grid Dependency.

The computational grid is formed by 400 x 200 cells. This permits to have an accurate simulated result in order to be compared with the experiments as it will be seen in future chapters. Nevertheless, some work has been also done in order to see how the results changed when the grid was refined; in particular grids formed by 800 x 500 cells were used. The results obtained did not reveal significant differences in the splash development or in the free surfaces between both cases and, due to the much longer time of calculations, the choice of the 400 x 200 grid was eventually taken.

New parameters.

The inclusion of the temperature function implies, as has been seen already, the inclusion of some new parameters that allow the calculation. However, other new variables have been added to the model and they are not linked to the temperature calculations. This is motivated by the desire to give more realism to the simulations. Also some parameters that were already included, such as surface tension, are

calculated in a different way in order to relate their values to the temperature in every cell.

Accordingly the new parameters that have been included or they way they have been calculated is changed as described next.

P.1. *Viscosity.*

The reason that the viscosity term is included is that observations (Trinh *et al.*, 1994 and Hallett, 1963) for super-cooled temperatures show this parameter increases dramatically at temperatures below freezing point, as can be seen in graph 3. The lower the temperature, the more viscous the fluid is.

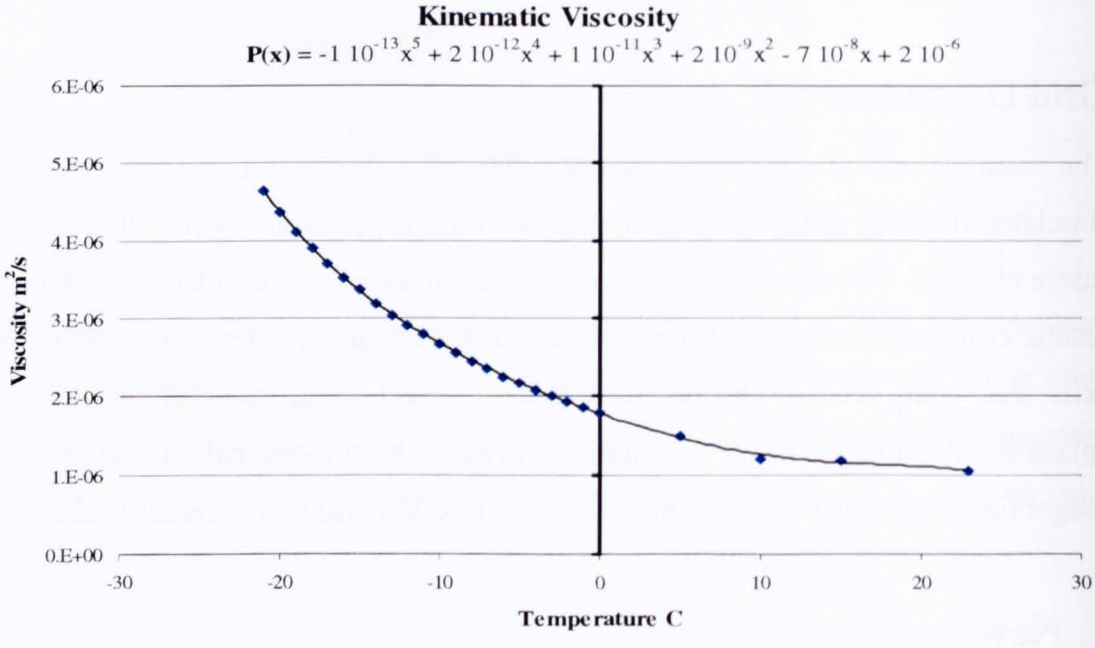

Graph 3.Kinematic viscosity against temperature for super-cooled water.

The value for the viscosity can be approximated by a polynomial and related to the temperature. If T represents the value of this parameter, the kinematic viscosity becomes given by:

$$P(T) = -1\ 10^{-13}T^5 + 2\ 10^{-12}T^4 + 1\ 10^{-11}T^3 + 2\ 10^{-9}T^2 - 7\ 10^{-8}T + 2\ 10^{-6}. \qquad (37)$$

The viscosity term appears in equation (8). Thus the viscosity term in (8) that affects the velocity is calculated solving equation (10). In order to find that term, a finite-difference approximation is made to the second order derivative. Hence the calculation to do is

$$\frac{\partial^2 u}{\partial x^2} \cong \frac{u(i+1,j)-2\cdot u(i,j)+u(i-1,j)}{(\delta x)^2}, \tag{38}$$

For the y direction and for term v of the velocity the procedure is analogous.

Once the viscosity is calculated, the dimensionless Reynolds number (36) is determined.

P.2. *Specific Heat C_p.*

Previously it has been seen that the inclusion of specific heat is required because of the use of the heat transfer equation and, in particular, with the non-dimensionalisation of the thermal diffusivity term using the Prandtl number (35). By definition:

$$Cp = \frac{k_c}{\rho \cdot k}, \tag{39}$$

where k_c is the Thermal Conductivity, ρ is the density and k is the Thermal Diffusivity.

P.3. *Thermal Conductivity k_c.*

In order to determine the appropriate value of the specific heat, the thermal conductivity for the water, including super-cooled features, is also considered as seen in (39). Graph 4 reflects the steady decreasing of the thermal conductivity when the temperature decreases. There is a weak change when the water is super-cooled,

although a slightly more marked decreasing is noticed (Benchikh *et al.*, 1985 and Saito *et al.* 1996).

The thermal conductivity is approximated by the polynomial

$$P(T) = 0.0336T^3 - 0.5033T^2 + 222.67T + 55511, \quad (40)$$

where T represents the temperature in the cell.

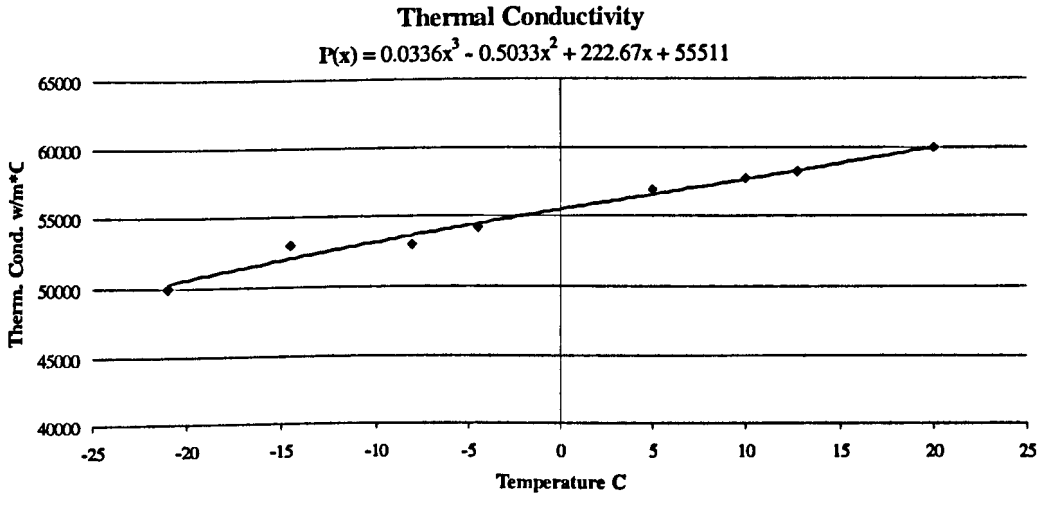

Graph 4. Thermal Conductivity against temperature for super-cooled water.

P.4. *Density ρ.*

This parameter has not been changed from Purvis's method or neither has the way of calculation. It is kept as it was originally. The value for the density is always considered as unity, independent of the fluid in question. This is because the changes are so small that they can be neglected.

P.5. *Thermal Diffusivity k.*

As has been mentioned already, this is a key parameter for calculating the heat transfer. However, it is also necessary to determinate the specific heat (39).

Based on experimental data (Benchikh *et al.*, 1985), the thermal diffusivity is approximated by using a polynomial depending on the temperature (41). Graph 5 shows the decreasing of the values of this parameter together with the decreasing of the temperature. Below freezing point the values for the thermal diffusivity decrease more rapidly. Here

$$P(T) = 2\ 10^{-13}T^3 - 1\ 10^{-11}T^2 + 6\ 10^{-10}T + 10^{-7}. \qquad (41)$$

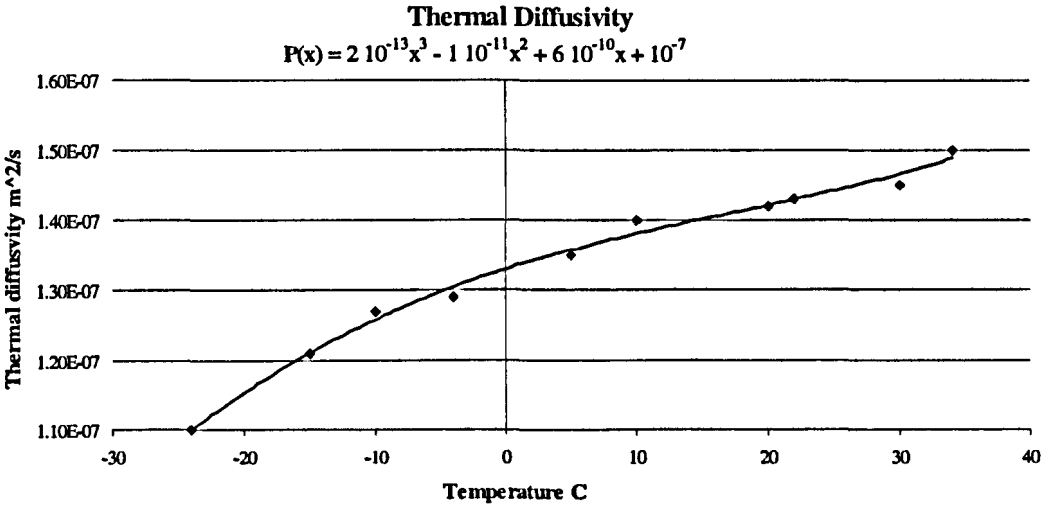

Graph 5. Thermal Diffusivity against temperature for super-cooled water.

Once the thermal diffusivity is calculated it is possible to determine the heat capacity and therefore the dimensionless Prandtl number (35). Thus the also dimensionless number a in (34), used for the calculation of temperature in every cell, is worked out.

P.6. *Surface Tension.*

Surface tension is one of the parameters included in the SOLA-VOF algorithm and also in Purvis's method although it is considered as a constant. However, in this model for the heat transfer calculation the surface tension is also linked to the

temperature. Hence the values depend on the temperature of every cell containing fluid at every time step.

Based on experimental data (Trinh *et al.*, 1994 and Hallett, 1963) the values for this parameter have been approximated by a polynomial depending on T

$$P(T) = -7\ 10^{-8}T^3 + 3\ 10^{-7}T^2 - 0.0001T + 0.075. \quad (42)$$

So it is possible for the model to apply the different values of this variable when the temperature decreases or increases as shown in graph 6.

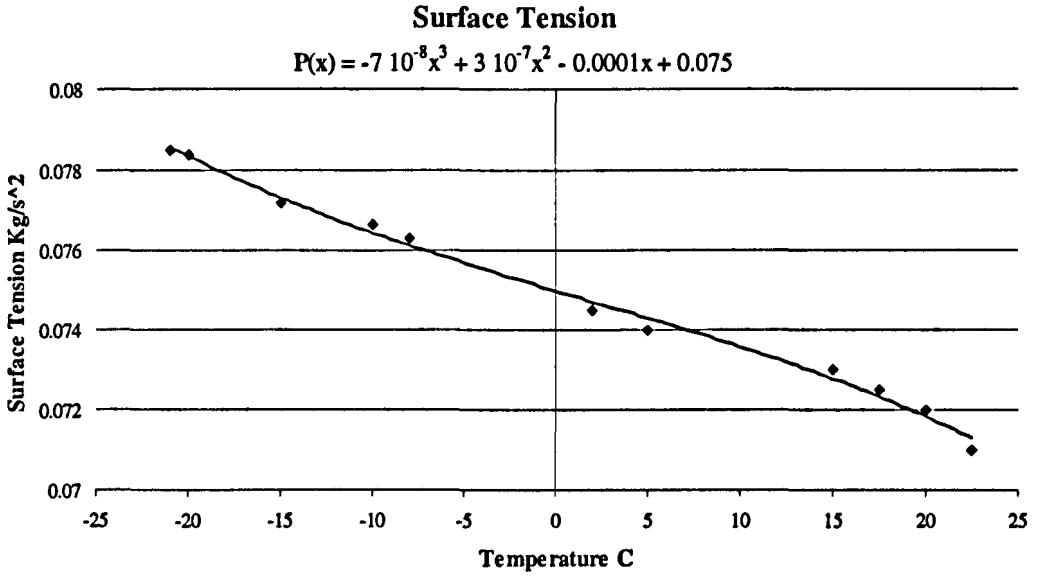

Graph 6. Surface Tension against temperature for super-cooled water.

In order to make use of the surface tension, another dimensionless number is included. It is the Weber number

$$We = \frac{V^2 D\rho}{\sigma}, \quad (43)$$

This number is necessary in order to calculate the pressure on the free surfaces. Here V is the velocity, D the droplet diameter or the water film thickness, ρ the density and σ the surface tension.

P.7. *Running Water Film.*

As has been explained above, one of the aims of the modelling is to compare the results with experiments. In order to achieve this it is important to recreate as accurately as possible the environment in which these experiments are developed. Thus, because of the running water film covering the target where the droplets impinge and produce the splash, the model is provided with a running layer simulating this moving film.

A horizontal velocity is applied to the layer at the left side of the domain, that is, $v(1, y) = 0$ and $u(1, y) > 0$ for all y, meaning that the whole film moves initially at constant velocity from left to right. Also the boundary conditions are changed so that the left side has a permanent steady horizontal velocity and the right side is changed in order to allow fluid to flow out of the mesh. Thus the running water film is applied. Different film thicknesses are also accommodated.

Figure 33 illustrates the velocity field at moments prior to impact. The droplet is represented by the oblique lines following the direction of the droplet track that will impact at 73 degrees. The horizontal lines at the bottom are the velocity fields for the water film.

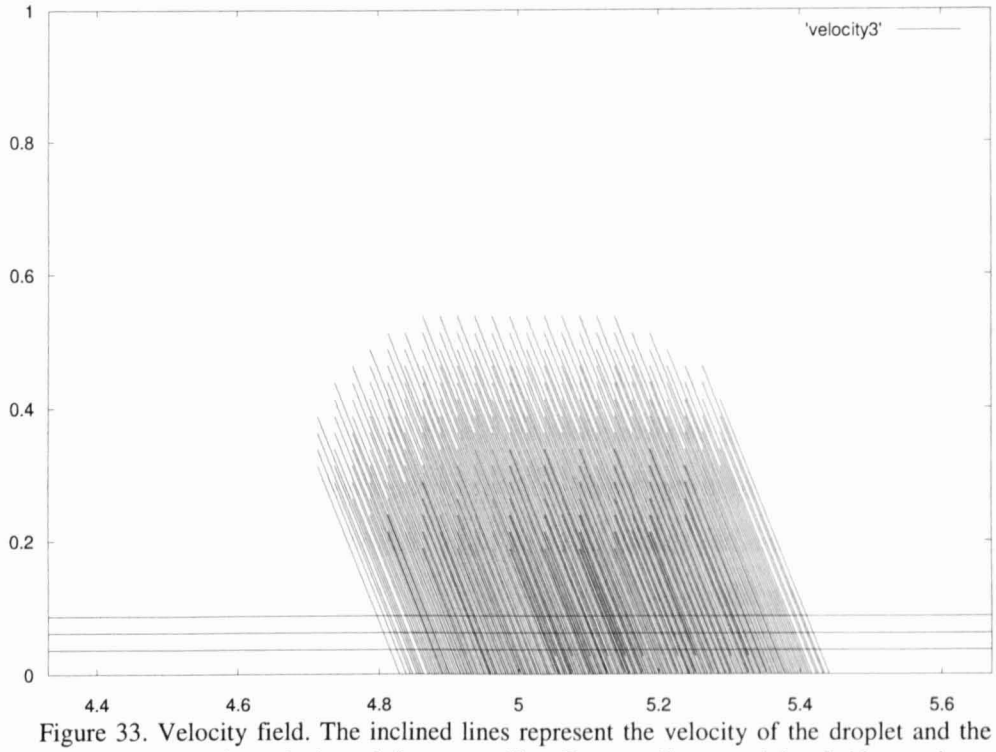

Figure 33. Velocity field. The inclined lines represent the velocity of the droplet and the horizontal ones the velocity of the water film. Every cell covered by fluid contains a number of velocity vectors pointing in the direction of the movement of every fluid.

P.8. *Oblate Droplet.*

Observing the results obtained from the experiments, the droplets before impacting the water film are flattened due to decelerating forces, as already has been mentioned. In order to recreate the experimental conditions within the simulation, the facility to define an oblate droplet impacting onto the layer is included in the model. Figure 34 illustrates an example of an oblate droplet in the computational mesh, at the immediate moment of impact with the water film.

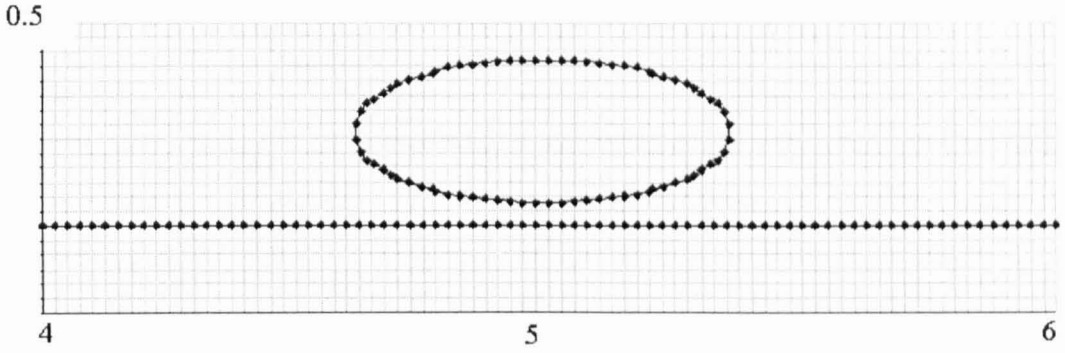

Figure 34. Typical mesh representing an oblate droplet at the moment of impact with the layer

Alternative Approaches to the Numerical Work.

The VOF method used in this study is not the only possible alternative for tackling the free surface deformation within the droplet impact problem. Another method is the Mesh-free Particle Method, in concrete, the Smooth Particle Hydrodynamics.

Mesh-free methods provide accurate and stable numerical solutions for integral equations or PDEs with all kind of possible boundary conditions with a set of arbitrary distributed nodes (or particles) without using any mesh that provides the connectivity of these nodes or particles. The Mesh-free Particle Method is a Mesh-free method that employs a set of finite numbers of discrete particles to represent the state of a system and to record the movement of the system.

This is a Lagrangian method which is a material description and is typically represented by finite elements method. The grid is fixed to or attached on the material in the entire computation process and, therefore, it moves with the material. It is useful for impacts and penetration problems. In a Lagrangian grid, mass momentum and energy are transported with the movement of the mesh cell. Because the mass within each cell remains fixed, no mass flux crosses the mesh cell boundaries. When the material deforms, the cells deform accordingly.

The numerical work developed during this investigation is based on an Eulerian method. This method is a spatial description and it is typically represented by finite differences method. The Eulerian grid is fixed on space in which simulated object is located and moves across the fixed mesh cells in the grid. Eulerian methods are dominant in the area of computational fluid dynamics where the flow of the material dominates.

Both, Eulerian and Lagrangian have different advantages and disadvantages. The main difference between them is, as mentioned, the fixed grid for the Eulerian and attached to the material for Lagrangian. For the first one, it is possible to track the mass, momentum and energy flux across grid nodes and mesh cell boundaries. For the second, the movement of any point on materials. When considering a moving boundary, this is

easier to track with a Lagrangian grid but when taking into account large deformations, Eulerian ones coup better with the situation.

The Smooth Particle Hydrodynamics (SPH) Method was developed to solve astrophysical problems in three-dimensional open space. However this has been extended to dynamic response with material strength as well as dynamic fluid flows with large deformations (Liu & Liu, 2003).

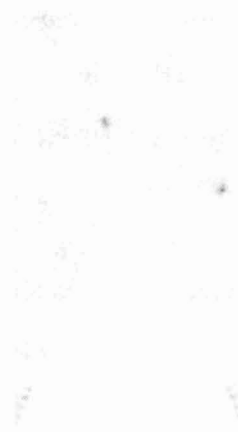

SPH particles. They are irregularly distributed.

The main advantage of SPH is the adaptability to the material which allows handling naturally problems that include extremely large deformations as mentioned above.

Some of the problems solved with SPH include simulations of binary stars and stellar collisions, supernova, collapse and formation of galaxies, coalescence of black holes with neutron starts, single a multiple detonation of white dwarf and even evolution of the universe (Liu & Liu, 2003).

Recent applications of SPH have been developed in fluid dynamics including fields such as elastic flow, magneto hydro-dynamics, multi-phase flows, gravity currents, heat transfer and mass flow, fracture of brittle solid and high (or hyper) velocity impact problems concerning the effects of projectiles impacting upon space assets among many others (Liu & Liu, 2003).

As droplet impingement into thin water films could be considered as a classical impact problem, SPH method could be taken into account to study the splash. However, because the VOF method is developed specifically to describe numerically the solution of a problem that involves time dependent flow of an incompressible and viscous fluid solving the Navier-Stokes equation, in this investigation work a numerical model based on this method has been used.

It should be mentioned that another work related to impacts of bodies is being developed at Cranfield University by Rade Vignjevic's group. This group helped to compare one of the runs modelled with our method with one of their simulations considering the same velocity and angle of impact and droplet size and layer thickness ratio. The results showed many similarities in terms of free surface deformation and jets velocities.

Numerical Results.

This section provides a full explanation of the results obtained through the different simulations. The computational code has been run considering different values of droplet velocities and sizes, angles of impact, water film thicknesses and temperatures. These results will be compared with the results obtained from the experiments in a following chapter.

The modelling provides wide information about the development and sizes of the jets formed during the splash and also about the temperature distribution on the fluids.

Free Surfaces Simulation.

As it has been mentioned previously, the model simulates the form of an impact event for which experimental data is available for comparison. It is important to remember that the experiments are 3-D whereas the simulations are 2-D.

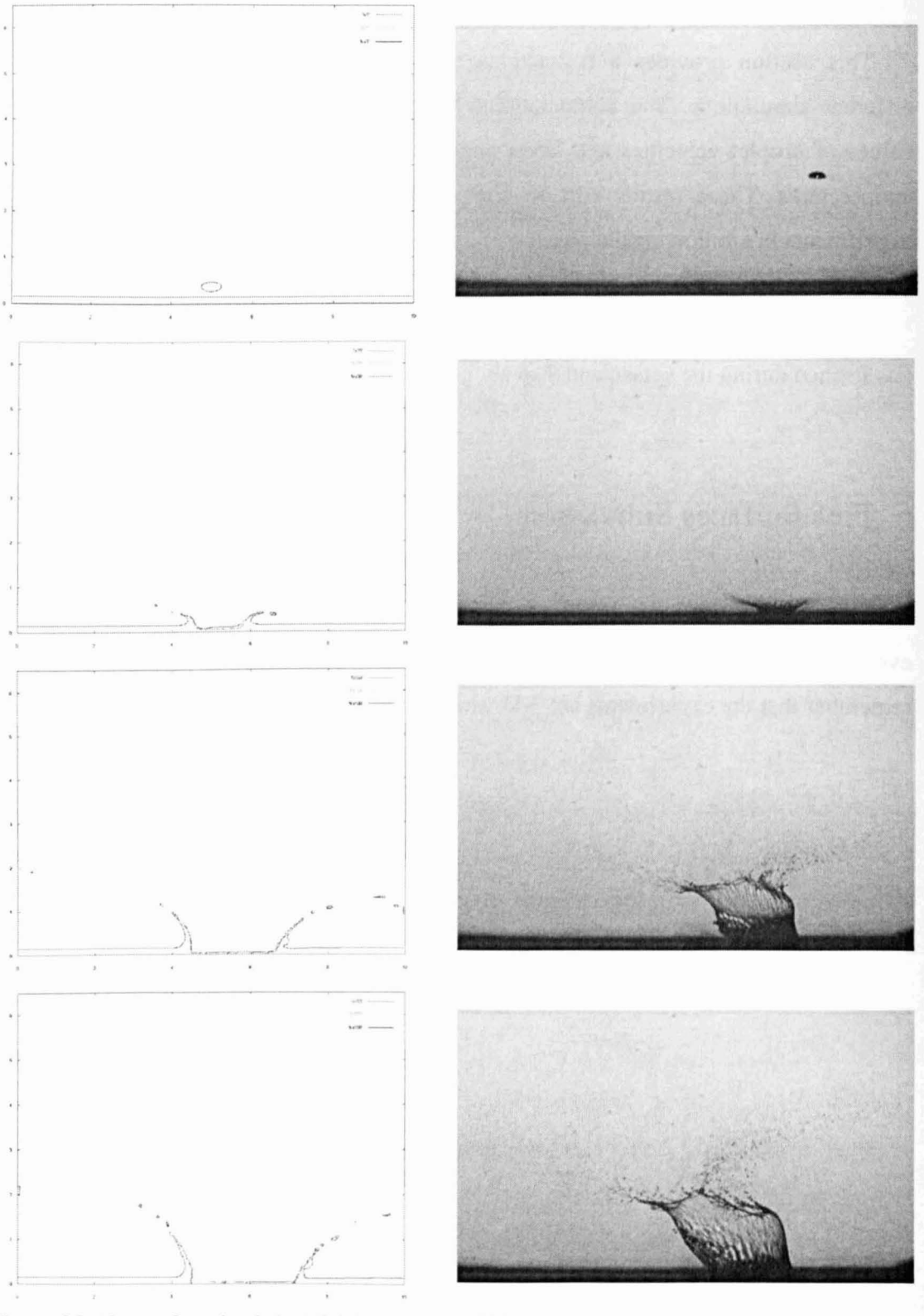

Figures 35a (free surface simulation) & b (experiment). 70° impact of a 483x170µm droplet at 55m/s over a 50µm water film thickness and at ambient temperature.

Figure 35a & b shows one such comparison. Note that in the figure, the droplet shown in the simulation is travelling from left to right and in the image of the actual droplet, this is travelling from right to left.

In the simulation, the initial droplet aspect ratio is chosen to match with the experimental data.

In the early stages of the splash, both the simulation and the experiment show a shallow cone or two jets of ejected fluid. As the process unfolds, the corona becomes wider and more steep sided. It is possibly apparent, both in the simulation and the experimental image that the side of the corona or jet into which the droplet would move contains more water.

As the splash evolves further the experimental corona shape begins to differ significantly from the shape of the simulated jets. This is thought to be at least in part due to the influence of the air movement.

In the simulation, colour has been used to show the boundary between the droplet water and the layer water. It can be seen, as postulated by other workers, that the ejected water originates largely from the layer.

To continue the analysis further, the experimental images have been used to make a series of measurements of the scale and speed of the corona development and break-up. These have then been compared directly with simulations made using the same input parameters.

The analysis is done comparing the different angle and velocity of impact, water film thickness and temperature. The scale and angular measurements used are defined in figures 36 and 37. The velocities of the corona were determined by measuring the growth of the left and right sides of the corona.

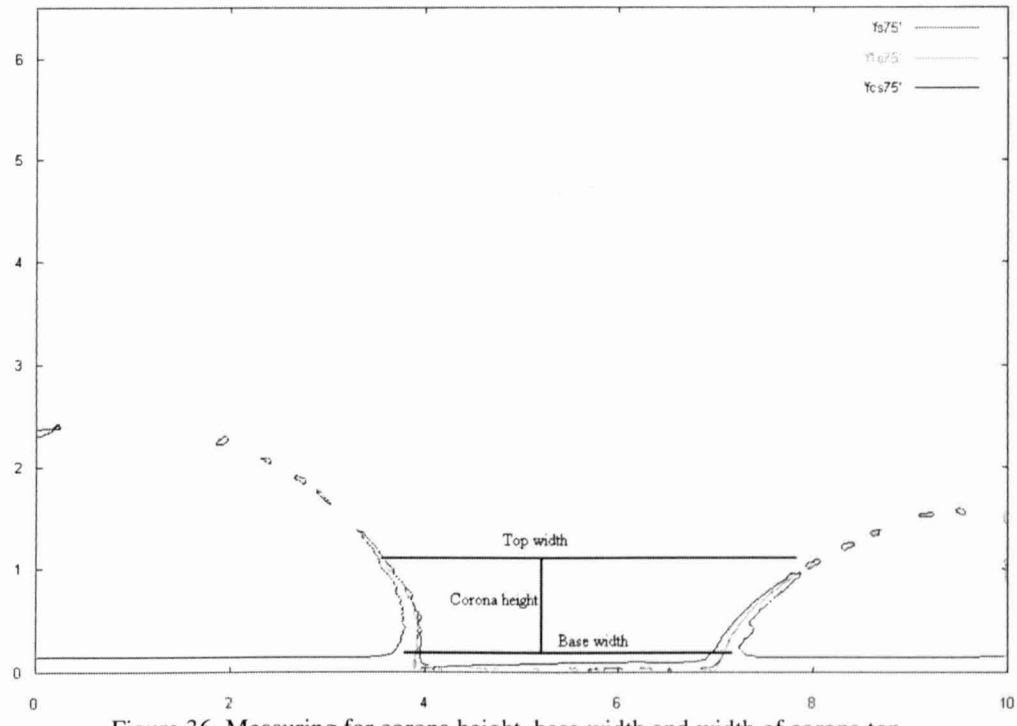

Figure 36. Measuring for corona height, base width and width of corona top.

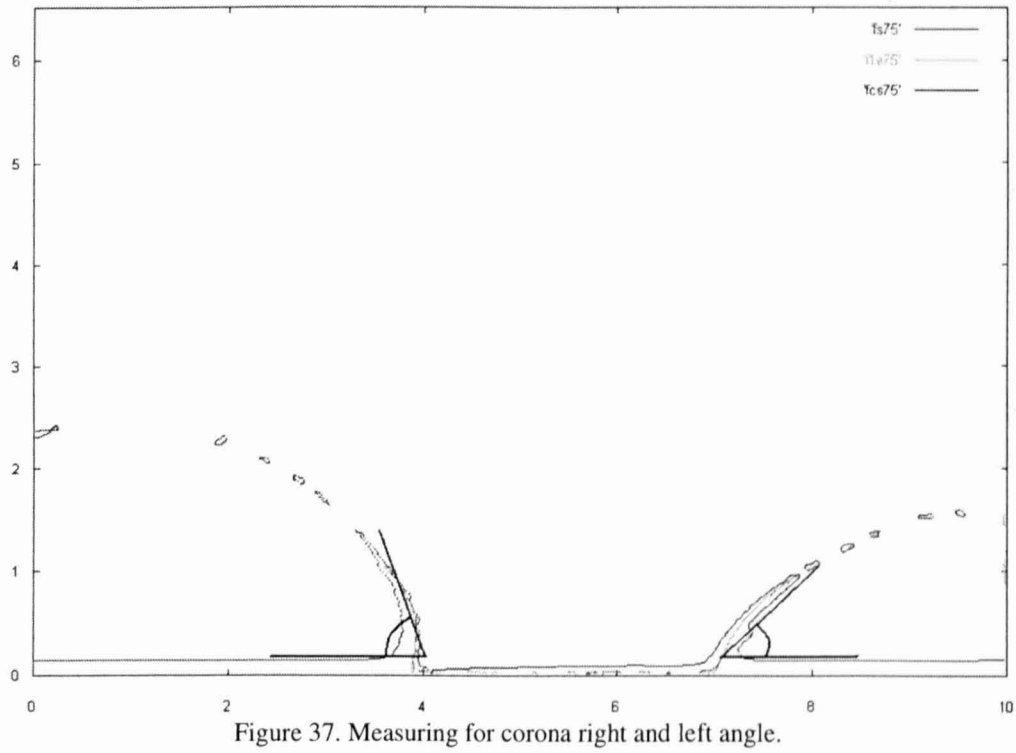

Figure 37. Measuring for corona right and left angle.

Comparison of Corona Size.

This section provides the analysis of the size of the different parameters considered when measuring the corona size. The corona height and the width of the

corona base and top are compared considering water film thickness and angle of impact. The impacts into the shallow water film includes, unless it is specified, both, droplets at +15°C and at -10°C while the impingements into the deeper layer includes only droplets at +15°C.

Effect of water film thickness on corona size.

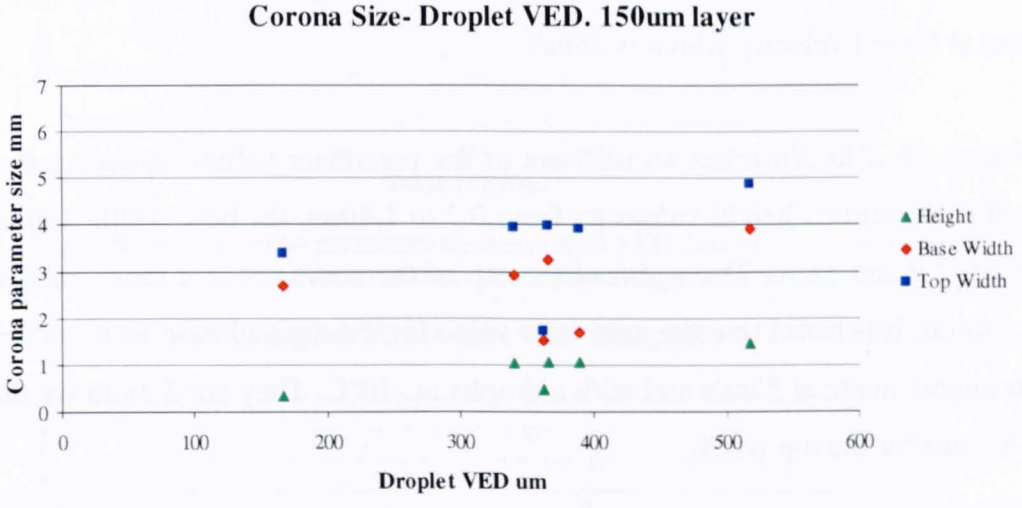

Graph 7a. Size of corona parameters against droplet VED. Impacts at 70° into a 150µm water film thickness and ambient temperatures.

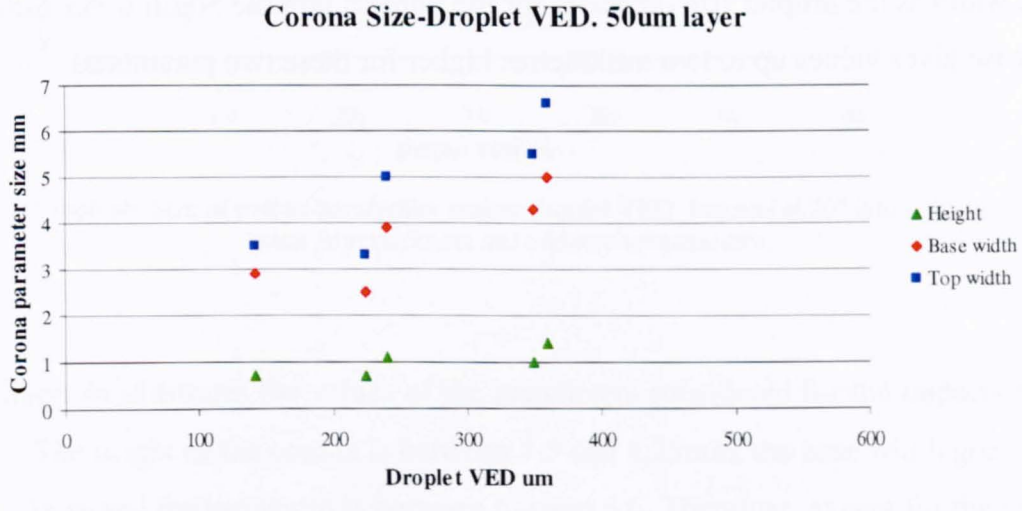

Graph 7b. Size of corona parameters against droplet VED. Impacts at 70° into a 50µm water film thickness and both, ambient temperatures and at -10°C.

Graphs 7a & b illustrate the values of height, base and top width of the corona after impacts at 70° into a 150µm and 50µm water film thickness respectively against the incoming droplet VED. In both cases it can be seen a continuous increase of the

parameters considered with the increase of the droplet size. However some differences are found in both of them.

Graph 7a shows a smooth increase of the parameters value. It is observed that the corona height goes from 0.3 to 1.5mm, the width of the top goes from 3.4 to 4.9mm and the width of the base is in a range between 2.7 and 3.9mm. Some values out of these ranges are found for the top and base width parameters. They are 1.7 for the top and 1.5 and 1.6 for the base. The lowest case for the top and base corresponds to the impact at lowest velocity which is 25m/s.

Graph 7b also illustrates an increase of the parameter values. However it can be seen that the corona height values go from 0.7 to 1.4mm, the base width is in a range between 2.9 and 5mm. The width of the top of the corona is in a range between 3.5 and 6.6mm. It is noted that the minimum value for the top and base width correspond to an impact made at 53m/s and with a droplet at -10°C. They are 2.5mm for the base and 3.3mm for the top width.

The comparison between both cases shows a very rapid increase of the top and base width as the droplet size increases for the impacts into the 50μm water film. This increase gives values up to two millimetres higher for these two parameters.

Effect of angle of impact on corona size.

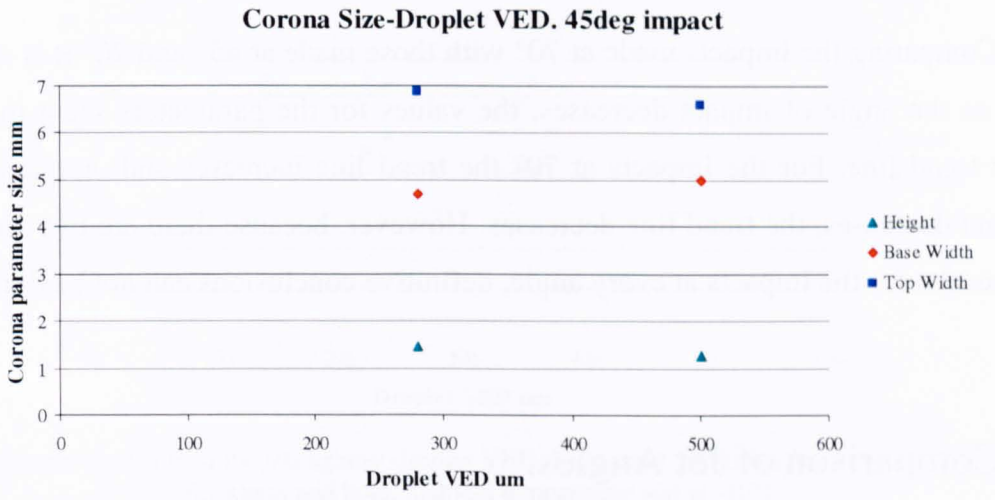

Graph 8a. Size of corona parameters against droplet VED. Impacts at 45° into a 50µm water film thickness and ambient temperatures.

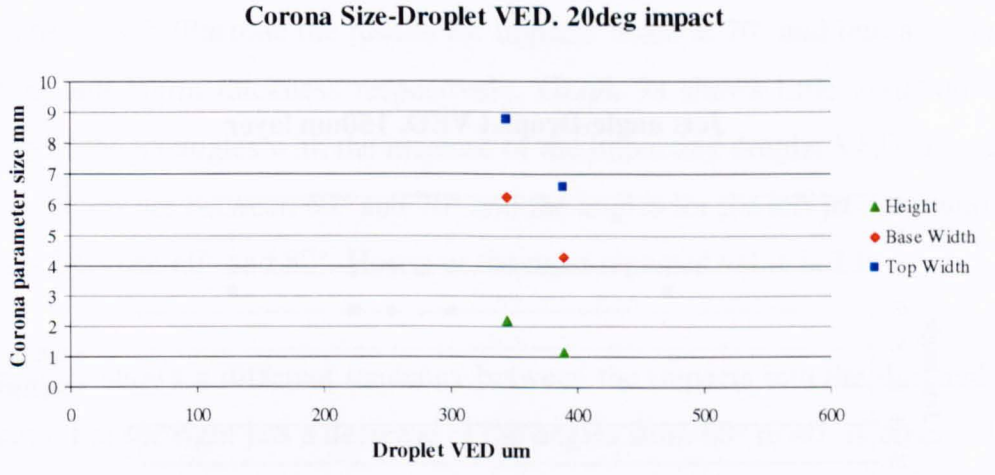

Graph 8b. Size of corona parameters against droplet VED. Impacts at 20° into a 50µm water film thickness and ambient temperatures.

Graph 8a illustrates the values of the parameters considered for the impacts made at 45°. The height of the corona is between 1.5 and 1.25mm, the base width goes from 4.7 to 5mm and the top width is between 6.9 and 6.6. Therefore, except for the values of the base width, a slight decreasing is noticed for the parameters as the droplet VED increases.

Graph 8b illustrates the results for the impacts made at 20°. Again a decrease of the values for the parameters is observed although this time the difference as the droplet VED increases is more significant. Thus the height is in a range between 2.2

and 1.1mm, the base width 6.25 and 4.25mm and the top width goes from 8.75 to 6.6mm.

Comparing the impacts made at 70° with those made at 45° and 20° it is observed that as the angle of impact decreases, the values for the parameters seem to change their trend line. For the impacts at 70° the trend line increases and, as the angle of impact decreases, the trend line decreases. However, because there are two values for the results for the impacts at every angle, definitive conclusions can not be done.

Comparison of Jet Angles.

Effect of water film thickness on the jets angle.

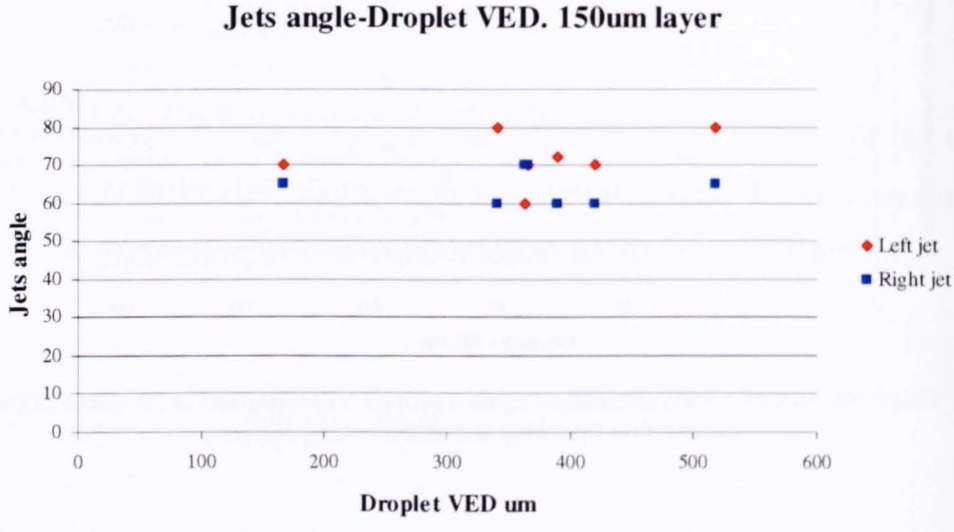

Graph 9a. Angle of the jets against droplet VED. Impacts at 70° into a 150µm water film thickness and ambient temperature.

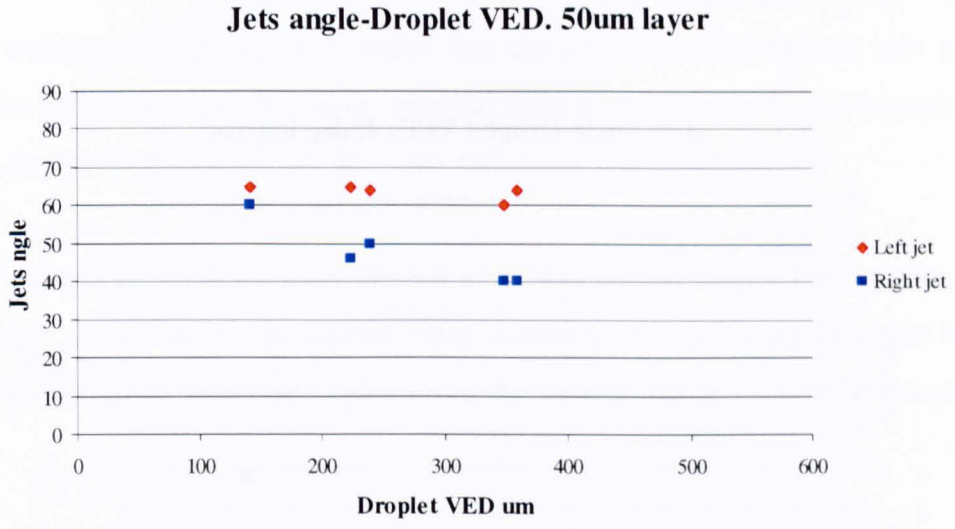

Graph 9b. Angle of the jets against droplet VED. Impacts at 70° into a 50µm water film thickness and both, ambient temperature and at -10°C.

Graphs 9a & b illustrate the results for impacts made at 70° and into a water film of 150µm and 50µm thickness respectively. Graph 9a shows little variation in the evolution of the jet angles with the increase of the impacting droplet VED. The angles for the right jets are between 60° and 70° and the angles for the left jet are found to be in a range between 60° and 80°. However the most repeated value is 70°

Graph 9b shows a different tendency between the impacts into the thin and thick water film. For the right jets a decrease of the angles from 60° to 40° is observed with the increase of the droplet size.

Effect of angle of impact on jets angle.

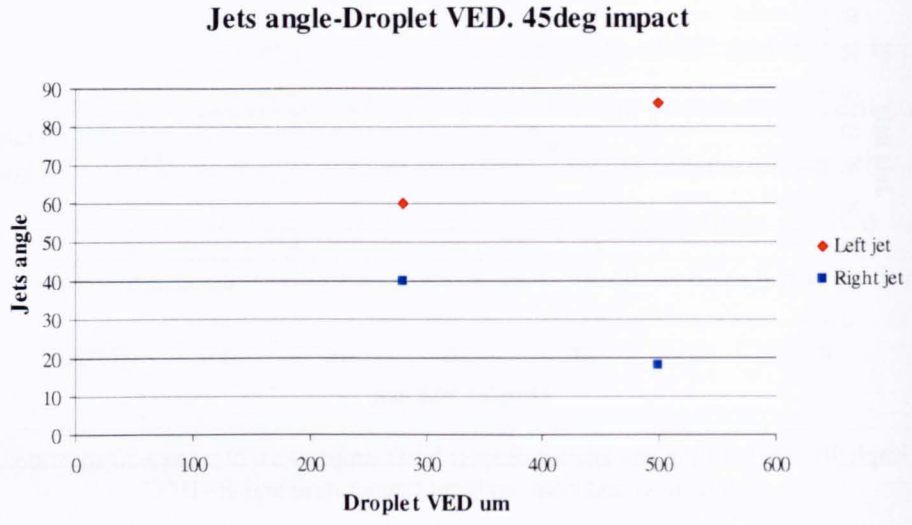

Graph 10a. Angle of the jets against droplet VED. Impacts at 45° into a 50µm water film thickness and ambient temperature.

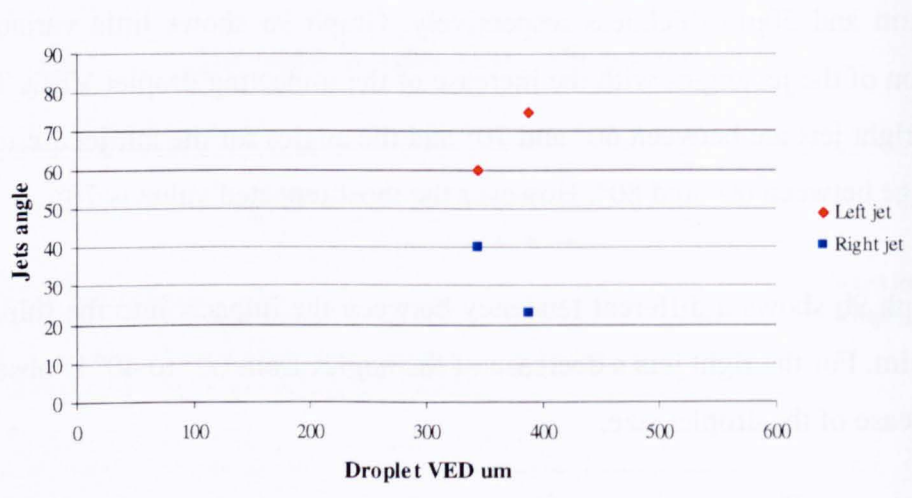

Graph 10b. Angle of the jets against droplet VED. Impacts at 20° into a 50µm water film thickness and ambient temperature.

Graphs 10a & b show that, as the droplet VED increases, the angles formed by the right jet decrease and the angles formed by the left jet increase. The values of these angles go, in the case of impacts at 45°, from 40° to 19° for the right jet and from 60° to 86° for the left one.

The impacts at 20° give values for the angles formed by the right jet that go from 40° to 23° and for the left one that go from 60° to 75°.

The comparison between the angles that the jets form after impact into a 50μm water film at 70°, 45° and 20° shows that the right jets are lower for the impacts made at small angles than for those at 70°. This difference can be up to 20°.

For impacts of small droplets the left jets form similar angles for impacts at 70°, 45° and 20°. However, as the droplet VED increases, the angles formed after impacts at 70° do not change while the angles formed after impacts at 45° and 20° increase up to 85°.

Comparison of Jet Velocities.

Effect of water film thickness on jets velocity.

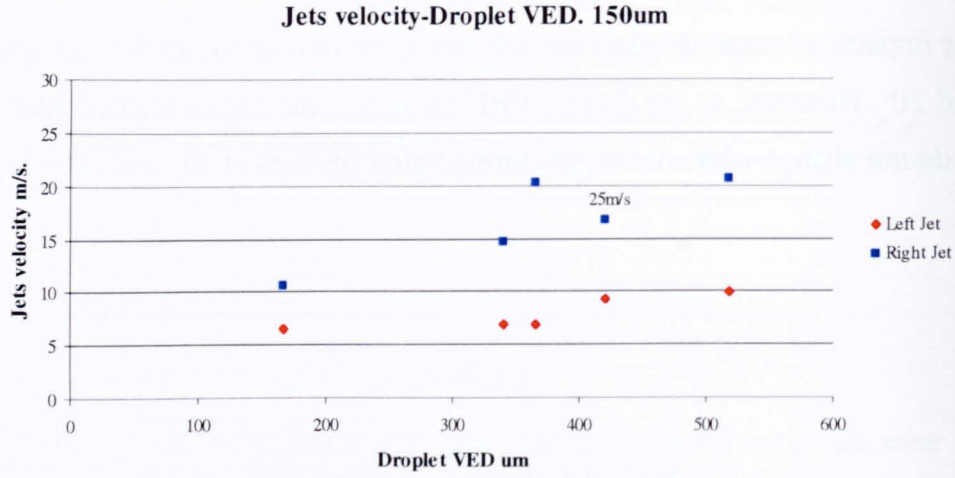

Graph 11a. Velocity of the jets against droplet VED. Impacts at 70° into a 150µm water film thickness and ambient temperatures.

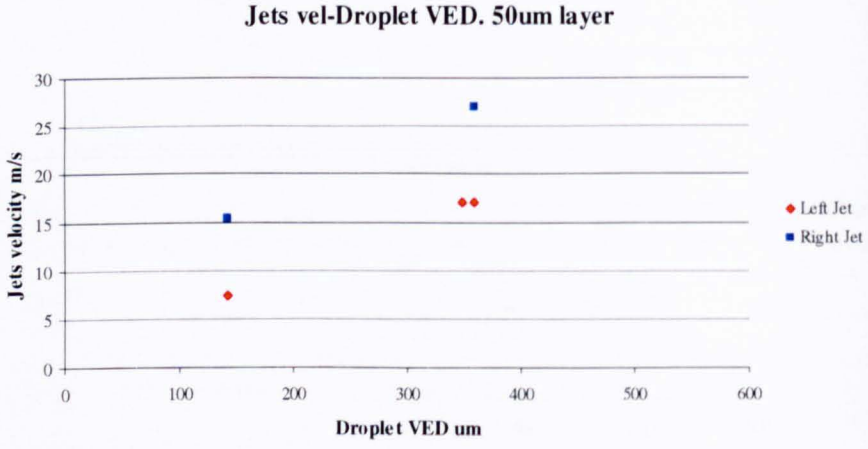

Graph 11b. Velocity of the jets against droplet VED. Impacts at 70° into a 50µm water film thickness and ambient temperatures.

Graph 11a illustrates the velocities for the jets during the splash after impacts at 70° into the 150µm water film. It can be seen that, as the droplet size increases, the velocity of the right and left jets increases. Thus, the velocities of the left jet go from 6.8 to 10.3m/s. The right jets velocities go from 15.6 to 22.5m/s.

Graph 11b illustrates the velocity of the jets after impacts into the thinner water film and for droplets at 20°C. This shows an increase of the right and left jets velocities as the droplet size increases. For the left jets, the velocities obtained go

from 7.4 to 17m/s and for the right from 15.3 to 27m/s. These values are up to 5m/s higher than those obtained from impacts made into a 150µm water film.

Effect of temperature on jets velocity.

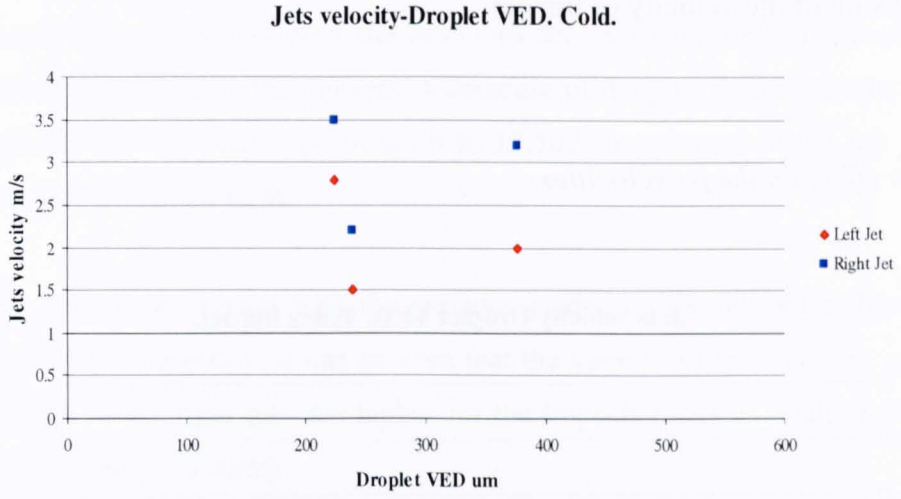

Graph 12. Velocity of the jets against droplet VED. Impacts at 70° into a 50µm water film thickness and at -10°C.

Graph 12 illustrates the velocities of the jets after impacts into the thin water film and droplets at -10°C. The temperature for the film is 15°C. The range of values for droplet sizes, velocities of impact and also the angle of impact is the same than in graph 11b. However, for the super-cooled droplet impact, the velocities of the jets are around ten times lower.

Droplet velocity effect on jets velocity.

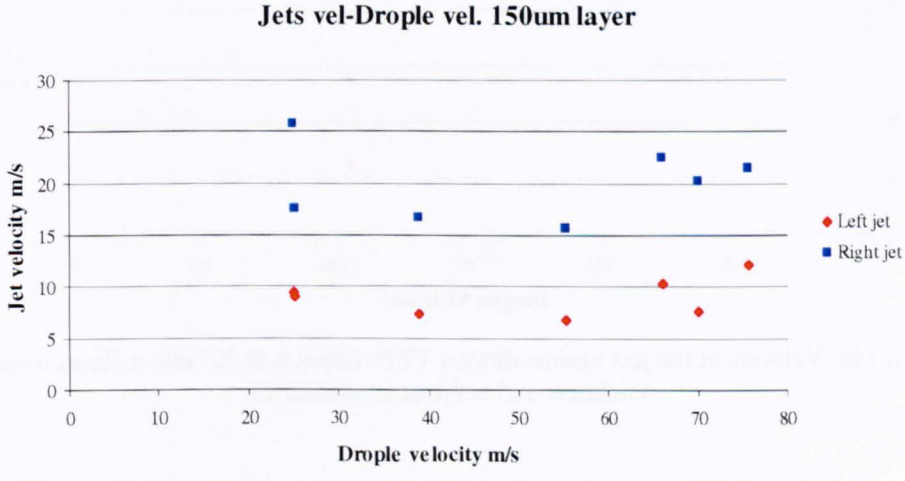

Graph 13. Jets velocities against droplet velocity Impacts at 70° into a 150µm water film thickness and ambient temperatures.

Graph 13 shows the velocity of the jets against the velocity of impact for the impingements into the 150µm thickness water film. The velocity of the right jet is in a range between 17.5 and 25.7m/s and the left jet between 9.1 and 9.5m/s. Apart of this, the results show that the velocity of the jets does not seem to change very much with the increasing of the velocity of impact.

Angle effect on the jet velocities.

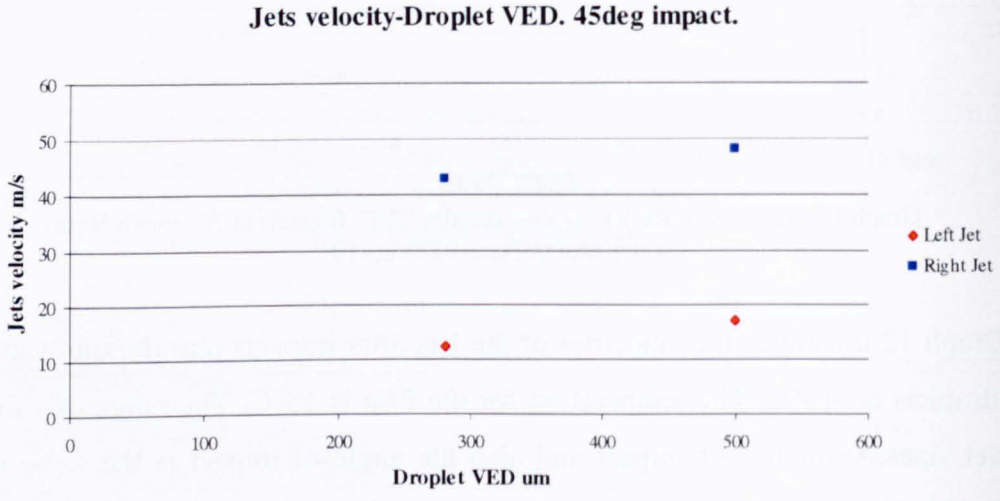

Graph 14a. Velocity of the jets against droplet VED. Impacts at 45° into a 50µm water film thickness and ambient temperatures.

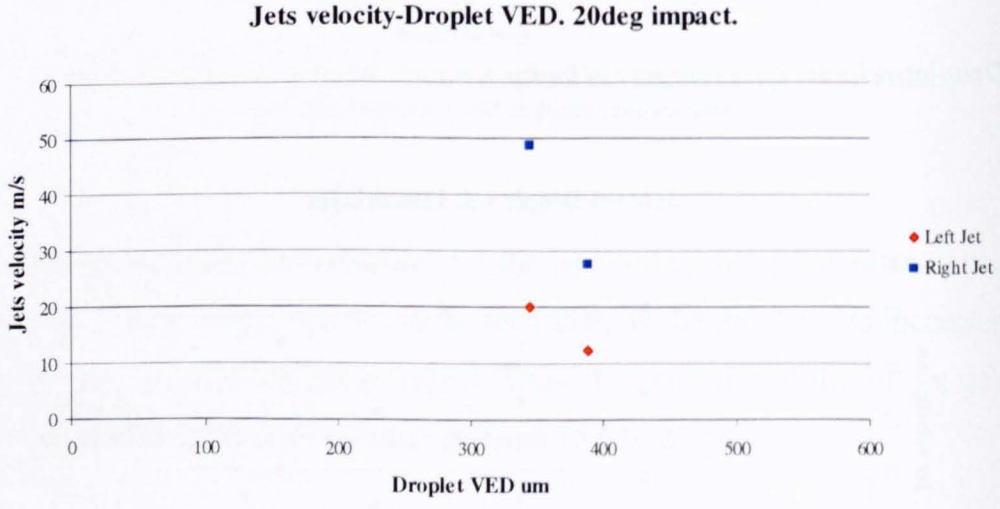

Graph 14b. Velocity of the jets against droplet VED. Impacts at 20° into a 50µm water film thickness and ambient temperatures.

Graph 14a illustrates the jet velocities for impacts at 45°. The velocity increases with the droplet VED although there are not found important differences. Thus, the left jet speeds go from 12.4 to 17.1m/s and the right from 42.8 to 48m/s.

The impacts made at 20° are illustrated in graph 14b. A relevant difference is appreciated. As it can be observed, the velocities decrease with the increase of droplet size. This is the only case that presents a decrease of the jet velocities as the droplet size increases. The velocities go from 20 to 12.5m/s in the case of the left jet, and from 48.8 to 27.7 for the right.

Comparing these impacts with the previous made into the thin water film at 70° and at ambient temperature, it can be seen that the values of the velocities, specially the velocities of the right jets, are higher for the impacts made at small angles. This difference can be up to 20m/s.

Satellite Droplets Size.

Effect of water film thickness.

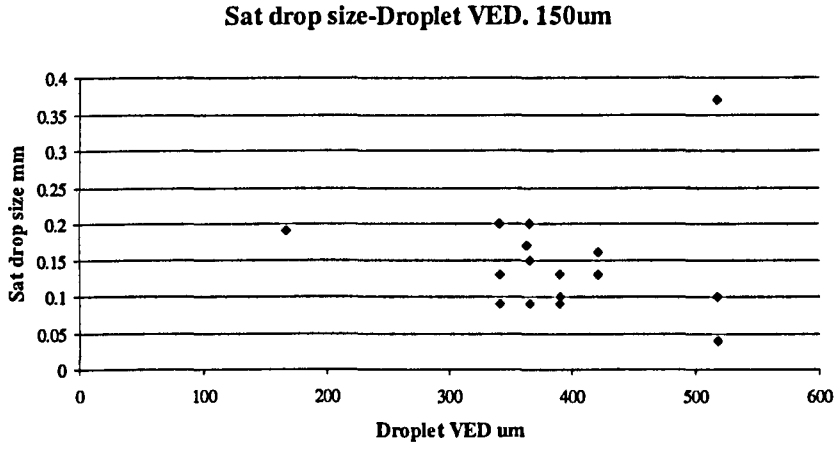

Graph 15a. Size of the satellite droplets against droplet VED. Impacts at 70° into a 150μm water film thickness and ambient temperature.

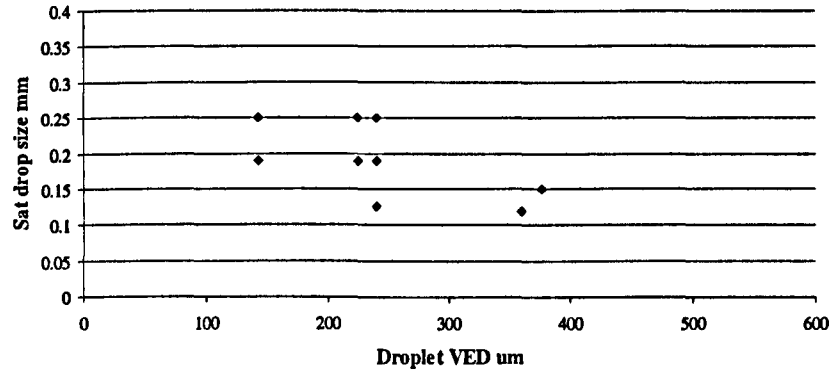

Graph 15b. Size of the satellite droplets against droplet VED. Impacts at 70° into a 50μm water film thickness and ambient and cold temperature.

Graphs 15a & b show the results for the impacts into a 150 and 50μm water film thickness respectively. The size of the satellite droplets in graph 15a are always between 0.09 and 0.2mm. They do not seem to be affected by the increasing of the droplet size. There is an exception found in the impact produced by the biggest droplet. The size of the satellite drops go from 0.04 to 0.37mm. The velocity of impact for this case is 66m/s.

The impacts into the thinner water film represented in graph 15b shows that the increase of the droplet size does not seem to affect the diameter of the satellite droplets. Thus their sizes are found in a range between 0.125 and 0.25mm which is slightly higher than the sizes obtained for the impacts into the 150μm water film thickness.

Angle effect on the satellite droplet size.

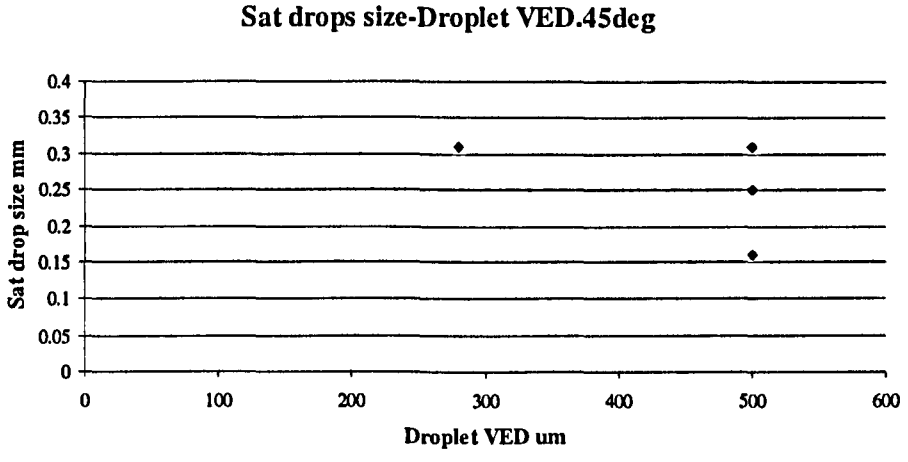

Graph 16a. Velocity of the satellite droplets against droplet VED. Impacts at 45° into a 50μm water film thickness and ambient temperature.

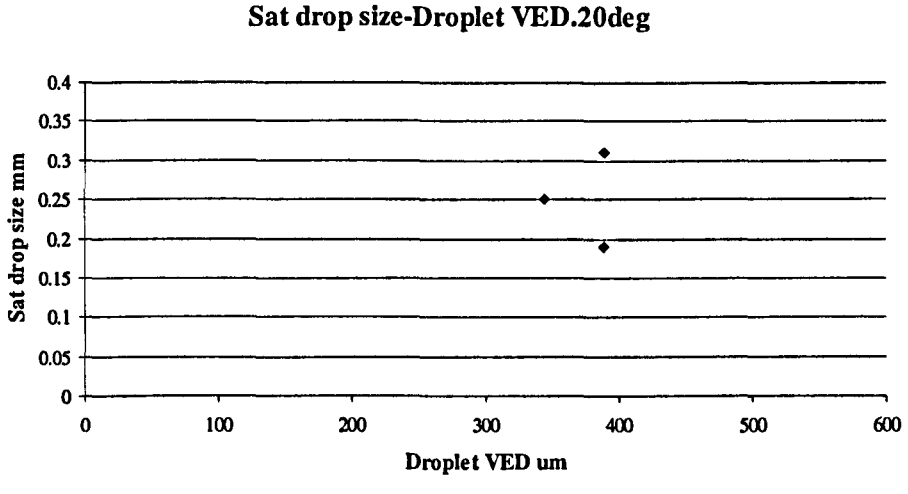

Graph 16b. Velocity of the satellite droplets against droplet VED. Impacts at 45° into a 50μm water film thickness and ambient temperature.

Graph 16a illustrates the sizes of the satellite droplets against the incoming droplet size for impacts at 45°. The results show that the satellite droplets are in a range between 0.16 and 0.31mm. When the impacts are made at 20° the sizes are between 0.19 and 0.31mm.

Comparing with the impacts made under the same considerations but at 70° it can be observed that the satellite droplets obtained from impacts at smaller angles are slightly bigger. The difference is around 50μm.

Satellite Droplets Velocity.

Effect of water film thickness on satellite droplet velocities.

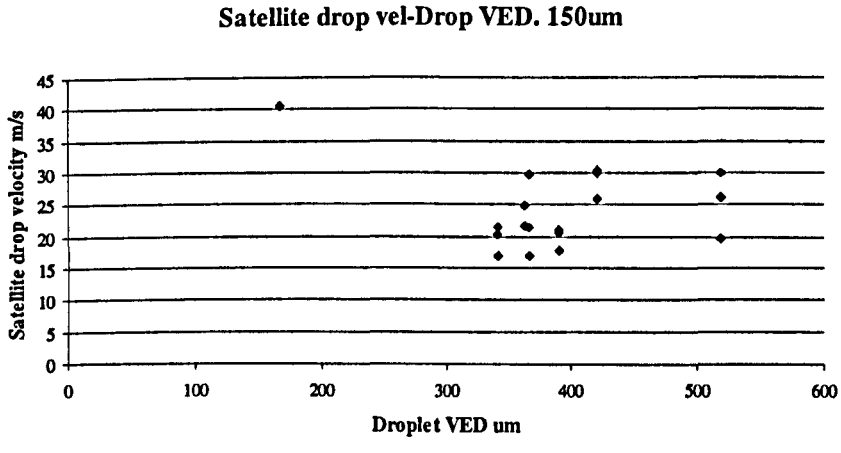

Graph 17a. Velocity of the satellite droplets against droplet VED. Impacts at 70° into a 150μm water film thickness and ambient temperature.

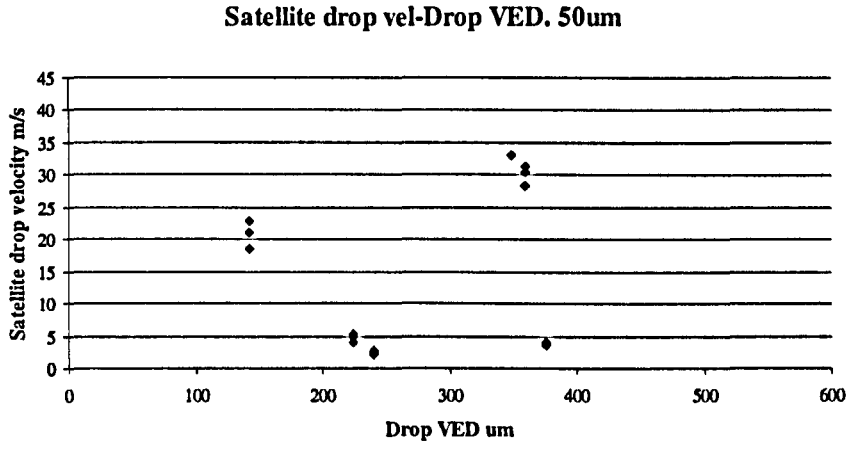

Graph 17b. Velocity of the satellite droplets against droplet VED. Impacts at 70° into a 50μm water film thickness and ambient and cold temperature.

Graphs 17a & b show the velocity of the satellite droplets against the incoming droplet size for impacts made at 70°. For the splashes considering the thicker water film, the velocities obtained are always in the range between 17 and 30m/s independently of the increase of the impacting droplet VED.

Graph 17b illustrates the results after impacts into the 50μm water film thickness. The impingements of droplets at -10°C are included. The values of the satellite droplet velocities for the impact at ambient temperatures increase from around 20m/s to around 30m/s as the impacting droplet size increases. The impacts made at cold temperatures show satellite droplet velocities around 5m/s independently of the impacting droplet size.

The comparison between impacts made into a 150μm and 50μm water film do not show any significant difference in the values for the velocity. However an increase in the values of the impacts into the 50μm water film is observed with the increase of the impacting droplet size.

The impacts made at cold temperatures show very low values in comparison with the impacts made at similar conditions but at warm temperatures.

Angle effect on the satellite droplet velocities.

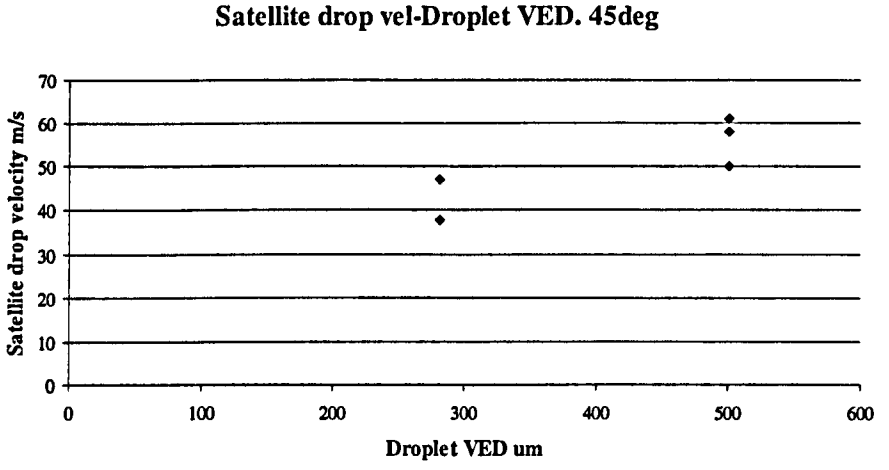

Graph 18a. Velocity of the satellite droplets against droplet VED. Impacts at 45° into a 50μm water film thickness and ambient temperature.

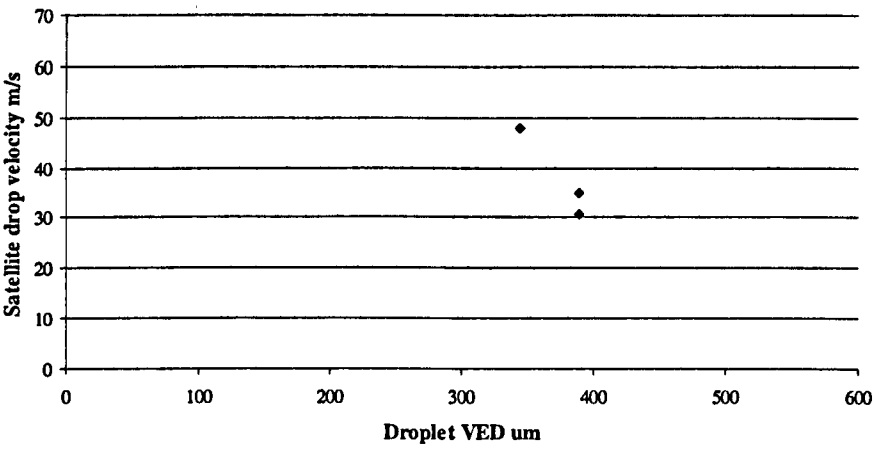

Graph 18b. Velocity of the satellite droplets against droplet VED. Impacts at 20° into a 50μm water film thickness and ambient temperature.

Graphs 18a & b show that for the impacts at 45° the velocity of the satellite droplets go from 37.7 to 61m/s and for the impacts at 20° the velocities go from 30.7 to 48m/s. These values are higher than impacts obtained under similar considerations but at 70° impact. The difference can be almost twice for the smaller angles.

Velocity effect on the satellite droplet velocities.

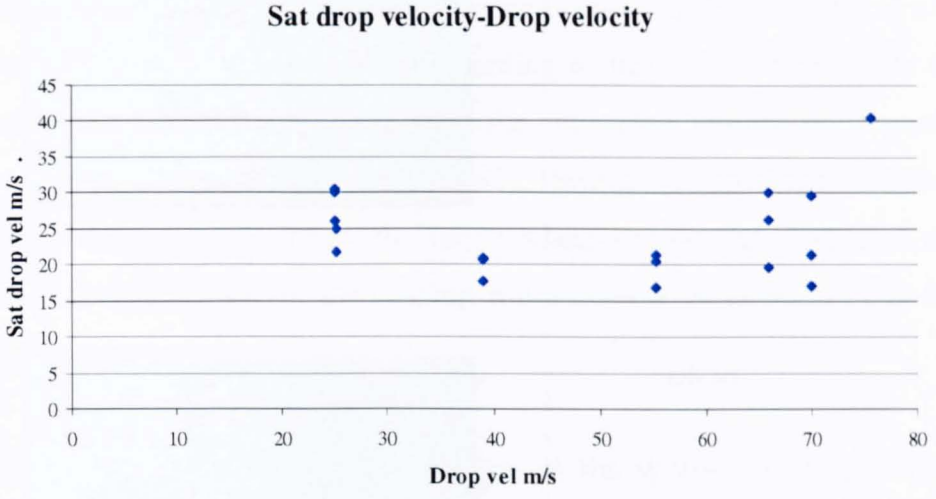

Graph 19. Velocity of the satellite droplets against droplet velocity. Impacts at 70° into a 150μm water film thickness and ambient temperature.

Graph 19 shows the velocity of the satellite droplets for impacts made at 70° into a 150μm water film. It is observed that the increase of the impact velocity has little influence in the velocity of the satellite drops. Thus the velocity of the satellite droplets goes from 17 to 30m/s with an exception of one droplet at 41m/s. This corresponds to the impact made at the fastest speed.

Temperature Simulations.

Impact of a Super-cooled Large Water Droplet.

Figures 38a & b show the typical thermal history of a simulation of an impact of a super-cooled water droplet at -10°C and a water film at 15°C. The droplet VED is chosen as 240μm, the velocity of impact is 39m/s and the water layer thickness is 50μm.

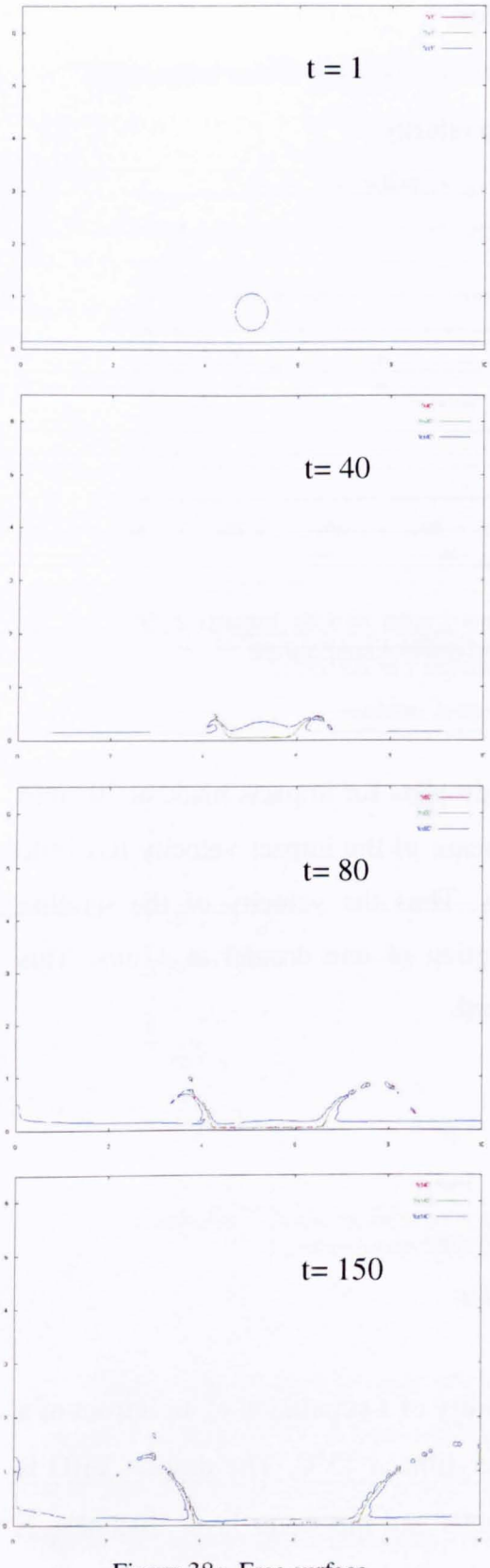

Figure 38a. Free surface.

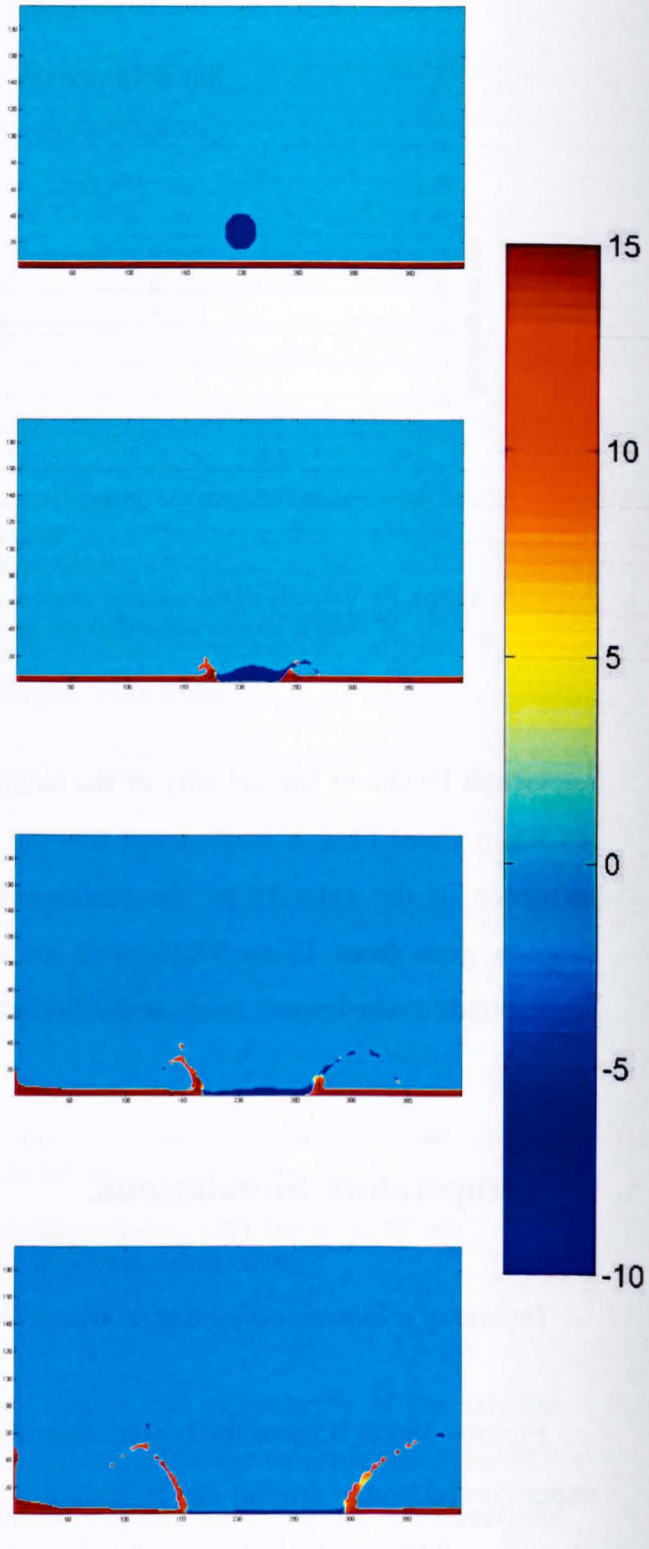

Figure 38b. Temperature distribution.

Impact at 70°. Droplet diameter: 240µm, droplet velocity: 39m/s. Layer thickness: 50µm, droplet temperature: -10°C and water film temperature: +15°C.

The droplet temperature is chosen according to the temperature reached inside the Cranfield Vertical Tunnel which coincides with the typical droplet temperature super-cooled droplet temperature that causes glaze ice (Politovich and Chapleo *et al.* 1994). The water film temperature is chosen according to the temperature inside this thin layer when the aircraft is in-flight with the anti-icing system on regarding the literature (Morency *et al.* and Al-Khalil, 1991). During the experiments carried out in the Cranfield University facilities, the target where the droplets impacted was also heated and the temperature for the running water layer is assumed to be in the same range of values.

The figure shows that, in the early stages of the splash, the temperature in the impact area is essentially the temperature of the incoming droplet. The right jet, which contains a considerable amount of water from the droplet, is significantly cooler than the left jet. Indeed the right jet is super-cooled.

As the splash evolves it is observed that the spreading impact zone remains super-cooled and the right jet continues to be cooler than the left jet. As time proceeds, and with the inclusion of more layer water into both jets, the right jet warms up and assumes a similar temperature to the left jet. The water in the impact area remains super-cooled.

Impact of a Warm Large Water Droplet.

A similar temperature analysis is done for the impacts made at ambient temperatures. The droplet is assumed to be at +20°C. The water film is considered at +10°C.

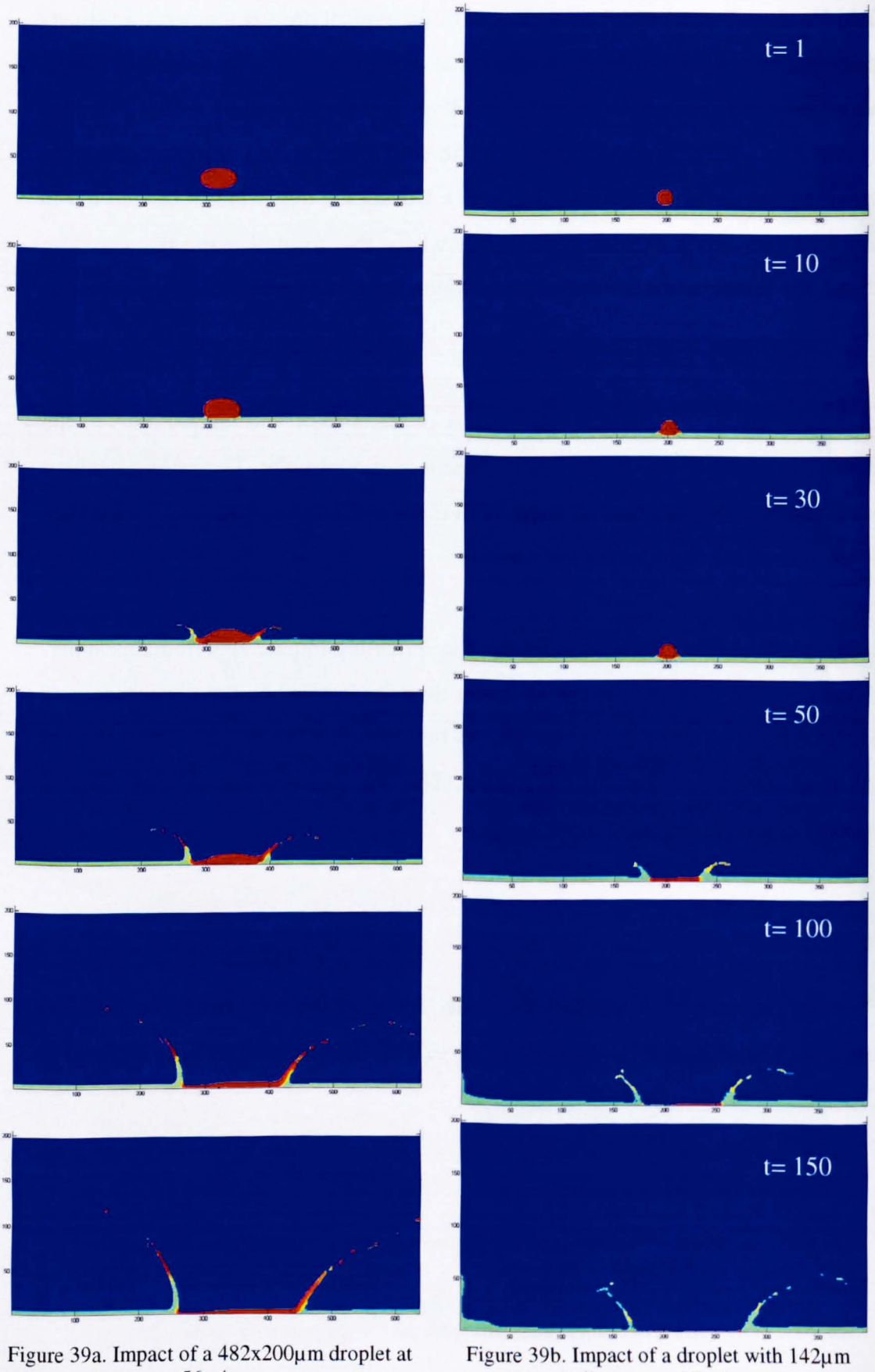

Figure 39a. Impact of a 482x200µm droplet at 56m/s.

Figure 39b. Impact of a droplet with 142µm diameter at 39m/s.

Droplet temperature +20°C, water film temperature +10°C angle of impact 70° and water film thickness 50µm.

Figures 39a & b illustrate the first stages of the splash of two different droplets at the same temperature and angle of impact but different sizes and velocities. In both cases the jets are developed in a similar way but the evolution of the temperature is different due to the droplet size film thickness ratio. Figure 39a shows the heat transfer during the impact and splash of a 482x200μm droplet at 56m/s. Figure 39b illustrates the impact of a droplet with 142μm diameter at 39m/s. Both impacts are made at 70° and into a 50μm water film thickness.

As the "coronas" or jets are formed, the right jets contain more water from the droplet, in particular in the case shown in Figure 39a. However the temperature of the jets is affected more by the bigger droplet than by the smaller. Thus by t = 50 only the temperatures of the jets formed by the impact illustrated in figure 39a are similar to the initial temperature of the droplet This temperature is around 16 and 18°C. Figure 39b shows that, due to the inclusion of more water from the film, the temperature of the jet is around 10 and 12°C.

Figure 39a shows a particularity for the left jet as the time evolves. It can be seen that the temperature in the tip of this jet is closer to 20°C while for the rest is closer to 10°C. This shows that also the right jet contains a substantial amount of water from the droplet since the beginning of the impact.

What is common for both cases is that the water in the impact area is apparently at the same temperature than the droplet, as happened in the impacts with super-cooled droplets.

The Viscosity Effect.

In order to see the effect that the viscosity has on the splash, a case similar to the example explained in figure 38a has been run. The only difference with this previous case is that viscosity is not taken into account. All the parameters, including velocity and angle of impact, droplet size, water film thickness and temperatures remind the same.

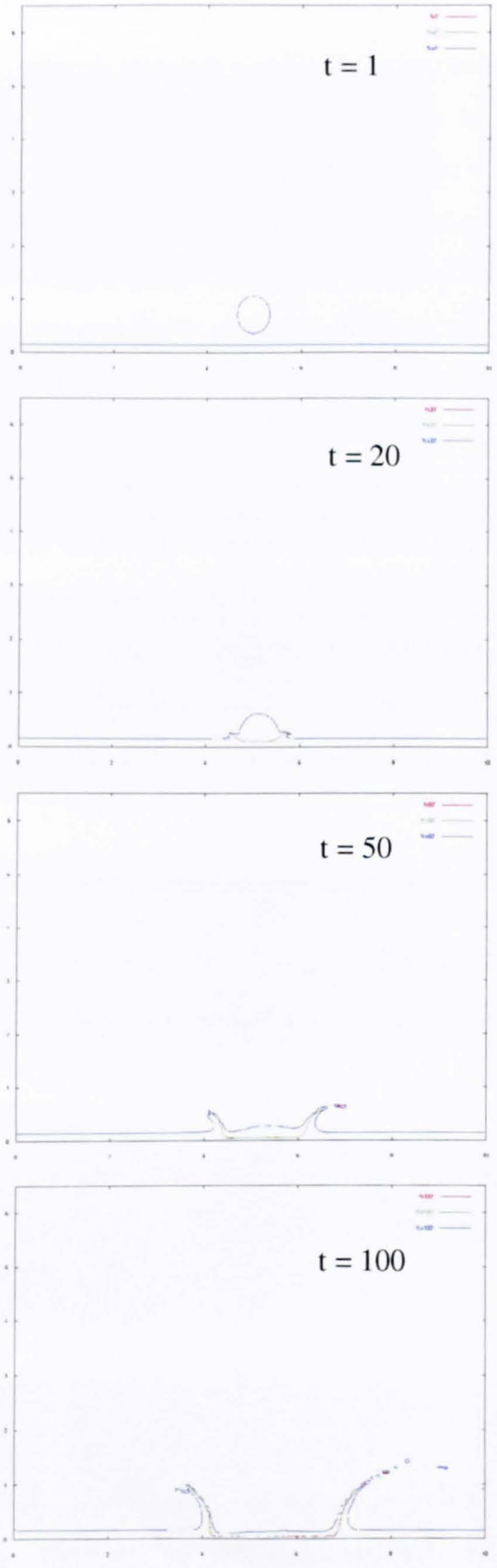

Figure 40a. No viscosity

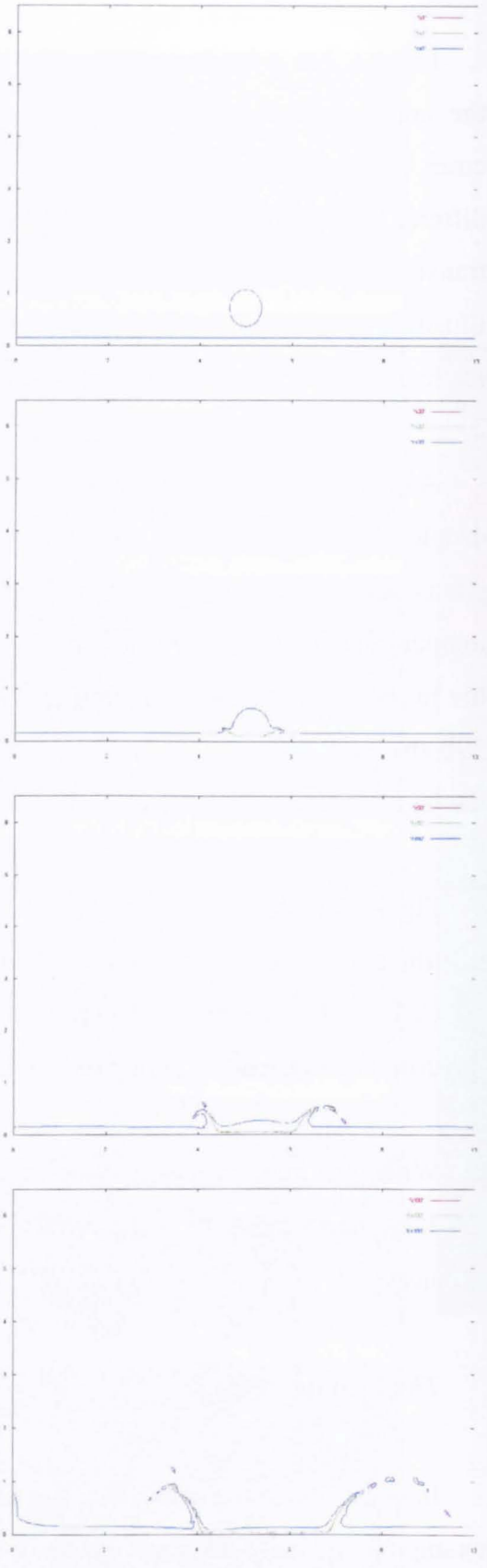

Figure 40b. Viscosity

The differences for the free surfaces are shown in figures 40a & b. For the first time steps there is no relevant variation between both cases. However, as the time increases, the jet formation starts to show some differences.

Figure 40a illustrates the non viscous case and figure 40b the simulation that includes viscosity term. From the time step t = 50 the right jet of the non viscous splash forms a bigger angle than the impact that considers viscosity terms. In particular, for t = 100 the non viscous splash presents angles of 74° and 60° for the left and right jet respectively while the splash that considers viscosity term form jets with angles 64 and 50°.

The angles are not the only parameters that are sensitive to the viscosity term. As a consequence of this the corona height, the corona base width and corona top width are approximately 20% higher in the case that considers viscosity.

This result agrees with Josserand and Zaleski (2003). They studied droplets impact although at lower velocities but comparing viscous and non viscous cases. The effect of the viscosity they obtained points in the same direction for both, angles and corona sizes.

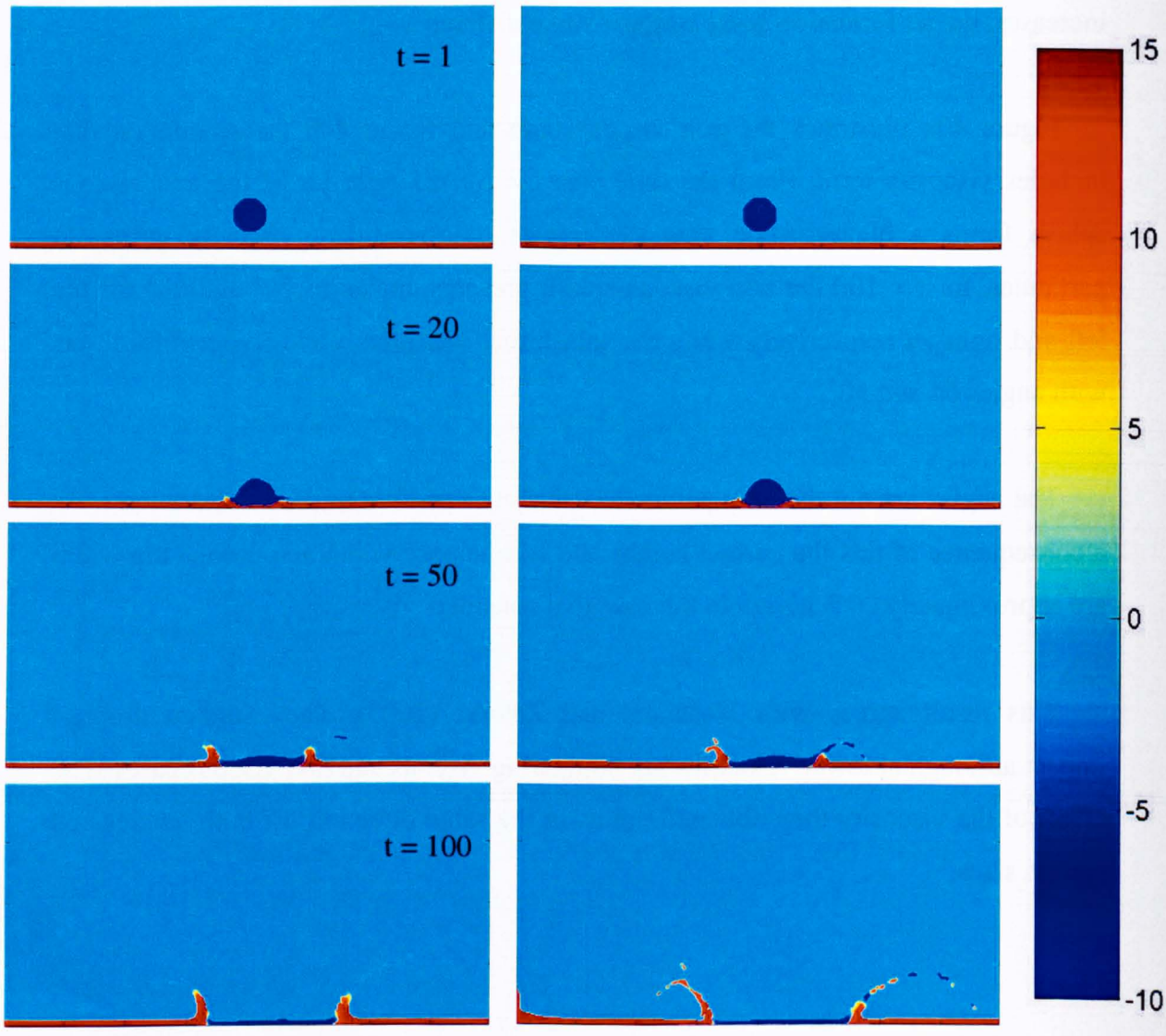

Figure 41a. No viscosity

Figure 41b. Viscosity

The analysis of the heat transfer shows that the viscosity also influences in the evolution of the temperature in the jets. Figures 41a & b illustrate this. For the first time-steps, when the droplet is entering the water film, there are no major variations between both cases. However, once the jets are formed, the values for the temperature seem to be affected by the inclusion of the viscosity term. Thus by time-step t = 50 it can be seen that the temperature of both jets in the non viscous case is influenced more by the water of the droplet. The tips of both jets are slightly below the freezing point. However, as it has been seen above, in the simulation including viscosity only the temperature of the right jet is significantly influenced by the droplet which is approximately at -10°C. At time-step t = 100 both jets produced in the impact without

viscosity are approximately at 0°C. In the viscous case the temperatures are significantly different between the two jets and the right one shows a noticeable temperature variation

Both cases have in common that the water in the impact area remains super-cooled.

PART II: EXPERIMENTAL WORK

Experiments: The Cranfield University High Speed Vertical Tunnel.

Cranfield University has the largest icing tunnel in the U.K. and one of the first designed specifically for SLD icing research in the world. Part of this facility is a vertical tunnel which has been built to study what happens as a water droplet strikes the surface of an aircraft. The aim of this study, therefore, is to observe the splashing of water droplets on a wetted target over the range of variables shown in Table 2. Hence, what has been done in the Vertical Tunnel is to inject droplets that are accelerated and cooled down until they reach the target covered by a thin water film. Then, the impact produces a splash that is recorded with a special high speed camera.

Variable	Range of interest
Droplet diameter	40 to 400μm
Velocity	20 to 120 m/s
Water film thickness	10 to 100μm
Angle of impact	10° to 90°
Droplet Temperature	+20° to -20°C
Film Temperature	+ 20° to 0°C

Table 2. Range of variables considered during the experiments.

The qualities of this vertical tunnel that make it suitable for this kind of work are as follows:

Firstly the trajectories of the droplets are not affected so much due to that they count with the help of the gravitational forces. Therefore the trajectories of the droplet do not suffer major distortion as they travel through the contraction section. Secondly, the working distance is shorter than in a typical icing tunnel. This facilitates the optical measurements. Finally, the contraction section produces a very gentle acceleration avoiding droplet break-up and major deformation.

The Vertical Tunnel design is a join project with Wichita State University in the U.S. (Tan, 2002).

The tunnel is placed on Cranfield University Campus. A general view of the facility is shown in figures 42 and 43. They give a plan view of the Vertical Tunnel and the main tunnel in the first figure and a picture of them showing the way they are connected in the second.

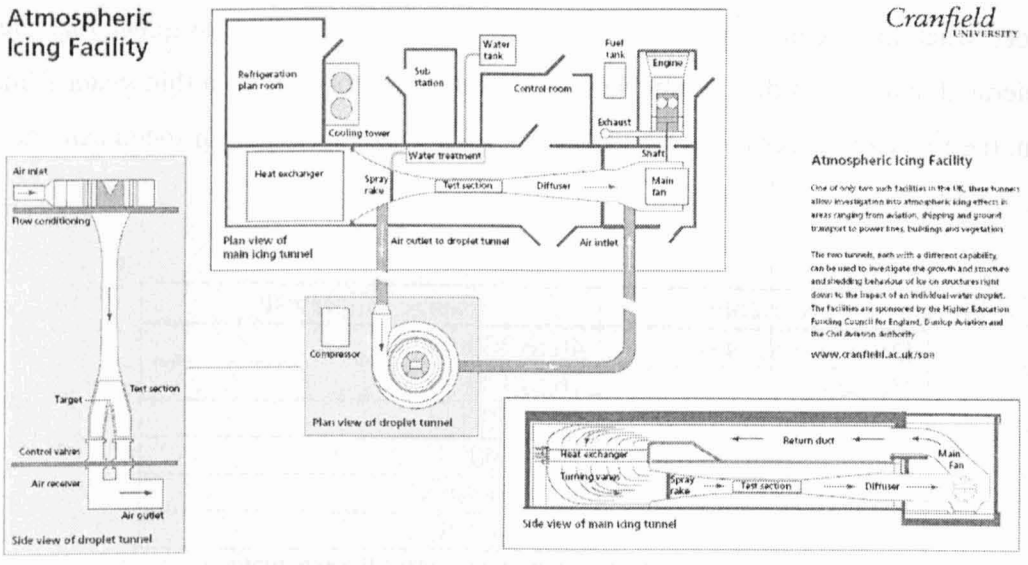

Figure 42. The Cranfield University High Speed Vertical Tunnel and Icing Tunnel.

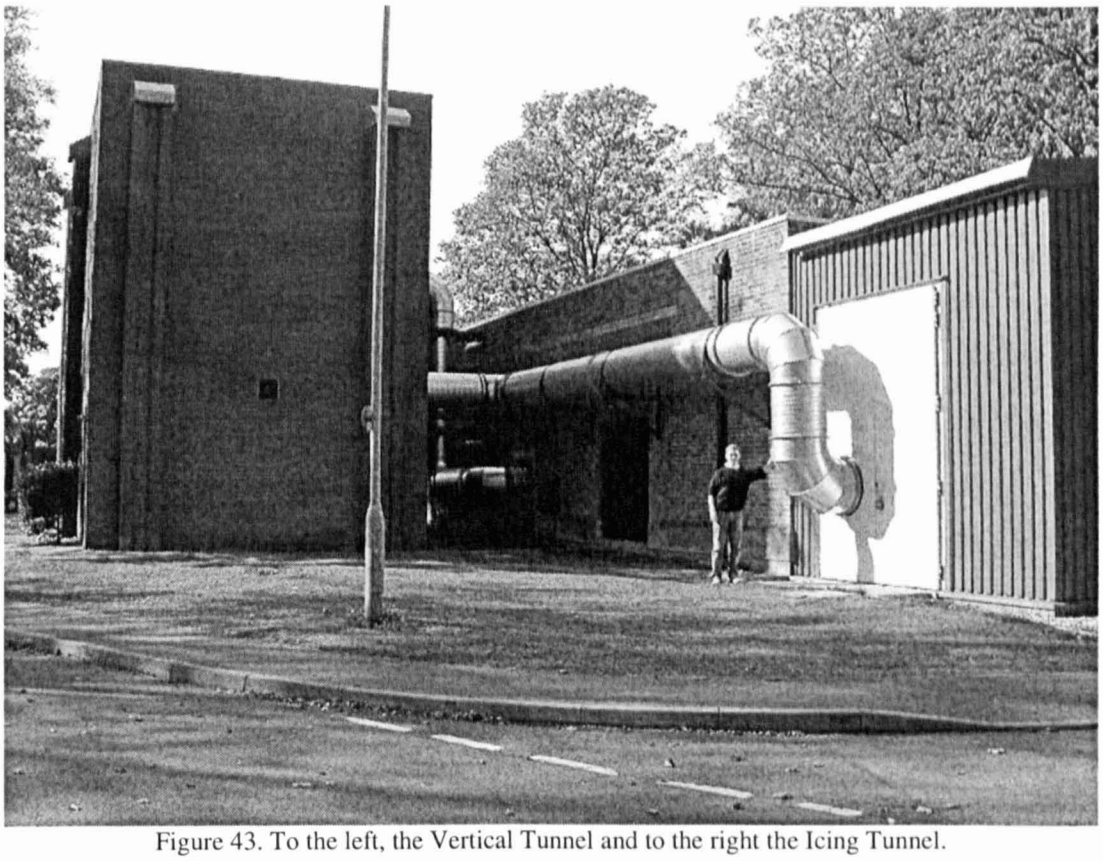

Figure 43. To the left, the Vertical Tunnel and to the right the Icing Tunnel.

The main fan and the refrigeration plant of the icing tunnel are used as a source of cold air for the Vertical Tunnel.

The main fan is a backward curved centrifugal suction fan with useable flow range of between 30 to 100 kg/s. The airflow is shown in figure 42. The refrigeration plant has a capacity of 400 KW and will produce air at temperatures between + 30° C to -30° C.

Figure 44 shows the back part of the refrigeration plant and the connection between the tunnels.

Figure 44. Tunnels and connections. The refrigeration plant can be observed on the left.

Once the air is cooled down, it is diverted to the Vertical Tunnel and enters the cone section (figure 45) where it will be initially accelerated (see figure 42). On the top of this cone section is placed the steering dish where the droplets generator is mounted (figure 46).

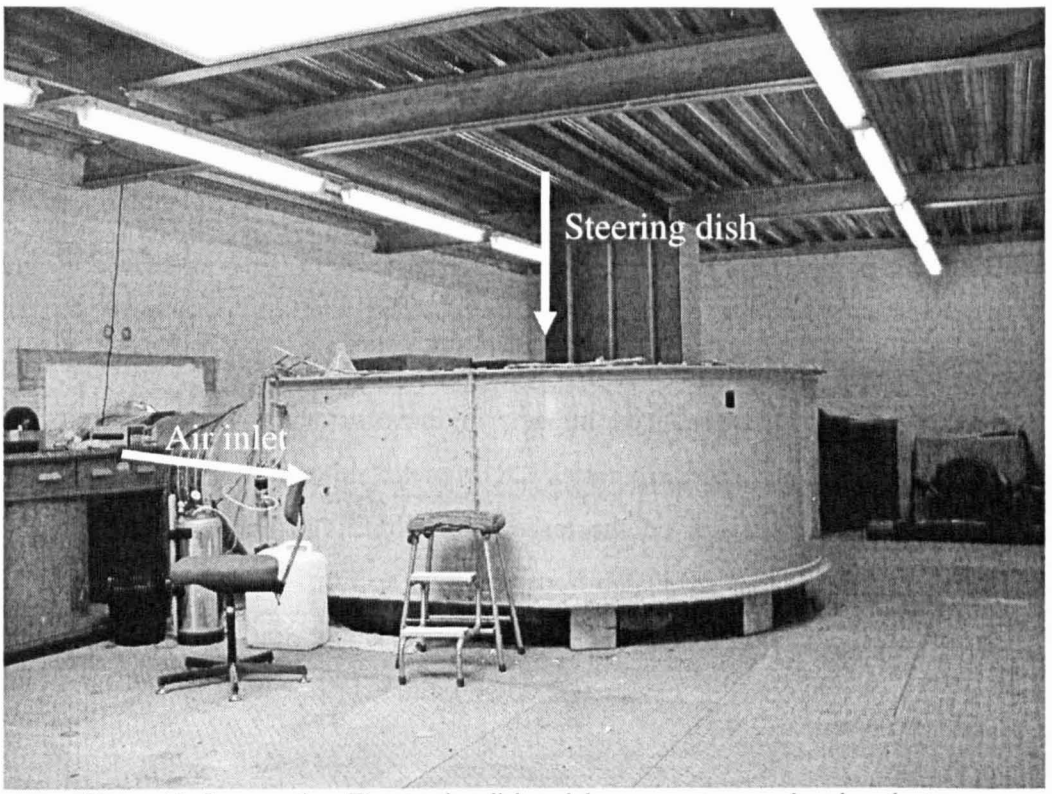

Figure 45. Cone section. The steering dish and drop generator are placed on the top.

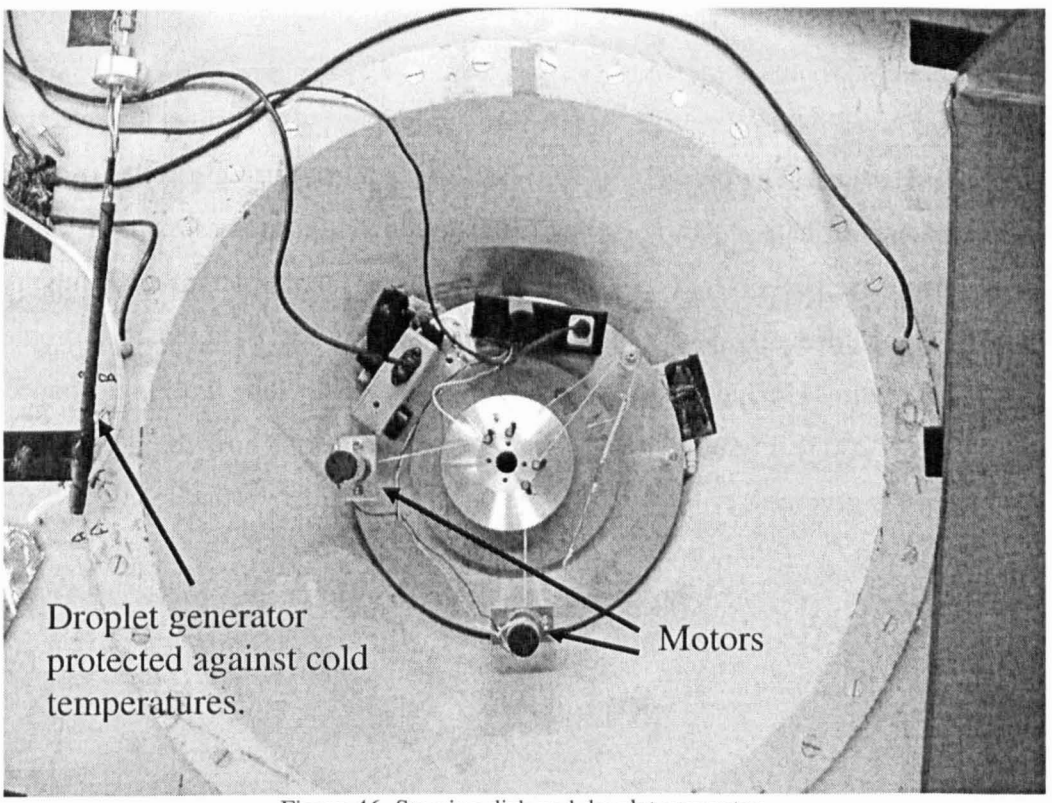

Figure 46. Steering dish and droplet generator.

The steering dish is motorized and remote controlled in order to lead the droplets to the target. The whole installation was kept a few degrees above freezing point and the droplet generator had to be coated to prevent the water from freezing. Sometimes the mechanism lacked manoeuvre and the system had to be controlled manually.

Part of my contribution includes final design of the steering dish and its control system as it was incomplete. During the experiments there were found problems with the range of angles. This produced impacts in the contraction section before the droplet reaches the target and some times the droplets, although they went down the tunnel, they did not impacted on the target. To sort this problem out the droplet generator had to be steered manually from the cone section. This supposed a major inconvenience when using super-cooled temperatures. The reason was that I had to be protected with special coats as I had to lie down on the cone section where the super-cooled air was passing though.

The droplet generator (figures 47 and 48) was developed by Geoff Luxfford (Ph.D. thesis 2005) made in Cranfield University as nothing commercial for this purpose was available. Water is forced through a precision orifice (an electron microscope aperture). The pressure of the water is modulated using a series of piezo electric elements to help synchronize the water jet break-up into a stream of mono-dispersed droplets. The generator allows the changing of the droplet size, a thing that had to be done manually and took a matter of minutes. It is noted that droplet coalescent sometimes happens with this kind of generator for long working distances (Luxford *et al.* 2005). Figure 49a & b show two examples of how the droplets are ejected from the generator.

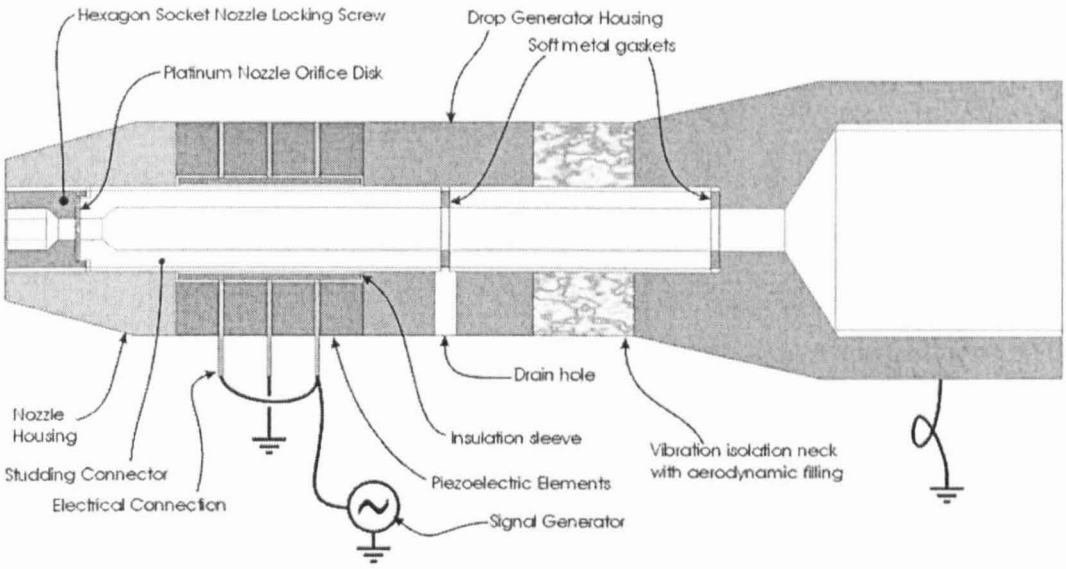

Figure 47. Drop generator scheme (Luxfford, 2005).

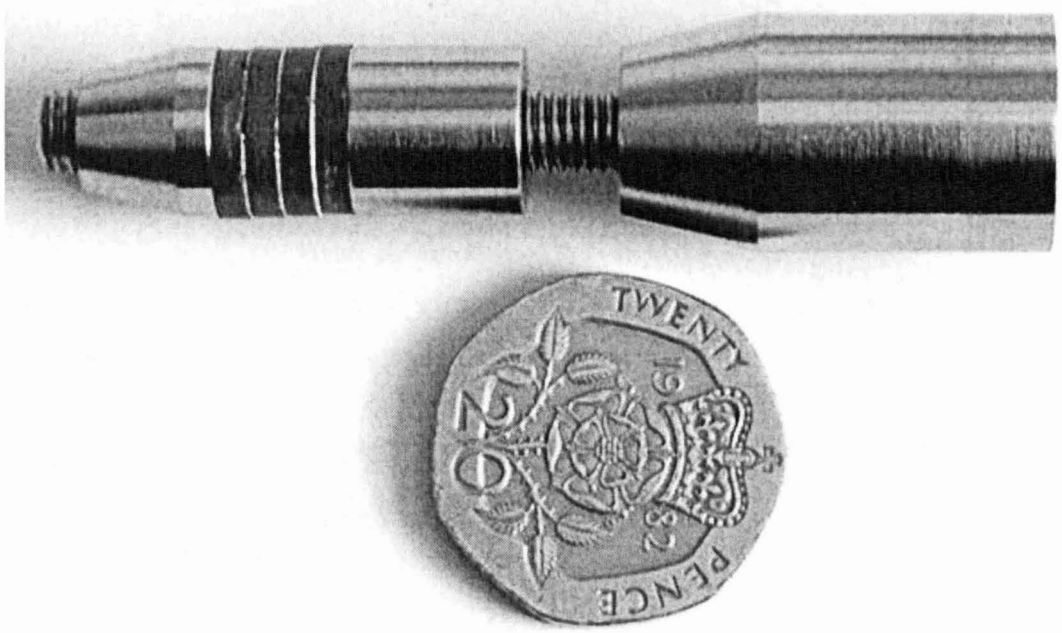

Figure 48. Picture of droplet generator (Luxfford, 2005).

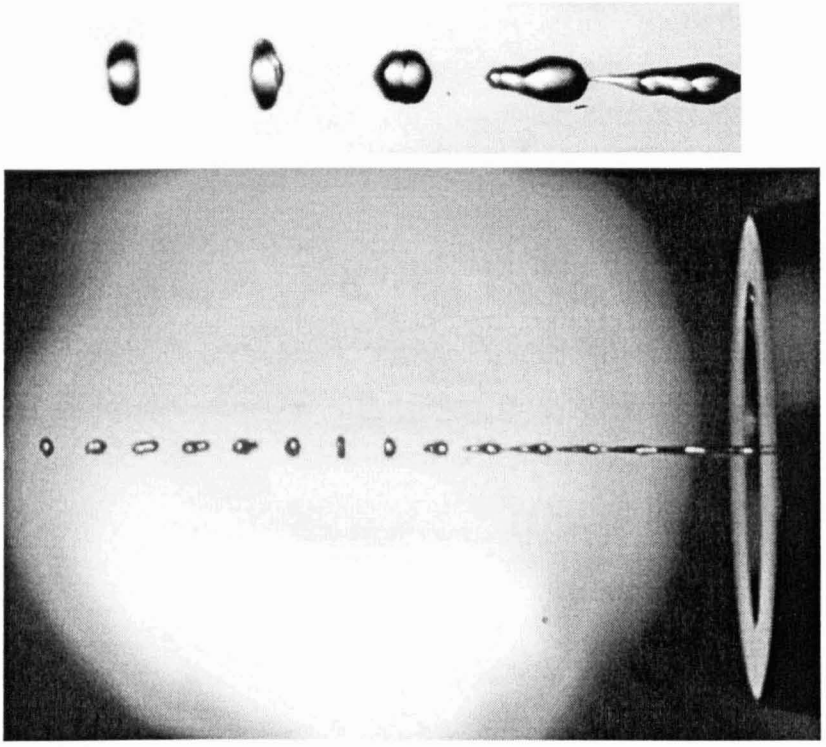

Figures 49a & b. Droplets coming off the droplet generator (Luxfford, 2005).

Once the droplets are ejected, they go through the tunnel contraction where they are accelerated and cooled down. This is approximately 5 metres long. Figure 50 shows part of that tunnel contraction section. It should be mentioned that due to the cold temperatures, some heating had to be provided to the windows of working section. Also, certain amount of ice was seen to build up on the walls.

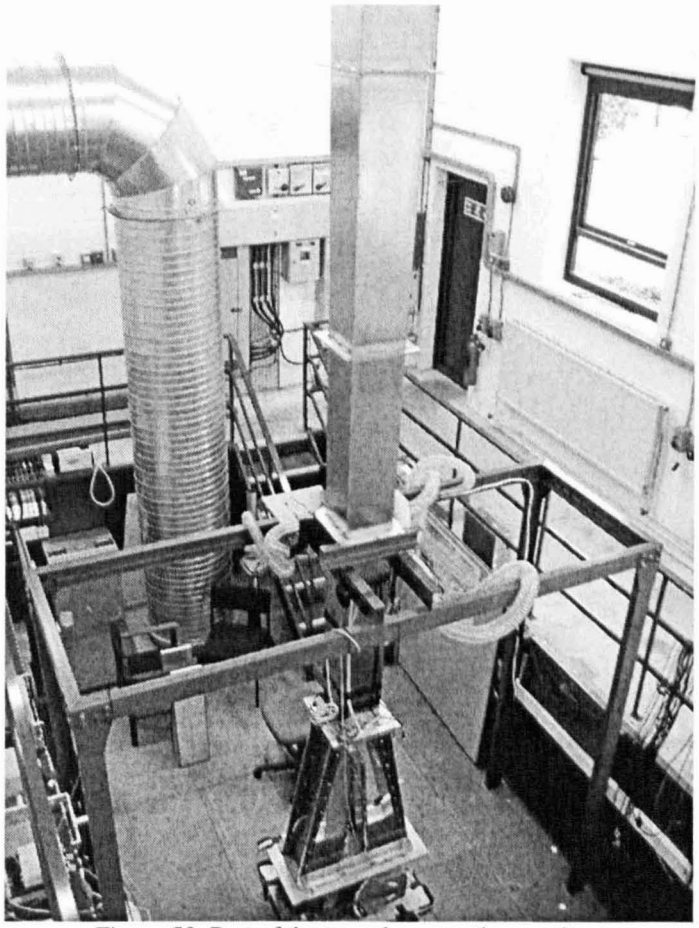

Figure 50. Part of the tunnel contraction section.

As the droplets reached the working section it was observed that not all of them impacted on the target, or also happened that although they impinged on it they did it in an area out of focus. In order to avoid the record of images when nothing was happening, a droplet detection system was installed.

The system is formed by two laser beams crossed at the point of the central axis of the tunnel and a few centimetres over the target. Only droplets near the centre of the tunnel caused significant obscuration of the beams. Two photodiode detectors with suitably fast response time were positioned on the opposite side of the tunnel from the lasers to pick up the passage of droplets. This was used to trigger an imaging sequence. Figures 51a & b show this detection system.

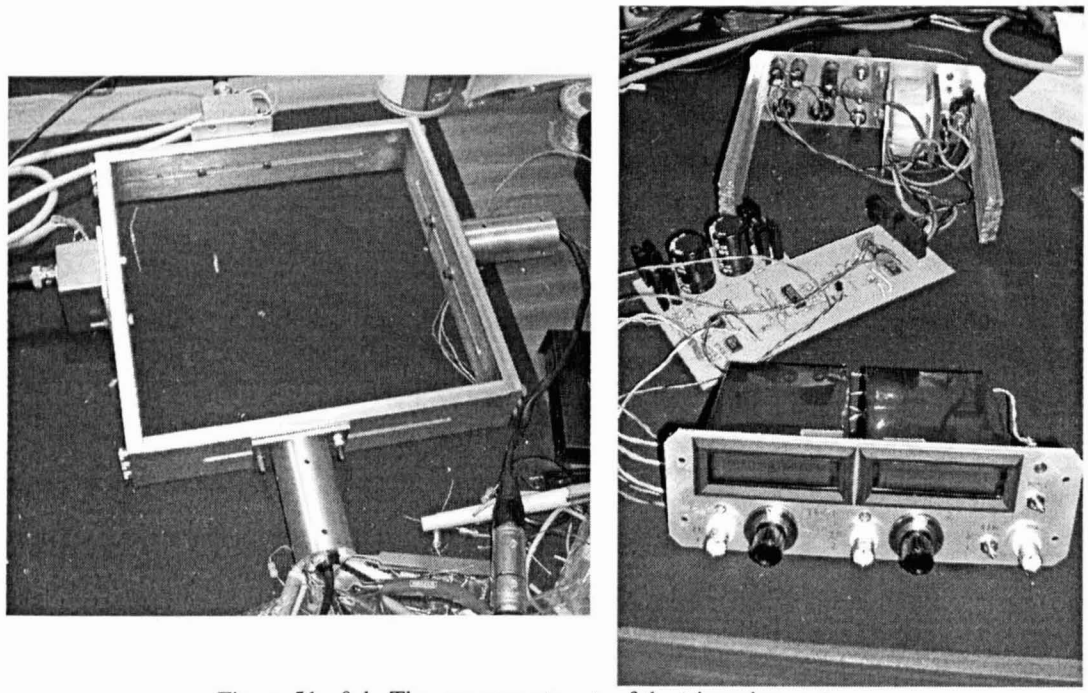

Figure 51a & b. The component parts of the triggering system.

Once the droplet is detected, it will impact on the target which is built of polished austenitic stainless pieces (figures 52a & b) and is covered by a thin and running water film. This layer is produced by pushing water and let it flow through a slot placed on the centre and top surface. This central target area also features two flush isolated electrodes which were used for resistance film thickness measurement. This was backed up by an ultrasonic measurement system (McGregor *et al.* 2004) based on a standard plane wave 50 MHz ultrasonic transducer mounted slightly beneath the target surface. The target block was heated and temperature was measured using the thermocouple.

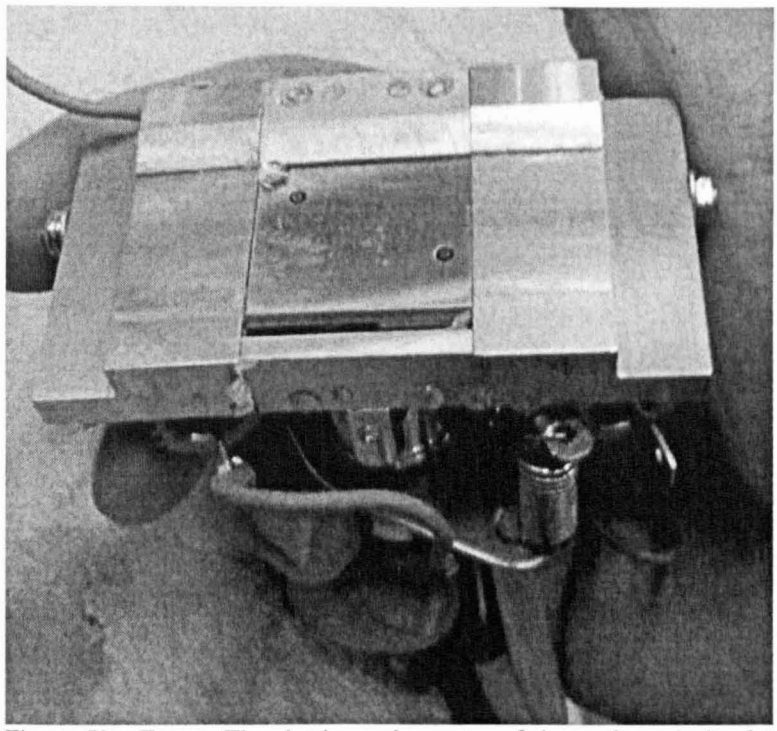

Figure 52a. Target. The slot is on the centre of the surface. A droplet coming from it can be seen. Both electrodes are placed on the left and top side and bottom and right side.

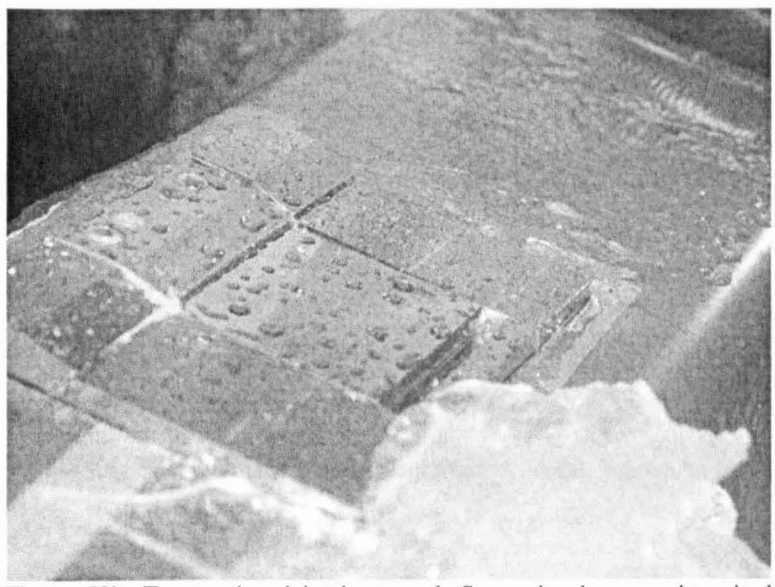

Figure 52b. Target placed in the tunnel. Some droplets are deposited over it.

The two different ways of water film thickness measurement suggest that the two layers used during the experiments are 50 and 150μm which is in consonance with some separated studies (Feo *et al.* 1991 and Hastings *et al.* 1984) which affirm that the water film can go from a few tens to lower hundreds of microns thickness.

The target can be placed at three different angles. They are, 70, 45 and 20° respect the vertical (figure 53). Figure 54 shows two of the pieces where the target is inserted. They are, respectively, for the study of impacts at 45 and 20°.

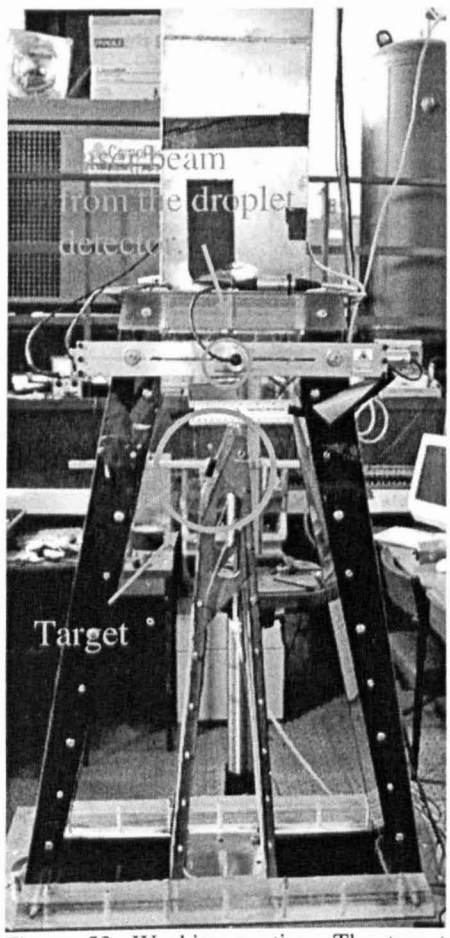

Figure 53. Working section. The target and the triggering system are also shown.

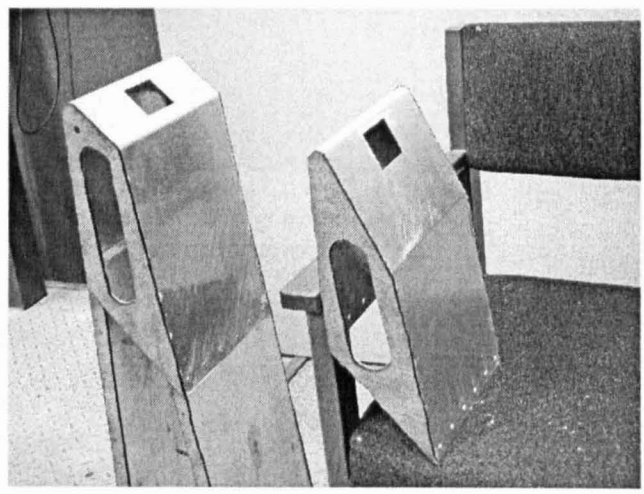

Figure 54. Section for two of the three angles used during the experiments. In particular 45° and 23°.

In order to take the pictures, a high speed camera was used. In particular a Phantom 7 high speed variable format video provided by the NASA icing branch which provided 10^4 pictures of 10^5 pixels per second. The timing of the light and camera are controlled by the droplet detector/triggering system. The imaging system is shown in pictures 55a & b. It can be seen in 55a the Phantom camera in front of the target and the light (green) source. The hot air coming from the white tubes were used

to keep the working section clean of condensation due to the low temperatures. Figure 55b shows a picture of the light source.

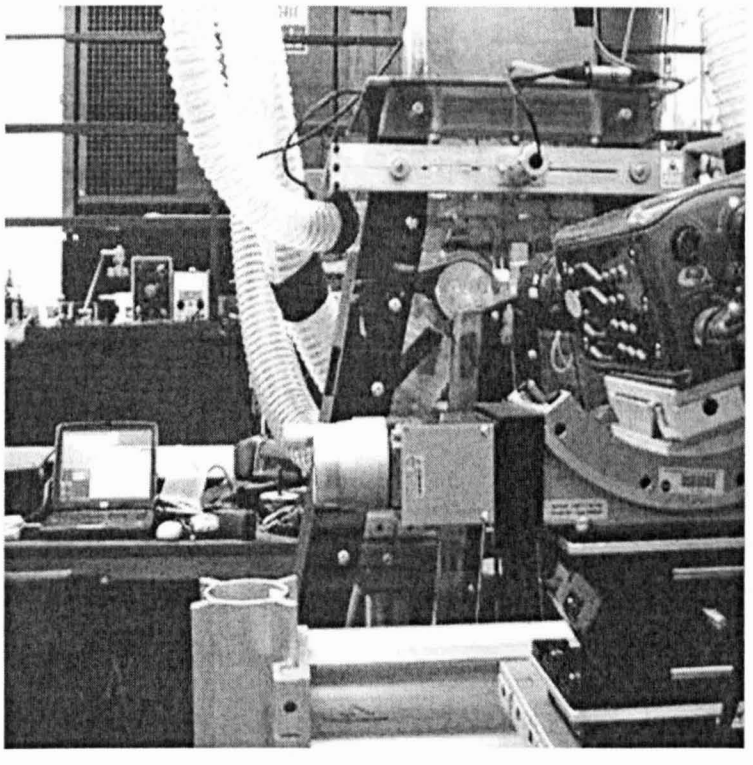

Figure 55a. Phantom camera, target and light.

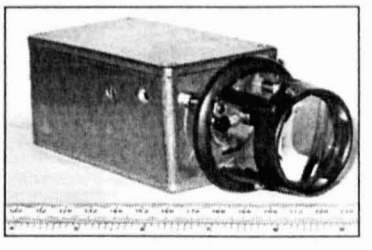

Figure 55b. Light source.

Finally the airflow is controlled in the tunnel diffuser by two valves by regulating the opening or closing them. This helps to get the stagnation point slightly above the target. Figure 56 shows the working section and bellow, the system that allows opening and closing the valves. (Hammond, 2005 and Pearson, 2005).

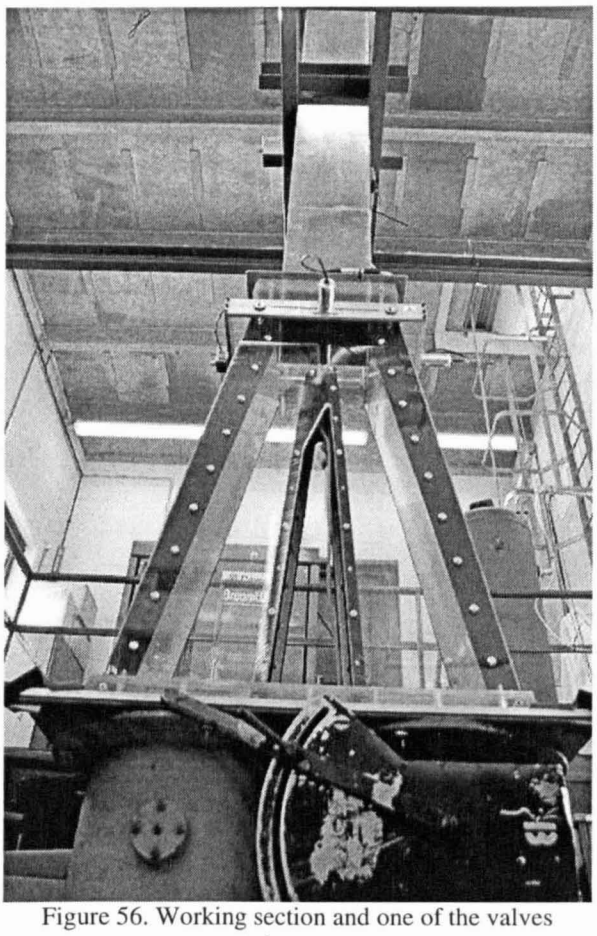

Figure 56. Working section and one of the valves opening system.

Presentation and Analysis of the Experimental Results.

The experiments provide images of the impacts and subsequent splashes. A wide range of variables has been used in order to give a general idea of how the corona develops for a range of the droplet sizes, droplet temperatures, velocities of impact, angles of impact and layer depths (see table 2).

Around ten thousand different impacts and splashes have been collected and recorded. One thousand of them have been studied and more than one hundred have been selected to be analysed because they represent most of the range of interest and the quality of images is adequate.

The pictures shown in figures 57 and 58 give examples of sequences of impact images. They reflect the initial oblate droplet, the corona at its most fully developed and the subsequent break-up. The time taken for the corona to reach its greatest size in these two cases is approximately 500 and 400μs respectively.

The main difference between the impacts depicted in figures 57 and 58 is the speed of the droplet (and also of the air flow). In figure 57, the incoming droplet is relatively spherical and the water sheet of the resulting corona is more smooth and conical than in the higher speed case. Also the satellite droplets generated as the corona breaks down are noticeably larger. In the higher speed case, the distortion of the droplet prior to impact is more noticeable. The general shape of the corona has changed but its overall height and width at the time it starts to break up is similar. These coronas are of the order of 2 to 3 mm in height and width.

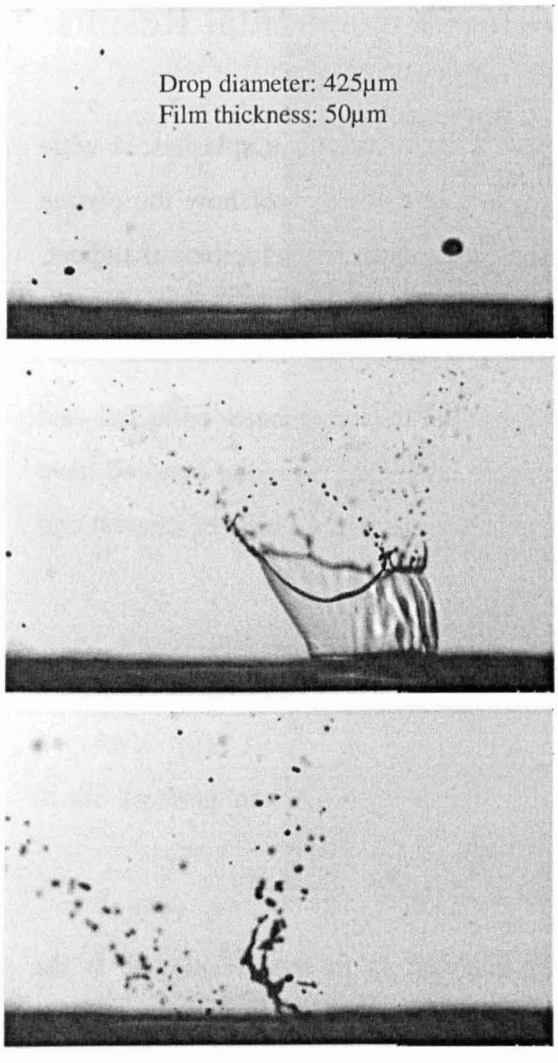

Figure 57. Impact at 24 m/s, 70° and ambient temperature. 150µm film.

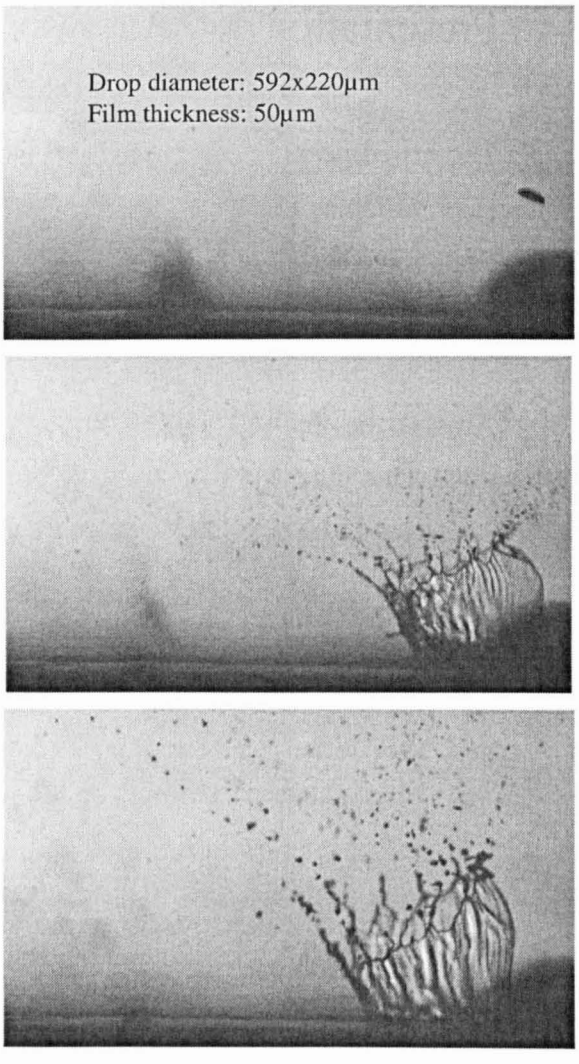

Figure 58. Impact at 49 m/s, 70° and -9°C. 50µm film.

Also, it is appreciable how the droplet is flattened when it approaches the target due to the decelerating forces as it has been commented previously. This happens for the high velocities. There are clear differences between these two splashes. These differences are found in the development of the corona and the number of the satellite droplets released. These findings will be analysed in later sections.

Other significant differences in the development of the corona occur when the impacts are made at more acute angles, this is, instead of impacts at 70° like in figures 57 and 58, at 45 and 20°. This is shown in figures 59 and 60.

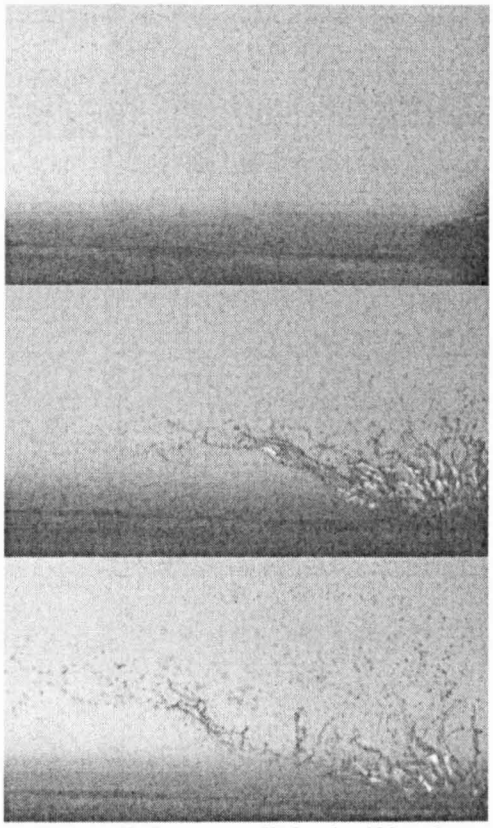

Figure 59. Impact at 57.2 m/s, 43° and ambient temperature. 50μm film.

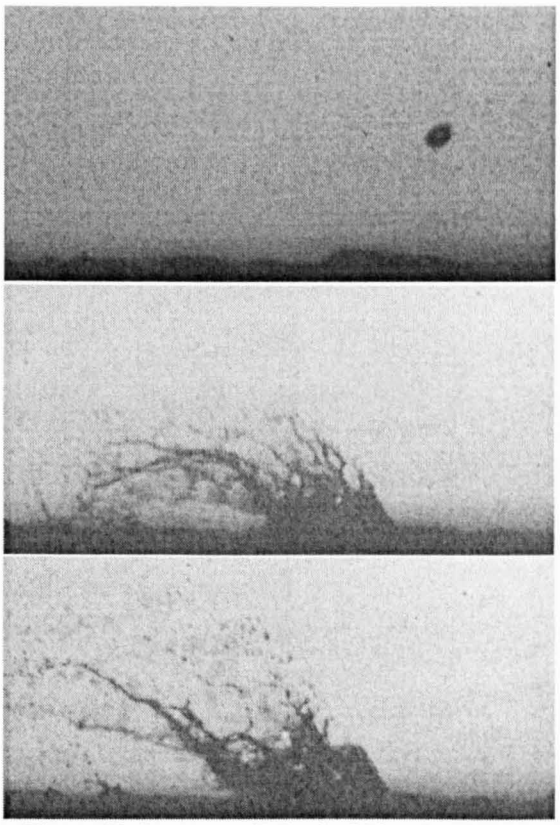

Figure 60. Impact at 68.5 m/s, 20° and ambient temperature. 50μm film.

The corona formation in these two cases is different to the impacts presented in figures 57 and 58. Now it can be seen how the left side of the corona is elongated and the right side is bent to the left. Also the water sheet forming the corona seems to be in a continuous breaking up.

Other particularities have been also taken into account and studied. Some of them are related to the fact that not all the impacts have been done into a thin water film but also using a dry target. These splashes do not form any corona. After the impingement, the droplet brakes up in multitude smaller droplets that are ejected to the air flow as it is shown in figures 61a, b and c.

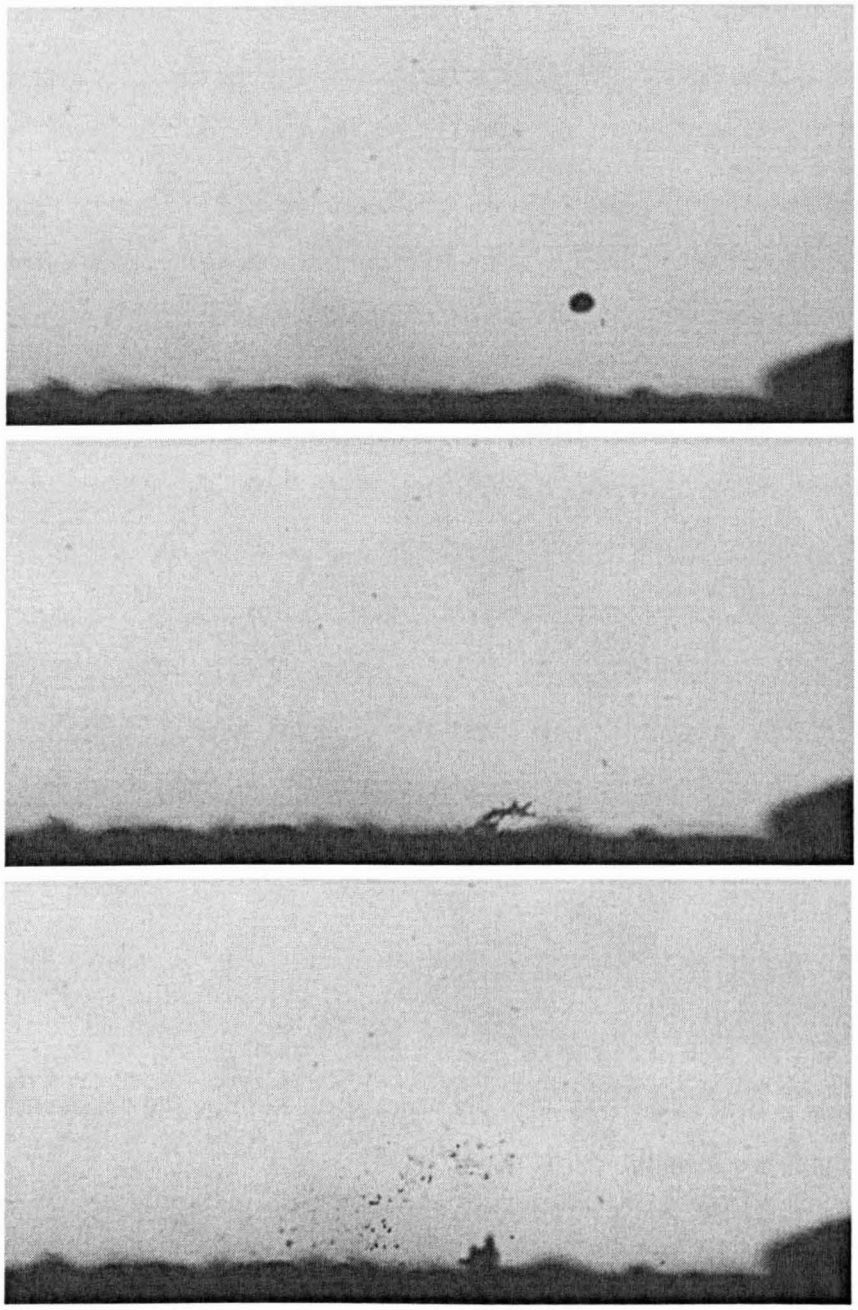

Figures 61a, b and c. Droplet impact upon a dry target.

Also, there are some other cases which have been observed when no corona is formed either. Some bubbles have been seen rolling down the target. This is illustrated at figure 62. Although this last case has been taken into account, however it has not been included in the final results as a general case because it has been found under very particular conditions.

Figure 62 shows the bubble formation after the impact of a very small droplet and relatively low velocity. Once the corona is formed, due to the airflow, it is attached from the rim and rolls down the target over the thin water film.

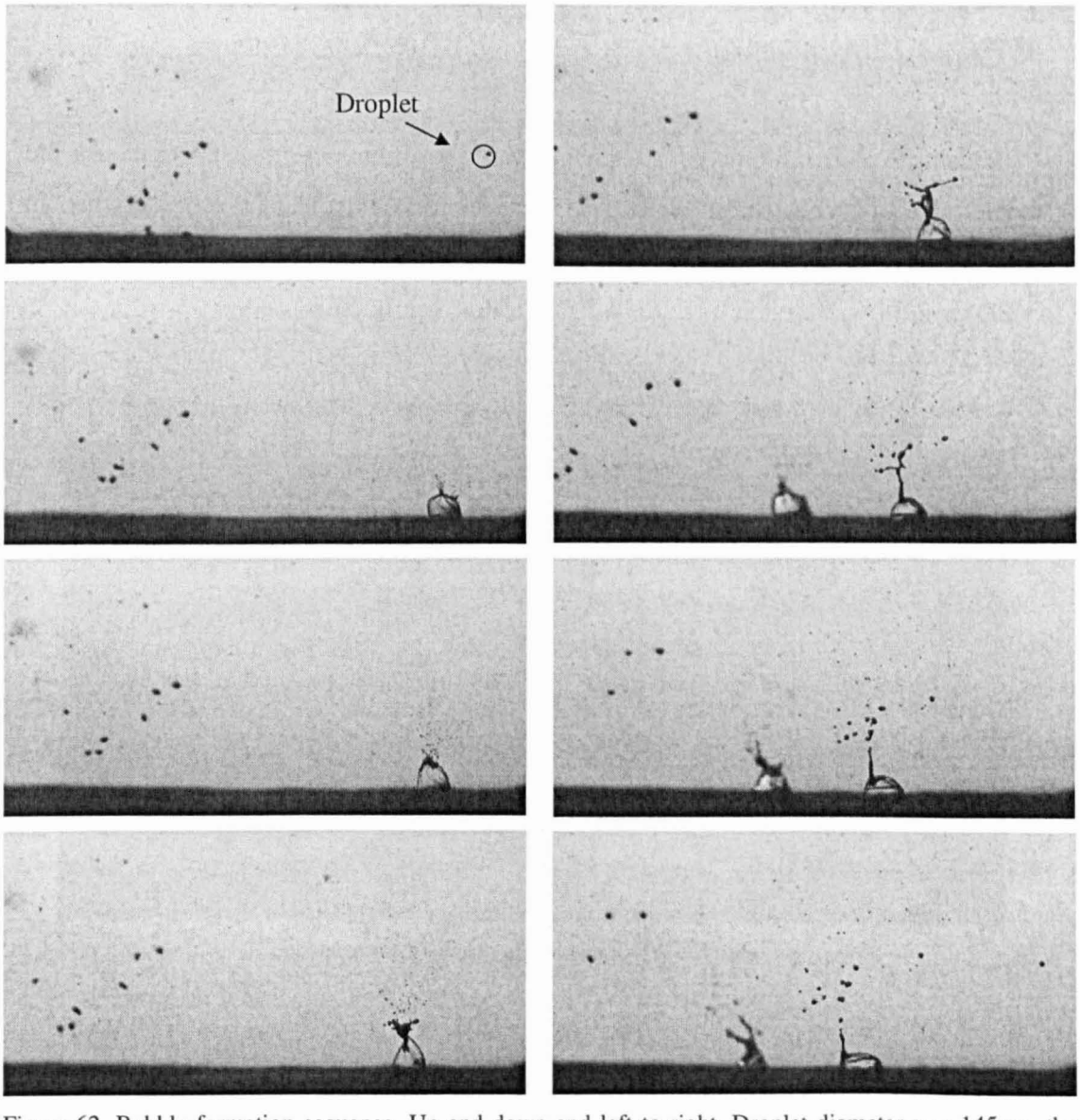

Figure 62. Bubble formation sequence. Up and down and left to right. Droplet diameter was 145μm, the velocity of impact was 44m/s, angle of impact 70°, water film thickness 150μm and ambient temperature.

Definition of Measurements Taken from the Images.

In order to analyse how the corona forms, a number of parameters is defined to facilitate comparisons between one case and another.

Characteristic droplet size.

It can be seen in some of the images that the droplet is non spherical. As the droplet size must be measured from the images, account must be taken of this. In order to have a single measure of droplet size, the Volume Equivalent Diameter (VED) is used. To explain how this VED is found, figure 63 is used.

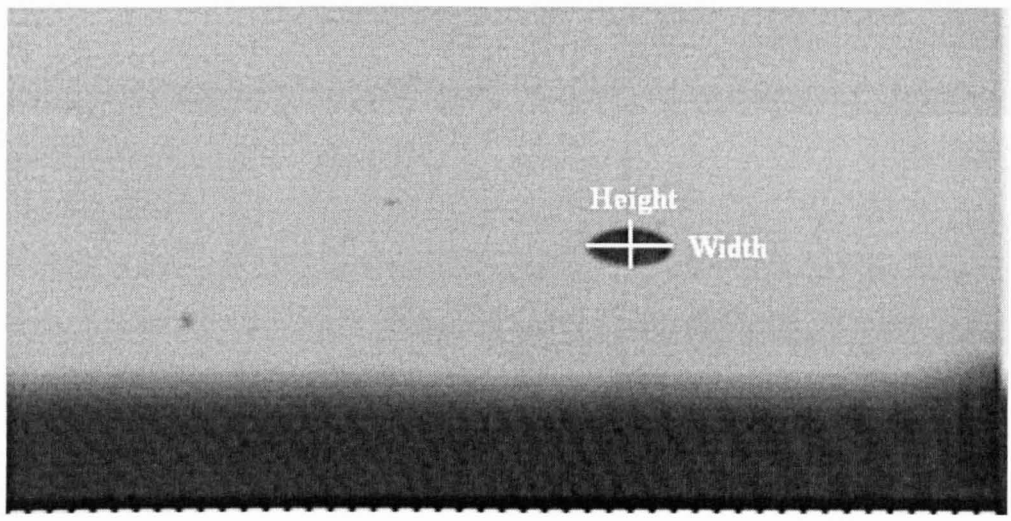

Figure 63. Width and height droplet measurement.

When the droplet approaches the target, both height and width are measured and the VED is calculated as follows:

$$\mathrm{VED} = \sqrt[3]{w^2 \cdot h} \tag{44}$$

Characteristics of the corona.

The corona variables considered are the height, base width and top width (figure 64) and also the angles formed by the corona sides and the water film (figure 65).

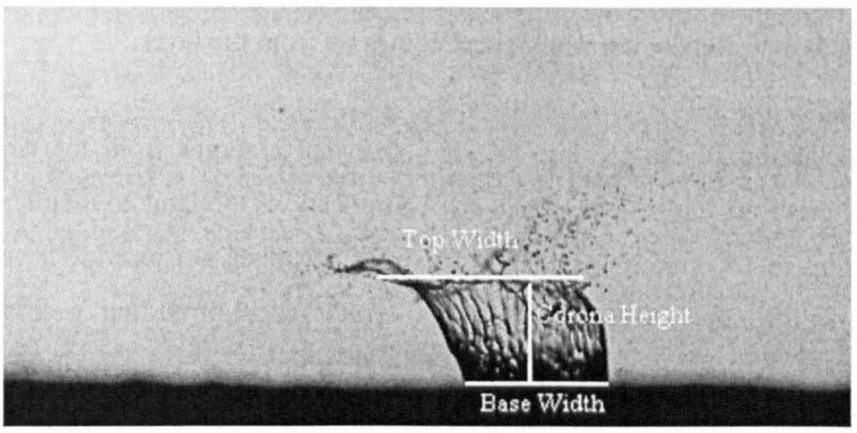

Figure 64. Height, Top Width and Base Width.

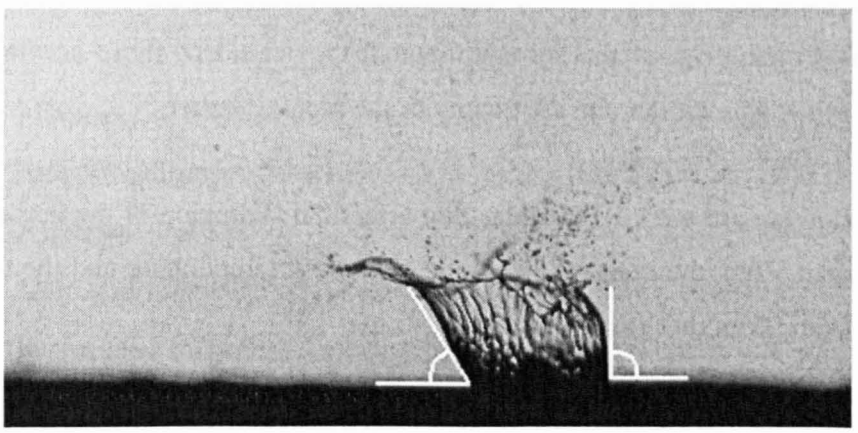

Figure 65. Left and right angles.

Besides the parameters mentioned, the velocities on the left and right side of the corona are also measured. The satellite droplets, that are those ejected from the rim of the corona, are also going to be considered and the velocity and sizes of these tiny droplets coming off the left side are determined as well.

The analysis process presents some difficulties that, in some cases, could affect to the measurement of the parameters. One important fact is that the inter-frame between images resulting from the experiment, which is 63μs, does not always allow capturing

the moment of the droplet reaching the water film. This will have some influence on the measurement of the time that the corona requires to reach the maximum size before collapsing and also measuring how long does this corona formation and later break up take. Some other uncertainties appear when measuring the parameters related to the size of the corona. Particularly, in order to determine the height of the corona it has to be considered that the images do not allow obtaining the exact location of the place where the water sheet comes up from the layer.

The calculation of the satellite droplets size that emerges from the rim of the corona (see previous figures), present some complications too. Due to their small size, the measuring of the size requires of a zooming that does not provide a very clear definition of the edge. This can result in errors when providing a final result. However, the most important errors can be found on the measurements of the velocity of these satellite droplets. This is due to the difficulties that emerge when tracking them from one frame to another. Nevertheless, the results obtained seem to fit with the velocities of the rim of the corona although they could be more accurate if the inter-frame time was shorter and the quality of the pictures better.

The following are the key variables that affect the formation of the corona. They are the droplet VED, the velocity and angle of impact, temperature and the thickness of the thin water film that covers the target.

Due to the large number of impacts that have been analysed and to the wide range of VED and velocities that are needed to be considered, some particular divisions between cases is taken into account.

Regarding the VED, three different sets of initial droplet sizes are given:

- Small droplets, which are going to be considered those with a VED lower than 300μm.
- Medium droplets are those with a VED between 300 and 500μm.
- Big droplets are those with VED greater than 500μm.

For the velocities, the division that is considered is:

- Low velocities are those below 30m/s
- Medium velocities are between 30 and 50m/s
- High velocities are when the droplet goes over 50m/s

The impacts have been developed considering three kinds of angles; they are 70, 45 and 20 degrees. For the water film, two different thicknesses are taken into account; they are believed to be 150μm and 50μm. The temperatures are in general of two types, one will be considered to be at ambient temperature which is assumed to be around 20°C and for the cold temperatures, they are in a range around -10°C.

Once the range of parameters is set, the analysis of the corona and satellite droplets sizes, velocities and angles is going to be done regarding the following variations:

- Incoming droplet sizes.
- Incoming droplet velocities.
- Angles of impact.
- Cold and ambient temperatures.
- Water film thickness.
- Wet and dry target.

In order to help a better understanding of the way the analysis is done, some idealise impacts are exposed explaining the angles of impacts, water film thicknesses and angles of corona sides.

Figures 66a, b and c illustrate the three different angles of impact of a droplet into the water film.

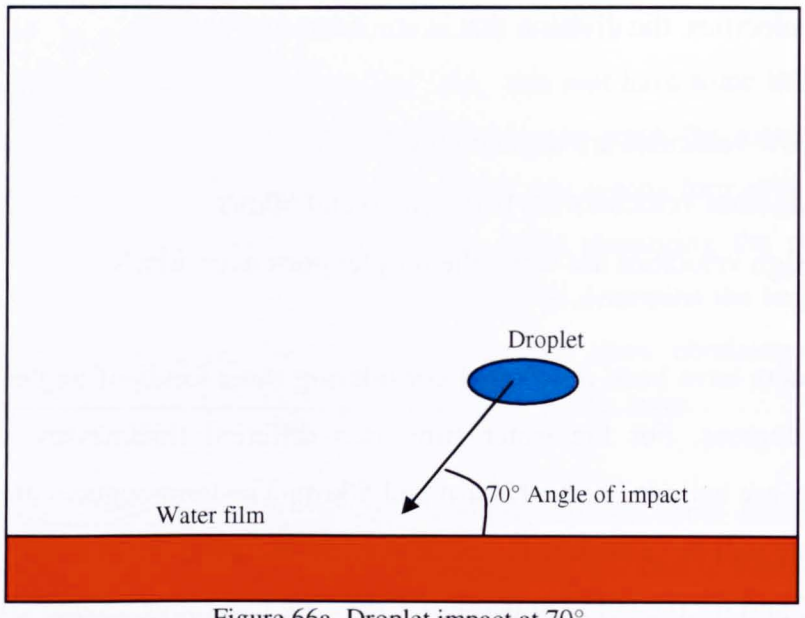

Figure 66a. Droplet impact at 70°.

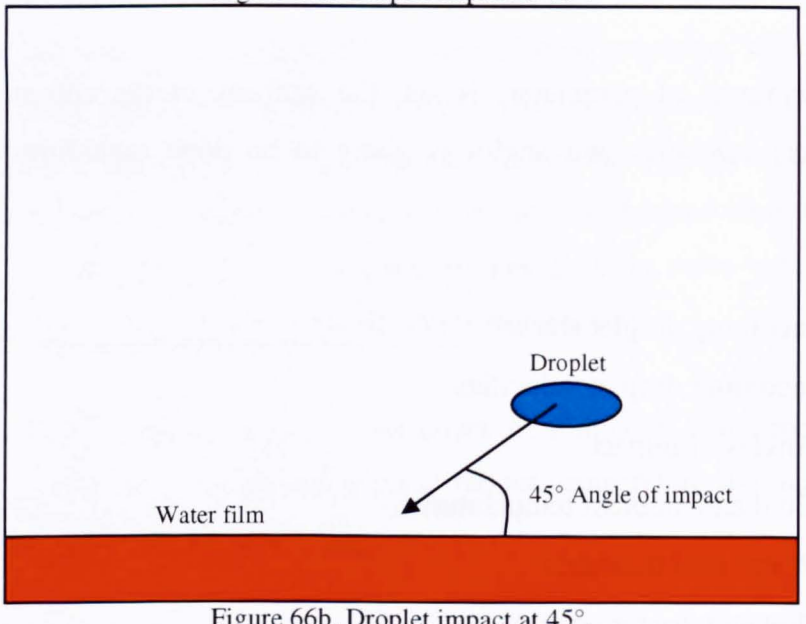

Figure 66b. Droplet impact at 45°.

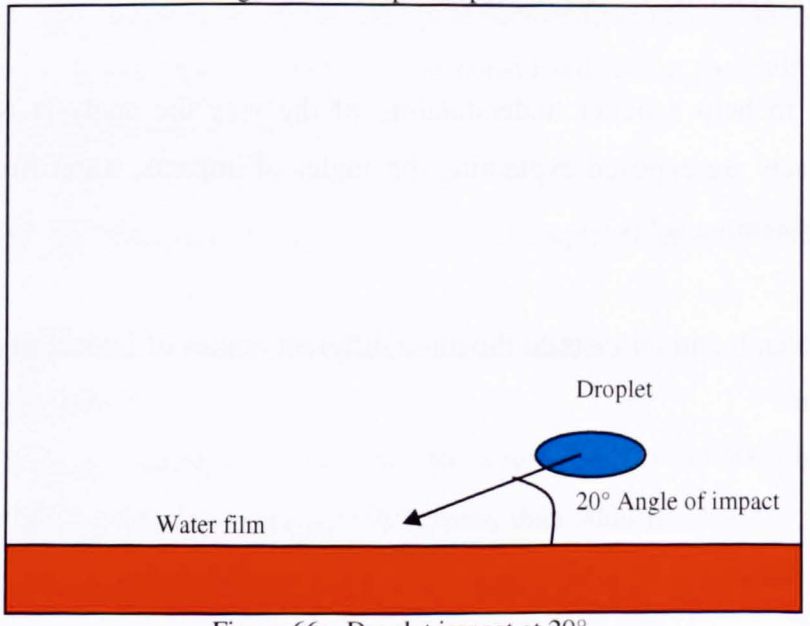

Figure 66c. Droplet impact at 20°.

Figures 67a and b show the difference between the two water film thicknesses used during the experiments.

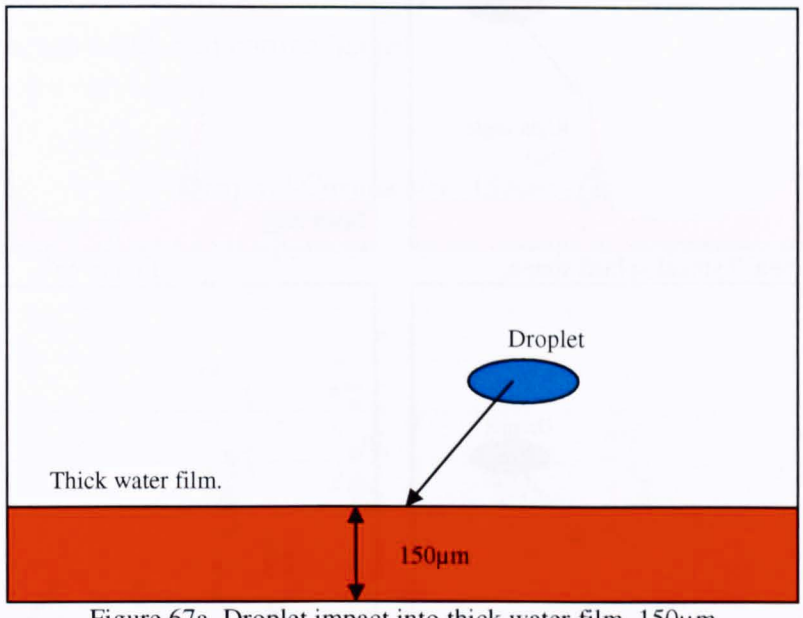

Figure 67a. Droplet impact into thick water film. 150µm

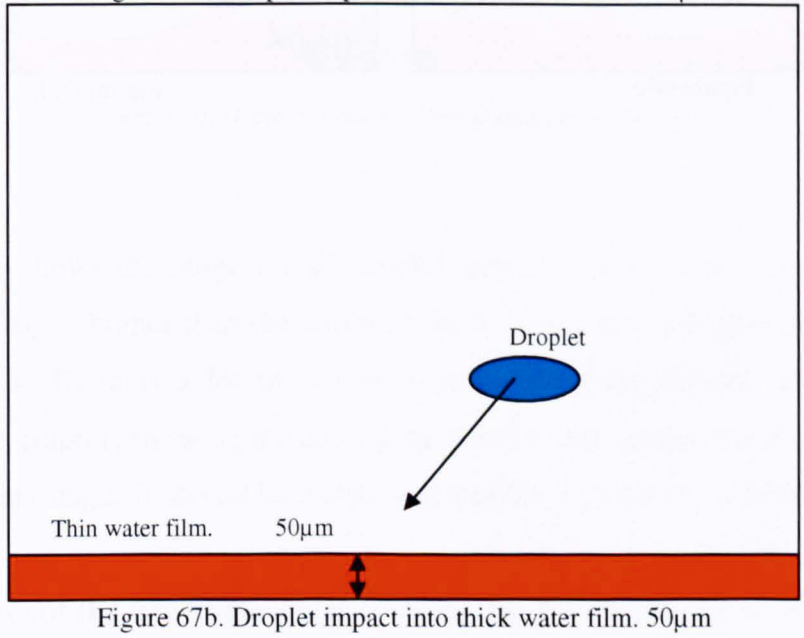

Figure 67b. Droplet impact into thick water film. 50µm

Figure 68a illustrates the general form of the corona side angles produced by the splash after the droplet impact. Two different angles can be observed (see also figure 65). However, as figures 68 b, c and d show, the splashes might produce some particularities regarding the droplet velocity (and airflow effects), droplet size, temperature or angle of impact.

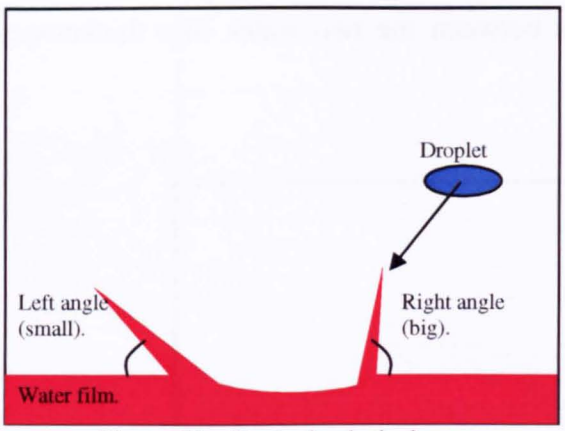

Figure 68a. Typical splash shape.

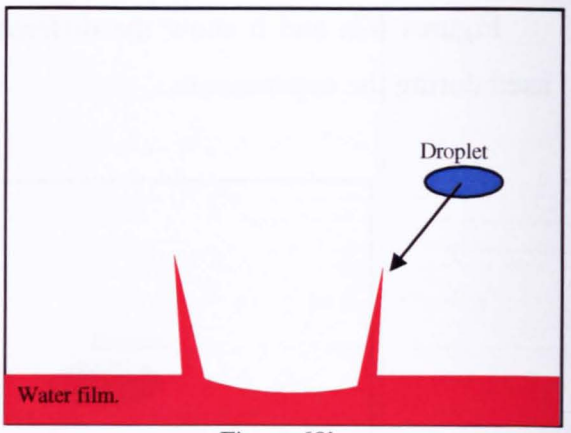

Figure 68b.

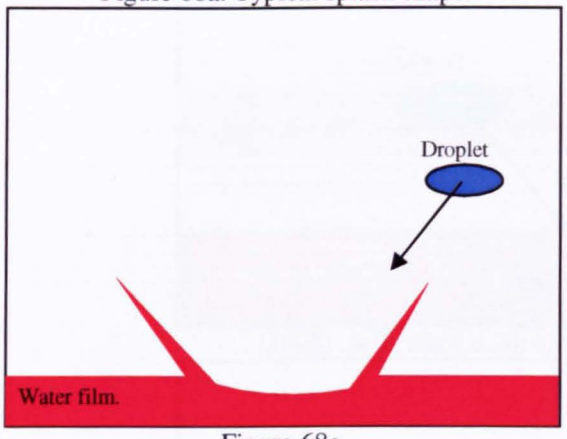

Figure 68c.

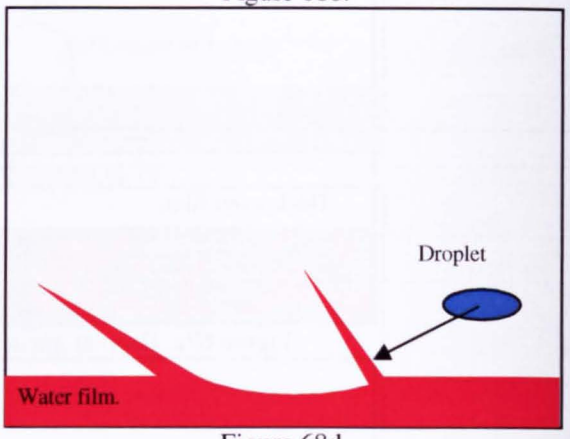

Figure 68d.

Comparison of Corona Size.

This section is going to provide an analysis of the sizes of the corona in terms of the base width, top width and corona height.

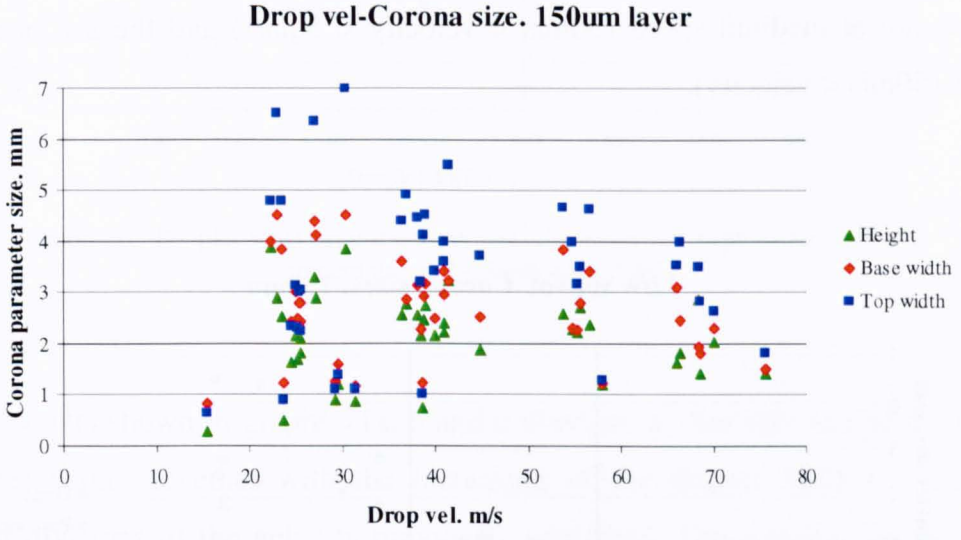

Graph 20. Droplet impact velocity against corona size.

Graph 20 shows the range for all droplet sizes. It can be seen that generally the width of the top is higher than the width of the base and this is higher than the height of the corona. There is a lot of scatter especially for the impacts made at lower velocity. The graph is showing the corona parameters size against the droplet velocity, although at this stages it should be mentioned that the air velocity is similar to it.

A decrease of the trend lines is observed as the velocity of impact increases. This might be due to the effect of the airflow. One of the reasons for the scatter could be that the graph includes the whole range of parameters including droplet size and angle of impact.

Effect of water film thickness on corona size.

The first case presented corresponds to the impacts at 70 degrees into a water film with a 150µm thickness. Graphs 21a, b and c show the behaviour of the corona parameters when the droplet VED increases. The difference between the graphs is that the first one reflects the impact at low speed (velocity < 30m/s), the second the impacts are at medium speed (30m/s < velocity < 50m/s) and the last one at high speeds (50m/s < velocity).

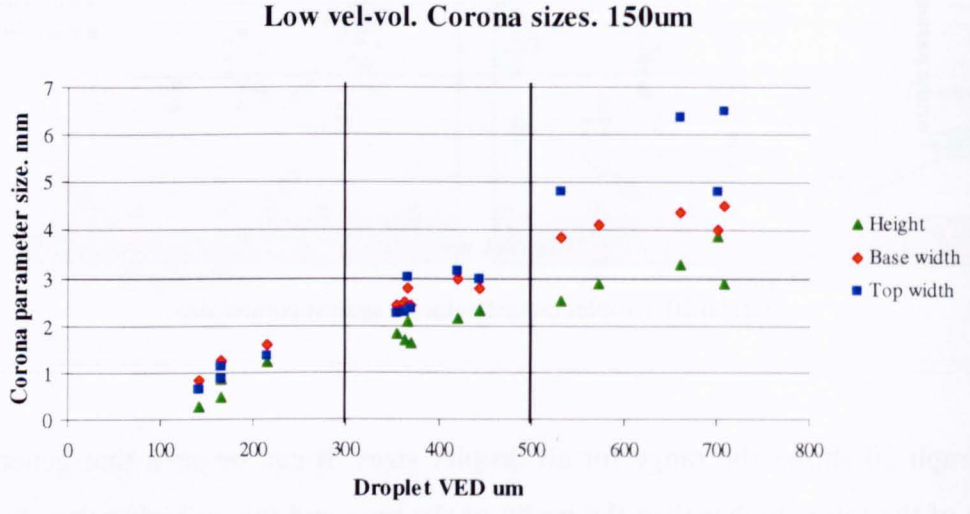

Graph 21a Droplet VED against corona size. Impact at 70°, low speed, ambient temperature and 150µm water film.

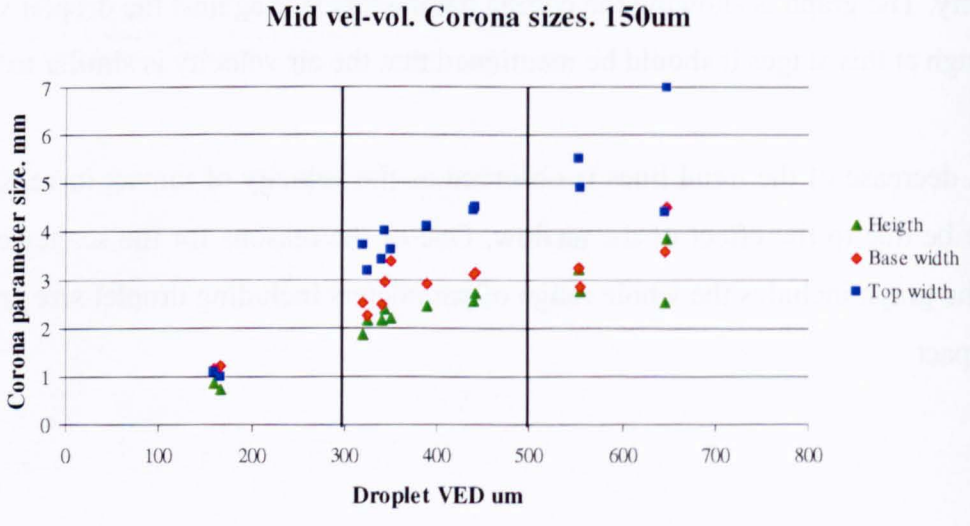

Graph 21b. Droplet VED against corona size. Impact at 70°, medium speed, ambient temperature and 150µm water film.

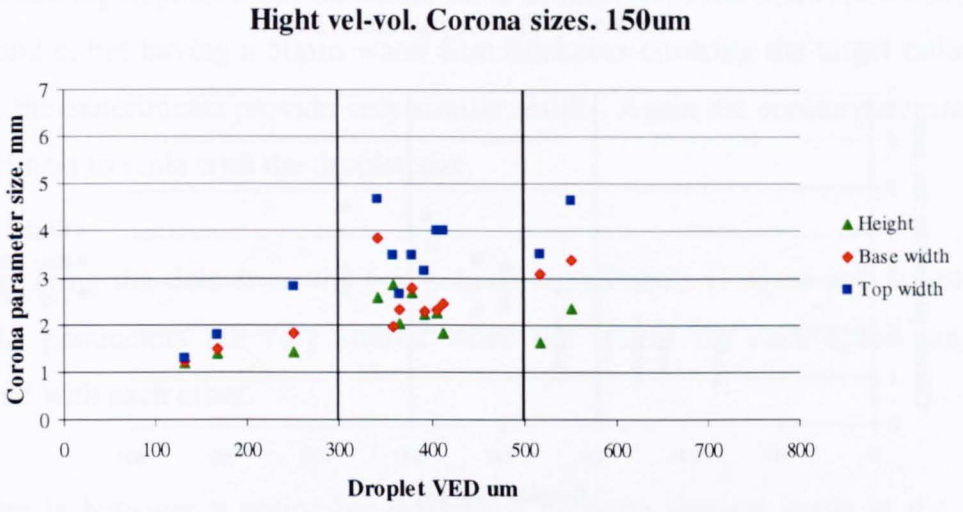

Graph 21c. Droplet VED against corona size. Impact at 70°, high speed, ambient temperature and 150µm water film.

The results shown in graphs 21a, b and c illustrate a clear increase of the corona parameter values together with the increasing of the droplet VED for the three different divisions of the velocity previously explained. The increase appears to be linear. Therefore, in these cases the three parameters considered appear to scale with the droplet size.

Considering the droplet speed, it is observed that, at least for the smallest droplets, the values of the parameters also increase for faster droplets around a millimetre. For the medium size drops no difference is apparent when the velocity increases, however for the biggest droplets a decrease can be seen in the values of these parameters when the impact is made at the highest velocities. This may be due to the airflow around the target that squashes the corona and sweeps it away faster. Another effect that the increase of the velocity appears to have is to that the values obtained for the parameters are more scattered although in general they increase linearly.

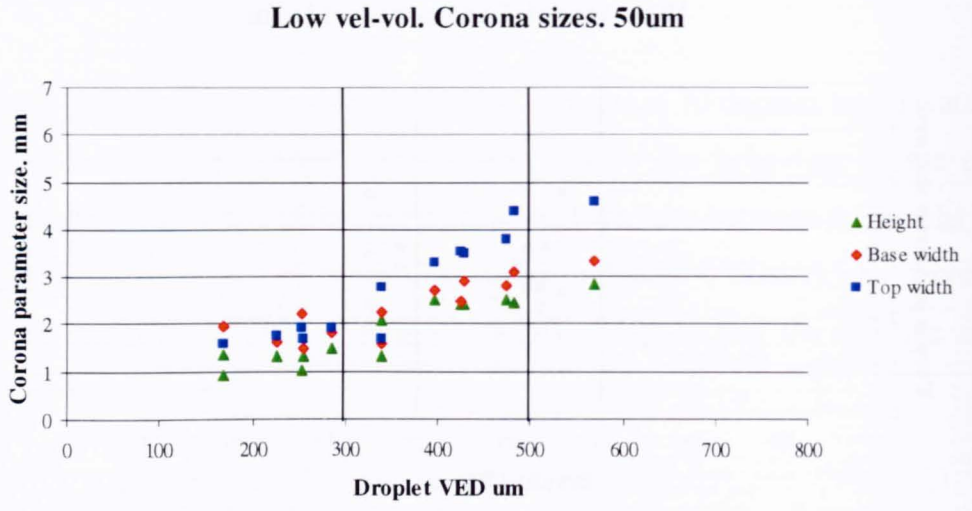

Graph 22a. Droplet VED against corona size. Impact at 70°, low speed, ambient temperature and 50µm water film.

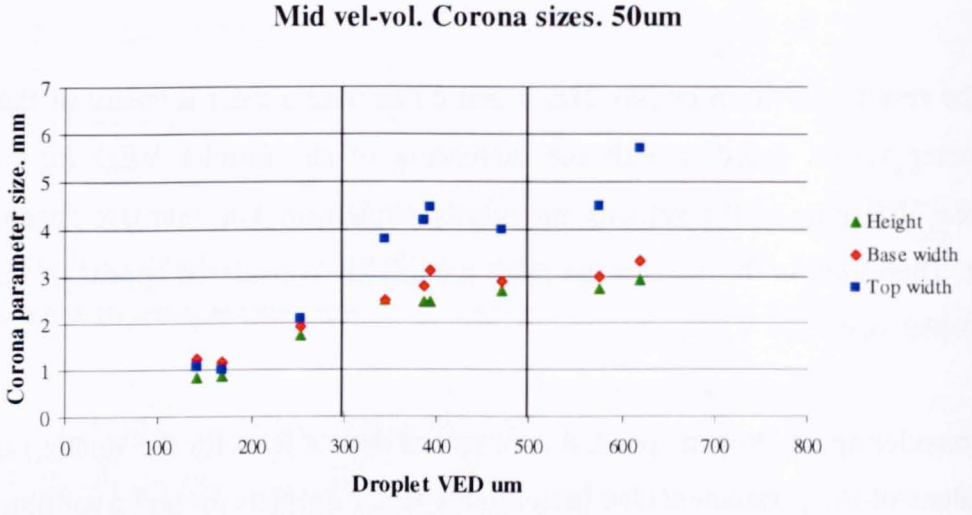

Graph 22b. Droplet VED against corona size. Impact at 70°, medium speed, ambient temperature and 50µm water film.

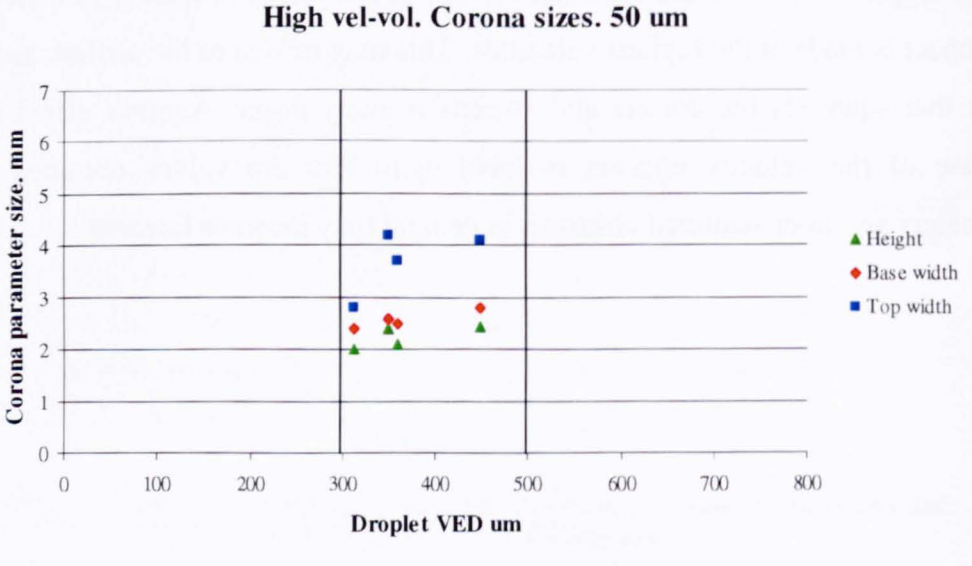

Graph 22c. Droplet VED against corona size. Impact at 70°, high speed, ambient temperature and 50µm water film.

Considering impacts made under the same conditions as the cases shown in graphs 22a, b and c, but having a 50μm water film thickness covering the target rather than 150μm, the experiments provide very similar results. Again the corona parameter size seems almost to scale with the droplet size.

Comparing the data from the two sets of experiments (150μm and 50μm water film) the parameters are very similar when the results for each speed range are compared with each other.

There is however a noticeable difference between impacts made at the lowest velocities and with the smallest droplets. These show higher values for the coronas with a shallower water film. This difference (graphs 21a and 22a) is lower than one millimetre for every parameter (parameter values approximately one millimetre). One more relevant discrepancy of the values of the parameters monitored is observed in the impacts at medium velocity (graphs 21b and 22b). In these cases is observed also that the width of the top of the corona can be wider in the cases with deeper water film than in the impact into the thinner one.

It is also observed that the velocity has very little influence on the values of the corona height, top and base width. In general the values for the impacts at low, medium and high speed have all the same results as graphs 22a, b and c illustrate. Thus the values of the parameters for the small droplets are between one and two millimetres for the impacts at low and medium velocity. For the medium size droplet the base width and corona height values are between two and three millimetres, however the top width increases slightly for the higher velocities. It is observed that for the impact at medium and high velocities the values of this parameter can be up to one millimetre greater. The impingements at high velocities do not show any particular variation in the parameters.

Effect of droplet temperature on corona size.

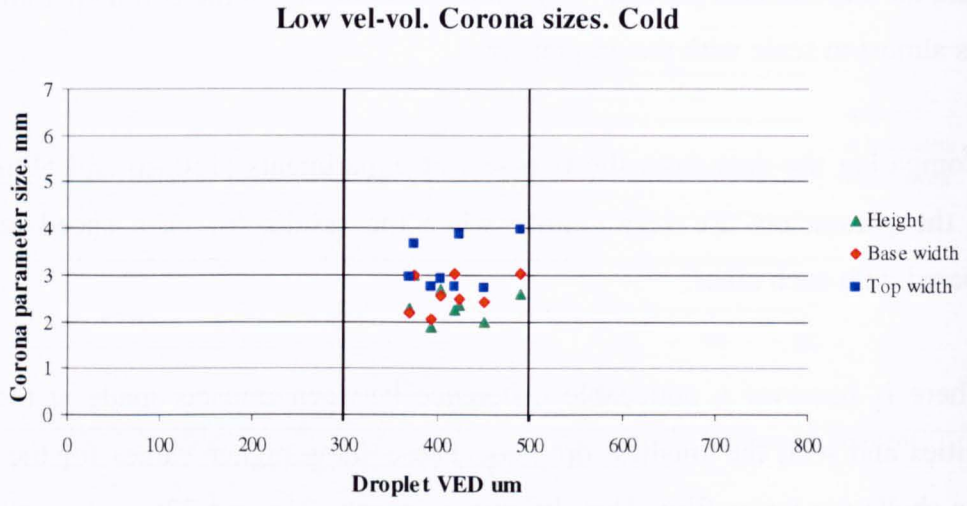

Graph 23a. Droplet VED against corona size. Impact at 70°, low speed, cold temperature and 50µm water film.

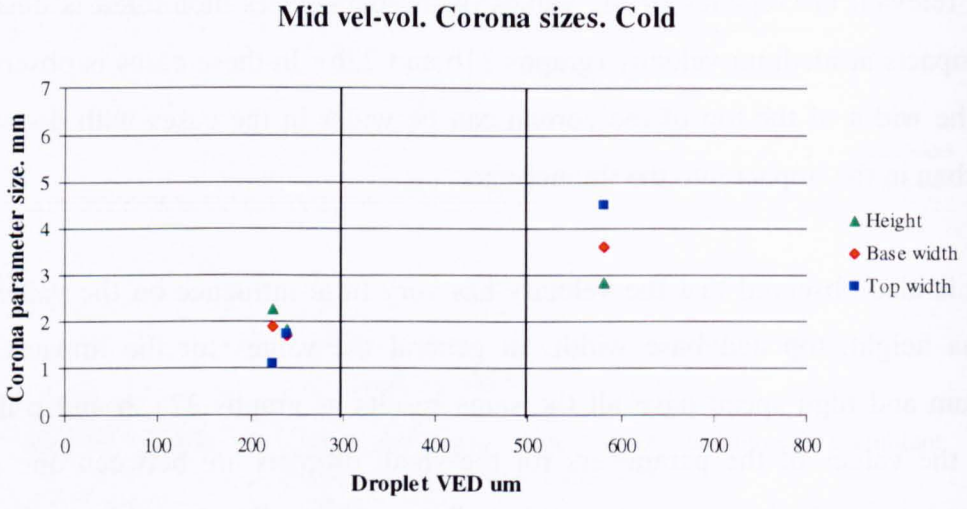

Graph 23b. Droplet VED against corona size. Impact at 70°, medium speed, cold temperature and 50µm water film.

Next, the impacts at super-cooled temperatures are analysed (the droplets are assumed to be a -10°C which is the temperature of the airflow). These cases are made under similar considerations that the ones analysed in graphs 22a, b and c except for the difference in temperature.

The comparison presents a problem; this is that the number of the recorded impacts at cold temperatures is not as numerous as the previous ones. This implies

that some restrictions are found in order to compare the impacts made at the whole range of velocities and droplet sizes.

The similarity between the cold and warm cases is that the parameters are in the same range. The difference is that in the warm case there is a clear trend between the corona size and droplet VED. However in the cold impacts the values no trend is visible.

When considering the impacts made at medium velocities (those in a range between 30 and 50m/s), it can be seen that only the impingements of the smallest and the biggest drops can be compared. Thus, graphs 22b and 23b show that for the smallest droplets the values for the parameters are nearly one millimetre higher at cold temperatures.

The comparison between the cold and warm cases droplets does not reflect any difference for impacts made with the biggest droplets.

There is not enough data at the cold temperatures to analyse the effect that the increasing of the velocity has.

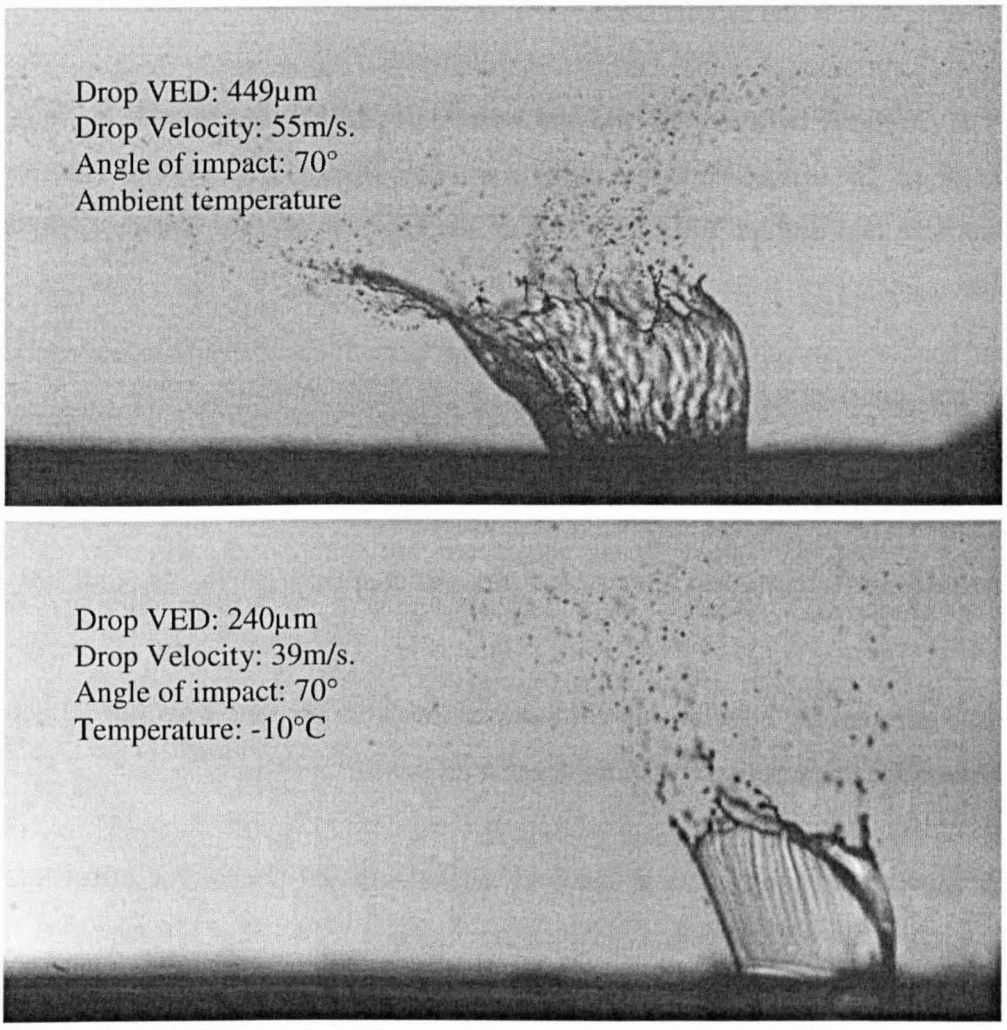

Figures 69a & b. In first frame there is a corona produced at warm temperature and second, a corona produced at super-cooled temperatures. Both impacts are developed under relatively similar conditions.

Effect of Angle of Impact on corona size.

To finish the analysis of the corona size parameters, the effects of the angle of impact is studied. The cases previously shown in graphs 21, 22 and 23 are at 70°. The following impacts are made at 45 and 20°, at ambient temperatures and into a 50µm deep water film. Because of theses conditions, the impacts at smaller angles can be compared with the cases shown in graphs 22a, b and c. The reason is that the only parameter that differs between the cases is the angle of impact.

Because of the lack of data for the impacts at 45 and 20°, there is not going to be a division between droplet sizes and velocities, therefore, the graphs 24a & b show the results recorded for all the impacts.

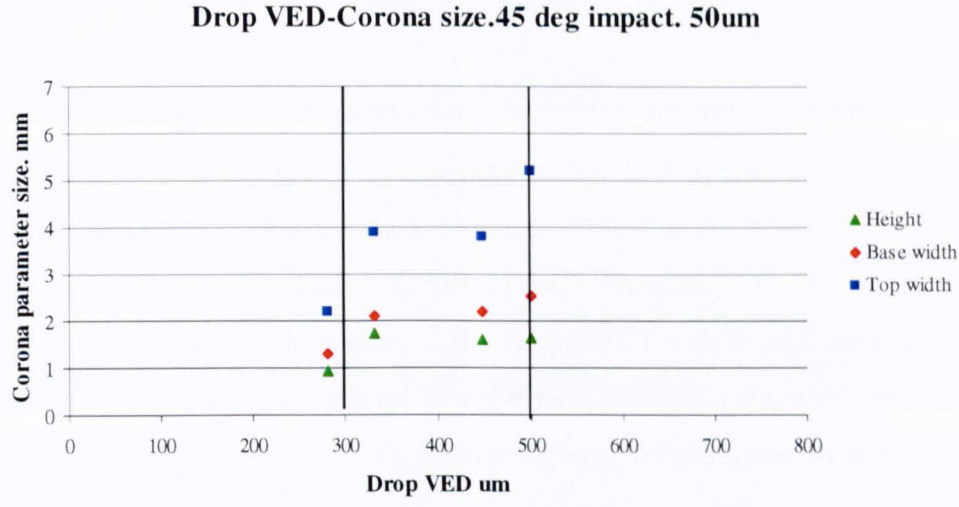

Graph 24a. Droplet VED against corona size. Impact at 45°, ambient temperature and 50µm water film.

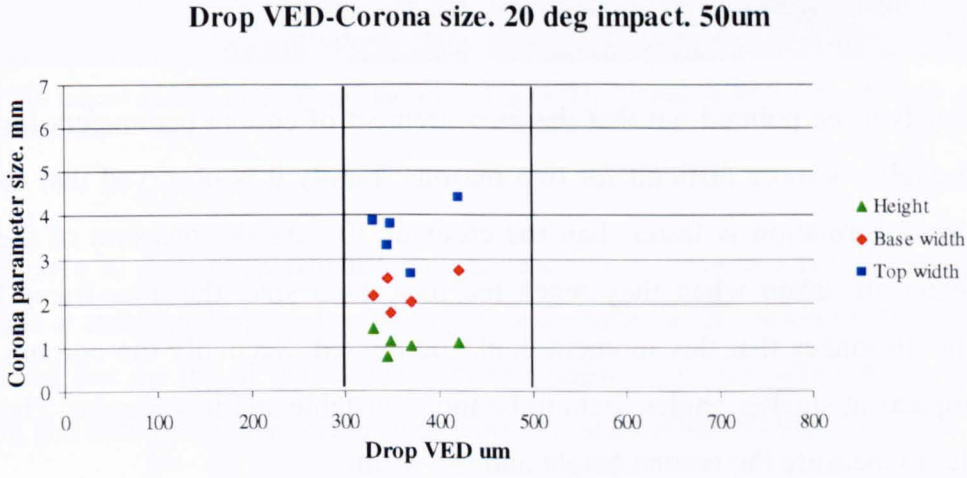

Graph 24b. Droplet VED against corona size. Impact at 20°, ambient temperature and 50µm water film.

Graph 24a shows impacts at 45°. It can be seen that the corona size parameters increase with the size of the impacting droplet. What is more relevant in this case is that, as the droplet VED increases, the values for the corona top width grow much faster than the corona base width and height.

It is observed that the values of the corona parameters are also different for the impacts at 70° and 45°. Graphs 24a & b show that for the smaller angle of impact, the values for the corona height and base width are around one millimetre lower than for the impacts at 70° as can be seen comparing with graphs 22b & c. However, the values for the top width, the values are in the same range.

Graph 24b shows that the corona size parameters do not appear very sensitive to the droplet VED increases. Comparing graph 24b with graphs 22a, b & c and 24a, the height and base width are not very sensitive to the droplet VED. Only the top width possibly shows a slight increase. Comparing the values obtained for the impacts at 20° with graphs 22a, b & c (70°impact), it is observed that the height and the base width are approximately one millimetre lower for the smallest angle. The data for the 45° impact lies between the 70° and 20° impacts.

The top width however seems to be in the same range of values for the entire range of impact angles.

It needs to be pointed out that the measurement of corona parameters for smaller impact angles is more difficult for two reasons: Firstly it is observed that the splash and corona formation is faster than the cases at 70°. As the measure of the corona parameters are taken when they reach the maximum size, the inter-frame between every photo makes that this moment could be missed. Secondly the coronas formed after impacts at smaller angles seem to be more unstable and less regular. Therefore it is harder to measure the corona height and top width.

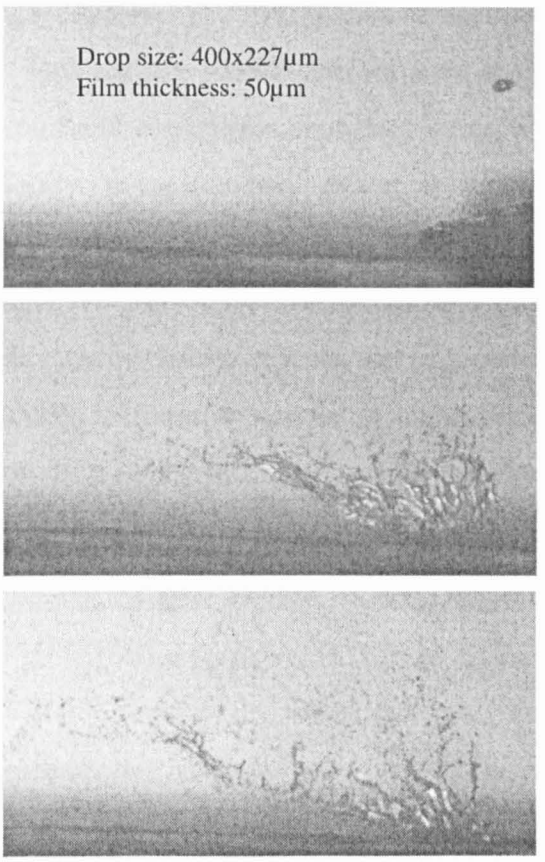

Figure 70. Impact at 57.2 m/s, 43° and ambient temperature. 50μm film.

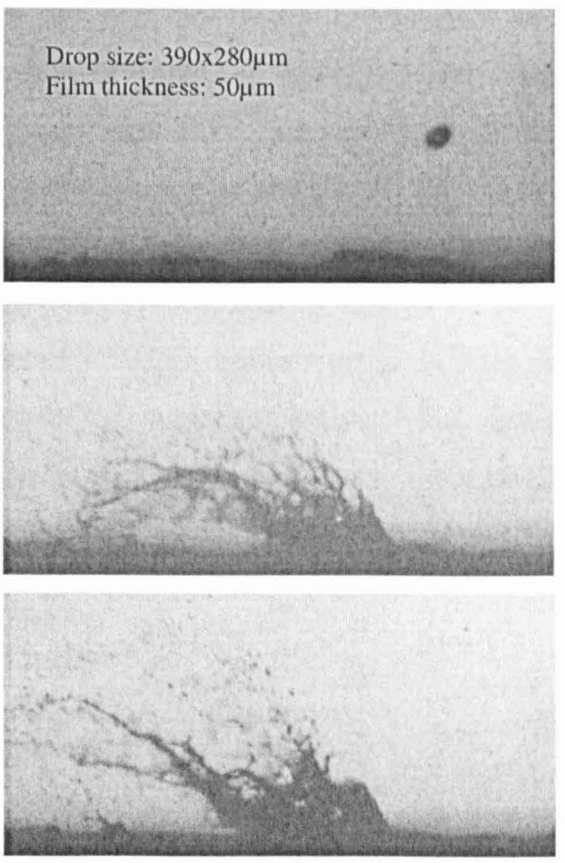

Figure 71. Impact at 68.5 m/s, 20° and ambient temperature. 50μm film.

Figures 70 & 71 show two different sequences that represent a typical example of impacts at small angles; one is made at 45° and another at 20° respectively. It can be observed that the top of the corona is more elongated, in comparison to the corona height and base width, than in the cases when the angle of impact was 70°.

A difference can be seen in the shape of the corona between these two examples and the ones in figures 57 & 58 and also figures 69a & b. The coronas for smaller impact angles seem to start to break-up at the beginning of the formation. More precisely, the collapse of the corona starts earlier for smaller angles of impact. An additional factor that may affect the corona is the change in the airflow due to the different orientation of the target.

Comparison of Corona Angles and Corona Velocities.

This section studies the velocity of the growth of the left and right sides of the corona and the angles that they form with the water film. The corona angles and velocity measurements given are related to the early stages of the corona development. This is because, as the time moves on, the airflow around it is going to distort the top of this crown increasingly, as can be observed in figures 72 & 73. These aerodynamic effects are not considered in depth but are noted as they are relevant to the comparison of experiment with the numerical analysis. The figures show that after some time and before the corona collapses, it becomes swept on the top by the airflow. Hence, because the model is assumed to work in a void, this distortion is not simulated, and therefore, can not be compared directly to the experiments.

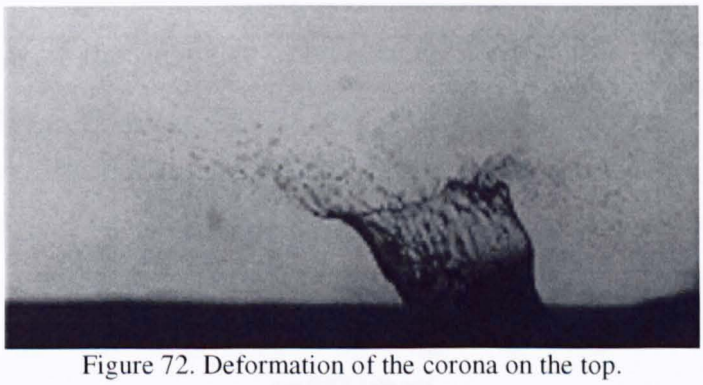

Figure 72. Deformation of the corona on the top.

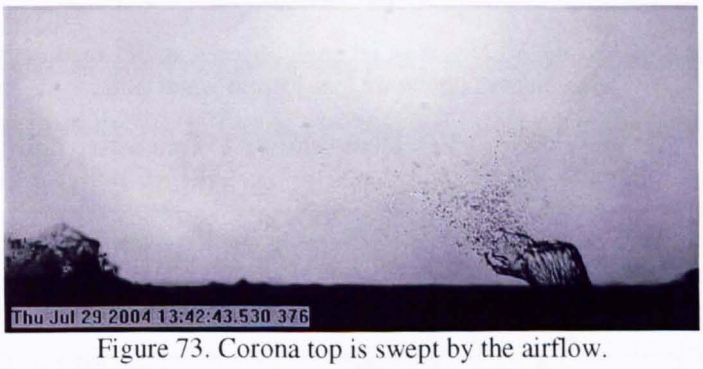

Figure 73. Corona top is swept by the airflow.

Comparison Corona Side Angles.

Effect of water film thickness on corona sides angles.

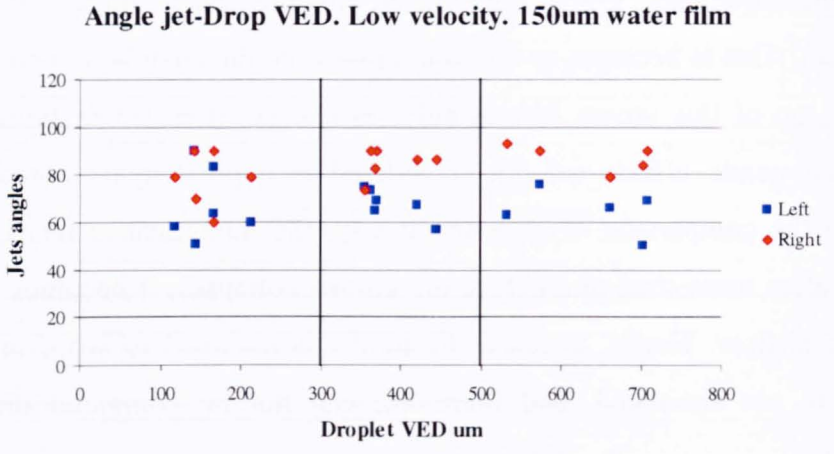

Graph 25a. Droplet VED against jet angle. Impact at 70°, low speed, ambient temperature and 150µm water film.

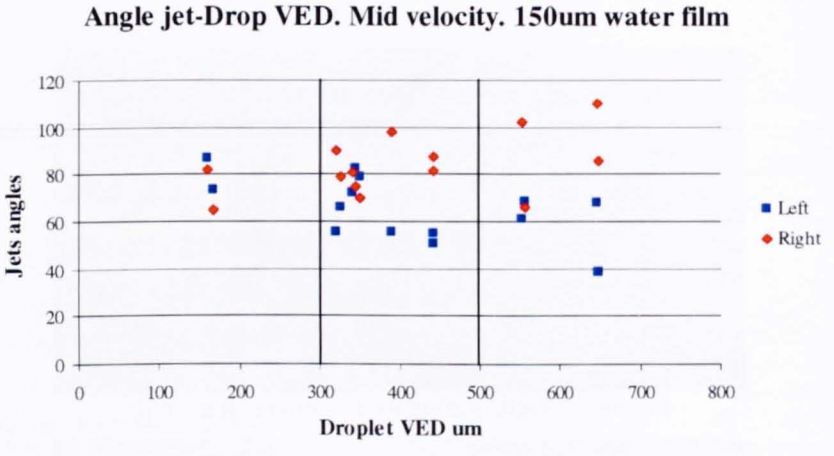

Graph 25b. Droplet VED against jet angle. Impact at 70°, medium speed, ambient temperature and 150µm water film.

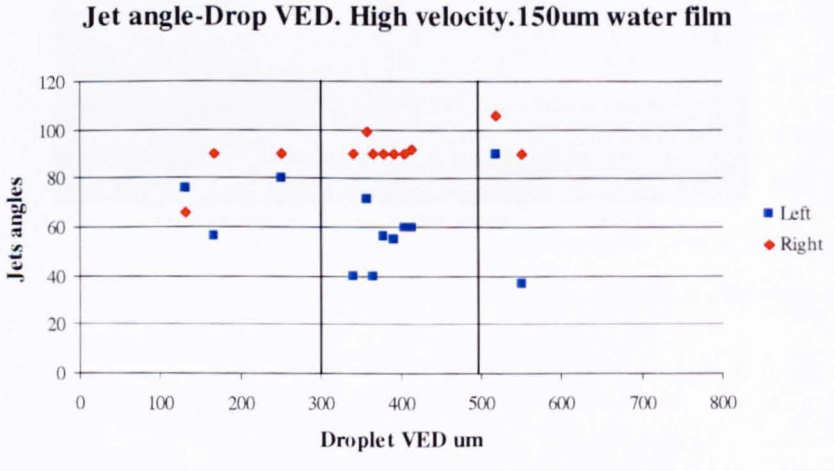

Graph 25c. Droplet VED against jet angle. Impact at 70°, high speed, ambient temperature and 150µm water film.

These three first sets of results illustrated in graphs 25a, b & c show a general decreasing of the values of the angles for the left side of the corona (or jet) and a slight increase of the angle formed by the right side, as the droplet VED increases. For low velocities (graph 25a) the two angles are not as sensitive to the variation of the droplet VED as the other two impacts made at higher velocities (graphs 25b & c). It is also noticed that, in general, the angle of the left jet is more sensitive to the increasing of the droplet VED than the right one.

Considering first the right jet, it is observed that, in general, the angles are perpendicular to the water film. However some particularities can be found regarding the velocity of impact and the size of the droplet. There is a very slightly increase of the values of the angles as the VED increases for the impact at low velocities (those below 30m/s). This variation in the angles goes from 80°, as average for the impact of the small droplets, to 90°. However it can be seen that there are occasional values for the angles of 60° for the smallest droplets.

Considering again the right side of the corona but for impacts at medium velocity, it is observed that the angles formed by these jets are typically, again, perpendicular to the layer. However, for the impacts of the biggest droplets (VED greater than 500μm) the coronas are found whose right sides form angles greater than 90°. This might be due to the airflow but of course it has been a very little time for airflow to cause deformation.

For the impacts at high velocity most of the data for the right jets is very consistent (approximately 90°). There are however some exceptions. One is recorded after the impact of a small droplet and forms an angle of 65°. The other two angles are formed after impact of bigger droplets and the angles that the right side of the corona forms are 100 and 110°. This might be because some variability in the experiments that have not been monitored.

The results for the left side of the corona are very different. Firstly it should be mentioned that these angles are, in general, very sensitive to the droplet size and velocity of impact (and air velocity). At low velocity it is observed that the angles formed by these jets use to be in a range between 60 and 80° (graph 25a). For the

impacts made at higher velocity the situation changes. In graphs 25b & c it can be observed that for the smallest droplets, the angle formed by this side of the corona is always around 70°. However, as the droplet size increases, the angle decreases to approximately 40° for impacts at medium and high speeds.

The airflow could be having a significant role in the decreasing of the values for the angles as the droplet velocity (and therefore the airflow velocity) increases. Remember that for bigger droplets the corona is higher and therefore maybe more influenced by the airflow.

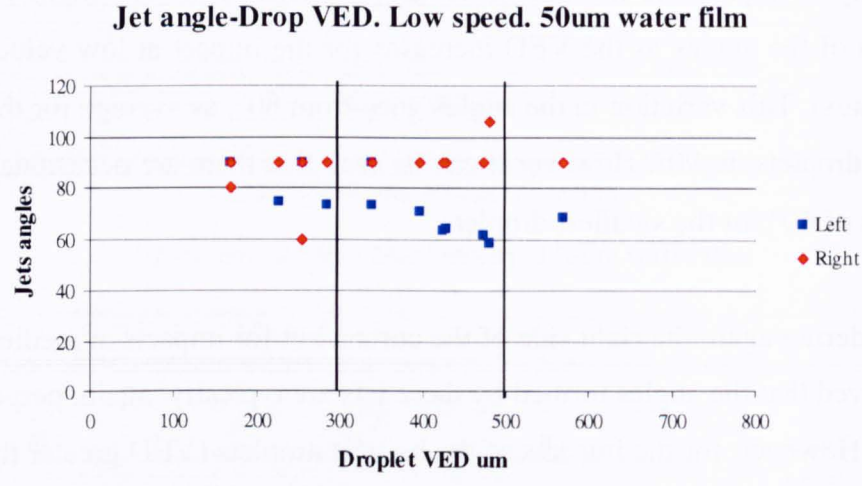

Graph 26a. Droplet VED against jet angle. Impact at 70°, low speed, ambient temperature and 50µm water film.

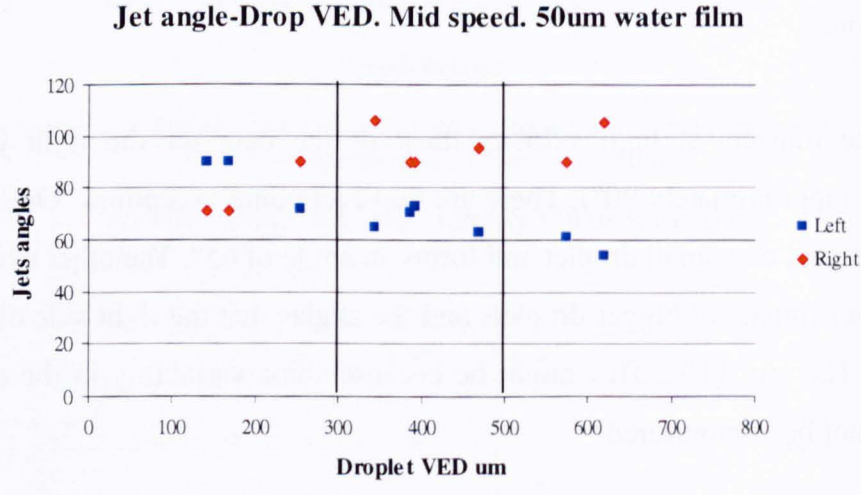

Graph 26b. Droplet VED against jet angle. Impact at 70°, medium speed, ambient temperature and 50µm water film.

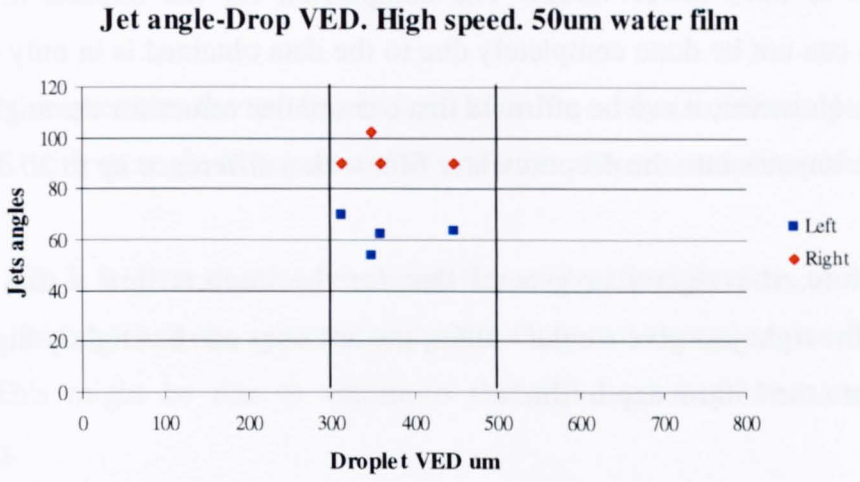

Graph 26c. Droplet VED against jet angle. Impact at 70°, high speed, ambient temperature and 50µm water film.

The impacts made into a 50µm water film thickness give similar results as the impacts made into 150µm water layer although graphs 26a, b & c show that there are some differences.

Considering first the right side, it is observed that the angle formed is near normal to the water layer. One difference is found on the cases corresponding to the impacts at medium velocity. Graph 26b shows that the angles formed go from 70° to over 100° as the droplet size increases.

Considering the results from the left sides of the coronas, a common behaviour is observed for the different impacts. For the smallest droplets the angles are around 70°, however, these angles decrease as the droplet VED increases. It is observed that the angles that the left sides form can be lower than 60° and even of 50 for the biggest drops.

Comparing the impacts made into a thin and into a thick water film, they show similar results for the right jets. There are some differences in the left jet angles. At low speed, for the left jet the result is scattered in the impacts into the 150µm film while for the 50µm the angles appear to be stable. For the impacts made at medium velocity and into the thin layer, the angles seem to follow a line that goes from 90 to 50° as droplet size increases while the impacts into the 150µm are more scattered and

are found to have lower values. The comparison for the impacts at the highest velocities can not be done completely due to the data obtained is in only one range of velocities. However, it can be affirmed that the smaller values for the angles are found during the impacts into the deepest water film with a difference up to 20 degree.

Therefore, it is found in general that for the impacts into a thin water film, although the right jets give similar values, the left ones can be slightly higher than the impacts into the 150μm depth film.

Effect of droplet temperature on corona angle.

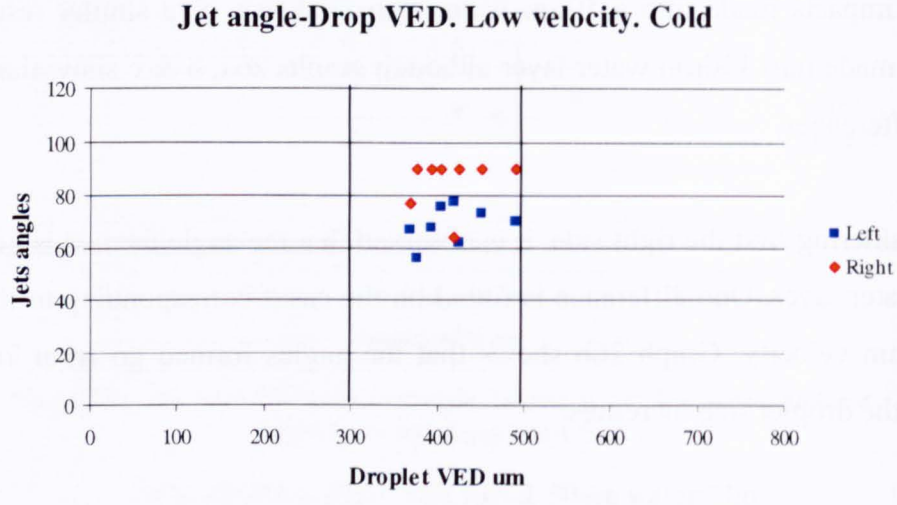

Graph 27a. Droplet VED against jet angle. Impact at 70°, low speed, cold temperature and 50μm water film.

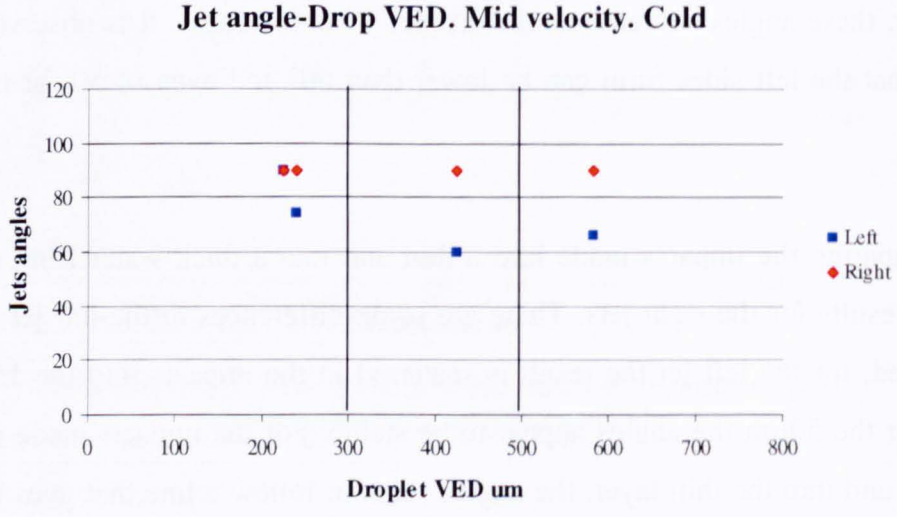

Graph 27b. Droplet VED against jet angle. Impact at 70°, medium speed, cold temperature and 50μm water film.

This section provides the results obtained after the analysis of the impacts carried out at -10°C, with an angle of impact of 70° and into a 50μm water film thickness.

Graphs 27a & b show that for the angles formed by the right sides of the coronas most of the data appear to be approximately 90°. Only two exceptions are found to be different. This might be due to variations that have not been monitored in the experiments.

Considering the left jet it is observed that the values for the angles lie in a range between 60 and 80° although there is found one case where the angle formed is 90°. This can be seen in graph 27b.

Comparing the impacts made under super-cooled temperatures with those shown in graphs 26a & b which were made under the same conditions but at ambient temperatures, it is observed that the only difference that can be appreciated is in the stability of the right jets angles. This is that the angles formed by the coronas at cold temperatures do not change as the droplet VED increases.

Effect of Angle of Impact on corona angle.

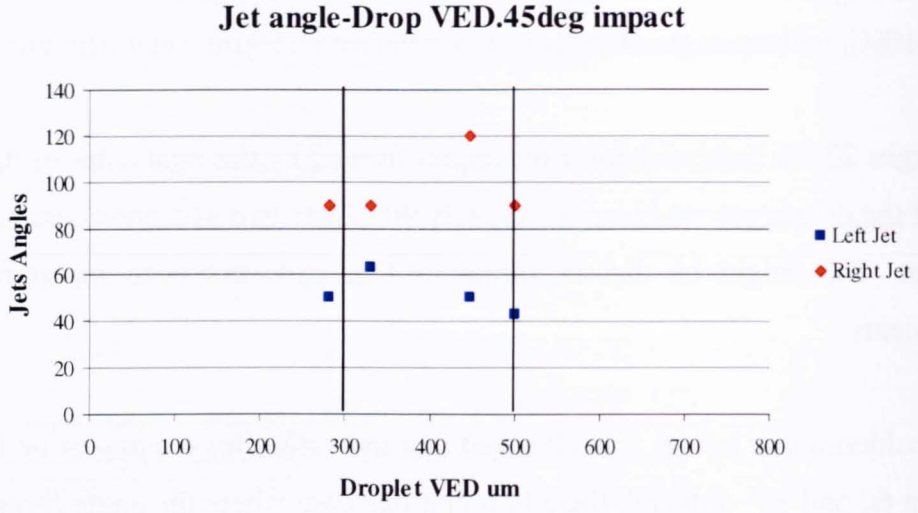

Graph 28a. Droplet VED against jet angle. Impact at 45°, ambient temperature and 50µm water film.

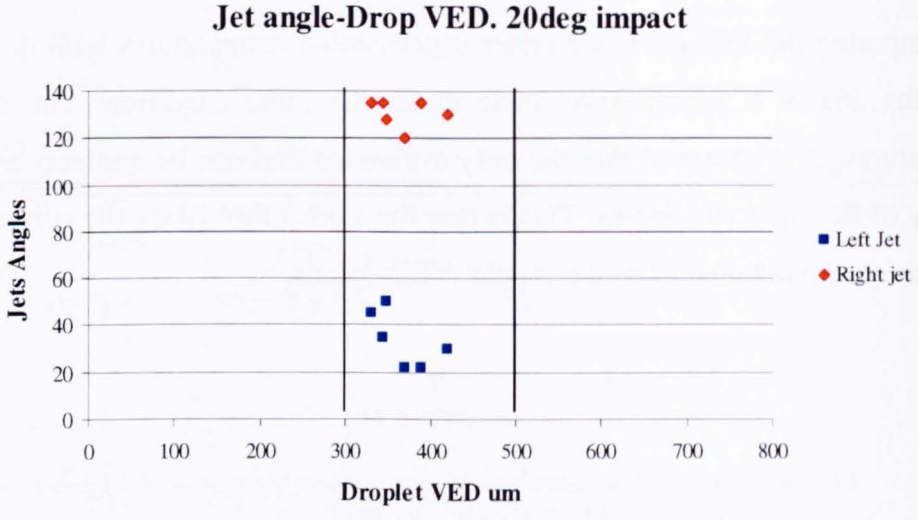

Graph 28b. Droplet VED against jet angle. Impact at 20°, ambient temperature and 50µm water film.

Next, the angles formed by the right and left sides of the coronas produced after impacts at 45 and 20° are analysed. Due to the small amount of data the impacts over the whole range of velocities are all included in the analysis.

Graph 28a shows the angles for the jets after 45° impacts. The right sides of the corona form 90° angles with the water film, except for one case which gives a 120° angle. This might be due to non monitored parameters during the experiments.

The left jet seems to form an angle in a range between 60° and 40° decreasing with the increase of droplet VED.

The impacts at 20°, as reflected in graph 28b, show that the right jets form angles in a range between 135° and 120° decreasing slightly as the droplet VED increases. The angles formed by the left jets seem to decrease with the increasing of droplet size and they are found to be in the range between 50° and 20°.

Comparing these impacts with those into a thin water film and at ambient temperature, but made at 70°, significant differences are found. The most relevant is related to the angles of the left jets. It can be observed that the smaller the angle of impact, the smaller the angle of the left jet.

Regarding the right jets it can be seen in graph 28b that some of the angles formed by the corona sides after impacts at 20° are at 90° and others at 120°. This is higher than the average of the results obtained after impacts at 45° and 70°. An example was presented in figure 71.

Comparison of Jet Velocities.

The velocities of the left and right side of the coronas have been measured and the results are discussed in this section. In order to determine these velocities, the distance covered by the rim of the corona is measured in the time interval between two frames inter-frame time equals to 63μs), as figures 74a & b show. The second frame is the one that illustrates the corona in its maximum size.

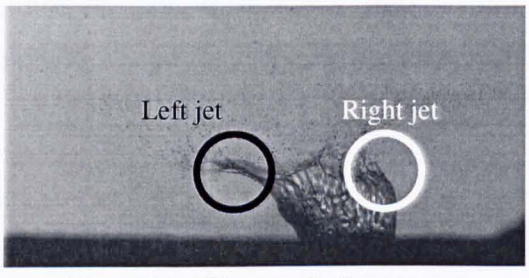

Figure 74a. Time t = 3 after impact

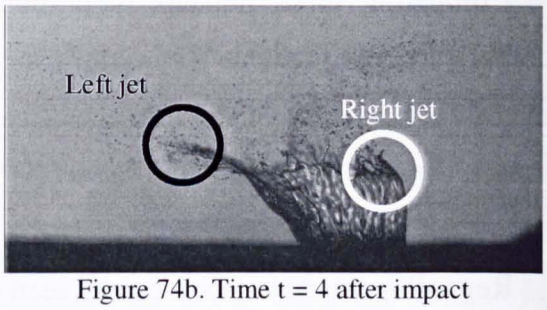

Figure 74b. Time t = 4 after impact

Effect of water film thickness on jets velocity.

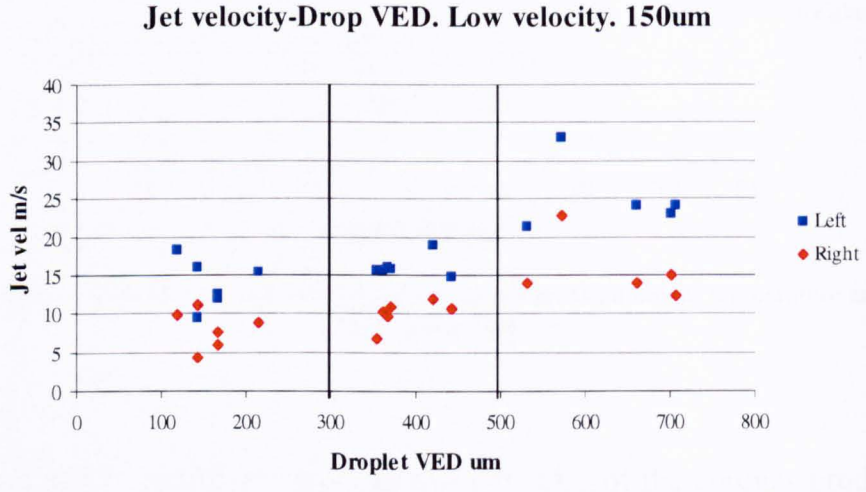

Graph 29a. Droplet VED against jet velocity. Impact at 70°, low speed, ambient temperature and 150μm water film.

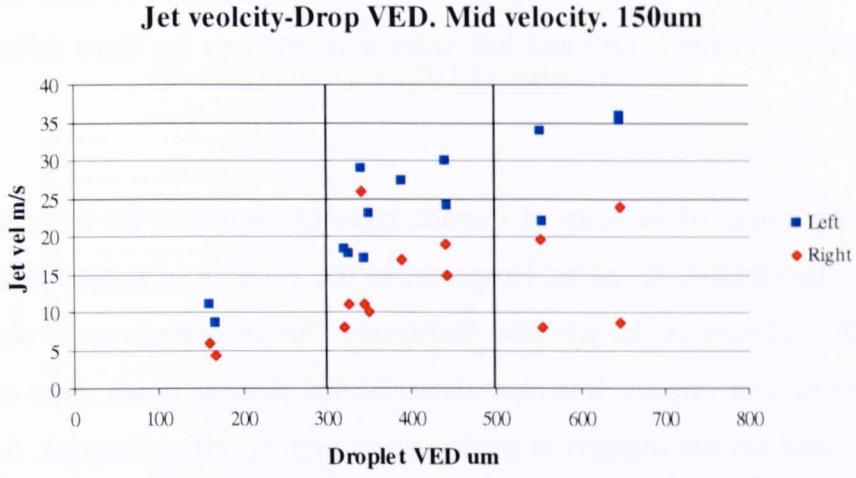

Graph 29b. Droplet VED against jet velocity. Impact at 70°, medium speed, ambient temperature and 150µm water film.

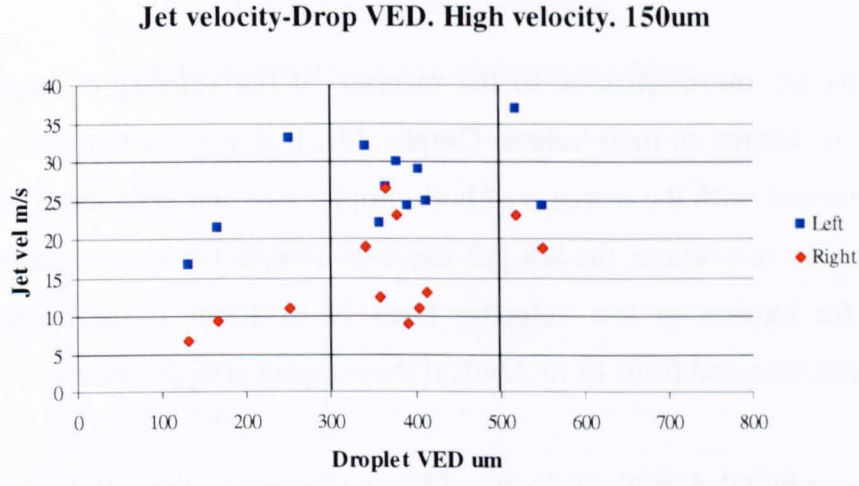

Graph 29c. Droplet VED against jet velocity. Impact at 70°, high speed, ambient temperature and 150µm water film.

The first case presented corresponds to the impacts at 70 degrees into a water film with 150µm thickness. Graphs 29a, b & c show the velocities of the right and left sides of the coronas when the droplets VED increase for the three different ranges of droplet speed.

The results shown in these graphs illustrate an increase of the velocity of the jets as the droplet VED increases. Also it is common in the three cases that the left jet moves faster than the right.

For every velocity range both jets follow an increasing trend line. However there are differences between right and left sides and between the three different velocity ranges.

For every range of velocity of impact, right jets move at the same speed for the impacts of the smallest droplets. However, as the velocity of impact and droplet size increase, the velocity of the jets also increases. This increase is more marked for the higher velocities of impact. It is also observed that there is much more scatter for the values obtained for the impacts at medium and high speeds of impact. As an average it can be said that the right jets velocity for impacts of big droplets go from 15m/s for the lowest speeds to 20 for the highest.

Left jets are more sensitive to the increase of the velocity of impact and also present more scatter on their values. Graphs 29a, b & c show that the speeds of the left side increase with the increase of both droplet size and velocity of impact. It can be said that, as an average, the left jets move in a range from approximately from 12 to 24m/s for impacts at low velocity, from 10 to 30m/s if the droplets strike at medium velocities and from 18 to 32m/s if they impact at high velocity.

It is noticeable that, as the velocity of impact increases, the difference between the velocities of the right and left side of the corona also increases.

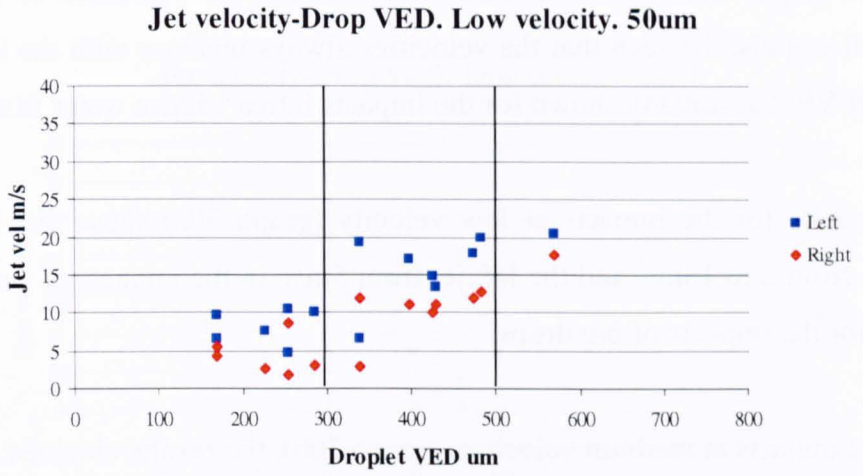

Graph 30a. Droplet VED against jet velocity. Impact at 70°, low speed, ambient temperature and 50µm water film.

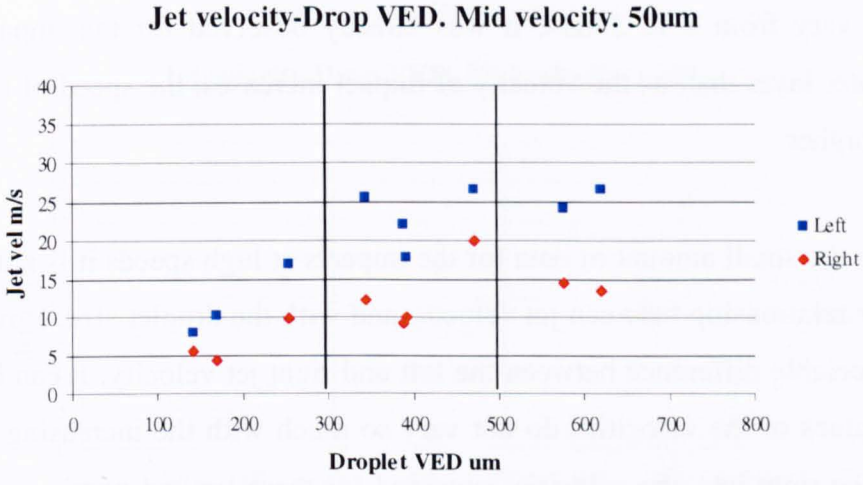

Graph 30b. Droplet VED against jet velocity. Impact at 70°, medium speed, ambient temperature and 50µm water film.

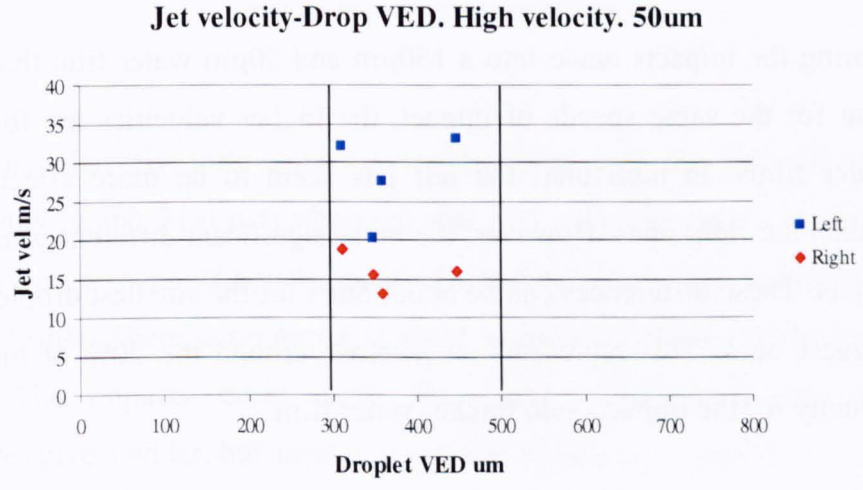

Graph 30c. Droplet VED against jet velocity. Impact at 70°, high speed, ambient temperature and 50µm water film.

For the impacts made into the 50μm water film thickness it is observed that, as the velocity of impact increases, the difference between the velocities of the jets also increase. It can also be seen that the velocities always increase with the increasing of the droplet VED as already shown for the impacts into a 150μm water film thickness.

The results for the impacts at low velocity (graph 30a) show that the right jet speeds go from 2 to 18m/s and the left jet from 5m/s, in the impacts of small droplets, to 21m/s for the impacts of big drops.

For the impacts at medium velocities (graph 30b), the results obtained for the right sides of the corona go from 4 to 15m/s as the droplet size increases, although there is found a peak for an impact produced by a medium size drop of 20m/s. The left jet velocities vary from 8 to 26m/s. It was already observed for the impacts into the deeper water layer that, as the velocity of impact increases, the speed of the jets is up to 10m/s higher.

Due to the small amount of data for the impacts at high speeds it is not possible to see a clear relationship between jet velocity and with the droplet size. However, there is an appreciable difference between the left and right jet velocity. It can be observed that the values of the velocities do not vary so much with the increasing of the drop size. For the right jets, the velocities obtained for these limited number of impacts is between 13 and 18m/s and for the left jets between 20 and 33m/s.

Comparing the impacts made into a 150μm and 50μm water film thickness, it is noticed that for the same speeds of impact, the higher velocities are found for the deeper water films. In particular, the left jets seem to be more affected by film thickness than the right ones. However, the more significant differences are observed in the left jets. These differences can be about 5m/s for the smallest droplets to 10m/s for the biggest ones. This represents an increase around the 20% of the incoming droplet velocity for the impacts into thicker water film.

Effect of temperature on jets velocity.

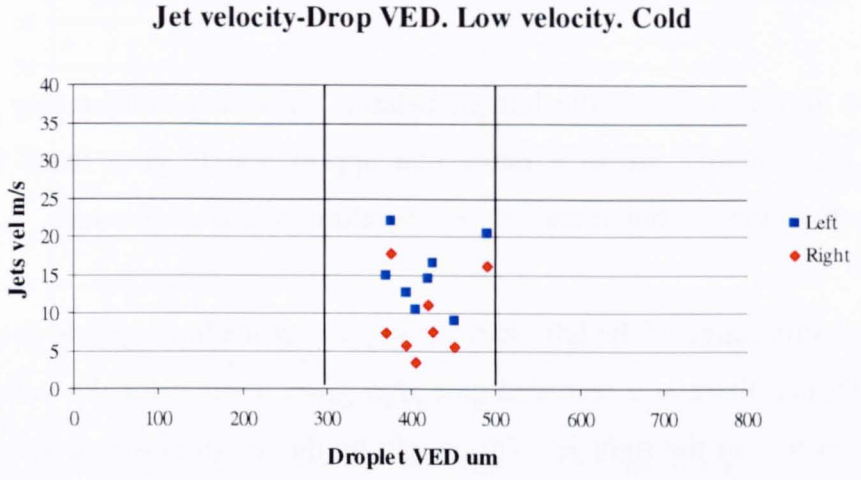

Graph 31a. Droplet VED against jet velocity. Impact at 70°, low speed, cold temperature and 50µm water film.

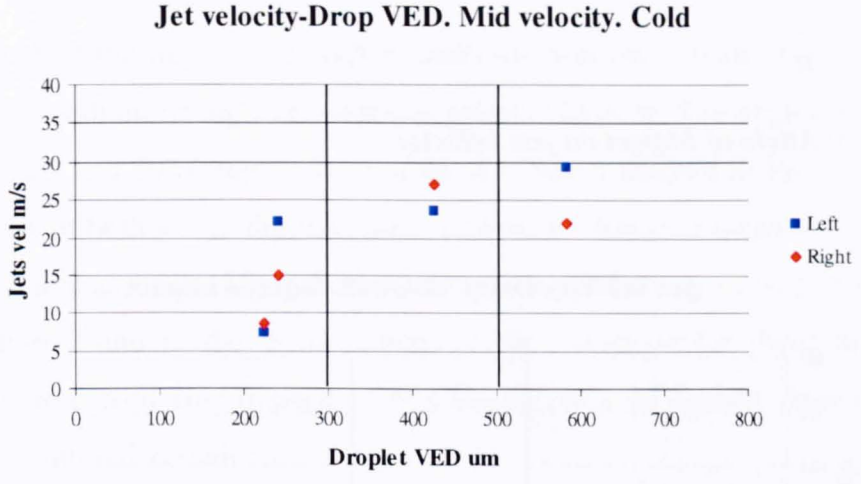

Graph 31b. Droplet VED against jet velocity. Impact at 70°, medium speed, cold temperature and 50µm water film.

There is relatively little data for super-cooled impacts. For the slow speed impingements (graph 31a) it is observed that generally, the speeds recorded for the right jets are in a range of approximately from 5 to 10m/s. The maximum recorded value was 18m/s. There is no apparent trend in the limited data as the droplet VED increases. The impacts made under the same considerations but at ambient temperatures give a wider, but similar, range for the results. It goes from 3 to 12m/s.

For the impacts at medium velocity, an increase of the velocities of both jets with the increase of the droplet VED is noticed. The right side of the corona goes from 8 to

an average of 25m/s. It is relevant that for the smallest droplets, in one case, the right jet moves faster than the left one. Making a comparison with the impacts made at ambient temperatures reveals that for super-cooled cases the right jet moves faster.

At low impact velocity the left jet behaves in a very similar way to the right, although its velocities are in a range that approximately goes from 10 to 20m/s. Corresponding impacts but at ambient temperature give similar values.

The velocity range of the left sides for impacts at medium speeds goes from 23 to 30m/s, although there is a recorded case that gives a value for the velocity of 7m/s which is lower than the right jet. This might be due to variations that have not been monitored in the experiments. The range of velocities for impacts made at ambient temperatures is, in general, lower.

Effect of Angle of Impact on jets velocity.

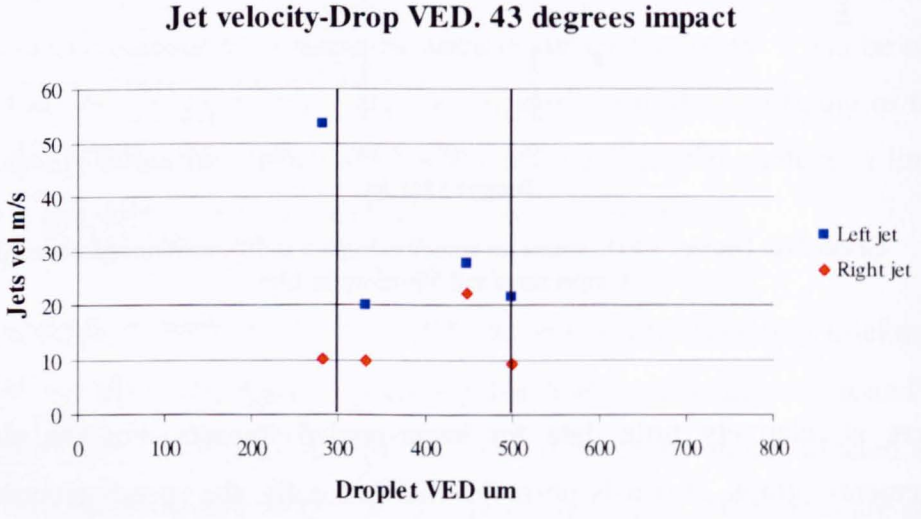

Graph 32a. Droplet VED against jet velocity. Impact at 45°, ambient temperature and 50μm water film.

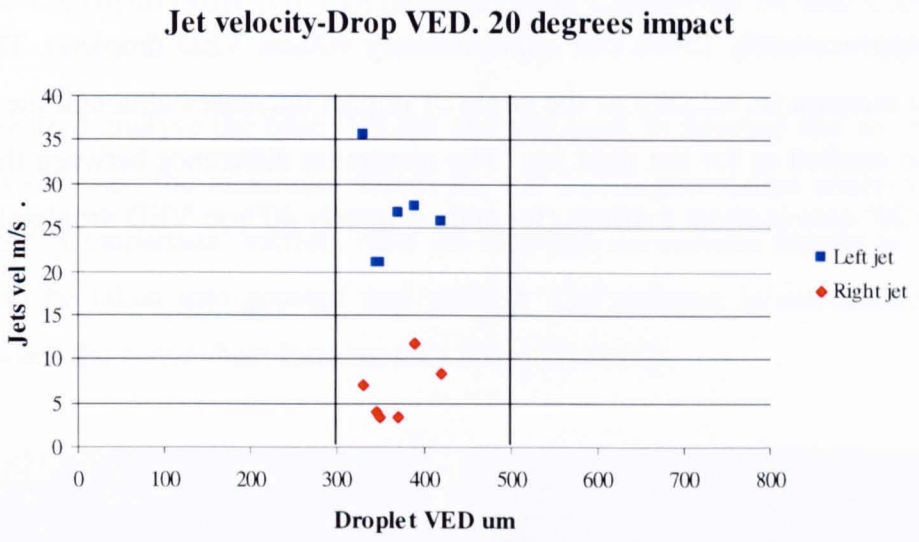

Graph 32b. Droplet VED against jet velocity. Impact at 20°, ambient temperature and 50µm water film.

The effect of the angle of impact is analysed without considering any division between low, medium or high velocities in graphs 32a & b. The angles analysed are 45° (graph 32a) and 20° (graph 32b). For the 45° case a marked increase is observed in the velocity of both jets as droplet size is increased. However it can be seen that the value for the impact of the biggest droplet decreases. This may be in part because of the difficulties found in the measurement of the velocities for these impacts and because we are considering impacts over a bigger range of speeds. Also it could be due to non monitored variations.

The velocities for the right jets are in the range from 10 to 20m/s and the velocities for the left jets are found to be between 20 and 28m/s.

Considering the impacts at 20° much higher values are observed for the velocities of the left sides of the coronas compared to the right sides. The velocities for the right jets increase with the droplet VED from roughly 3.4 to 12m/s. The left jets range from approximately 21 to 27m/s with a peak of 36m/s in one case. These values do not seem to be affected by the increase of the drop VED.

Comparing these two sets of results made at 45 and 20° with the impacts at 70° into a 50µm film thickness, a decrease of the velocities of the right jets is observed as

the angle of impact decreases. The maximum difference between the 70° case and the 20° is approximately 15m/s (for approximately 400μm VED droplets). The left jets seem to increase in velocity as the angle of impact decreases although the difference is not so marked as for the right jets. The maximum difference between the 70° case and the 20° case is about 5-10m/s (for approximately 400μm VED droplets).

Time Comparison for Formation and Collapse of the Corona.

This section analyse the time that the coronas need to develop and to reach the maximum size, i.e., the maximum values for the corona parameters analysed in the 'Corona Size Comparison' section. Also the time that the coronas require to collapse is going to be taken into account and studied. The collapse is considered as the moment when the water sheet forming the corona breaks up.

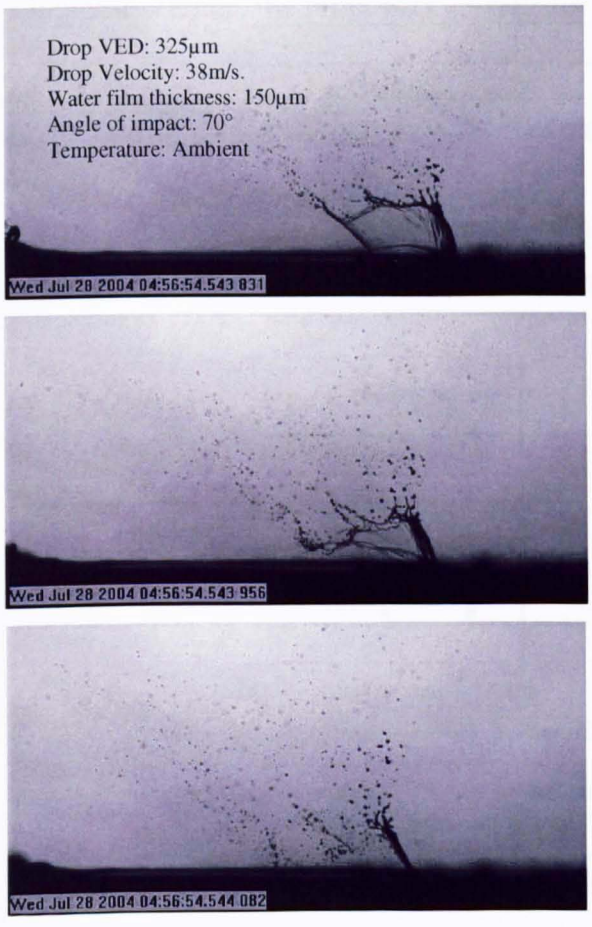

Figure 75. Typical collapse of the corona warm case.

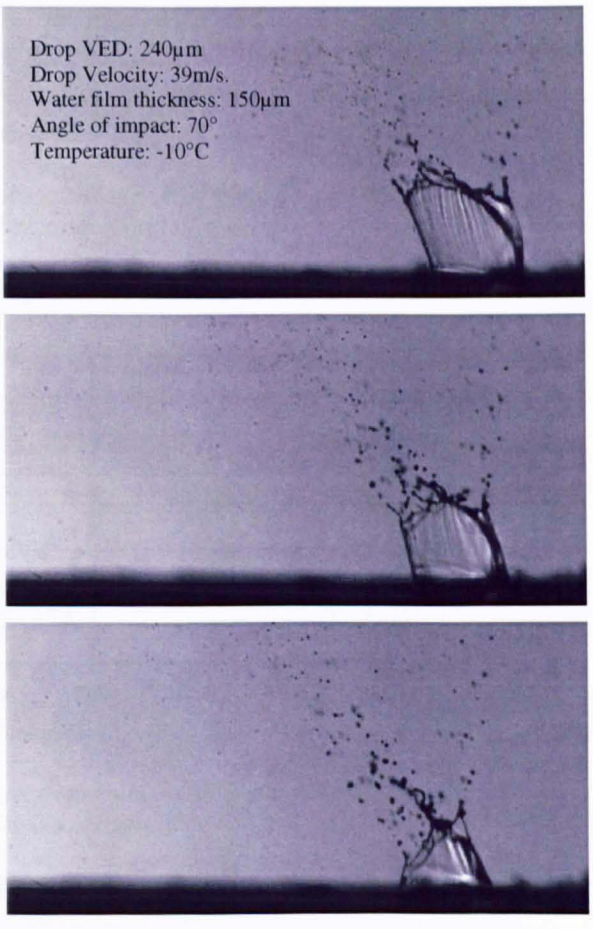

Figure 76. Typical collapse of the corona cold case.

Two examples of the collapse of the corona for impacts at 70° are illustrated in figures 75 & 76. For the warm case the typical break up starts generally at the left side of the corona. The water sheet vanishes starting in the bottom and going up to the rim and finally reaching the right side. Figure 76 shows the collapse of a corona produced by a super-cooled droplet. In this case the water sheet seems to fall down as many satellite droplets are released.

Effect of water film thickness on corona time history.

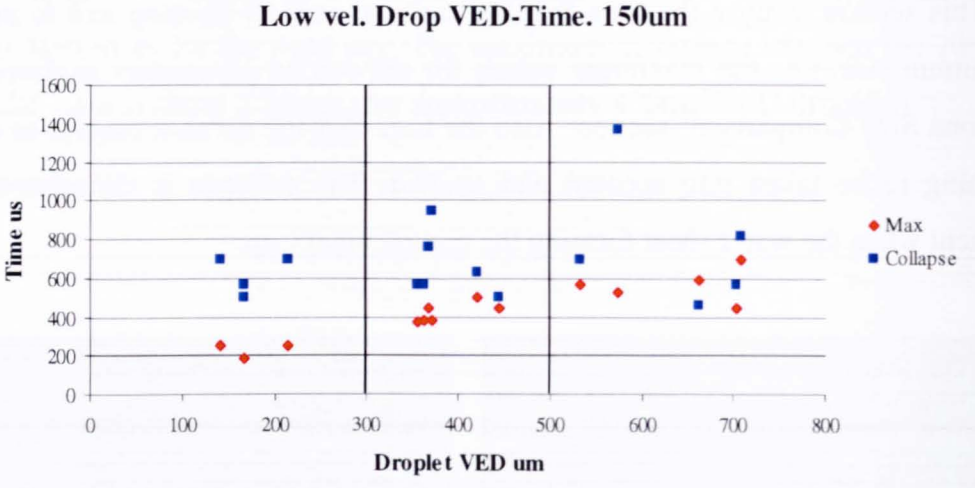

Graph 33a. Droplet VED against corona time. Impact at 70°, low speed, ambient temperature and 150µm water film.

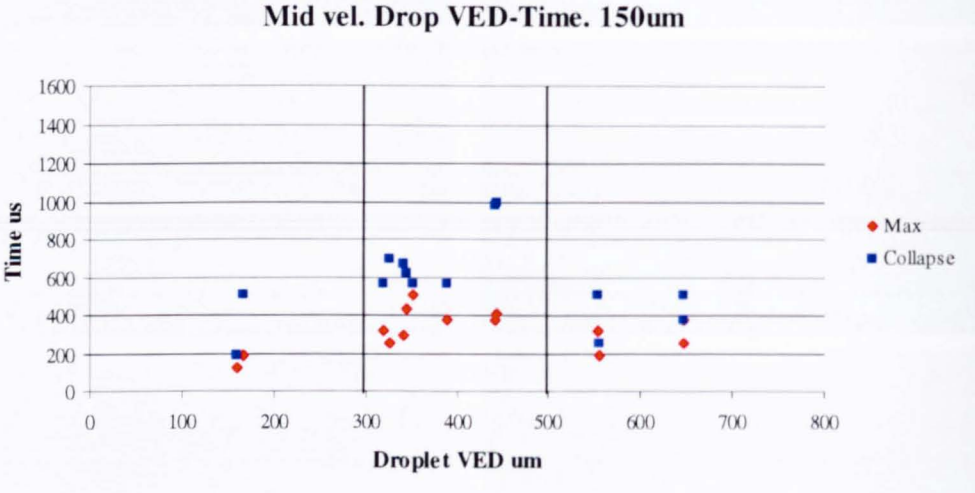

Graph 33b. Droplet VED against corona time. Impact at 70°, medium speed, ambient temperature and 150µm water film.

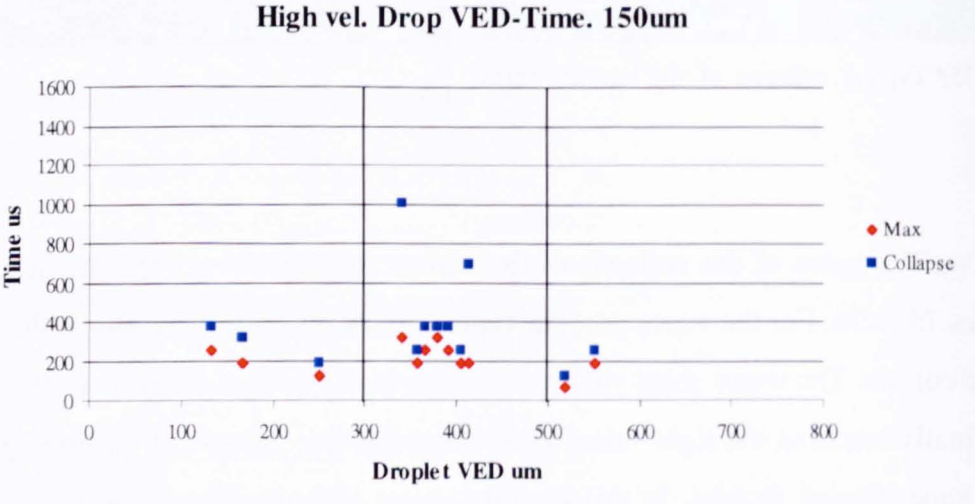

Graph 33c. Droplet VED against corona time. Impact at 70°, high speed, ambient temperature and 150µm water film.

The time that the coronas need to form during the 70° impacts into a 150μm water film thickness is analysed. Graphs 33a, b & c illustrate the variation of the time with the increasing of the droplets VED.

It is observed that for the three velocity divisions there is an initial increase of the time together with the growth of the droplet size. However in general, when the droplet VED reaches the higher values the time that the coronas need to form and collapse is shorter. It is also shown that the time decreases when the impact velocities increase. Hence, the process is quicker for the highest velocities.

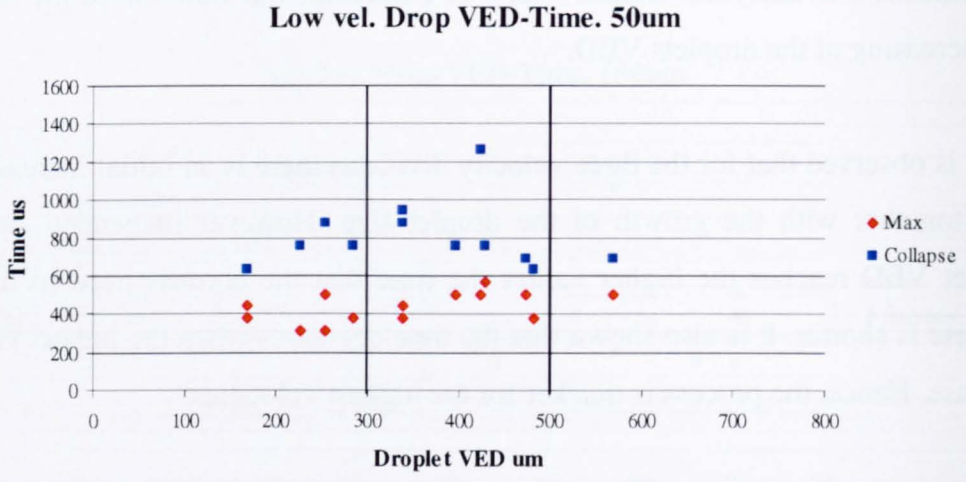

Graph 34a. Droplet VED against corona time. Impact at 70°, low speed, ambient temperature and 50µm water film.

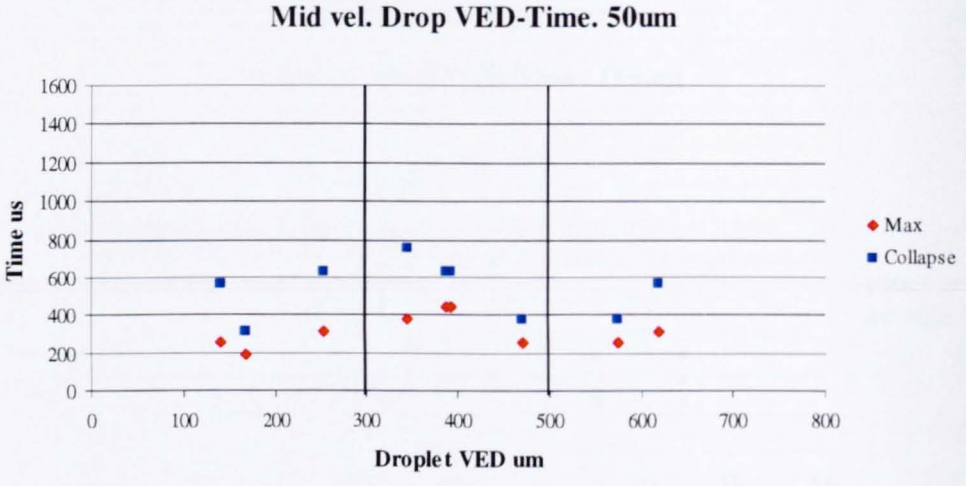

Graph 34b. Droplet VED against corona time. Impact at 70°, medium speed, ambient temperature and 50µm water film.

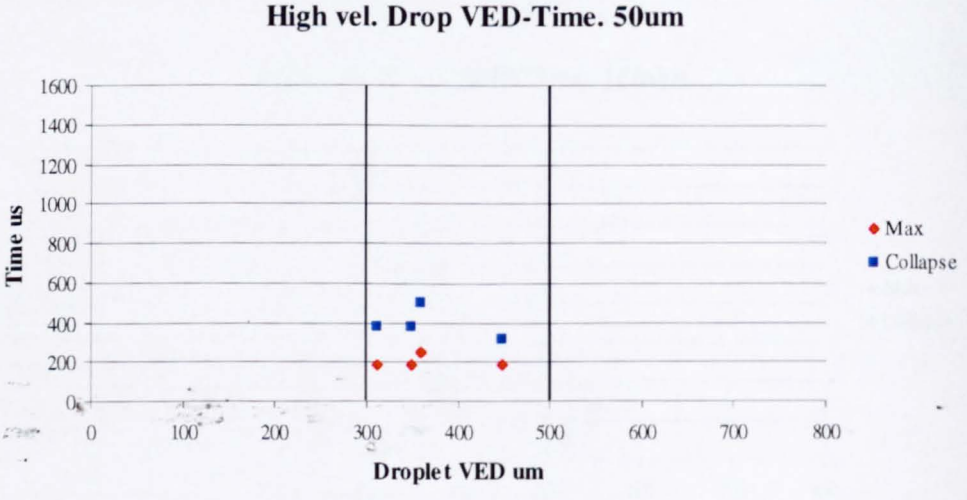

Graph 34c. Droplet VED against corona time. Impact at 70°, high speed, ambient temperature and 50µm water film.

The impingements into the 50μm water film show a similar behaviour in the trend lines (graphs 34a, b & c). Therefore, the time increases as the droplet VED is increased, but again for the biggest sizes a decrease of the time is observed.

Comparing the graphs 33a, b & c with 34a, b & c, it is, the impacts into a water film of 150μm and 50μm depth, few differences are found.

The time of corona formation for the impacts into the thickest layer and lowest velocities (graphs 33a), is in a range between 200 and 700μs and they follow an increasing linear trend. In comparison, the impacts into the thinner layer seem to be more constant. Thus the values obtained for the times of corona formation are around 400μs for all the droplets sizes although there are found exceptional values of 300μs and 600μs.

Graphs 33a and 34a show that the time for the collapse is, in general, in a range between 600 and 1000μs for impacts into both water films. However there are found particular values of 1400μs and 1250μs in graphs 33a and 34a respectively.

For the impacts at medium velocity (graphs 33b and 34b) it is observed that the time that the coronas need to be form is in a range between 200 and 400μs with two only exceptions found in graph 34b of 450μms. Regarding the time to collapse, it can be seen that there is a lot of scatter, particularly in the results obtained during the impacts into the 150μm water film. In general the results obtained for the impacts into the thicker layer are in a range between 200 and 700μs and for the impacts into the thin layer are between 400 and 800μm with one exception at 320μs.

The comparison between the results obtained when the impacts are made at the highest velocities (graphs 33c and 34c) also seem to be very similar. It can be seen that the for impacts into the thick film the time of corona formation is between 300μs and 400μs and the time for collapse is between 100 and 300μs. For impacts into the thin film the time of corona formation is around 200μs and for the collapse around 400μs.

Effect of temperature on corona time history.

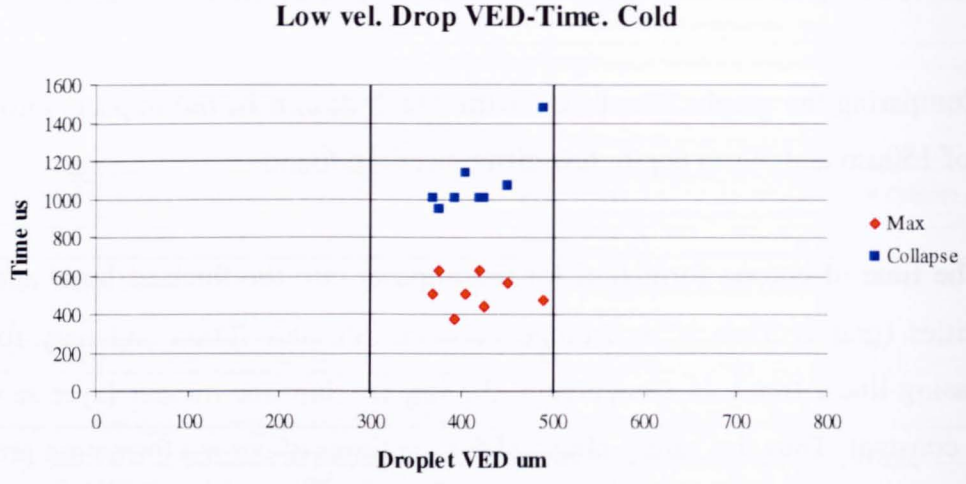

Graph 35a. Droplet VED against corona time. Impact at 70°, low speed, cold temperature and 50µm water film.

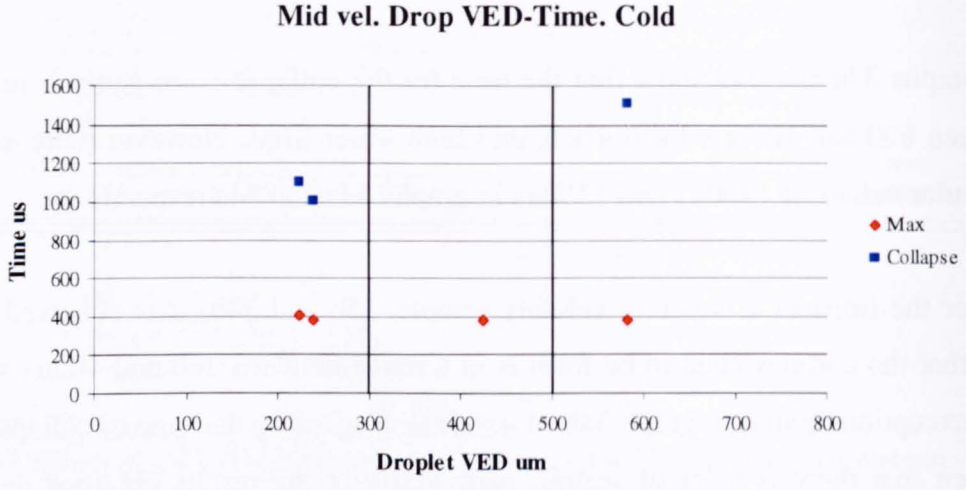

Graph 35b. Droplet VED against corona time. Impact at 70°, medium speed, cold temperature and 50µm water film.

The influence of super-cooled droplet temperatures on impact is considered in this section. The results show a different behaviour of the times than in previous impacts at ambient temperature. There is not so much data, but a general idea of how the coronas develop for droplets at super-cooled temperatures can be given. It is observed that the time the coronas need to be formed does not seem to change with the increasing of the droplet size. For the low velocity impacts the corona time formation is in a range between 400 and 600µs and for the medium velocity impacts the time is, for every droplet size, 400µs.

Observing the time that the coronas need to collapse, it is seen a continuous increase of the time as the droplet size increases. For the impacts at low velocity, the collapse times are approximately between 950 and 1400μs, and for the medium velocity impacts from 1000 to 1500μs. Although for this last case there is not as much information as in other previous cases, it is observed a clear increasing tendency.

The comparison between the cases presented in graphs 34a & b with 35a & b provides relevant information about the influence of the temperature. It is observed that the time that the coronas take to be formed is very similar in warm and cold cases. However, considering the time that the coronas take to collapse, the differences are remarkable. For the cold cases it is found that the values of the time are longer than in impacts at ambient temperatures. For the impacts at low velocity (graph 34a and 35a) the times for the warm cases and medium size droplets are below 1000μs and for the cold cases are over 1000μs. Considering the impacts at medium velocity, the difference is more relevant and if the time that the coronas take to collapse for the impacts at ambient temperature is below 800μs, for the cold impacts is always over 1000μs.

Effect of Angle of Impact on corona time history.

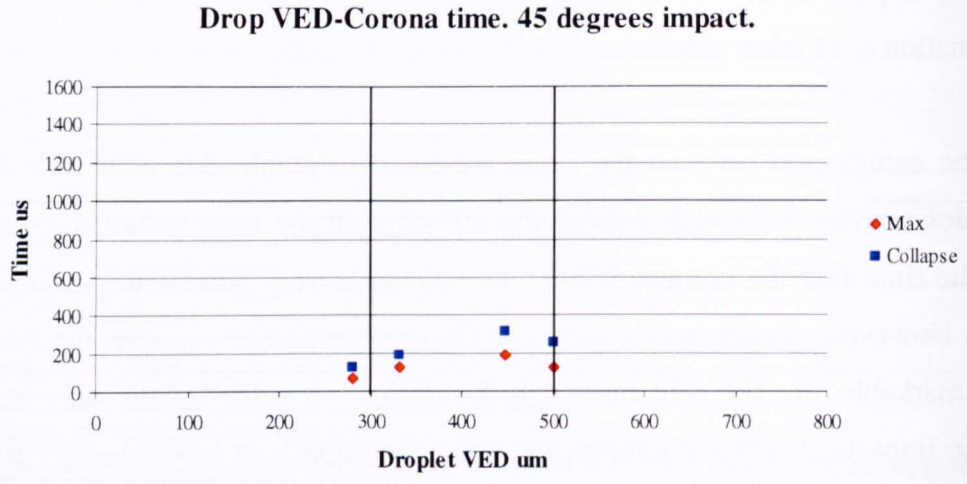

Graph 36a. Droplet VED against corona time. Impact at 45°, ambient temperature and 50µm water film.

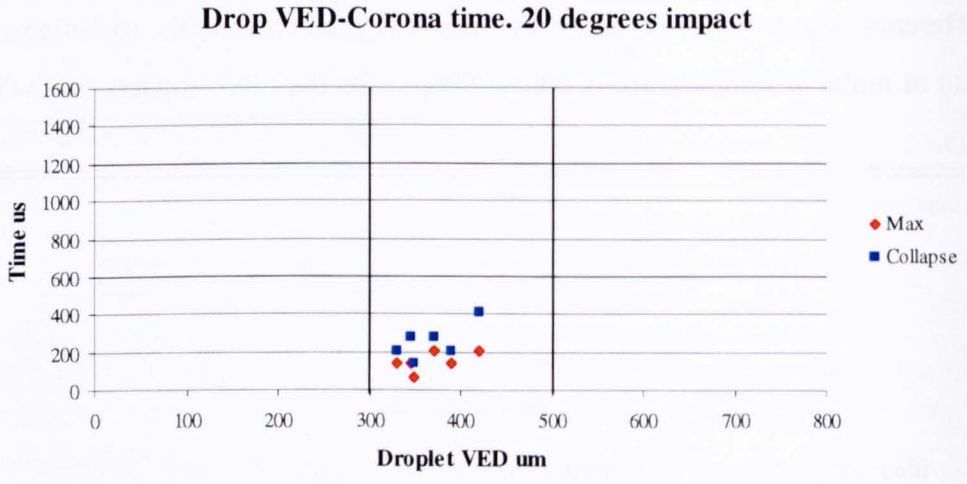

Graph 36b. Droplet VED against corona time. Impact at 20°, ambient temperature and 50µm water film.

The times for the impingements at 45 and 20° are going to be studied. This will help to see how the decreasing on the angle of impact affects to the time that the coronas take to be formed and to collapse.

Firstly the 45° impacts are considered. It is observed in graph 36a that initially the time that coronas need to be form and to collapse are longer as the droplet VED increases, but finally it is appreciate a slight decreasing as happened with the previous cases illustrated in graphs 34a, b & c which represented impacts made at 70°. The

time that the coronas need to be formed is always below 200μs and the time to collapse is slightly longer, in particular 63μs longer. This is because, as it was mentioned during the presentation of the experimental results, 63μs is the inter-frame time. It is observed though, that the corona formation and corona collapsing was much quicker for the small angles impacts than for those at 70°.

The corona formation for impacts at 20° are also very fast in comparison to those made at 70°, as can be observed in graph 36b. However it can not be confirmed that the times for bigger droplets size is going to be shorter due to the available data is only for medium size droplets. Therefore the graph shows that, as the droplet VED increases, the time that the coronas need to be formed and to collapse is longer although, definitely, much shorter than in the impacts made at 70°.

Analysis of Satellite Droplets.

This section shows the analysis of the sizes and velocities of the satellite droplets that are expulsed to the air during the splash and which, in some cases, may re-impinge in the aircraft surface. The measurements taken for sizes and velocities are made when the corona starts to collapse.

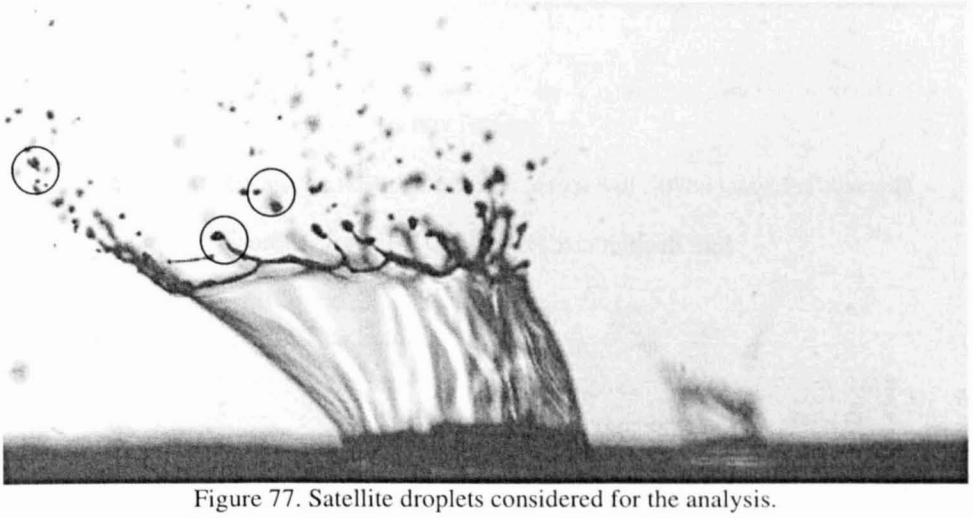

Figure 77. Satellite droplets considered for the analysis.

Analysis of the Size of Satellites Droplets.

The size of the satellite droplets are analysed considering the three different sets of velocities of impact, droplet VED, angles of impact and water film thicknesses.

Effect of water film thickness on satellite droplets size.

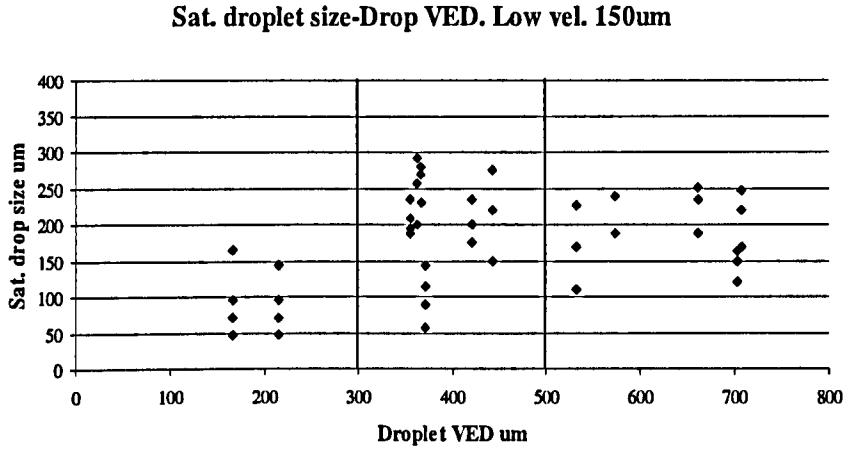

Graph 37a. Impact at 70°, low speed, ambient temperature and 150μm water film.

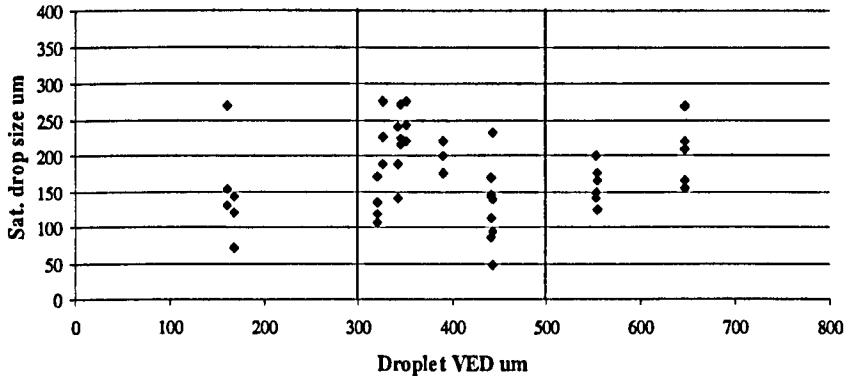

Graph 37b. Impact at 70°, medium speed, ambient temperature and 150μm water film.

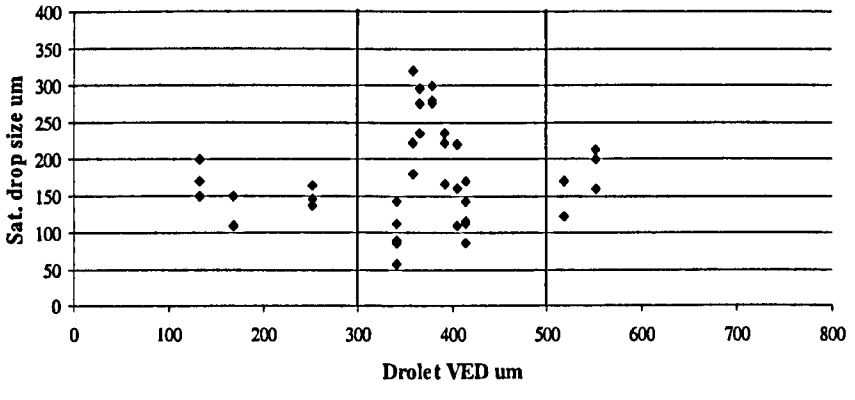

Graph 37c. Impact at 70°, high speed, ambient temperature and 150μm water film.

The first cases analysed are impacts into a 150μm water film thickness. Graphs 37a, b & c give the results for the sizes of the droplets measured against the impacting droplet size and divided in the three different range of velocity.

Only for impingements at low velocity an increase of the satellite droplets size is noticed as the impacting droplet VED increases. There is a variation up to 100μm between the impacts made by the smallest and the biggest droplets. There are not found relevant differences for the cases when the velocity of impact increases. In general, it can be said that the size of all the satellite droplets can be found in a range between 50 and 300μm.

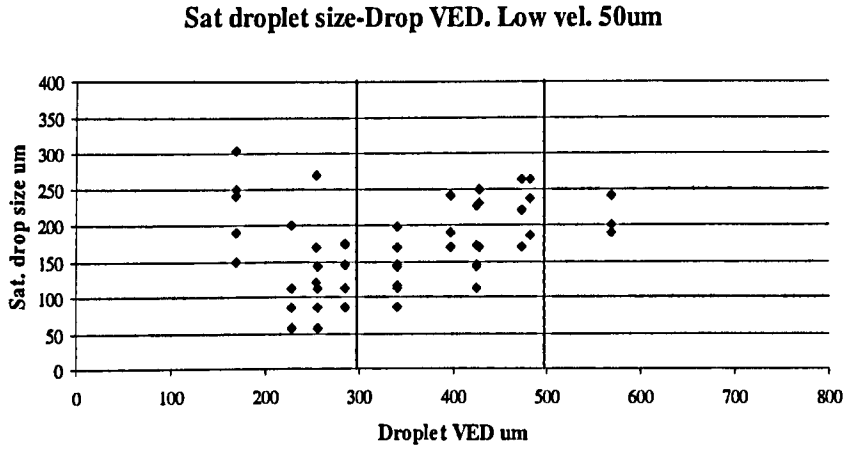

Graph 38a. Impact at 70°, low speed, ambient temperature and 50μm water film.

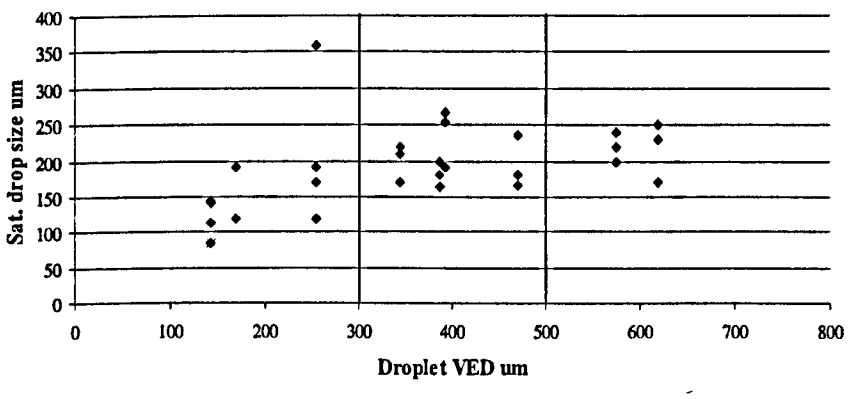

Graph 38b. Impact at 70°, medium speed, ambient temperature and 50μm water film.

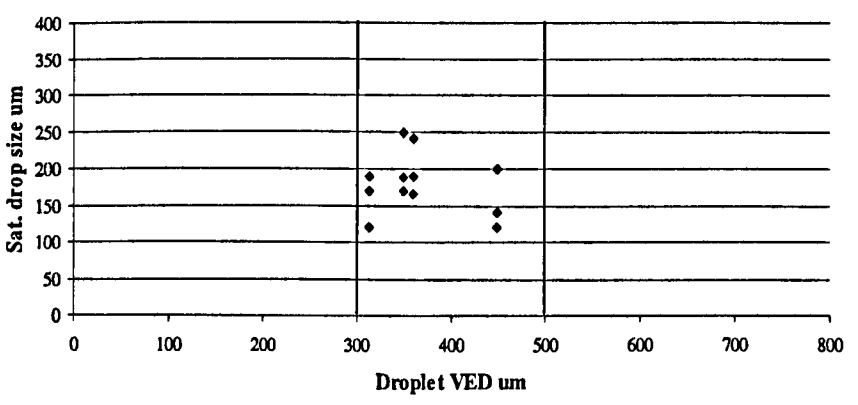

Graph 38c. Impact at 70°, high speed, ambient temperature and 50μm water film.

Figures 38a, b & c show the results for the impacts made under similar conditions than previously but using the 50μm water film. The results illustrate that for the

impacts at low and medium velocity, it can be appreciated an increase of the size of the satellite droplets with the increase of the incoming droplet size. The difference between small and big impacting droplet size can be around 100μm. However for the impacts at high velocity no trend line is apparent. Also it has to be mentioned that the number of cases recorded is lower than in the previous impacts.

Comparing impacts into the two different water layers, it can be said that those made into 50μm water film thickness release satellite droplets with sizes in a range between 50 and 250μm, which is slightly lower than the droplets obtained after the impacts into a 150μm layer thickness. These impacts produced satellite droplets up to 300μm.

Effect of droplet temperature on satellite droplets size.

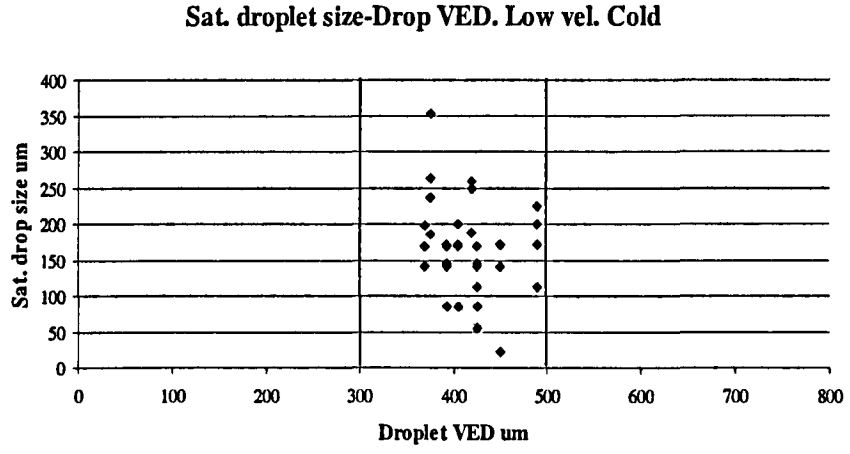

Graph 39a. Impact at 70°, low speed, -10°C and 50μm water film.

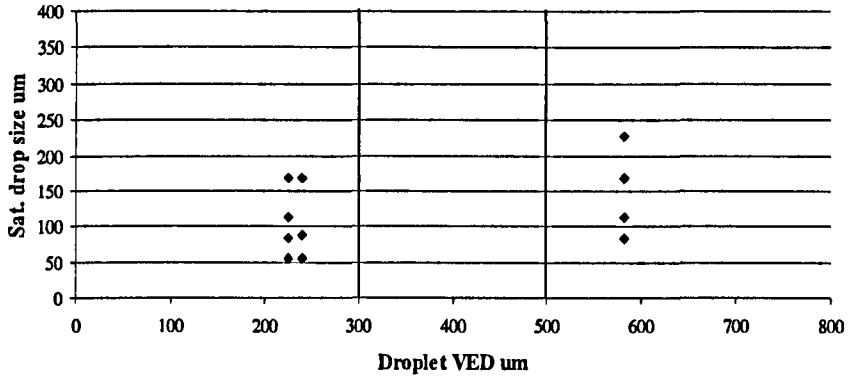

Graph 39b. Impact at 70°, medium speed, -10°C and 50μm water film.

The analysis of the impacts made into the 50μm water and under temperatures at -10°C is presented. It has to be mentioned that the number of cases recorded is relatively low and, as consequence, there are not shown impacts made at high velocities.

The results illustrate in graphs 39a & b that there is not much variation regarding the droplet VED or when the velocity of impact increases. Only a very slight increasing is observed in the case when the impacts are made at velocities between 30 and 50m/s. Thus, the values obtained for the sizes of the satellite droplets go again

from 50 to 250μm which are similar to the sizes obtained after impacts made at ambient temperatures, at the same angle of impact and water film thickness.

Effect of Angle of Impact on satellite droplets size.

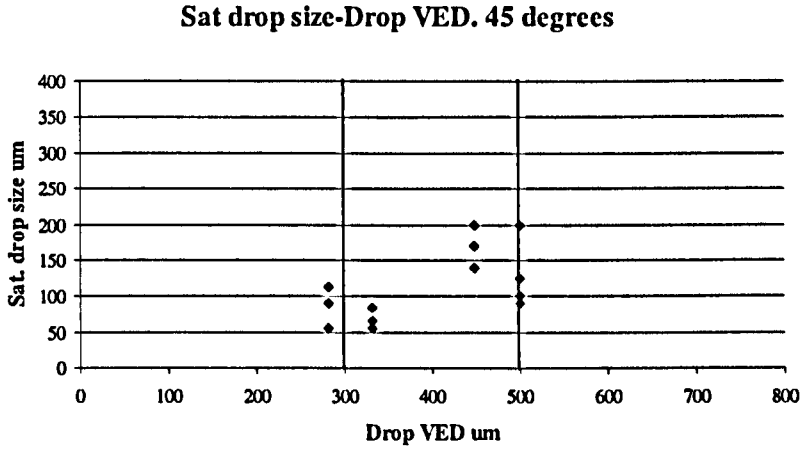

Graph 40a. Impact at 45°, ambient temperature and 50μm water film.

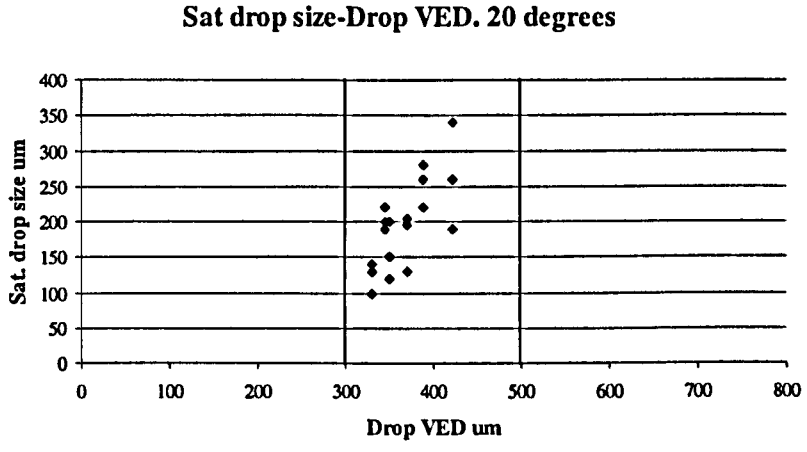

Graph 40b. Impact at 20°, ambient temperature and 50μm water film.

The analysis done for the impacts at small angles (45° and 20°) reflects a different tendency compared to the impacts made at 70°. It is observed that there is a clear increase of the satellite drops size as the VED of the impacting droplets is increased. Graphs 40a & b show this and also the fact that the droplets ejected from the corona formed after the impacts at very sharp angles, are significantly bigger than the ones obtained for impacts at 70°. Thus the values for the satellite droplets sizes are in a

range between 50 and 200μm for the impacts made at 45° and between 100 and 350μm for the impacts made at 20°.

Dry impacts (no water film).

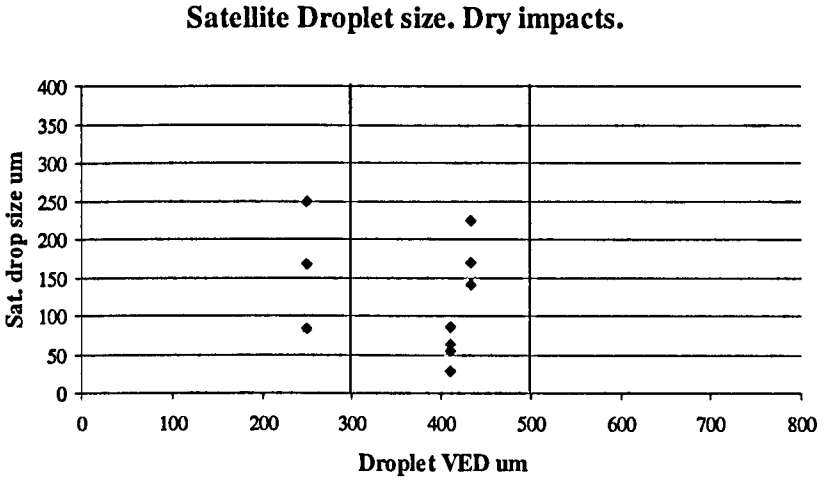

Graph 41. Impact over a dry target and 70°.

To finish the section, the impacts over a dry target are analysed. The airflow was at -10°C and, because there was not water film, an ice shade was formed on the target. Over this ice layer the droplets impacted. The satellite droplets produced during the splash are considered in this analysis. Some pictures are shown in figures 78a, b & c.

Graph 41 illustrates the variation of the satellite droplets size when the drop strikes a dry target at 70°. Because there is not so many data, all cases have been considered at the same time and they include all sorts of velocities and droplet size. The most significant conclusion is that there are found some satellite droplets with lower size than in all the previous cases where the impacts were made into a thin film. However the general range of value for the satellite droplets size is between 50 and 250μm which is not very different to the results obtained from the impacts made into a thin water film.

Some times the impacting droplet could strike into another droplet that was recently placed in the target and not frozen yet. This can be the reason that explains

some high values for the satellite droplets sizes that can be comparable to the size of the satellite droplets obtained after impacts into a water layer. Besides this, graph 41 does not shown any significant variation of the size of the satellite droplets with the increase of the size of the impacting droplet.

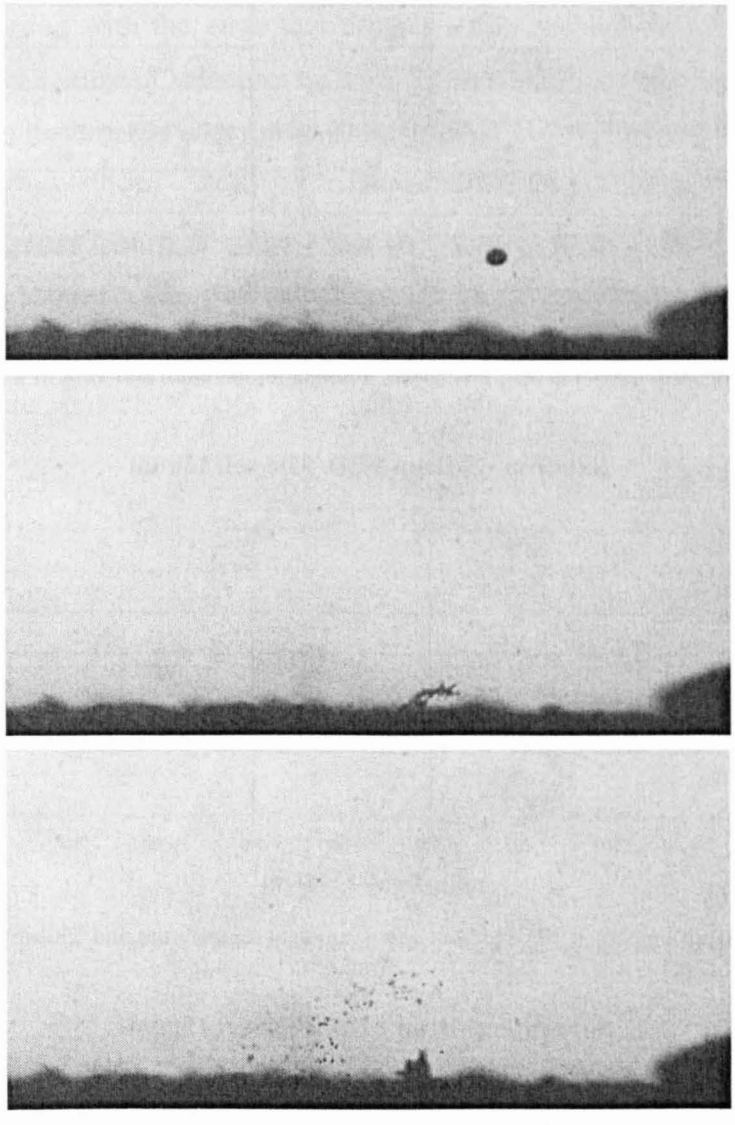

Figures 78a, b & c. Droplet impact upon a dry target.

Analysis of Satellites Droplets Velocity.

The velocity of the ejected droplets is measured against the incoming droplet size considering three ranges of velocities and the same type of analysis that previously is followed.

Effect of water film thickness on satellite droplets size.

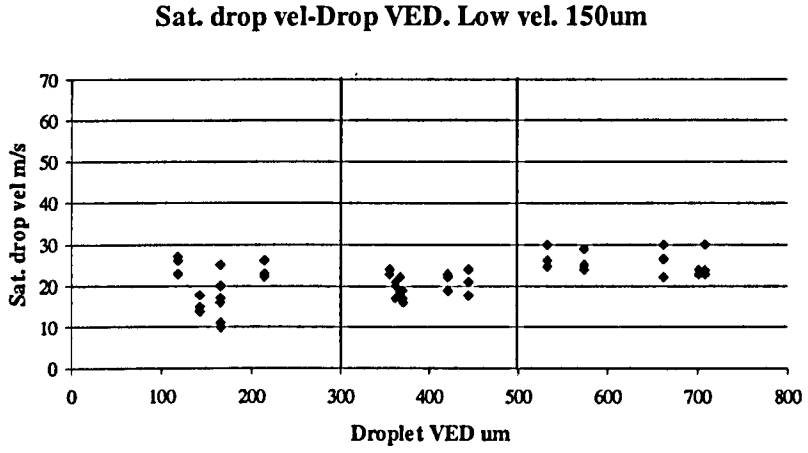

Graph 42a. Impact at 70°, low speed, ambient temperature and 150μm water film.

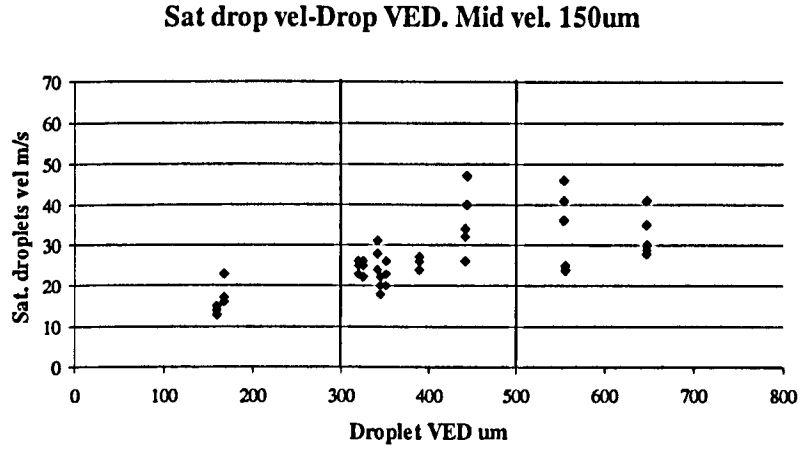

Graph 42b. Impact at 70°, medium speed, ambient temperature and 150μm water film.

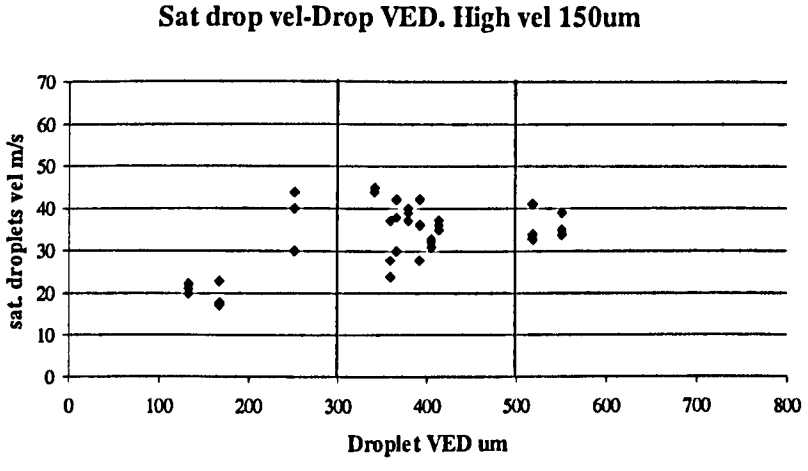

Graph 42c. Impact at 70°, high speed, ambient temperature and 150μm water film.

In first place, the impacts into the 150μm water layer thickness are considered. As graph 42a illustrates, the speed of the satellite droplets is in a range between 15 and 30m/s although for the smallest droplets there are found velocities of 10m/s. 42b & c also show a variation of the speeds as the droplet VED increases. Thus for the impacts at medium velocity, it is observed that the velocities are in a range that goes from 12 to 48m/s increasing with the impacting droplet VED. At high velocities of impact graph 43c shows a range of velocities between 20 and 45m/s, corresponding again the lowest values to the droplets with the smallest size.

Therefore graphs 42a, b & c show that the velocity of the satellite droplets for impacts into a 150μm water film thickness and at 70°, generally increases as the velocity of impact and the droplet VED increase. This was also observed as was with the velocity of the jets.

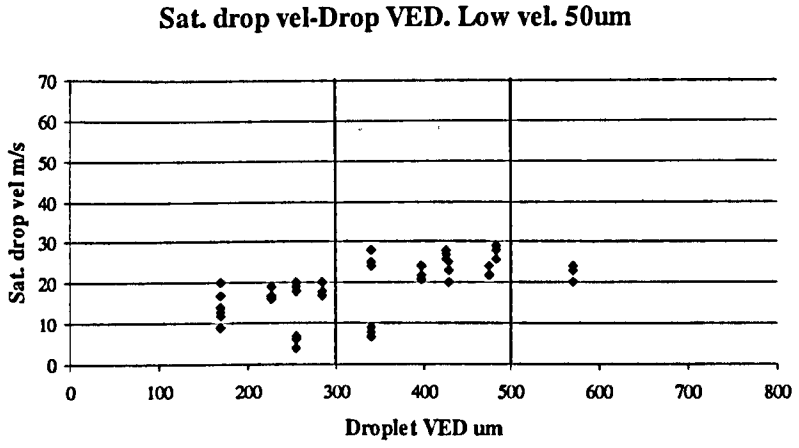

Graph 43a. Impact at 70°, low speed, ambient temperature and 50μm water film.

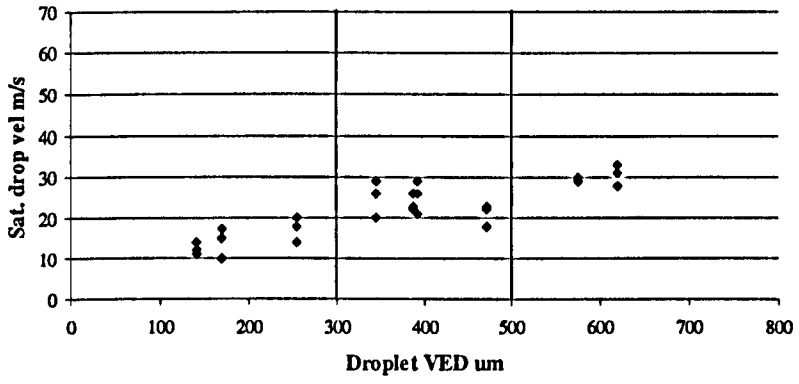

Graph 43b. Impact at 70°, medium speed, ambient temperature and 50μm water film.

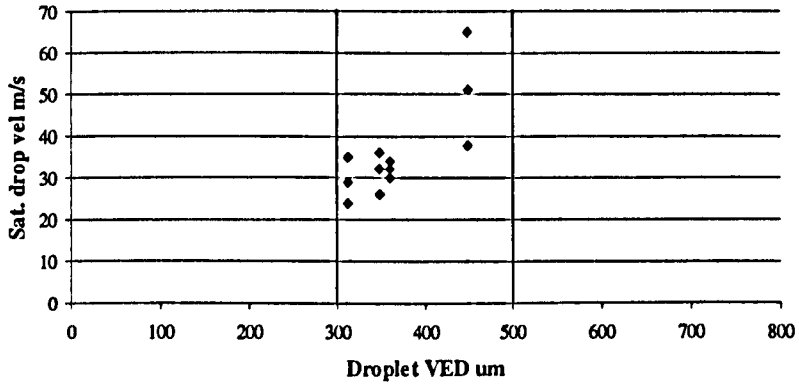

Graph 43c. Impact at 70°, high speed, ambient temperature and 50μm water film.

It can be observed that the velocity of the satellite droplets obtained after impacts into a 50μm water film is more sensitive to the incoming droplet VED and speed of impact than in the previous case. Graph 43a illustrates that the range of velocities for the impacts at low velocity goes from 5 to 30m/s as the droplet VED increases. For impacts at medium speed, a significant increase of the satellites droplets velocities is observed. Thus these drops are ejected at velocities that go from 10 to 30m/s. Finally, the impacts at high velocities, shown in graph 43c, illustrate that the speed for the satellite droplets go from 25 to 66m/s. It should be remarked that for this last case the incoming droplets VED are only in a range between 300 and 500μm.

Comparing these impacts with those made into a 150μm water film thickness, it is observed that the velocities are generally higher for the impacts into the thicker layer. An exception is found for the cases at high velocities where the satellite droplets with the highest speeds correspond to the impacts into the shallower layer. The variation of the velocities depending on the water film thickness does not use to be higher than 10m/s.

Effect of droplet temperature on satellite droplets size.

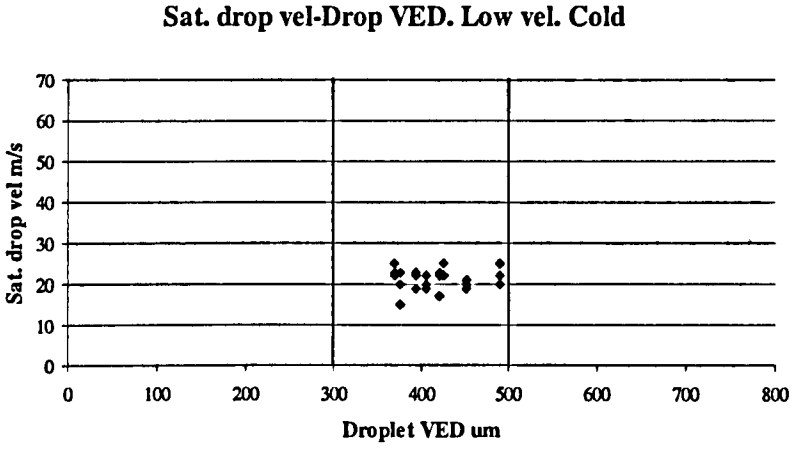

Graph 44a. Impact at 70°, low speed, -10°C and 50μm water film.

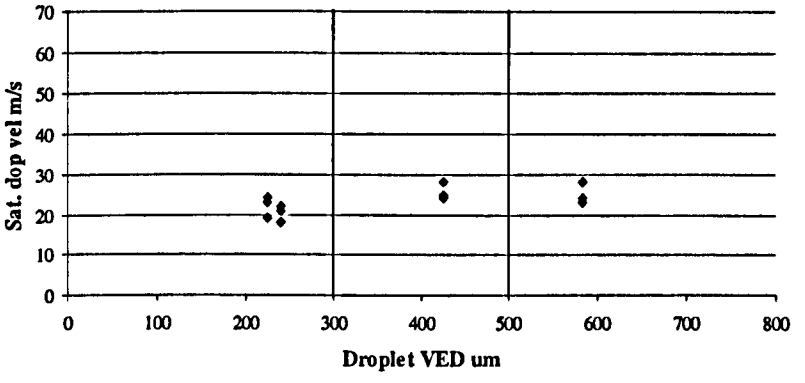

Graph 44b. Impact at 70°, medium speed, -10°C and 50μm water film.

The impacts observed at super-cooled temperatures reflect a very little change on the velocities of the satellite droplets independently on the size and velocity of the impacting droplet. Graph 44a shows the results obtained for the impacts made at low speeds. It can be seen that the satellite droplets velocity is approximately 20m/s. Graph 44b illustrates the velocities of the satellite droplets for the impacts made at speeds between 20 and 30m/s. It shows a slight increase of the values of the velocity as the incoming droplet VED increases. Thus the speeds go from 18m/s for the small droplets to 24-29m/s for the biggest, which is only a bit higher than the velocities obtained for impacts at low speed.

Comparing with the impacts made at ambient temperature it can be observed that the only significant differences in the satellite droplets velocity are found after impacts made by small droplets at velocities between 30 and 50m/s. Here, the velocity of the satellite droplets is 10m/s higher for the cold case, which is approximately the 20% of the impact speed.

Effect of angle of impact on satellite droplets size.

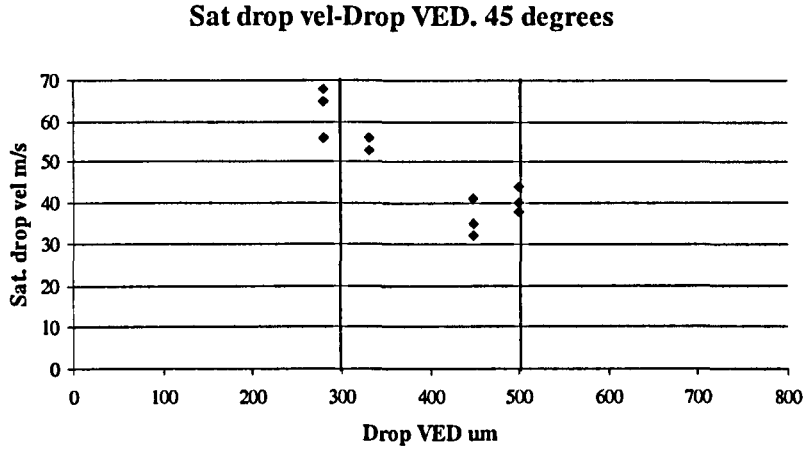

Graph 45a. Impact at 45°, ambient temperature and 50μm water film.

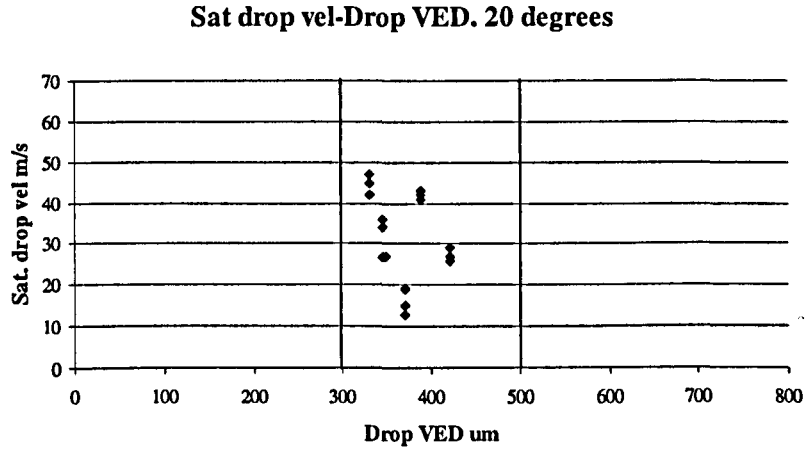

Graph 45b. Impact at 20°, ambient temperature and 50μm water film.

To continue this section, the impacts at small angles are analysed. They reflect a very different tendency of the results of the satellite droplets velocities. These results appear to show a decrease (instead of an increase) of the satellite droplets velocity

when the impacting droplet size increases. Also the satellite droplet velocities are much higher than in all the previous cases. Hence, the velocities of the ejected droplets go from nearly 70m/s to around 30m/s for the impacts at 45° and from nearly 50 to more than 10m/s for the impacts at 20°. Graphs 45a & b show these relevant differences.

Dry impacts (no water film).

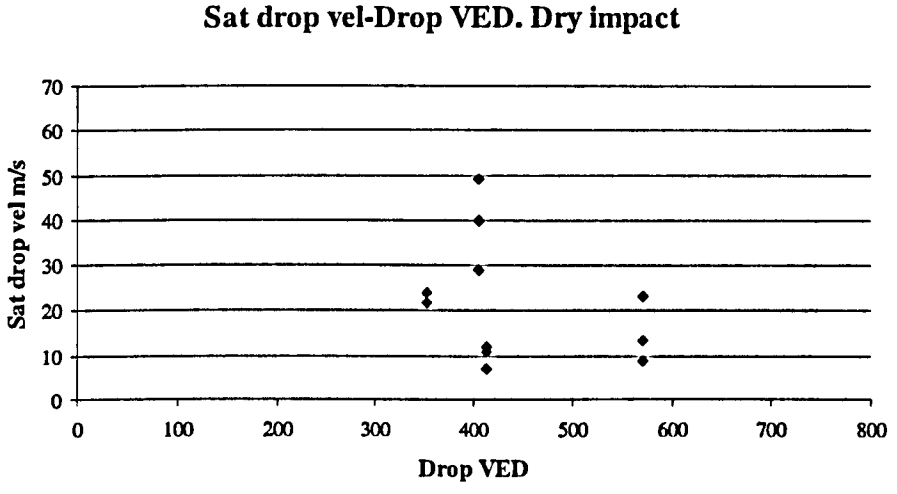

Graph 46. Impact over a dry target and 70°.

To conclude this section the velocities of the satellite droplets produced by an impact over a dry target are considered. It is not possible to give a final conclusion because there are not measured so many data. The few results give a lot of scatter. As graph 46 shows, the velocities are, in general, in the same range than the cases where a water film was present, this is, between 8 and 50m/s.

PART III: SOLIDIFICATION

A Numerical Method for Fluid Solidification.

With the aim of studying when and how the super-cooled droplets start to freeze after the impact into a thin water film, a numerical method based on simple mathematical modelling has been developed. Initially it has been considered with some ice roughness set on the bottom of the thin water layer, simulating the initial stages of the building up of the ice on the most sensitive surfaces of the aircraft, and with a super-cooled droplet impacting on the water film (figure 79). The ice starts growing as the temperature in the film decreases and also, when the droplet touches it. Later, during the splash process, due to a very rapid growth of the ice on the computational mesh, some numerical problems have been found and remain, at the moment, still unsolved.

Therefore, what it is presented here is a numerical model that works out the fluid solidification, the results produced by the ice growth inside the water film due to freezing of the water, the initial stages of the splash and jets formation, and some suggestions to extend the work improving the numerical code.

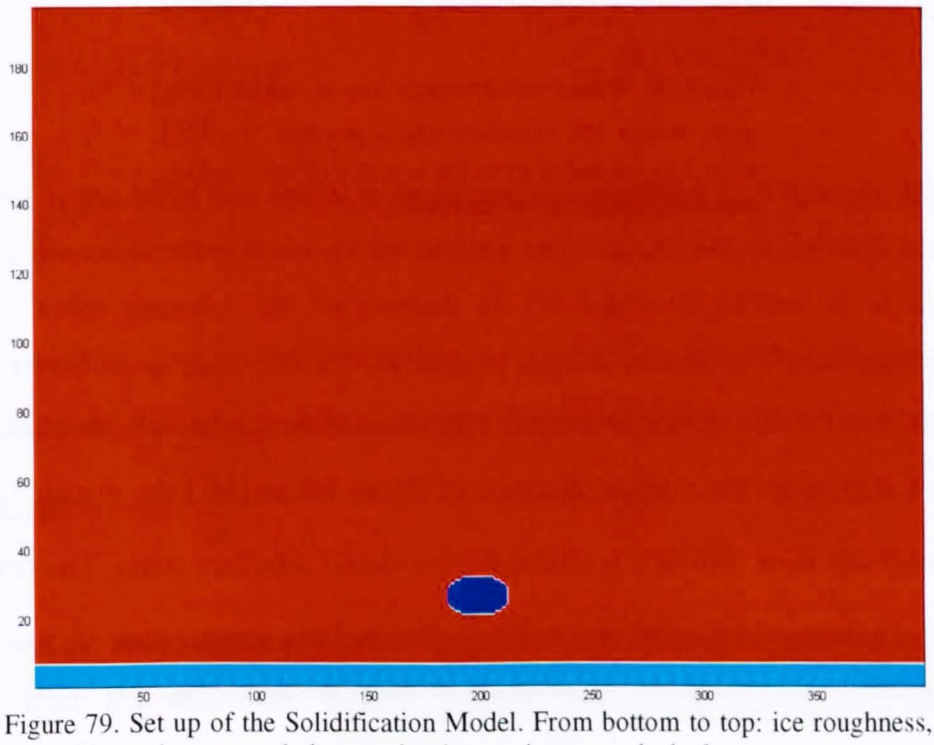

Figure 79. Set up of the Solidification Model. From bottom to top: ice roughness, water film and super-cooled water droplet moving towards the layer.

The Mathematical Model.

The analytical work behind the model is based on extending a part of the 'Theory of Solidification' (Davis, 2001). This mathematical model takes into account, in one dimension, the freezing into an under-cooled melt. What this theoretical method considers first, is a semi-infinite body (figure 80) that is cooled below $\hat{T}_m$ to $\hat{T}_\infty$. Here $\hat{T}_m$ is assumed to be the melting temperature and $\Delta\hat{T} = \hat{T}_m - \hat{T}_\infty$ typical temperature difference. At $\hat{t} = 0$ a plate is inserted at $\hat{z} = 0$ at temperature $\hat{T}_m$. The densities of the solid and the liquid are considered to be the same ($\rho^s = \rho^l$). It is whished to determine how the system evolves. In the solid, $\hat{T} = \hat{T}_m$ always, and thus heat conduction is absent there.

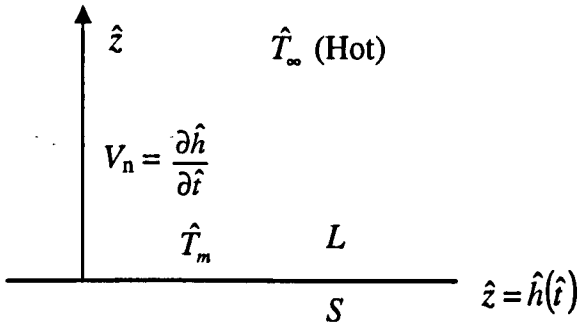

Figure 80. Planar solidification into an under-cooled melt, where the interface has a position $\hat{z} = \hat{h}(\hat{t})$. Here V_n is assumed to be the velocity of the interface, which is normal to the interface.

The temperature profile at a fixed time $\hat{t} > 0$ for this case is shown in figure 81 and illustrates the change in the temperature depending on the solidification. Thus, if the axis z represents the vertical distance of figure 80 and $\hat{h}(\hat{t})$ the distance thickness of the solid ice, then, $\hat{h}(0) = 0$ is where the ice-liquid interface starts. The temperature below this point, occupied by the solid, is the melting temperature $\hat{T}_m$ and above it, $\hat{T}$ starts to increase continuously (as shown by $\hat{T}_1(\hat{z})$).

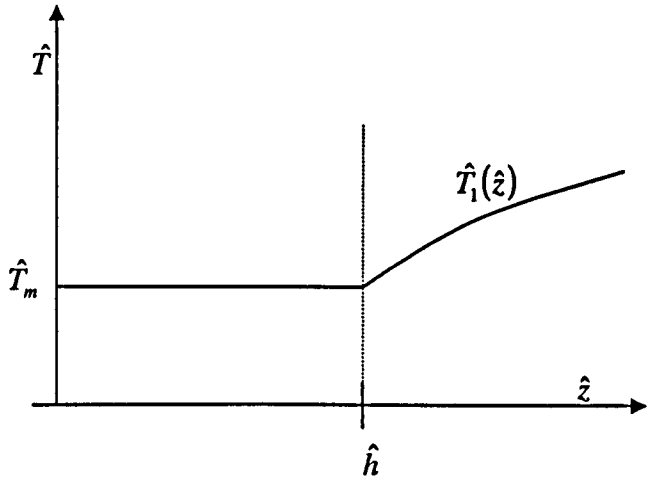

Figure 81. Temperature profile for one-dimensional freezing.

Therefore, the governing system of equations and boundary conditions is as follows:

$$\hat{T}^s = \hat{T}_m \qquad \text{On solid, } \hat{z} < \hat{h}(0) \qquad (45)$$

$$\hat{T}_t^l = k^l \hat{T}_{zz}^l \qquad \text{On liquid, } \hat{z} > \hat{h}\ (0) \qquad (46)$$

$$\hat{T}^l = \hat{T}^s = \hat{T}_m$$
$$\rho^s L \frac{\partial \hat{h}}{\partial \hat{t}} = -k_T^l \hat{T}_z^l \qquad \text{On } \hat{z} = \hat{h}\ (0) \qquad (47)$$

Here L is the latent heat and k_T is the thermal conductivity. (45) indicates that on the solid, the temperature is always the melting temperature. (46) is the heat transfer equation which provides the temperature of the liquid depending on time. As boundary conditions, (47) imposes that the temperature in the interface is the same for the solid and the liquid, in particular, it is $\hat{T}_m$, and also gives the advance on time of the ice-liquid interface $\frac{\partial \hat{h}}{\partial \hat{t}}$.

Second, the above approach can be adapted to the problem of droplet impact with solidification; the analytical method contemplated addresses the problem of

solidification of any liquid fluid in contact with the same fluid which is already frozen. However, for the impact problem, two parts of liquid fluid at two different temperatures are involved, which means that some new considerations have to be taken into account.

Because another part of fluid is going to play an important role, the temperature profile at the initial time $\hat{t} = 0$ for this new case, which is shown in figure 82, is going to be affected by the super-cooled droplet. Thus, it can be observed that, after the position $\hat{h}_0$, the temperature is again increasing but only until a certain position $\hat{h}_1$, which refers to the boundary between the original liquid (water) layer and the liquid droplet, where the temperature falls suddenly with a discontinuity until the droplet temperature $\hat{T}_2$ is encountered.

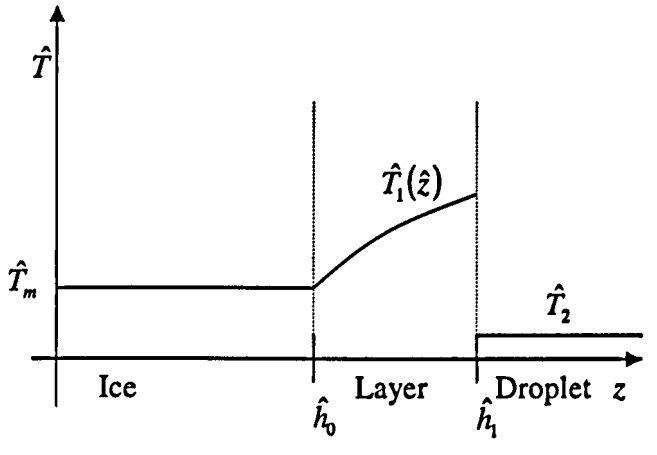

Figure 82. Initial temperature profile for the case of ice-layer-droplet.

Based on equations 45, 46 and 47, seeking a non-dimensional form, the variables for the problem considered here are:

$$\begin{aligned} \hat{T}^l &= \hat{T}_\infty + \left(\hat{T}_m - \hat{T}_\infty\right)\cdot\theta, \\ \hat{t} &= \left(\frac{\hat{h}_0^2}{k^l}\right)t, \\ \hat{z} &= \hat{h}_0 z, \\ \hat{h} &= \hat{h}_0 h. \end{aligned} \tag{48}$$

The symbol ^ refers to the dimensional variable, θ to the non-dimensional form of the temperature and T_∞ denotes the temperature of the droplet or the layer (for convenience) depending on the distance between the ice and the drop. Therefore, if this is "far", the temperature T_∞ considered will be the one of the water in the layer, and vice versa. (In numerical terms, the distance is considered "far" if there is not found in the same computational cell water from the droplet and from the ice). The reason this has been done in this way for our context is that not all the ice roughness is going to be affected by the super-cooled droplet. Figure 79 shows, for example, that the ice placed to the left or to the right of the domain is not going to be influenced much by the droplet impact, at least, at the very early stages of the process which is what is being considered for now.

The equation for the heat transfer then has to be solved:

$$\frac{\partial \theta}{\partial t} = \frac{\partial^2 \theta}{\partial z^2} \tag{49a}$$

with:

$$\begin{aligned} \theta &= 1 && \text{at } z = h(t), \\ \frac{\partial \theta}{\partial z} &= -S\frac{dh}{dt} && \text{at } z = h(t). \\ \theta &\to 0 && \text{as } z \to \infty. \end{aligned} \tag{49b}$$

The initial conditions at $t = 0^+$ are $h(0) = 1$ and

$$\begin{aligned} \theta|_{t=0^+} &= 1 && \text{for } 0 \le z \le 1, \\ \theta|_{t=0^+} &= T_1(z) && \text{for } 1 \le z < \alpha, \\ \theta|_{t=0^+} &= 0 && \text{for } z > \alpha. \end{aligned} \tag{49c}$$

Here

$$S \equiv \frac{L\rho^l k^l}{k_T^l\left(\hat{T}_m - \hat{T}_\infty\right)} \tag{50}$$

is the Stefan Number, k^l is the thermal diffusivity in the liquid and α is explained in connection with the temperature profile at time $t = 0^+$ shown in figure 83:

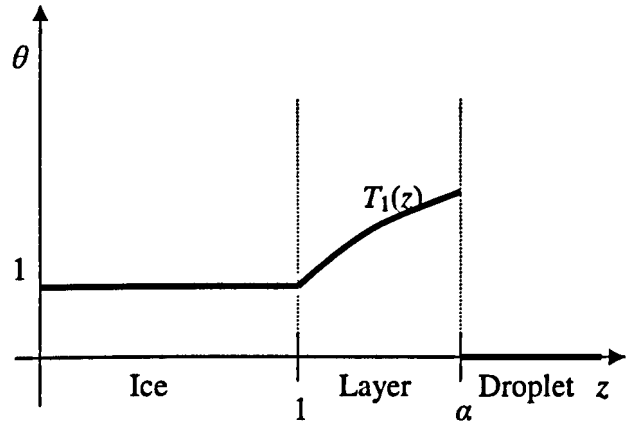

Figure 83. Temperature profile for the non-dimensional problem.

Once 5a is solved with 5b and 5c, the temperature can be calculated and also $h(t)$ which provides the position of the boundary between the ice and the liquid for every time step. The solution is found to give:

$$\theta(z,t) = 1 - 4.5\frac{z-1}{t^{1/2}} + o(\eta^3) \tag{51}$$

where, $\eta = \frac{z-1}{t^{1/2}}$. Also,

$$h(t) = 1 + 9.027 \cdot t^{1/2} S^{-1} \tag{52}$$

Therefore, dimensionalising (51) and (52), the results are:

$$\hat{T}(\hat{z},\hat{t}) = \hat{T}_\infty + (\hat{T}_m - \hat{T}_\infty)\left[1 - 4.5 \cdot \frac{\hat{z} - \hat{h}_0}{\sqrt{k^l \hat{t}}}\right], \tag{53}$$

$$\hat{h}(\hat{t}) = \hat{h}_0 + 9.027 \cdot S^{-1}\sqrt{k'\hat{t}}\,. \qquad (54)$$

Hence, (53) provides the temperature of the fluid close to the ice at every time-step and (54) the advance of the interface with time.

The Computational Method.

Based on use of the equations presented above, a computational method that accommodates them, and, therefore, works out the solidification problem, is presented. This section shows how the method of calculation of temperature, e.g. as it decreases in the larger fluid due to the contact with the ice, and the advance in time of this ice roughness set at the bottom of the layer, has been developed. The mathematical method presented above is modified slightly here because the problem that has to be solved is in two dimensions and not in one. However, the equations used below are based on the previous ones.

The set up.

To start, a series of triangles, which are all of the same size, and simulate the ice shape are set at the bottom of the domain. Figure 84 shows these triangles at the first time step. The water film is just slightly thicker than the height of the ice crystals. This can be compared with figure 21 which shows the first time step for the general case. Figure 85 shows a detail of the set up of these triangles.

The equations defining the sides, or lines, of the different triangles are set. This helps as well to give the initial volume of ice in every cell. As was done with the amount of fluid in every cell, now the ice is considered as another volume which is initially given once the equations for the lines are calculated. Therefore, Fh(i, j) is defined as the function that determines the quantity of ice in the cell. Also this function takes the value zero when no ice is found, one when the cell is full, and

values between zero and one for cells partially filled with ice. These last cells are considered surface cells because the fluid does not fill them completely. Specifically, they will be called "ice surface cells". The function Fcc(i, j) will have a value between zero and one and thus it will be considered a surface cell too.

In order to set initially the lines defining the triangles in the computational mesh (figure 86), the cells have to be worked out individually. Hence, in every ice surface cell there is a line and, obviously, two ends that are labelled with four different names depending on their positions. These names are VB, VT, VL, VR for the ends placed at the bottom, top, left and right side of the cell respectively, and they are calculated and set for the first time step for every single surface ice cell. An example is shown in figures 87a & b. In each of them two ends can be observed. These ends are going to advance as the water is cooled down and, therefore, the lines dividing the ice from the fluid, then advance.

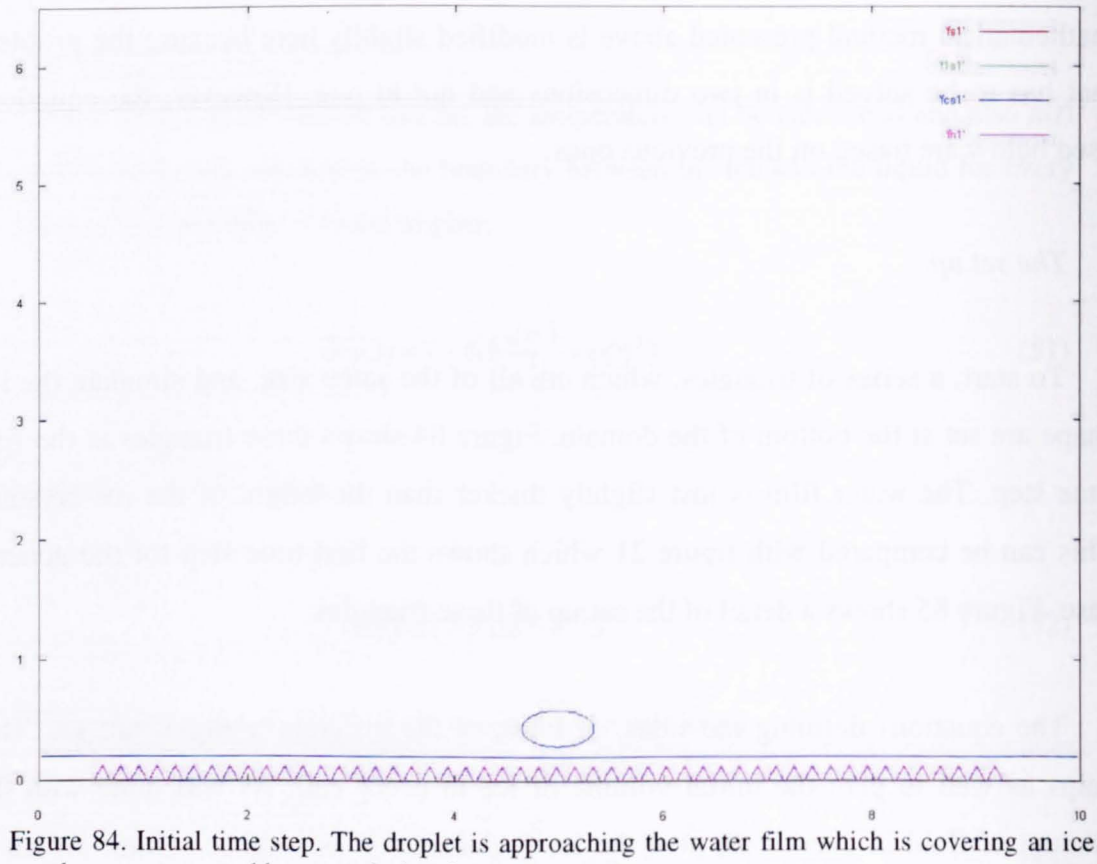

Figure 84. Initial time step. The droplet is approaching the water film which is covering an ice roughness represented by several triangles

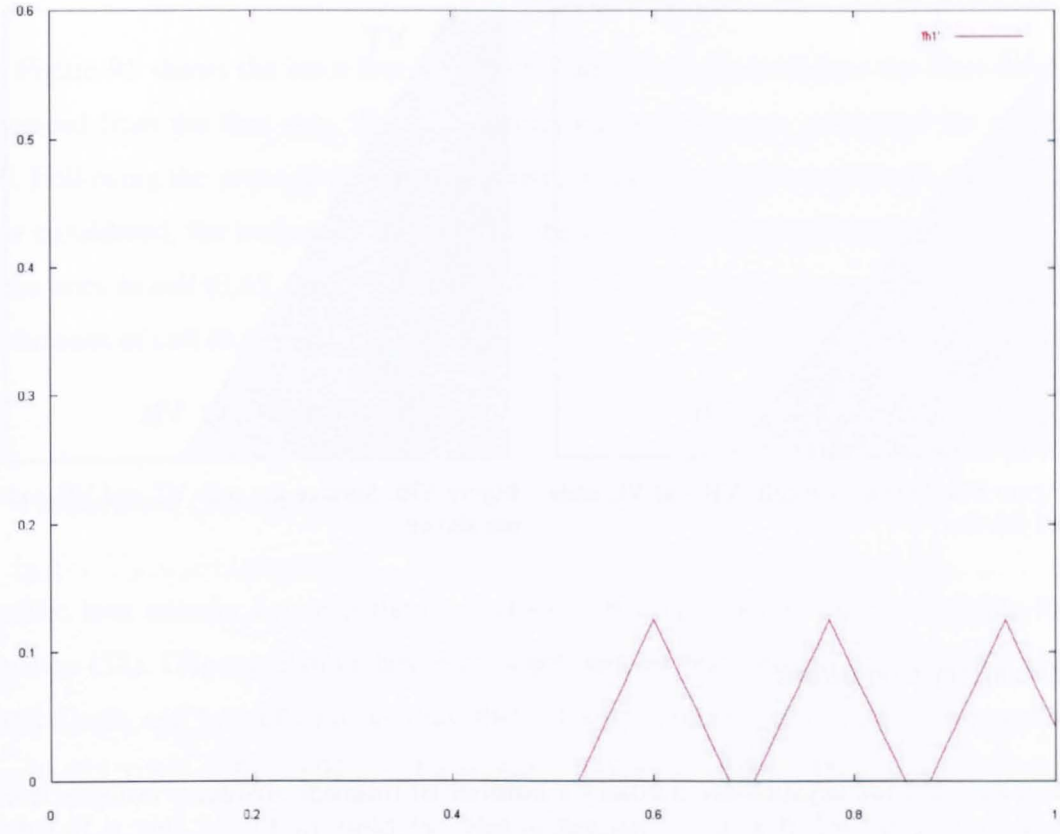

Figure 85. Detail of the ice crystals at the first time step.

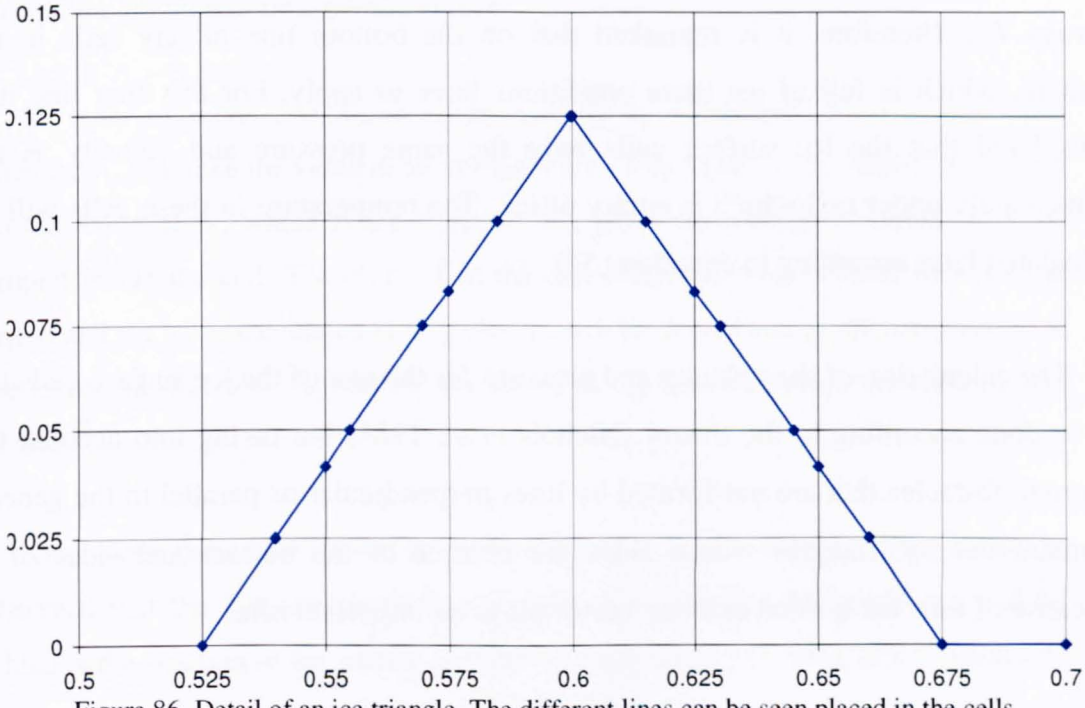

Figure 86. Detail of an ice triangle. The different lines can be seen placed in the cells.

The normal exterior vectors to the straight lines representing the ice crystals have been also calculated. This is going to be used in the present study in order to calculate the ice-liquid interface position as the ice grows for the next time steps.

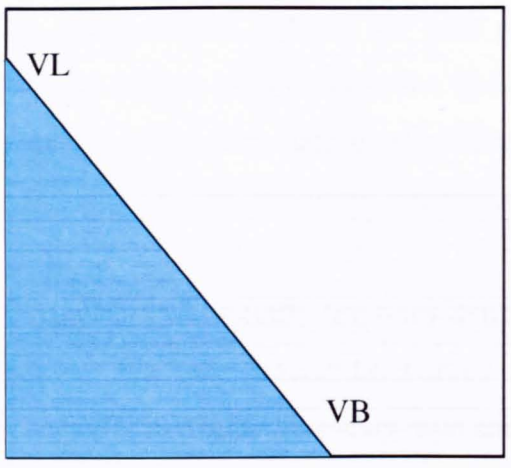

Figure 87a. Surface ice cell. VB and VL ends are shown

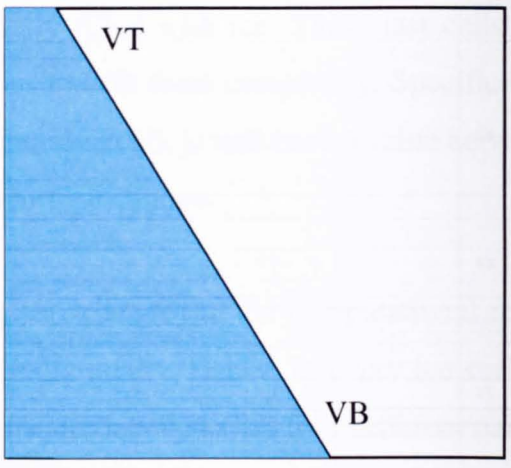

Figure 87b. Surface ice cell. VT and VR ends are shown

Boundary Conditions.

Because the ice crystals are actually a number of internal obstacles boundaries, the boundary conditions have to be modified. It has to be taken into account that inside the ice, there is no fluid, velocity or pressure, and the temperature is going to be always T_m. Therefore, it is remarked that on the bottom line of any cells in the domain, which is full of ice these conditions have to apply. For this first line it is considered that the ice surface cells have the same pressure and velocity as the immediately upper cell which is empty of ice. The temperature in these cells will be calculated later according to equation (53).

The calculation of the velocity and pressure for the rest of the ice surface cells has to be done according to the theory (Nichols *et al.* 1981) but taking into account the internal obstacles that are not formed by lines perpendicular or parallel to the general domain, but by triangles whose sides are oblique to the bottom and sides of it. Because of this, the normal exterior vector plays an important role.

According to the theory, for a left boundary formed by a vertical rigid free-slip wall (see figure 89), the normal velocity to it must be zero and the tangential velocity should have no normal gradient, i.e., in equations 21a & b method chapter. However, this is not a case that can be applied to the triangles for the reason already mentioned above (see figure 90). In fact the velocity normal to the triangle side must be the

PAGES ARE MISSING IN ORIGINAL

Figure 91 shows the ice a few time steps later. It can be seen how the lines have advanced from the first step. The unit normal vectors are again calculated for every cell. Following the procedure described above, if for example the cell (0.65, 0.025) is now considered, the tangential velocity and the pressure on this cell will be the same as the ones in cell (0.65, 0.05). For cell (0.675, 0) the velocity and pressure given will be the ones of cell (0.675, 0.025).

Temperature Calculation.

The heat transfer between the ice and the water film is calculated according to equation (53). This calculation, however, is not done for the entire layer but for the ice surface cells and for cells full of fluid that are very close to the ice. Therefore, cells like (0.525, 0.05) of figure 91 are also included in the calculation. The condition given is that if a cell is full of fluid (so that it has no ice at all) but for any of the neighbouring cells $Fh \geq 0.5$, the heat transfer calculation in equation (53) between the ice and the liquid will be applied also here.

In order to solve (53), some issues have to be considered. As was mentioned already, T_∞ will take the value of the temperature of the layer or the droplet depending on the value of f1, which is the function that gives the amount of liquid from the droplet inside the cell. Therefore, if in the cell where the heat transfer between the liquid and the ice is calculated $f1 = 0$, then T_∞ will be considered as the temperature of the layer and if $f1 > 0$, T_∞ will be considered as the temperature of the super-cooled droplet.

One more detail has to be taken into account before solving (53). It can be observed that the last term includes the difference between the position z and h_0, which is the position of the ice-liquid interface (see figure 81). This term is identified as:

$$z - h_0 = \frac{dx}{16\sqrt{2}} \qquad (55)$$

We recall that dx is the size of the cell and, in this code, $dx = dy$. That distance has been chosen in order to get a position z "close" enough to the ice boundary in the direction of the cell diagonal.

Ice Propagation.

Once the temperature in the liquid water "close" to the ice-liquid interface is calculated, the temperature between the droplet and the layer is sought. This is achieved as was explained in the chapter related to the numerical model and therefore the temperature in all the cells of the computational mesh can be obtained.

One first thing to take into account here is what temperature T_∞ has to be considered, the one of the liquid or the one of the droplet. An option to select this to obtain the Stefan number is given now in order to use the right temperature. Once the Stefan number is obtained, the second term on the right of equation (54) is calculated. This term is called the "Ice Growth Ratio", and it will be the average of the ice growth ratios between the considered cell and all the neighbouring cells. This term is always positive, but, for those cases in which Fh > 0 and the temperature obtained for the cell considered is greater than $T_m + \varepsilon$, the ratio will change the sign and therefore the ice will be able move back if necessary.

The next step is based on the Piecewise Linear Interface Calculation (PLIC) Method (Li, 1995, Scardovelli *et al.* 1999 and Gueyffier *et al.* 1999). This algorithm is developed for tracking the motion of interfaces by reconstructing them with segments in each cell. Because only one part of this method is used in the solidification model, it will be explained only briefly.

Basically, the method takes a computational mesh formed by cells such that, depending on the fluid fraction they store, the function that represents them will take the values 0 if empty, 1 if full, and something intermediate if the cell is cut by the interface. The algorithm is divided into two parts, a reconstruction step and a propagation step. For the reconstruction, the key point is to determine the orientation of the segment that forms the interface, which is equivalent to the determination of the

unit normal vector $\vec{n}$ to the segment. So the normal vector and the fluid fraction the cell stores uniquely determine the straight line. This PLIC method describes how the normal vector has to be calculated and also the area of the region contained in every cell. Once the interface is constructed, its movement due to the flow is modelled by using an advection algorithm. Hence a determined cell, in every x and y direction, has three contributors of fluid. If for example the direction x is considered, these three contributions come from the cell to the right, the cell to the left and the area of fluid which is contained at the beginning of the step in the cell and remains there.

The PLIC method is used in the solidification model basically to determine the straight line that represents the ice-liquid interface. What it is applied to is the estimation by finite differences for the normal vector calculation. According to the PLIC method, this vector is obtained as follows.

The normal (not necessary unit) vector $\mathbf{m}_{i,j}$ is calculated which is cell centred and is approximated first by evaluating the cell corner values of $\mathbf{m}$, for example at position $(i + ½, j + ½)$:

$$m_{x,i+1/2,j+1/2} = \frac{1}{2h}\left(Fh_{i+1,j} - Fh_{i,j} + Fh_{i+1,j+1} - Fh_{i,j+1}\right), \tag{56}$$

$$m_{y,i+1/2,j+1/2} = \frac{1}{2h}\left(Fh_{i,j+1} - Fh_{i,j} + Fh_{i+1,j+1} - Fh_{i+1,j}\right). \tag{57}$$

The required cell centred value is obtained by averaging, with

$$\mathbf{m}_{i,j} = \frac{1}{4}\left(\mathbf{m}_{i+1/2,j-1/2} + \mathbf{m}_{i-1/2,j-1/2} + \mathbf{m}_{i+1/2,j+1/2} + \mathbf{m}_{i-1/2,j+1/2}\right). \tag{58}$$

Once the normal vectors to the segments identifying the ice-liquid interface in every cell are determined, the advance of the interface as the temperature decreases has to be calculated. To achieve this, the ends of the segments labelled VT, VB, VL and VR are going to be moved according to the growth rate mentioned before. Thus four cases regarding the direction of the vectors are identified. They are:

1. $m_x > 0$ and $m_y > 0$.

2. $m_x < 0$ and $m_y > 0$.
3. $m_x > 0$ and $m_y < 0$.
4. $m_x < 0$ and $m_y < 0$.

Each of these four cases has been also divided into another four sub-cases depending on the distribution of the line inside them. Only the first one will be described here, since the others are analogous. Figures 92a, b, c & d illustrate these possible four divisions in every cell. First a case is shown that could be associated with the cell (0.65, 0.025) of figure 90. In order to allow for this segment advancing, the ice growth rate is added to VB and VL. Once one of them reaches the corner of the cell, for example VL, the cell becomes of the type shown in figure 92b, where the ice growth rate is applied as was already presumed to VT and VB. Consequently, if VL reaches the cell corner this parameter becomes VT. In the same way, if VB reaches the corner it becomes VR and the cell becomes of the type presented in figure 92c.

The second case illustrated can be compared with cell (0.625, 0.05) of figure 90. The growth rate is applied to VT and VB, and once VB reaches the corner this becomes VR and so the cell becomes of the type shown in figure 92b. The case represented in figure 92c is similar to cell (0.675, 0) of figure 91, with the only difference that m_x has a different sign here. The ice growth rate is applied to VL and VR and when VL reaches the corner it becomes VT, the cell changes and becomes of the type of figure 92d. Finally, figure 92d shows a case that can be compared with cell (0.6, 0.075) of figure 90. As usual the growth rate is applied to VT and VR. However, when one of them reaches the corner the cell is considered to be completely full of fluid.

This estimation of the normal is based on the sometimes called Parker and Youngs approach which is intermediate between first and second order. However, for medium resolution which less than 20 grid points along the ice surface (in our case there are 18), the results for those methods truly second order are not always better.

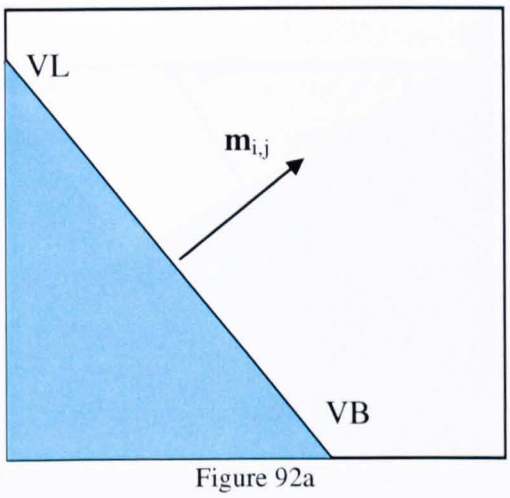

Figure 92a

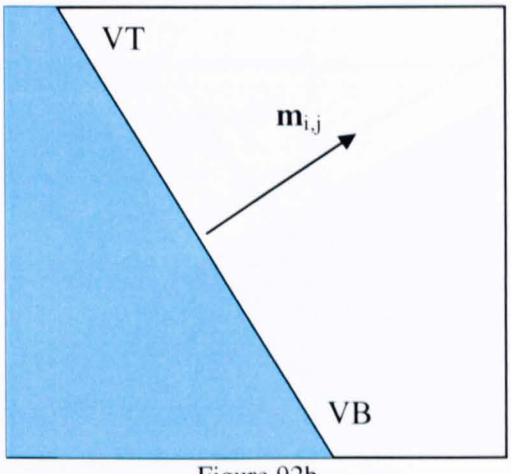

Figure 92b

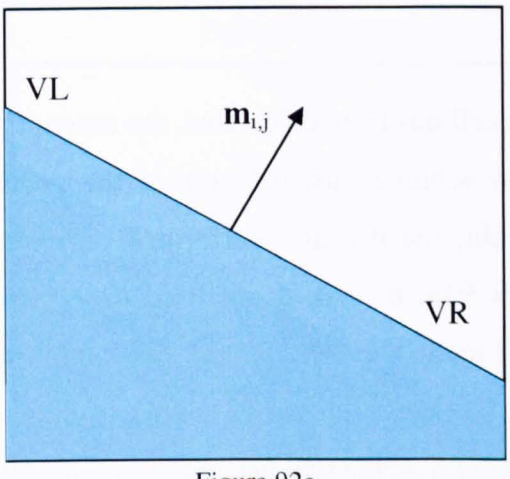

Figure 92c

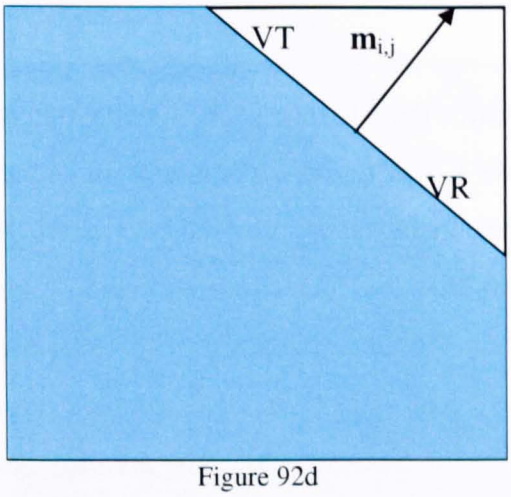

Figure 92d

What is achieved, then, is the advance of the segment representing the interface over every time step, as figures 93a & b illustrate. Considering the example shown in figure 92c, the ice growth rate is added to VL and VR. Hence the segment moves forward in the direction of the normal vector, increasing the volume of the ice inside the cell.

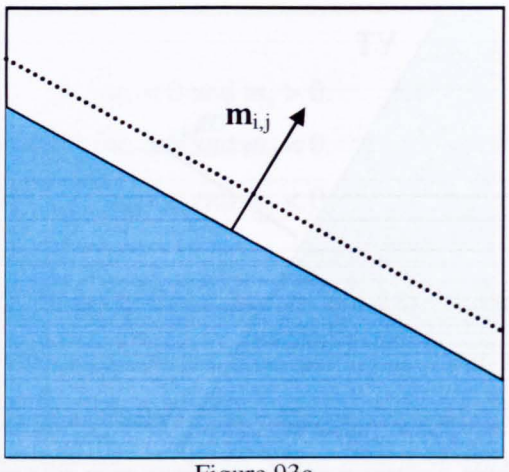

Figure 93a

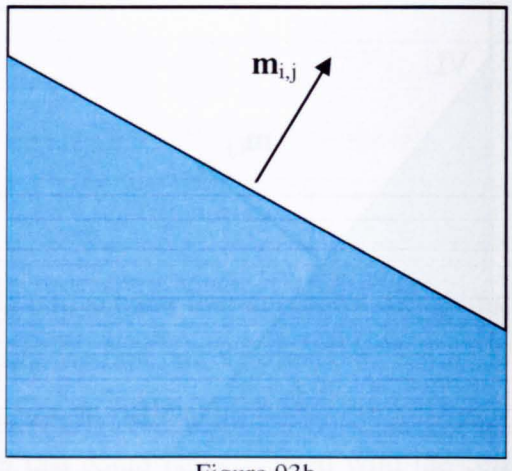

Figure 93b

Once the advance of the interface in the cell has been calculated, the amount of ice inside it has to be determined. In order to achieve this, the area of the geometric shapes inside every cell is calculated. Again, the division performed previously is considered and the cases shown in figures 94a, b, c & d are used to explain the process for the calculation of the amount of ice in the cells for the first option where $m_x > 0$ and $m_y > 0$. In cases such as figure 94a the amount of ice corresponds to the area of the triangle ABC. The area for cases such as the one presented in figure 94b is the same of the areas of the triangle ABC and the square ACDE. In the same way, for ice cells such as figure 94c the area is again the addition of the areas of the triangle ABC plus the square ABDE. The area for cases such as that in figure 94d is the difference between the area of the whole cell and the area of the small triangle ABC.

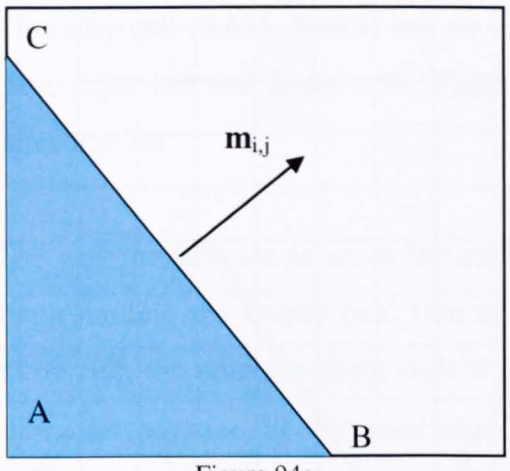

Figure 94a

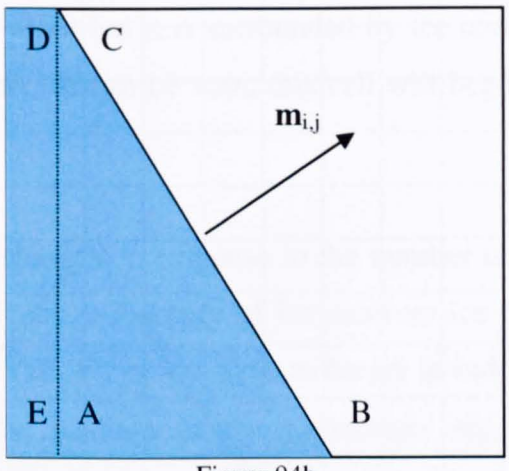

Figure 94b

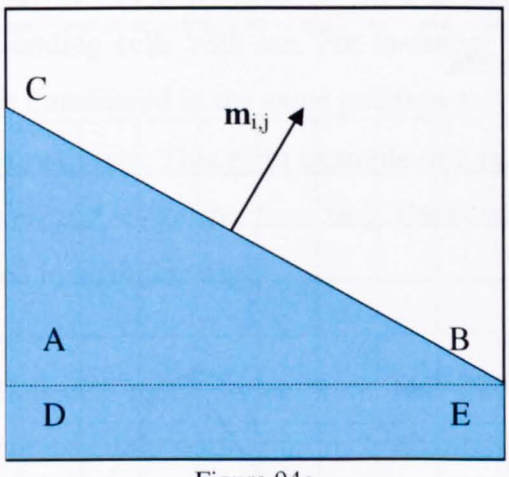

Figure 94c

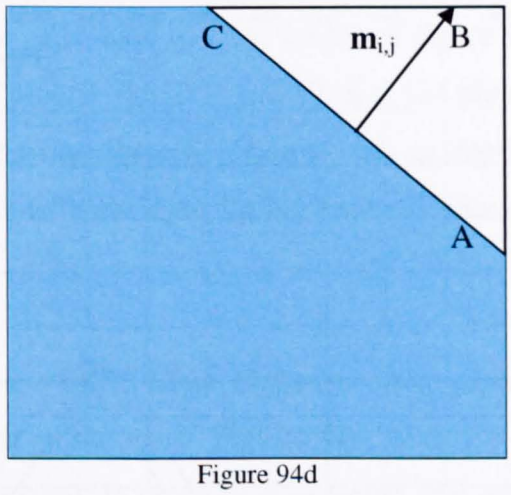

Figure 94d

The next stage consists of determining the ice formation in cells where initially Fh = 0. This happens when a cell with fluid but no ice in it has a temperature less than $T_m + \varepsilon$. In order to compute the first time that the ice appears in a cell three cases are distinguished. They are when the cell receives the ice from one, two or three different cells. The cells considered are those to the left, right, up and down. An example of ice growing for first time under the influence of one cell can be seen in figures 90 and 91, particularly in cells (0.5, 0) and (0.6, 0.125). An example of new ice coming from two cells is shown in figure 95a cell (0.675, 0). This cell is initially empty of ice (figure 90) but, due to the cooling down, ice starts to build up here. The volume of ice in the new cell is also determined immediately following the process already explained.

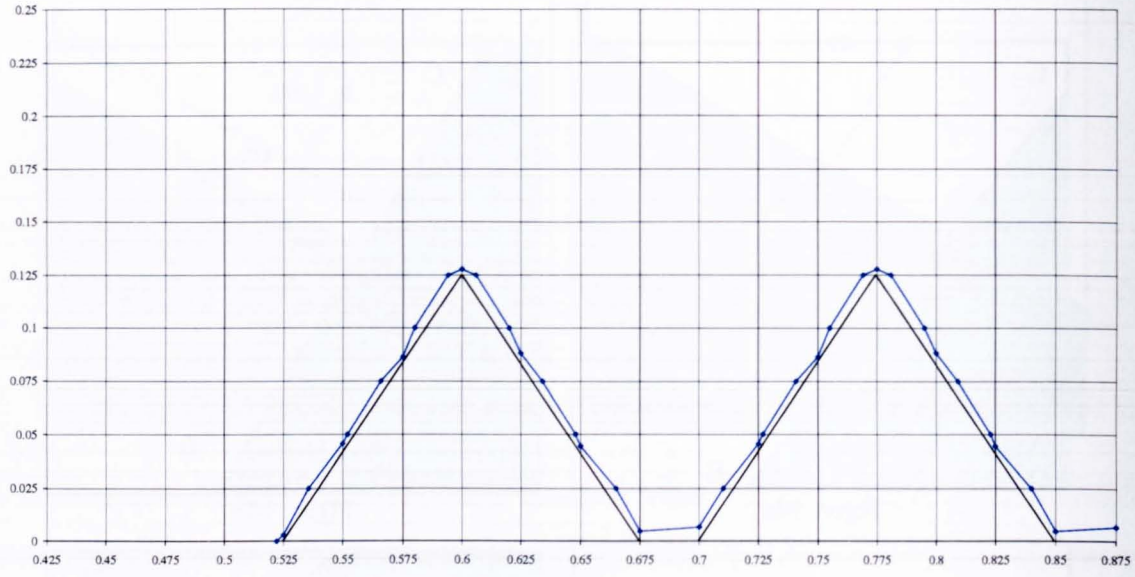

Figure 95a.

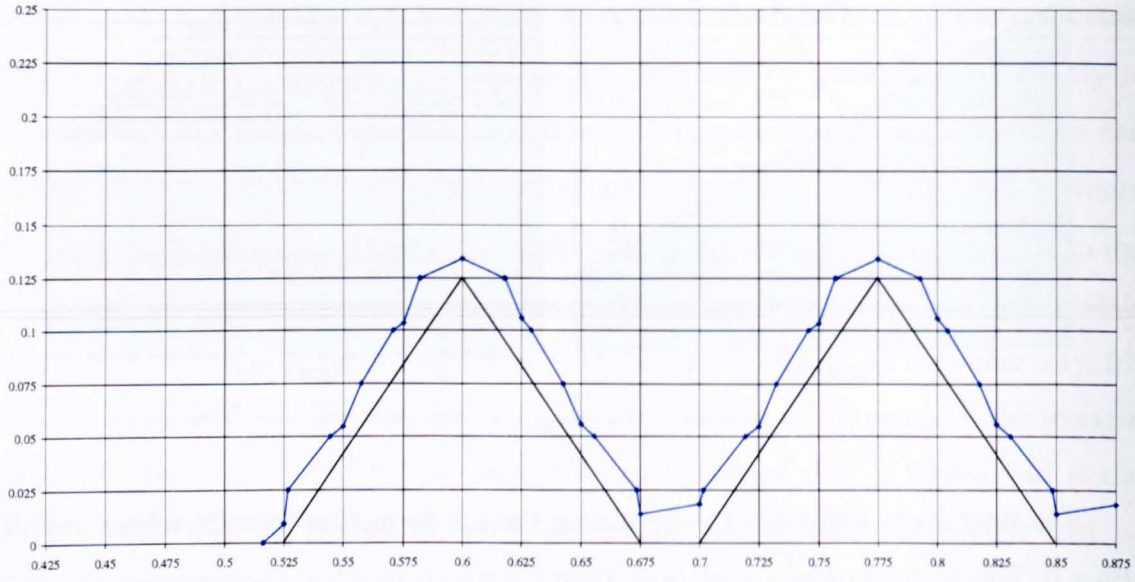

Figure 95b.

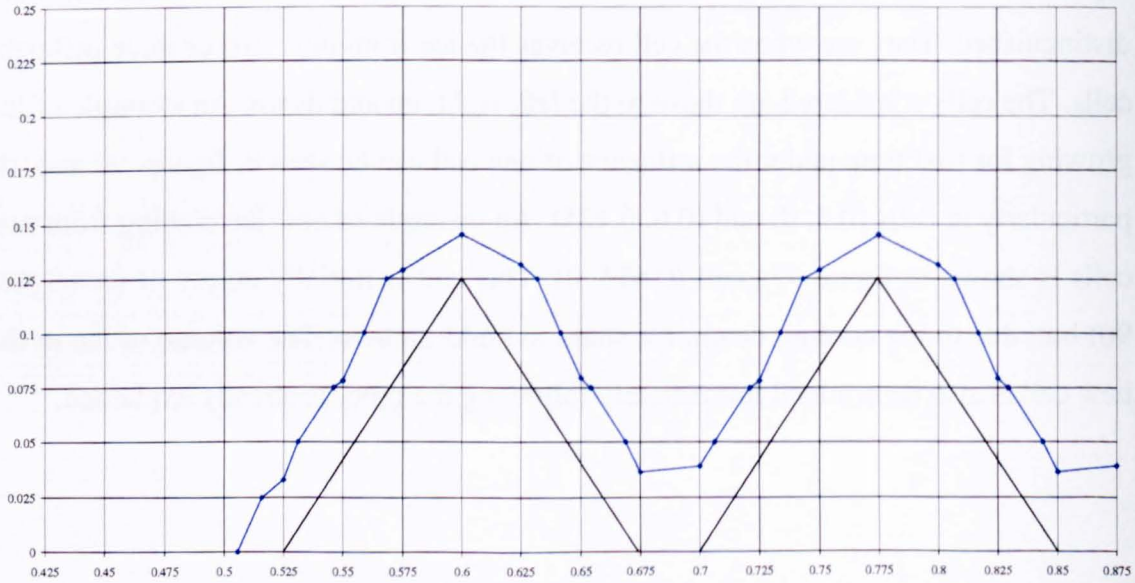

Figure 95c.

An example of ice in a new cell coming from three cells is observed in figures 95b & c. Initially cell (0.675, 0.025) has no ice at all but it is surrounded by ice coming from the right, left and down cells. Therefore, as can be seen, this cell will begin to contain some ice.

The way the new ice is set in the cells changes in response to the number of ice cells surrounding the empty one. Hence, if one cell empty of ice receives ice only from one cell, the corresponding ends VT, VB, VL or VR have to be set in order to compute the advance of the interface. The position of the appropriate segment terminations depends on the normal exterior vector and on the position of the surrounding cells with ice. For instance, for cells such as (0.6, 0.125) of figure 95a, VB is considered in the same position as VT in cell (0.6, 0.1) and VL is 0.125 plus the ice growth rate. This is an example of a case where the cell giving ice has an interface with m_x and m_y greater than zero. Cases with different signs for the normal vectors are solved in a similar way.

If a cell receives ice from two different cells, some different cases must be distinguished depending on their distribution on the mesh. Figures 96a, b, c, d, f & e give an example of the different cases considered. In cases such as figure 96a, which is similar to cell (0.675, 0) in figure 95a, new ice will appear in the cell and the two ends of the segment representing the interface are VL and VR which are the same as VR of the left cell and VL of the right one respectively, and the m_y component of the normal vector will be positive.

Figure 96b is similar to the previous case. Here the ends of the new segment are VT, at the same position as VB in the top cell, and VB which is placed at the same location as VT in the lower cell. The normal exterior vector in this case has its m_x component greater than zero. The next four cases represent the moment when some ice enters a new cell but coming in via the corner. If figure 96c is considered, the new ice is placed in the top left corner and the boundary has as ending, the variables VT and VL which are, at the same position as VB of the upper cell and VR of the left cell respectively. For the three left cases, everything is analogous.

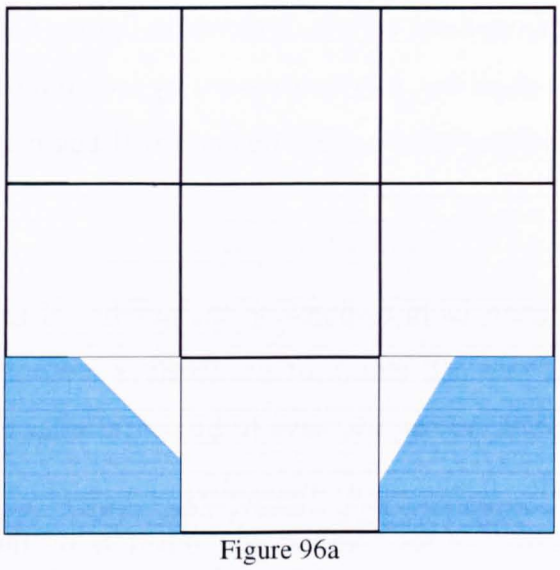

Figure 96a

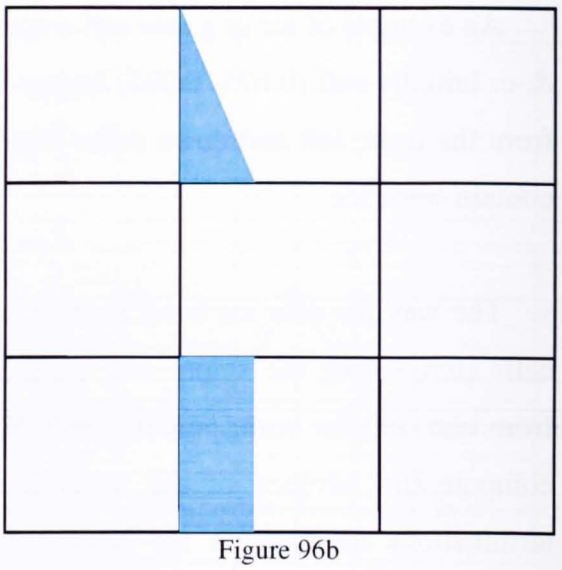

Figure 96b

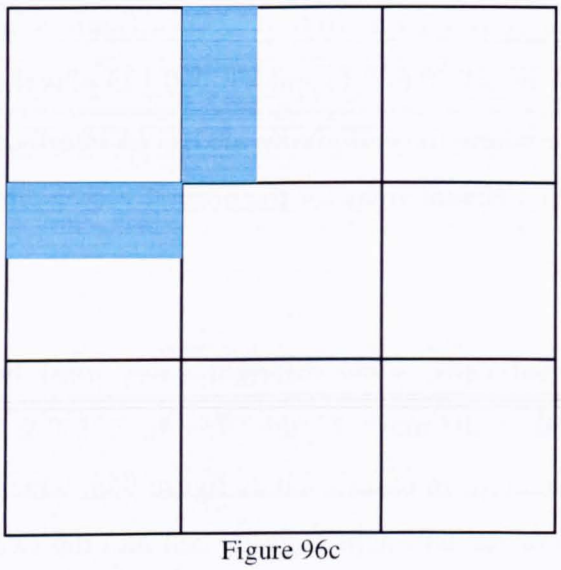

Figure 96c

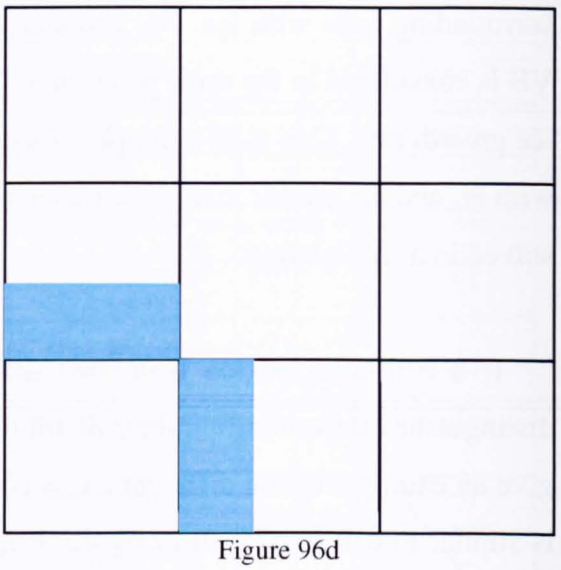

Figure 96d

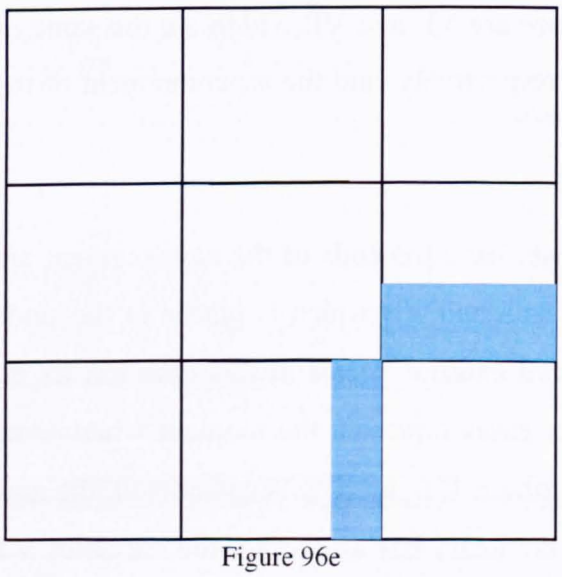

Figure 96e

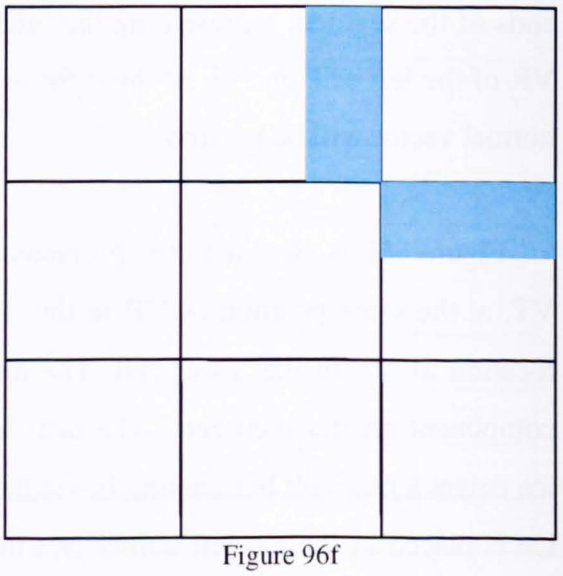

Figure 96f

Next figures 97a, b, c & d represent when new ice coming from three cells appears in another one which is empty.

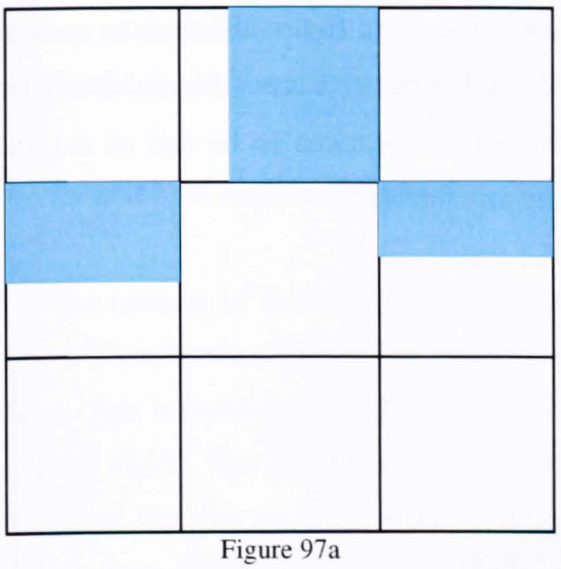

Figure 97a

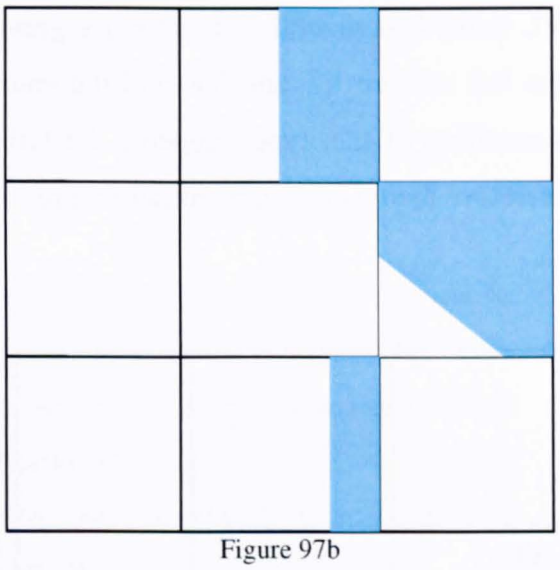

Figure 97b

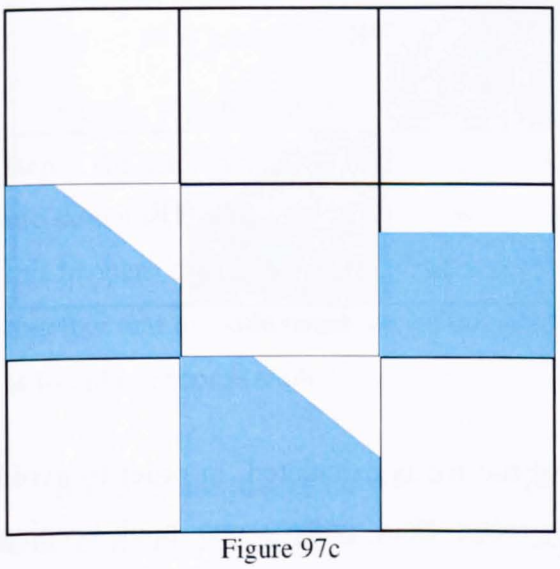

Figure 97c

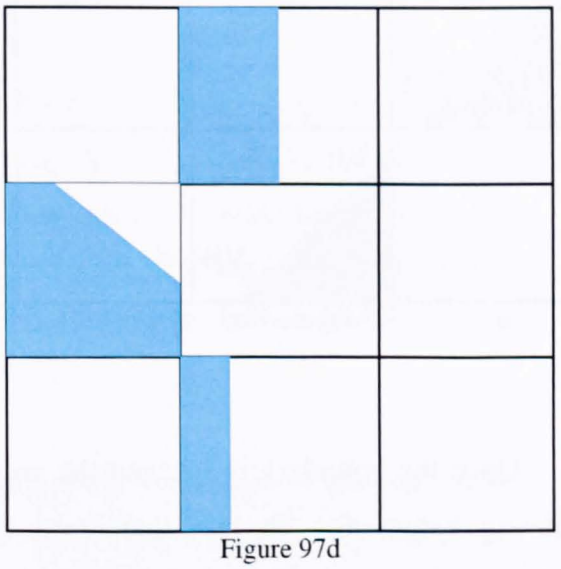

Figure 97d

All four cases work in the same way. Taking into account figure 97a, first, the normal exterior vector points downwards, i.e. m_y is negative. The endings of the segment representing the ice-liquid interface are VL, which is in the same position as VR in the left cell, and VR at the same place as VL in the right cell. The upper cell is covered immediately with ice.

If there is a case where an empty cell is surrounded by ice present in the four neighbouring cells, the ice will cover that cell immediately.

In addition, some further consideration has to be given particularly in cases like that in figure 98a. The ice in the cell placed at the bottom left has an interface with endings VT in the same position as VB in the left cell and VR in the same position as VL in the bottom cell. When the ice grows, we observe in figure 98b that the ends of the left cell are VT and VR and the ends of the bottom cell are VT and VR. When something of this type happens, the left bottom cell is taken to be full of ice and therefore there is no segment here representing any interface.

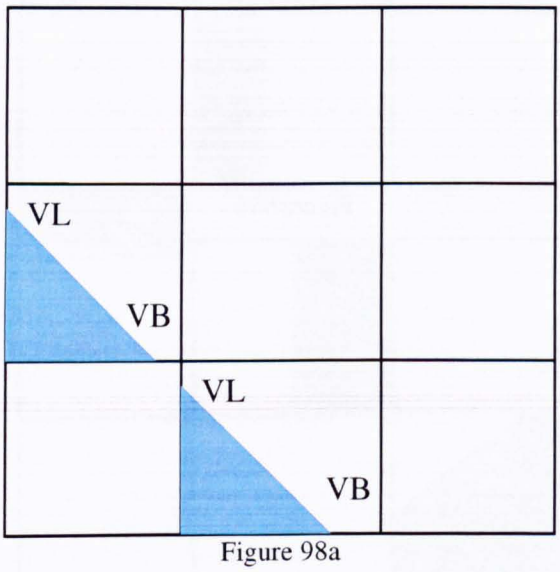

Figure 98a

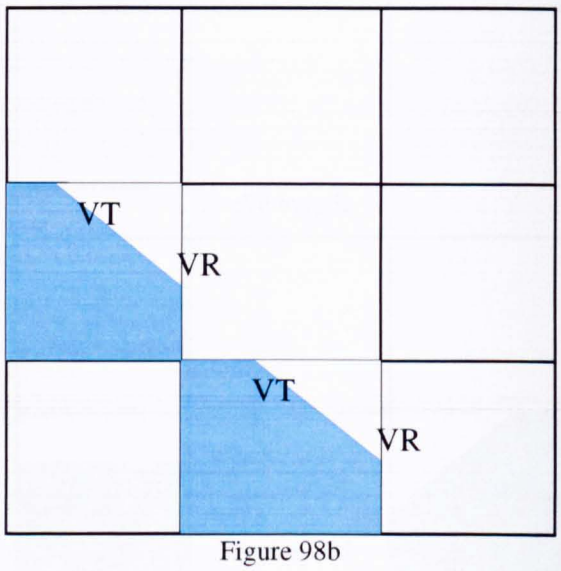

Figure 98b

Once the boundary is set, and the area of the ice is calculated, in order to avoid having values for Fh less than zero or greater than unity some book-keeping adjustments are made. The process used is similar to the one mentioned during the explanation of the VOF methods. To avoid roundoff errors a cell is considered empty of ice if Fh less than ε_{Fh} and full of ice if Fh is greater than ε_{Fh}. The value of ε_{Fh} is taken to be 10^{-6}.

The Solidification Computational Model Results.

The code predicts the temporal growth of the ice, which is set initially at the bottom of the domain, and the change of temperature as this ice growth takes place and the droplet impacts the water film.

Ice and Free Surface Evolution.

The advance of the ice is shown for the early stages of the impact. As shown in figure 84, at the first time step a rough ice layer is placed at the bottom of the water layer. This is represented by 50 triangles all of the same size and shape and assumed to be at -0.1°C. The top of the water film is slightly above the top of the ice layer and the water film has an initial temperature of 1°C. Also there is an oblate droplet at -10°C which is about to impinge on the film vertically.

Figures 99a, b, c, d, e & f show in detail the growth of the ice for the first time steps. The ice represented in these pictures is that which is placed on the left side of the domain. The change of the boundary is observed as the time steps advance. As this happens the temperature of the water film decreases. The segments move forward together and the volume of the ice increases within the layer. The tip of each triangle is found to become smoother as the time advances.

It is relevant that at the very first time steps the ice boundary recedes as can be seen in figure 100. After this, the ice-water interface grows continuously and grows faster in the areas where the temperature decreases more. These locations are particularly found where the droplet is in contact with the film or even the ice crystals.

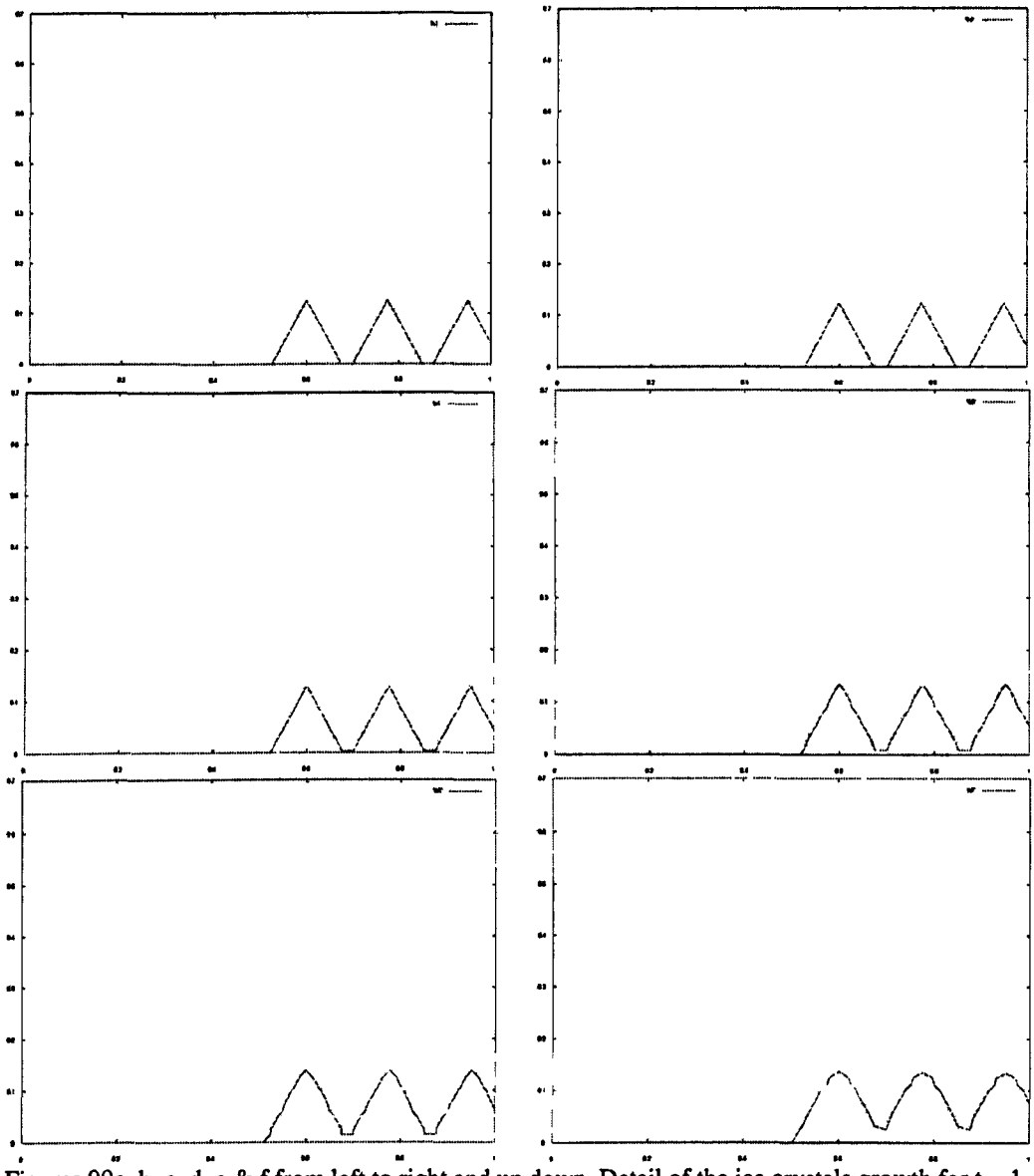

Figures 99a, b, c, d, e & f from left to right and up down. Detail of the ice crystals growth for t = 1, 2, 3, 4, 5, 6 and 7.

Figure 101 shows the different layers of ice as it grows in the domain. The effects of the lower temperature as time advances are reflected in the fact that, as it can be seen, the distance between the ice layers increases for higher times. Thus if the first layer is very close to the original ice-liquid interface, once the temperature drops, the last one is in comparison very separated from its previous position.

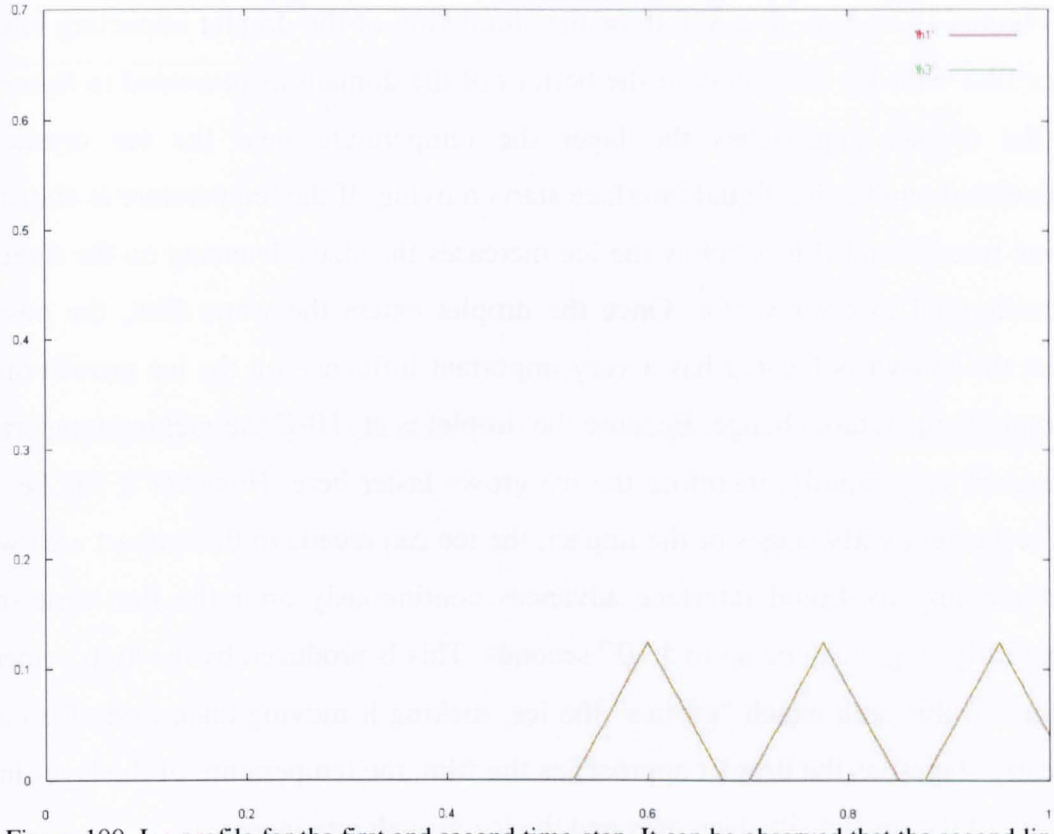

Figure 100. Ice profile for the first and second time-step. It can be observed that the second line (green) representing the crystal is below the first (red).

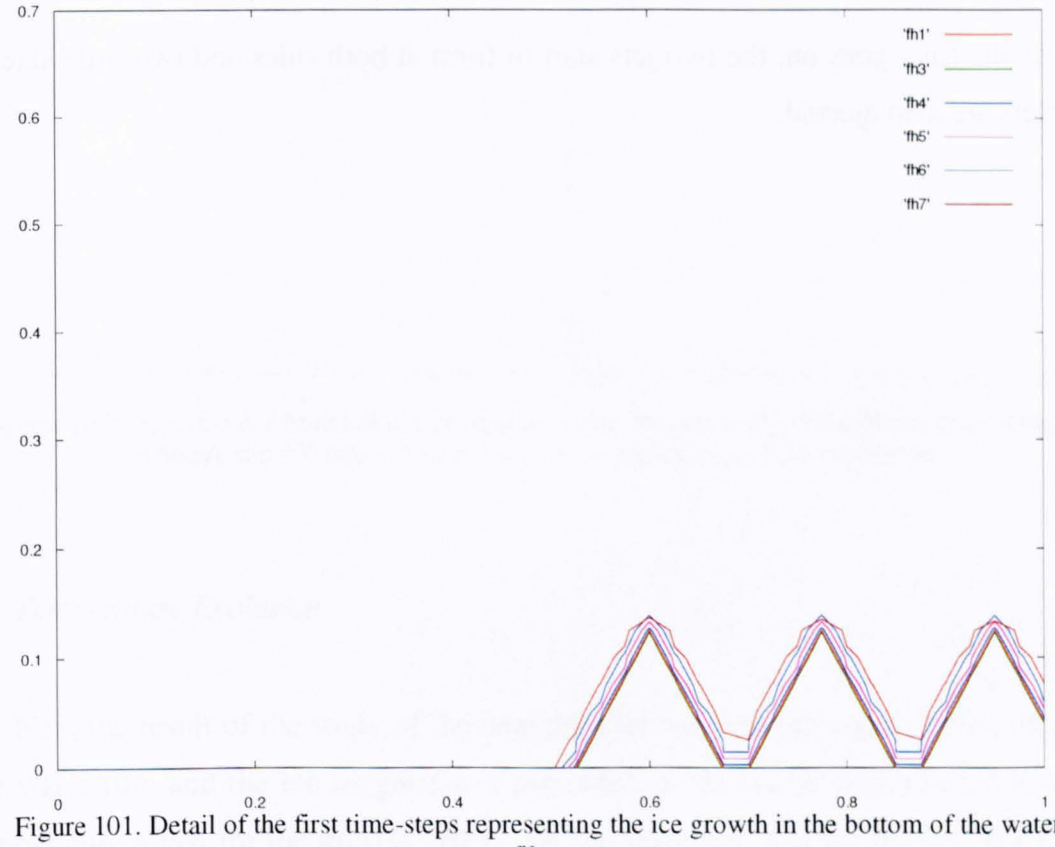

Figure 101. Detail of the first time-steps representing the ice growth in the bottom of the water film.

Figures 102a, b, c, d, e & f show the simulation of the droplet impacting into the water film with ice roughness in the bottom of the domain as presented in figure 84. As the droplet approaches the layer the temperature near the ice crystals is recalculated and the ice-liquid interface starts moving. If the temperature is above T_m, the ice recedes and if it is below the ice increases the size advancing on the direction of the normal exterior vector. Once the droplet enters the water film, the position where the impact is located has a very important influence on the ice growth due to the rapid temperature change. Because the droplet is at -10°C the melting temperature is reached very rapidly, therefore the ice grows faster here. However it can be seen that at the very early stages of the impact, the ice can recede in this impact area while the remaining ice-liquid interface advances continuously after the first time-steps. These early stages can be up to $5 \cdot 10^{-6}$ seconds. This is produced by the high velocities reached in this area which "pushes" the ice, making it moving backward. Thus after the early stages, as the droplet approaches the film, the temperature of the layer in the vicinity of the impact site decreases and the ice growth rate increases.

As the time goes on, the two jets start to form at both sides and two little satellite droplets are also ejected.

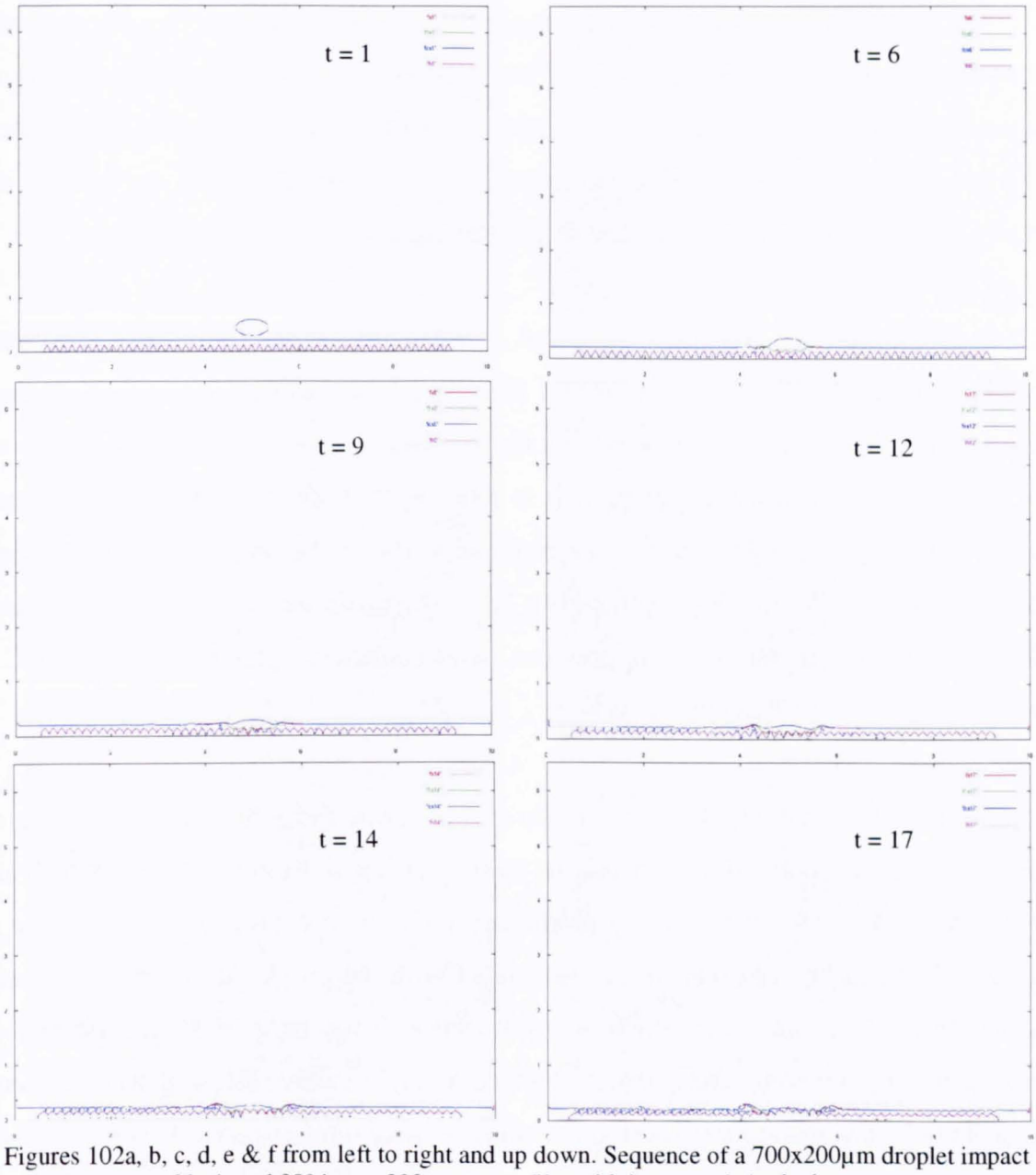

Figures 102a, b, c, d, e & f from left to right and up down. Sequence of a 700x200µm droplet impact at 66m/s and 90° into a 200µm water film with ice crystals in the bottom.

Temperature Evolution.

Next the result of the study of the heat transfer between the super-cooled droplet, the water film and the ice roughness is presented. It should be remembered that the temperature given for the drop is -10°C, for the layer 1°C and for the ice -0.1°C. At the three first time-steps it is difficult to see any important change in the ice growth as observed previously. However a slight cooling in the temperature is appreciated, especially in the base of the triangles representing the ice crystals and the top of them.

The most relevant change in the temperature is observed when the droplet starts entering the film. This behaviour has been observed only in another simulations considering ice roughness but not for cases run without it. As figure 38b illustrated, the super-cooled temperature of the droplet is rapidly transferred to the area of the water film closest to the droplet. The rest of the water layer is not affected.

As the number of time-steps increases, it can be seen in the figures the decreasing of the temperature in the areas around the ice crystals which allows the interface growth. In other hand, it is observed that the two jets at super-cooled temperature start to form in both sides of the droplet. It is relevant that, as difference with previous impacts that did not consider any ice roughness, the temperature of the droplet jets does not increase so quickly. Although it has to be taken into account that the water film is much colder than in these previous cases considered, this is, instead of 1°C a temperature of 10°C was considered.

As the splash starts to develop, the ice crystals grow faster and the temperature of the water film is cooled down, mainly in those areas away from the droplet which are less affected by the high velocities produced by the impact. From t = 12 a change is observed. It can be seen that the ice in contact with the droplet starts growing much faster and enters the drop which starts freezing. Thus by t = 20 the droplet is considered to be completely frozen and only the satellite drops that have been detached are assumed to be liquid and at super-cooled temperatures. This is observed until the end of the simulation.

These results can be observed in figures 103a, b, c, d, e, f, g & h. They illustrate the sequence of pictures showing the heat transfer during the droplet impact and splash.

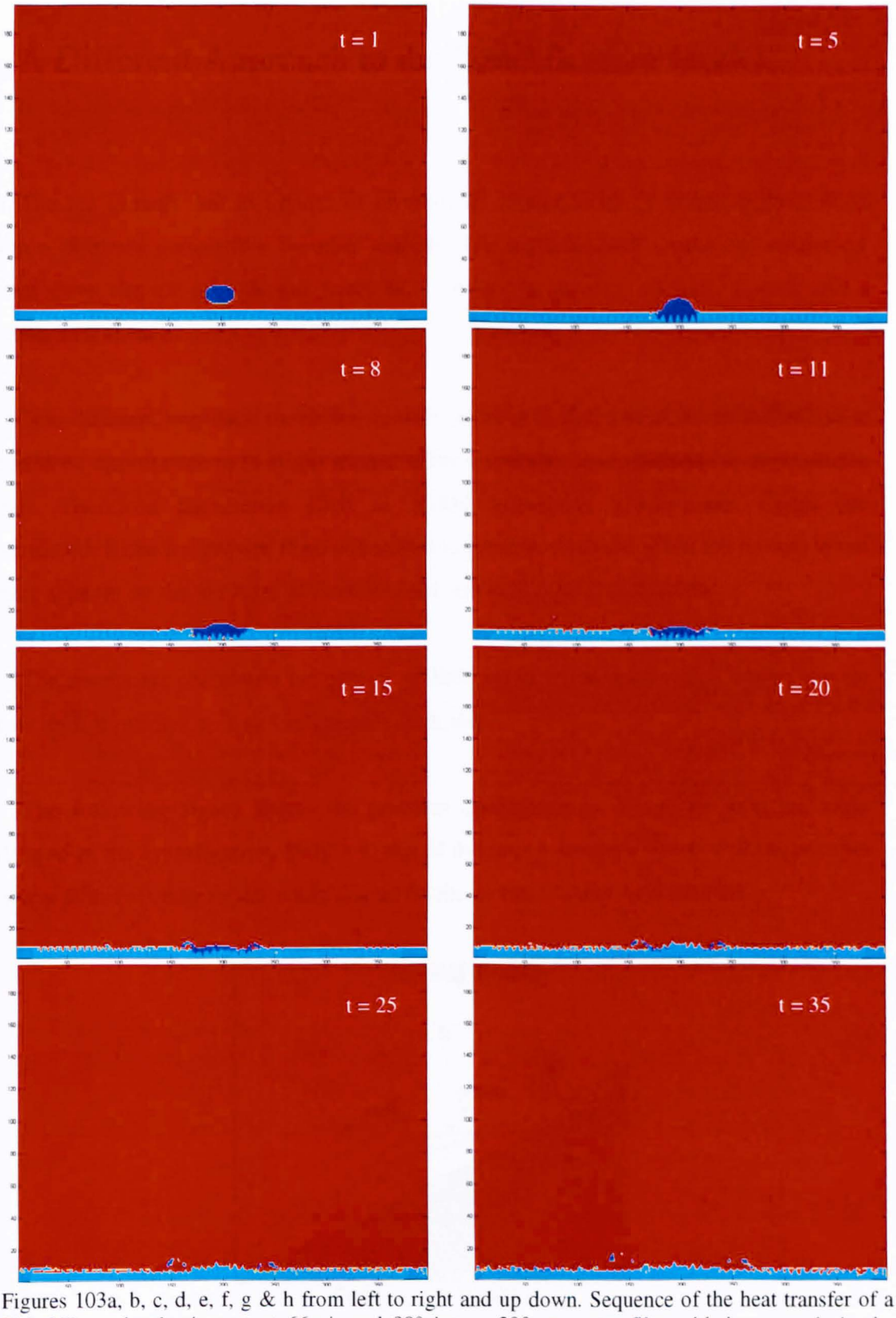

Figures 103a, b, c, d, e, f, g & h from left to right and up down. Sequence of the heat transfer of a 700x200µm droplet impact at 66m/s and 90° into a 200µm water film with ice crystals in the bottom.

A Different Approach to the Solidification Model.

The ice growth due to impact of droplets of super-cooled fluid has been tackled from a different perspective by other authors. The mathematical model and numerical result show the ice growth and water flow driven by gravity, surface tension, and a constant air shear.

This different approach to the ice growth problem is developed for an airfoil under conditions appropriate to in-flight icing and for a cylinder in conditions for atmospheric icing. Therefore parameters such as airfoil curvature, gravitational forces are considered. Rime ice growth if no water film is present. Also the glaze ice growth when water appears on the ice layer is modelled (Myers *et al.*, 2002 and 2004).

The results are calculated for periods of time up to 15 minutes which allows the ice grow until it reaches several centimetres thickness.

The following figure shows the problem configuration. It can be seen the scale attended in the investigation. Here a group of incoming droplets which will impact into a water film covering an ice shade placed on the airfoil is taken into account.

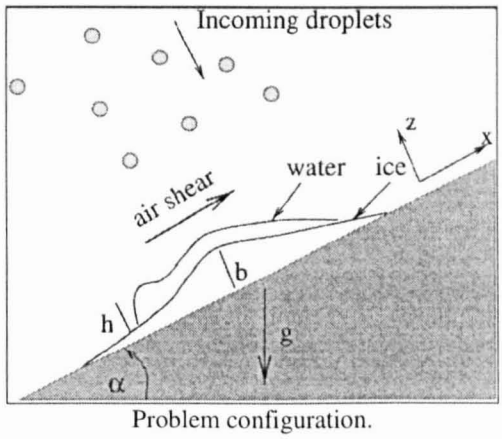

Problem configuration.

Therefore the results obtained by this model and numerical technique provide information about the ice shape in the whole airfoil as shown in the next figure.

PART IV: COMPARISONS AND CONCLUSIONS

Comparison between Experiments and Modelling.

The results of the droplet impacts obtained during the experiments and in the simulations are compared in this chapter. These comparisons are done considering impingements made under similar conditions, this is, considering droplets sizes in the same range, same water film thickness and angles of impact.

The temperature is not considered independently. This is included in the impacts made into the 50μm water film thickness.

Corona parameters comparison for impacts at 70° into a 150μm water film.

The corona height and the corona top and base width are compared for impacts made at 70° considering the 150μm water film.

Corona top width parameter comparison.

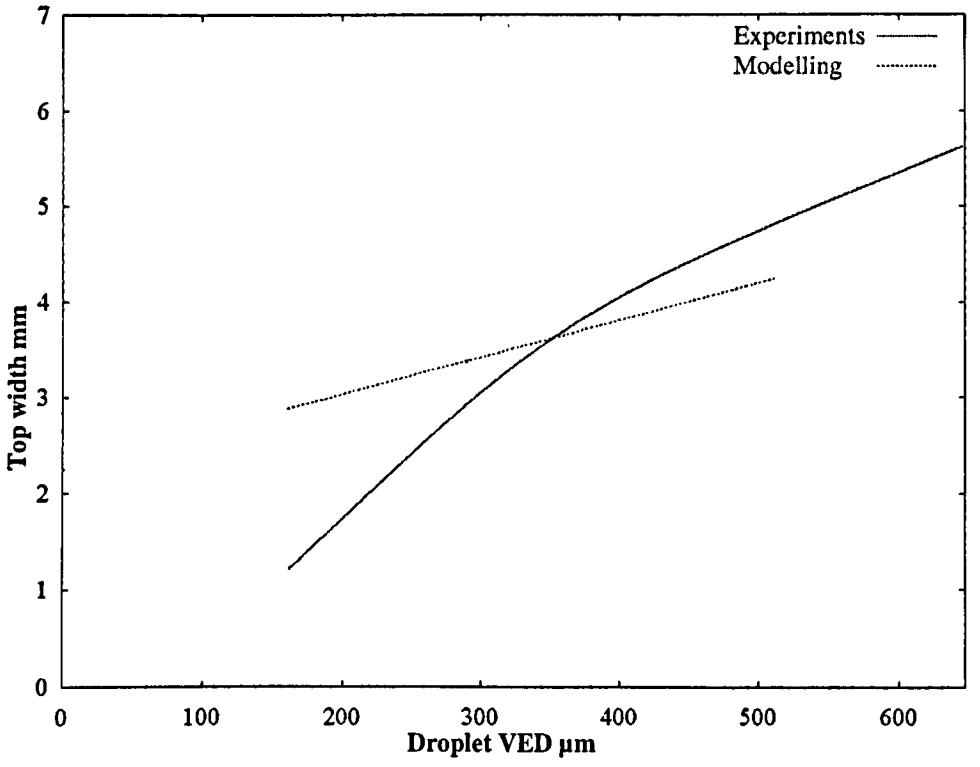

Graph 47. Comparison of corona top width for impacts into a 150µm film at 70° and ambient temperatures

Graph 47 shows that both, the results from the simulations and the experiments, give an increase of the top width of the corona as the droplet size increases. However this increase does not have always the same values for both cases. It can be seen that for the smallest droplets there is a difference up to one and a half millimetres between the experiments and the modelling, although this discrepancy is reduced as the VED of the impacting droplet increases. For medium size droplets the experimental values and the modelling values are very similar. For the biggest drops the results from the experiments is around 0.5 millimetre higher than in the simulation.

Corona base width parameter comparison.

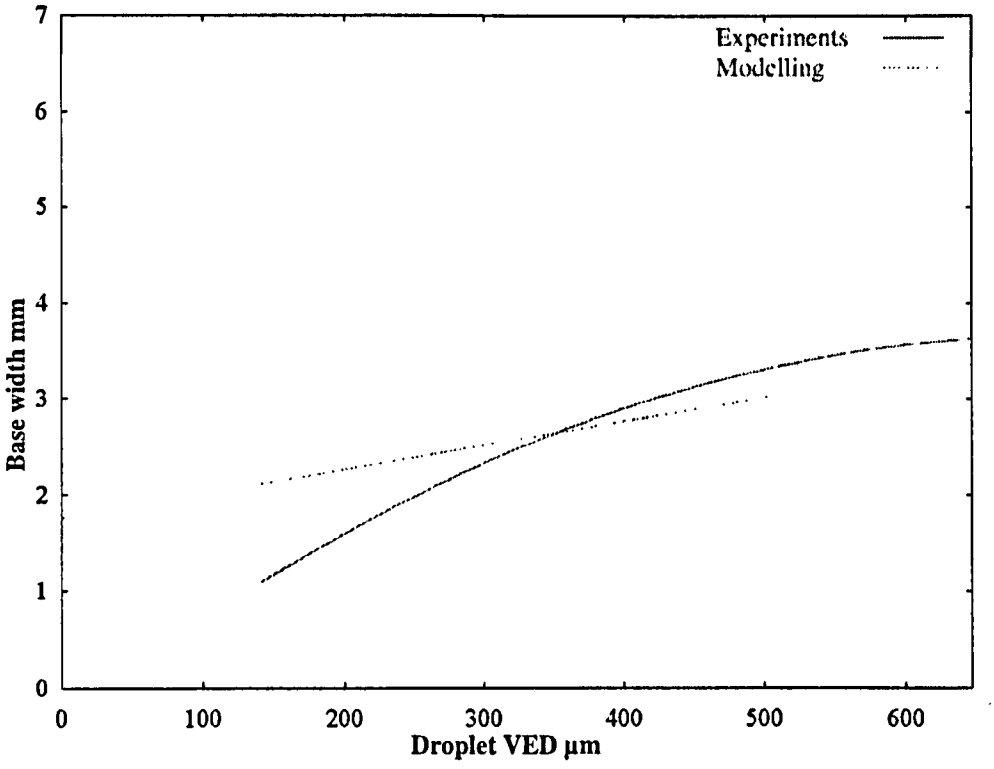

Graph 48. Comparison of corona base width for impacts into a 150µm film at 70° and ambient temperatures

Considering again the impacts at 70° into 150µm water film thickness, the base width of the coronas are compared. Graph 48 illustrates the evolution of the values of the base width parameter as the droplets VED increases. This graph shows again that there is in both cases an increase in the corona base width with the increasing droplet size. Also, as already happened for the top width parameter, the difference is more significant for the small droplet impacts. This variation in the results is nearly one millimetre for the impacts of small droplets, and less than half millimetre for the big. Again for the medium size droplets the experiments and modelling are more or less in agreement.

Corona height parameter comparison.

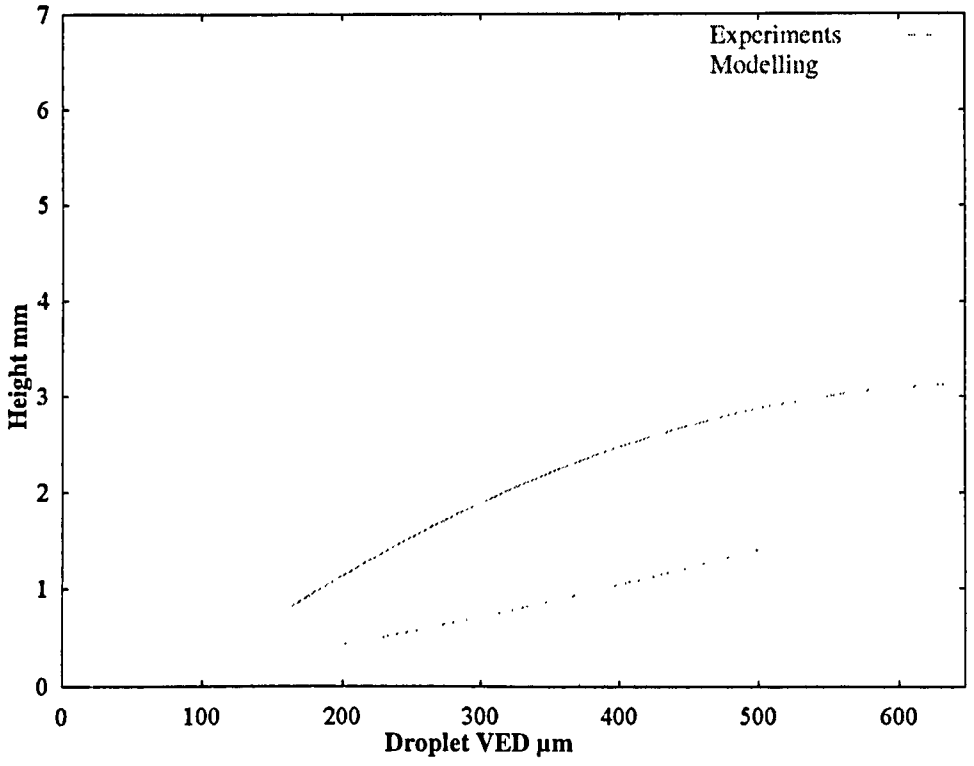

Graph 49. Comparison of corona height for impacts into a 150µm film at 70° and ambient temperatures

The comparison between the values for the corona height obtained from the experiments and the modelling is illustrated in graph 49. A steady increase of these values can be observed as the droplet VED increases for both sets of data. For this parameter it can be seen that the values found in the experiments are always higher than the values obtained from the simulations. This difference goes from half a millimetre for the smallest droplets to one millimetre and a half for the big drops.

Jets angle comparison for impacts at 70° into a 150μm water film.

It should be noticed that the droplet shown in the simulation is travelling from left to right whereas in the image of the actual droplet, the droplet is travelling from right to left. Because of this, the left angle of the corona in the experiments is compared with the right jet of the modelling and vice-versa. Thus, instead of angle formed by the left or right jet, the terms "big" angle for the angle formed by the right jet in the experiments and left in the simulations and "small" angle for the left jet in the experiments and right in the simulations are introduced.

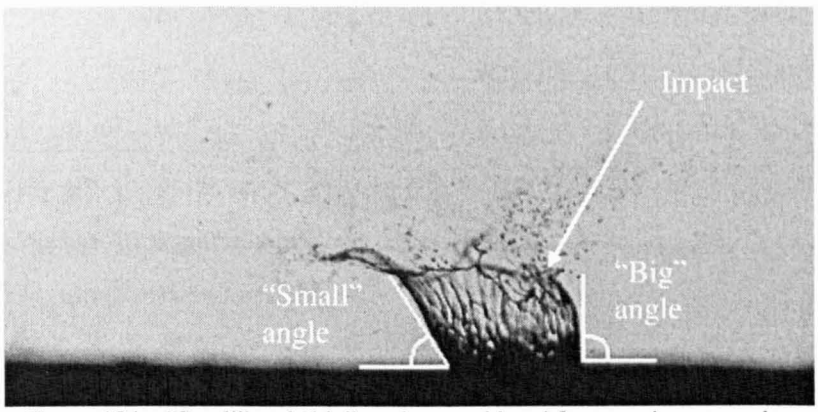

Figure 104a. "Small" and "big" angles considered for experiment results.

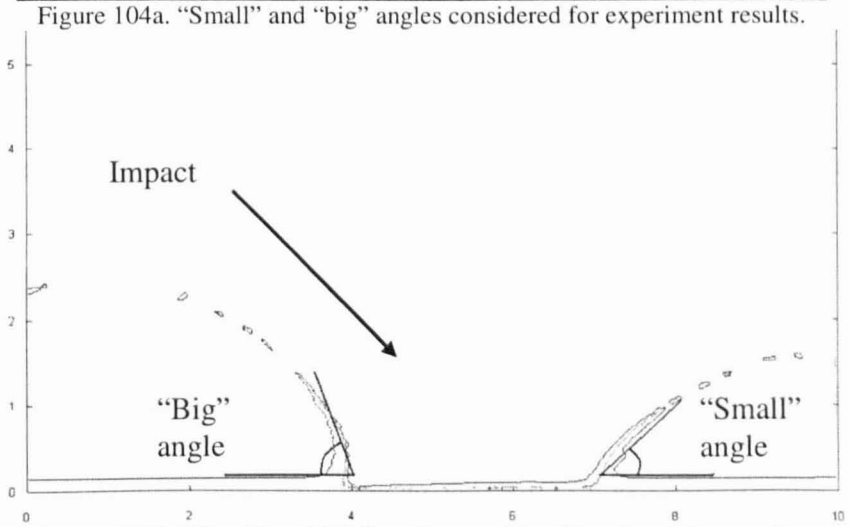

Figure 104b. "Small" and "big" angles considered for simulation results.

Big angle comparison.

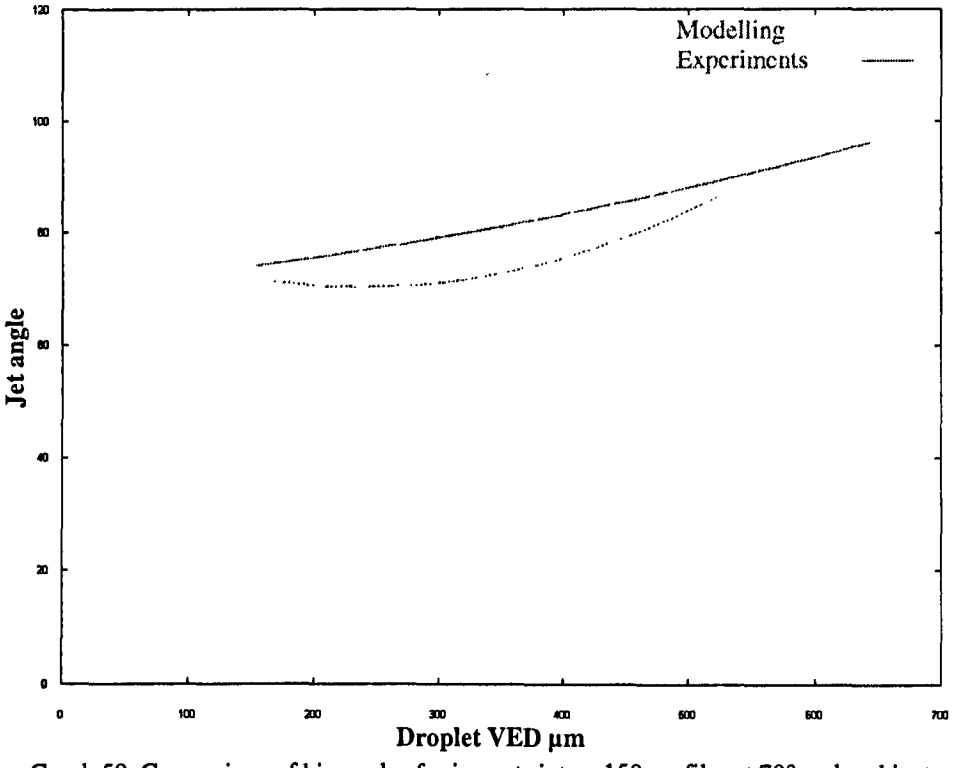

Graph 50. Comparison of big angles for impacts into a 150µm film at 70° and ambient temperatures.

Graph 50 illustrates the variation of the "big" angle formed by the jets as the droplet size increases in the impacts. It can be seen that there is a good agreement between experiments and simulations. The maximum difference found between both cases is around ten degrees for the impacts made by medium size droplets.

Small angle comparison.

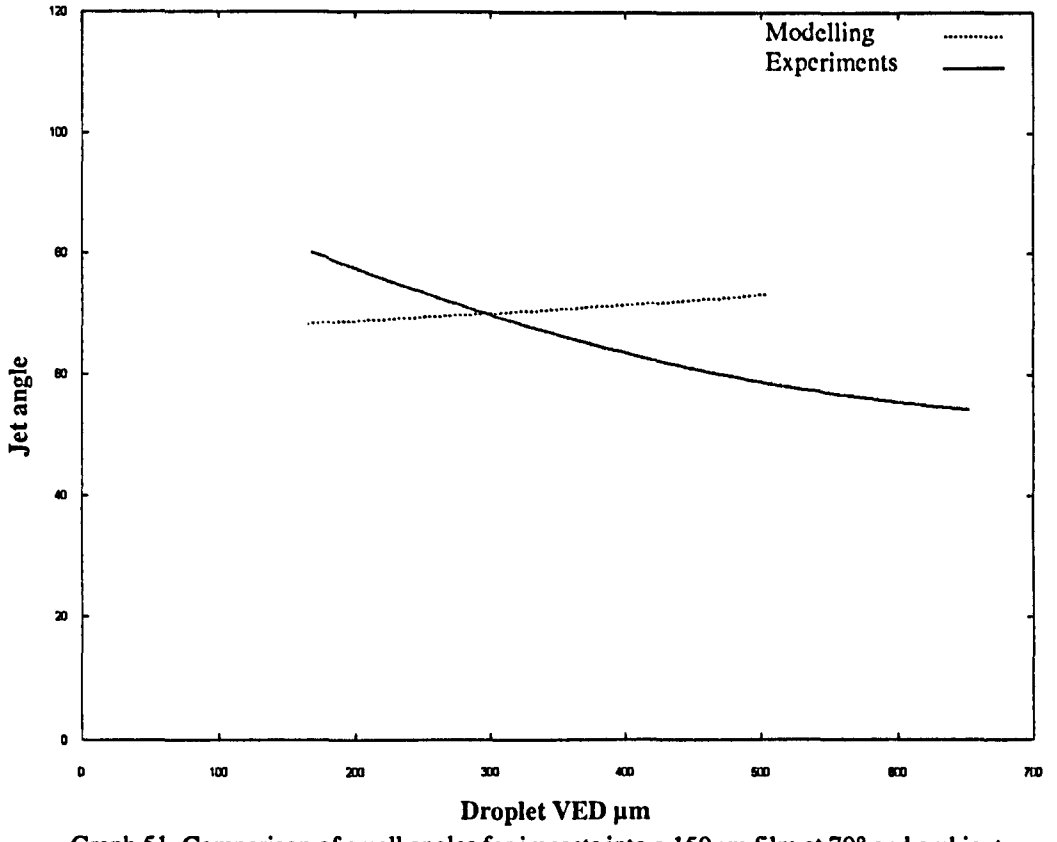

Graph 51. Comparison of small angles for impacts into a 150µm film at 70° and ambient temperatures.

Graph 51 shows the comparison between the modelling and the experiments for the small angle. In this case it is possible to see some significant differences, in particular for the impacts made by big droplets that can vary up to twenty degrees. For the impacts made by small droplets the difference is around ten degrees. It can also be seen that, as the values for the angles obtained from the modelling tend to increase slightly together with the droplet size, for the experiments the values decrease.

Jets velocity comparison for impacts at 70° into a 150μm water film.

Again, because the droplets are travelling in different directions in the experiments and the simulations, the nomenclature "big" and "small" are used. Thus, in order to provide the results of the velocities of the two different jets, it will be called velocity of the "big jet" to the velocity of the jet that forms a big angle with the water film and vice versa.

Big jet velocity comparison.

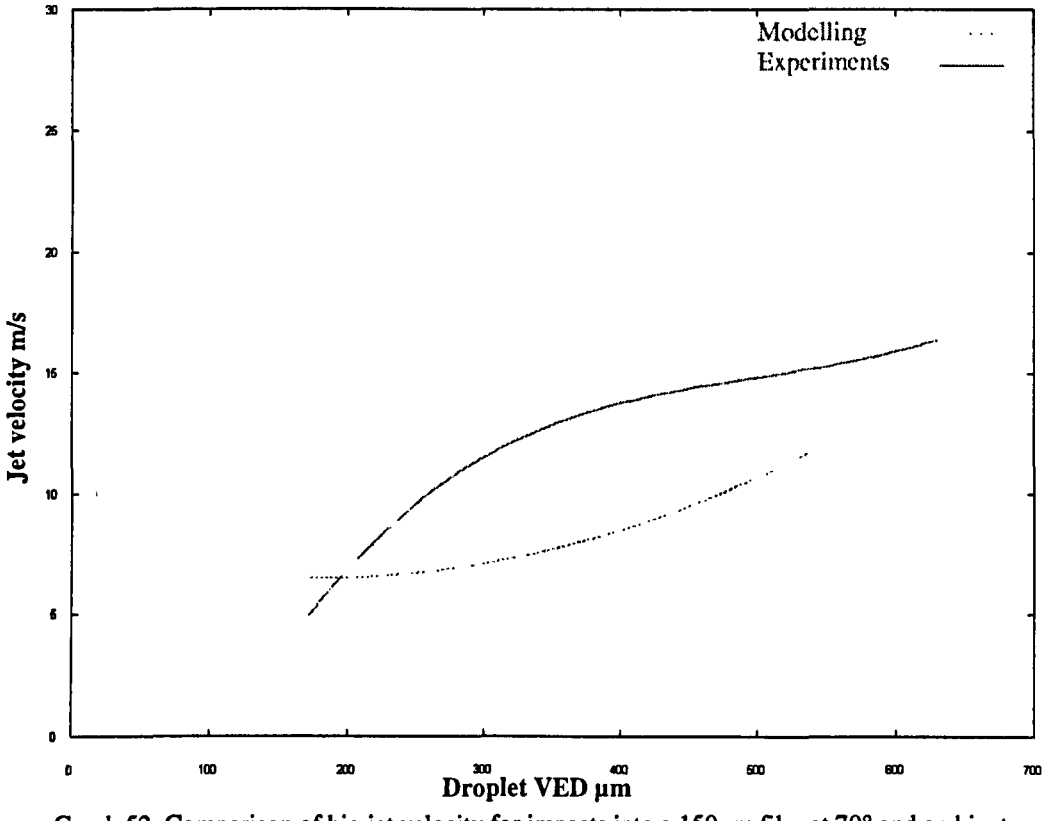

Graph 52. Comparison of big jet velocity for impacts into a 150μm film at 70° and ambient temperatures.

Graph 52 illustrates the increase of velocity for both jets together with the droplet size. The values for the experiments and simulations differ by less than 10m/s although for the small droplet impacts the results give similar values.

Small jet velocity comparison.

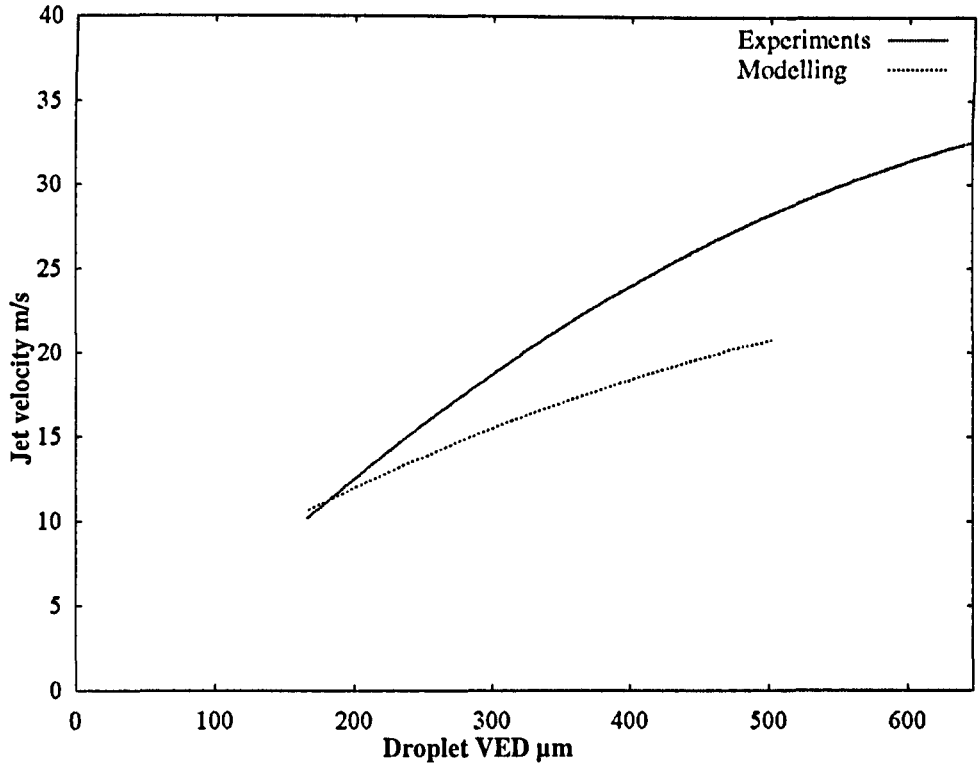

Graph 53. Comparison of small jet velocity for impacts into a 150µm film at 70° and ambient temperatures.

Both experiments and modelling show a good agreement in the results for the velocities of the jets that form a small angle with the water film (velocity of "small jet"). This agreement is particularly good for impingements of small droplets. The maximum disagreement is for impacts of the biggest droplets. For this case there is a difference of 10m/s.

Corona parameters comparison for impacts at 70° into a 50μm water film.

The corona height and the corona top and base width are compared for impacts made at 70° considering the 50μm water film thicknesses.

Corona top width parameter comparison.

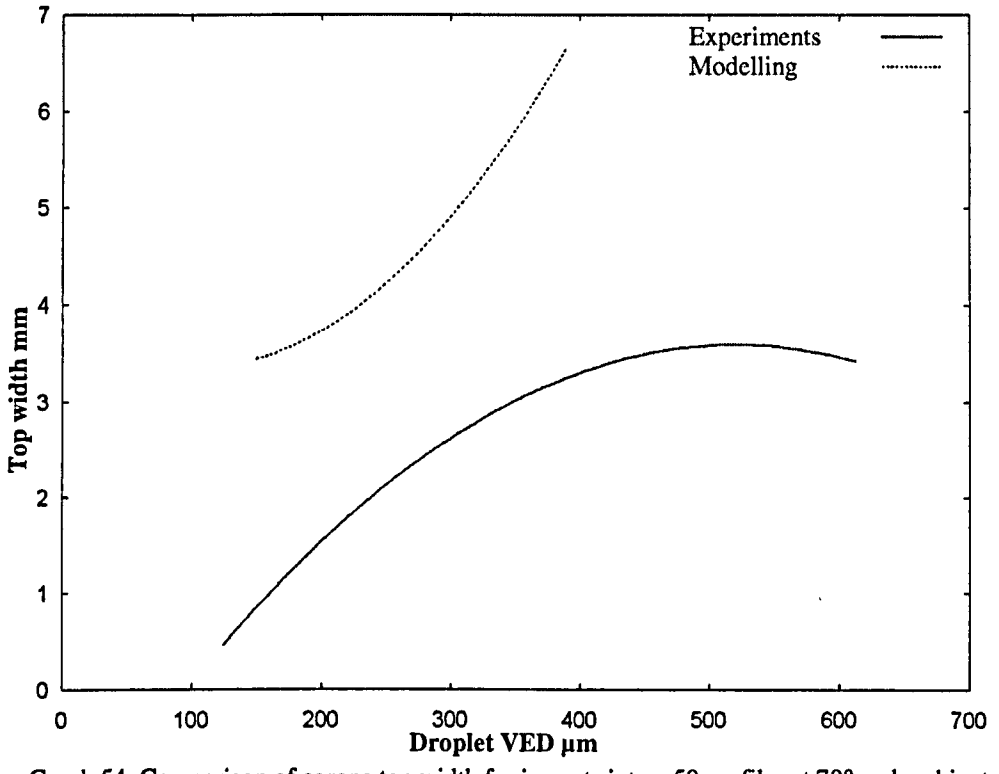

Graph 54. Comparison of corona top width for impacts into a 50μm film at 70° and ambient temperatures.

Graph 54 illustrates the differences in the results for the corona top width. It can be seen that the best agreement is found for droplets with 300μm VED although a difference of nearly 3 millimetres is observed. These results show that the top of the corona is wider in the simulations that in the experiments. The values of this parameter can be even twice in the results coming from the model than in the experiments.

Corona base width parameter comparison.

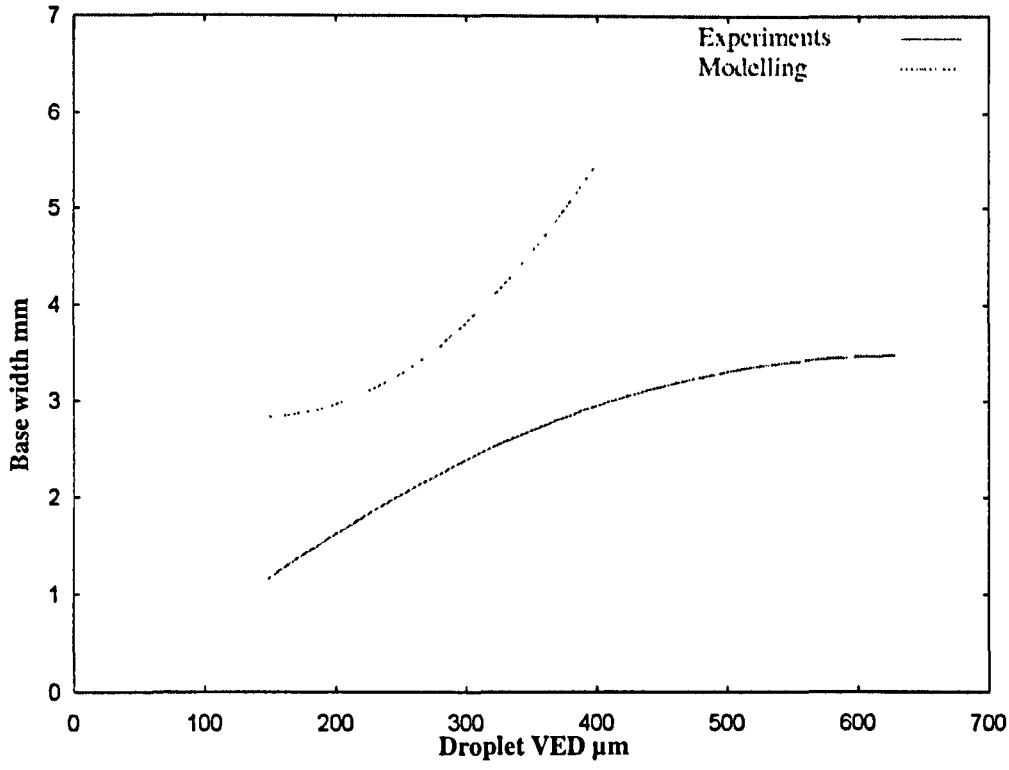

Graph 55. Comparison of corona base width for impacts into a 50µm film at 70° and ambient temperatures.

The comparison between of the values of the corona base width between the model and the experiments reflects a similar behaviour for the curves than in the previous case. The values for the parameter are higher in the simulations than in the experiments. For the impacts of 300µm droplets size the difference is around one millimetre although for bigger droplets is more than two millimetres.

Corona height parameter comparison.

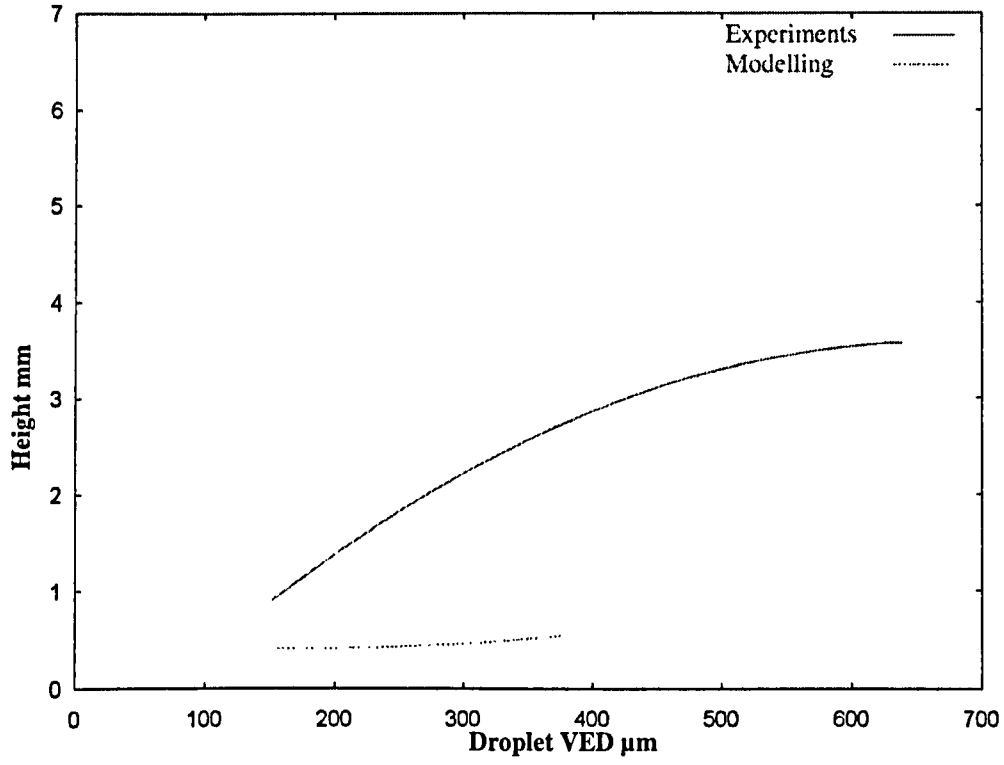

Graph 56. Comparison of corona height for impacts into a 50µm film at 70° and ambient temperatures.

The results for the comparison of the corona height parameter illustrated in graph 56 show that, as the values from the experiments increase significantly with droplet VED but the increase of the values from the simulation is very low. Thus, differences of half a millimetre for the small droplets impact are obtained. For the big droplets impact it can be up to two millimetres.

Jets angle comparison for impacts at 70° into a 50μm water film.

Big angle comparison.

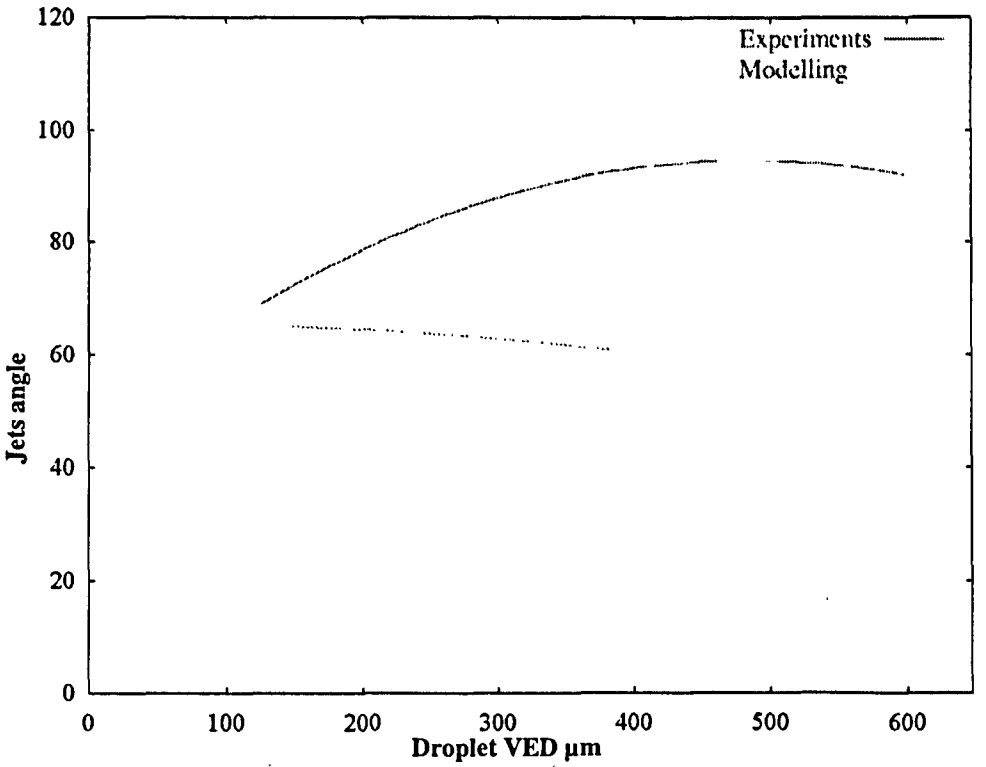

Graph 57. Comparison of big angles for impacts into a 50μm film at 70° and ambient temperatures.

Graph 57 show that for impacts of small droplets there is a good agreement between experiments and simulations. However, as the droplet size increases, the differences can be up to 30 degrees.

Small angle comparison.

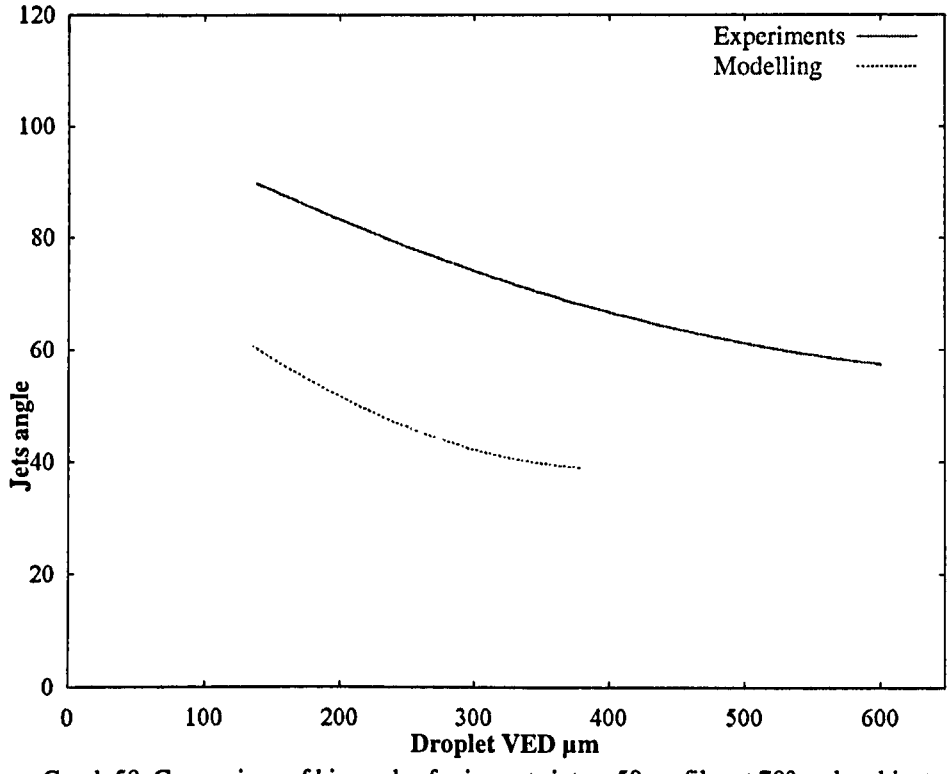

Graph 58. Comparison of big angles for impacts into a 50µm film at 70° and ambient temperatures.

Graph 58 shows a very similar behaviour between the results obtained from the experiments and from the modelling. However there is an important difference, the values obtained for the angles differ continuously by approximately 30 degrees.

Jets velocity comparison for impacts at 70° into a 50μm water film and ambient temperatures.

Big jet velocity comparison.

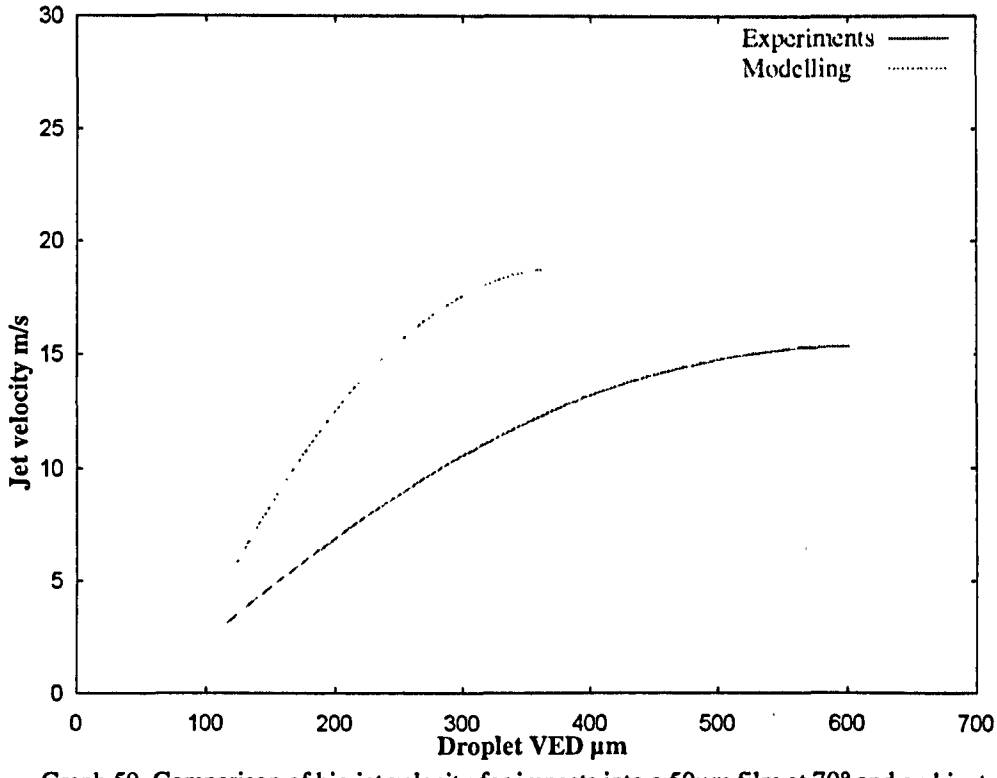

Graph 59. Comparison of big jet velocity for impacts into a 50μm film at 70° and ambient temperatures.

Graph 59 shows a similar increase of the values of the jet velocity for the modelling and the experiments. For the impacts of the small droplets there is a difference of 5m/s between both cases and for the impacts of the bigger droplets that difference can be up to 8m/s.

Small jet velocity comparison.

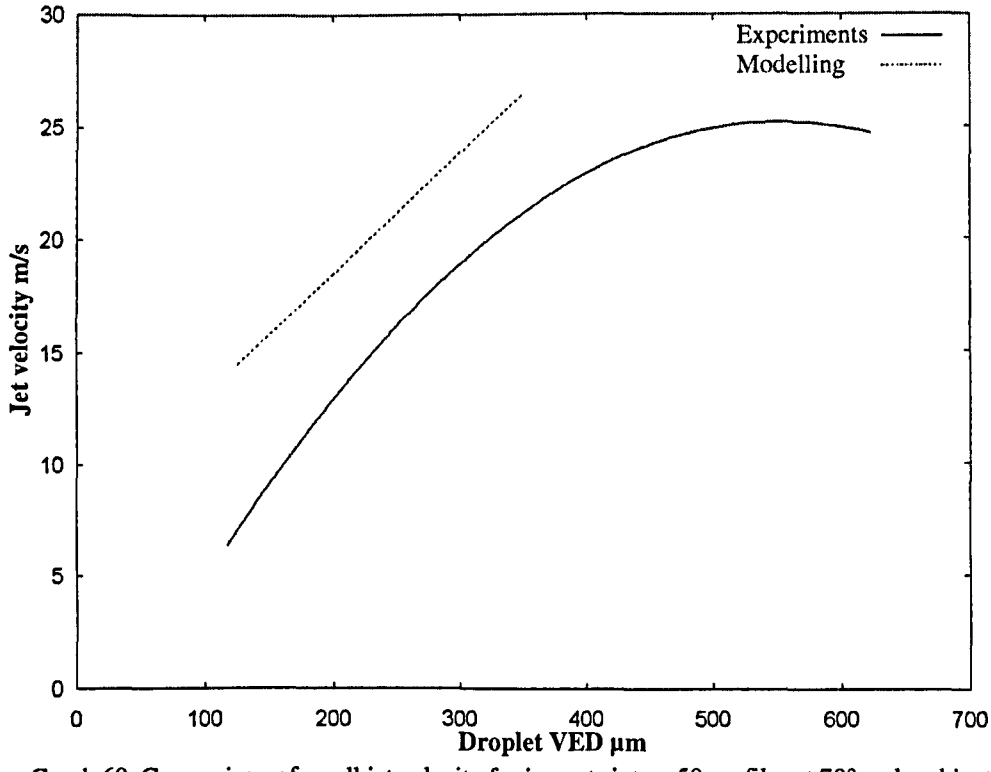

Graph 60. Comparison of small jet velocity for impacts into a 50µm film at 70° and ambient temperatures.

For the range of droplets sizes where a comparison between experiments and modelling is possible, the results show that in both cases there is an increase of the values of the velocity as a function of the droplet VED with a difference of 10m/s.

Corona parameters comparison for impacts at 45° into a 50μm water film.

The corona height and the corona top and base width are compared for impacts made at 45° considering the 50μm water film thicknesses. Because of the low number of impacts made at 45° and 20°, it should be noted that the comparisons might not always reflect a definitive result. Sometimes there are only two values for the parameters analysed which is not sufficient to get a definitive trend line and consequently, to support a strong conclusion.

Corona top width parameter comparison.

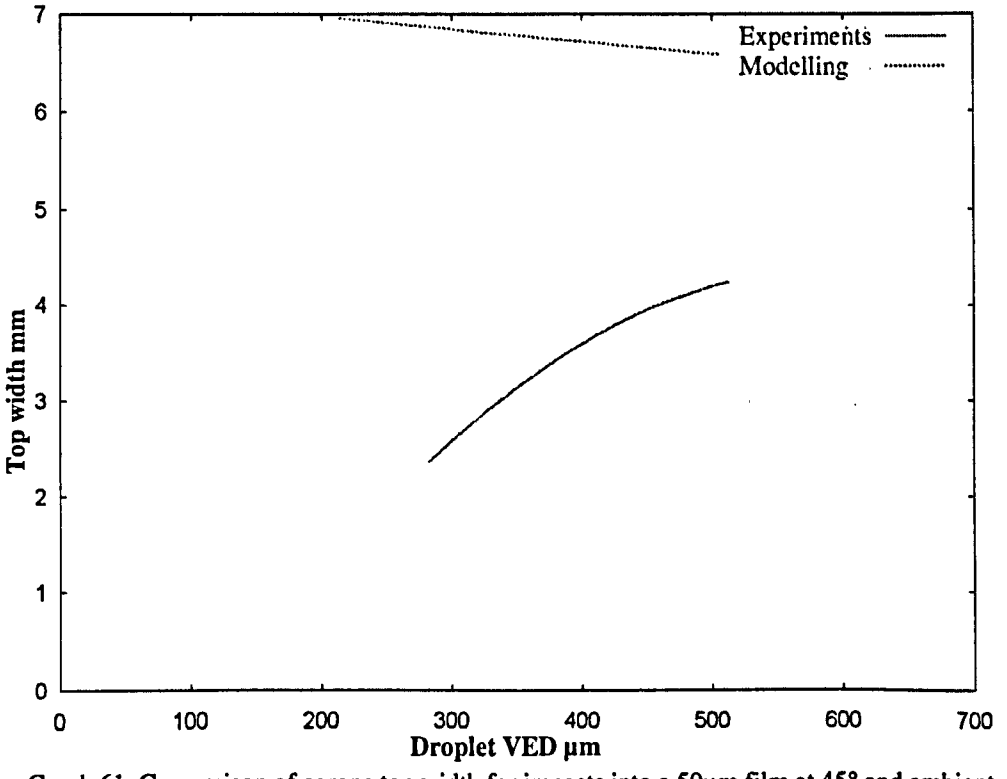

Graph 61. Comparison of corona top width for impacts into a 50μm film at 45° and ambient temperatures.

Graph 61 shows a different behaviour for the results of the experiments and the model. As the values of the corona top width for the experiments increase with the increasing of the droplets size, for the simulation it is found to decrease. Also the values are very different between both cases. The closest approach is found for the impacts of the biggest droplets which give a difference of two millimetres.

Corona base width parameter comparison.

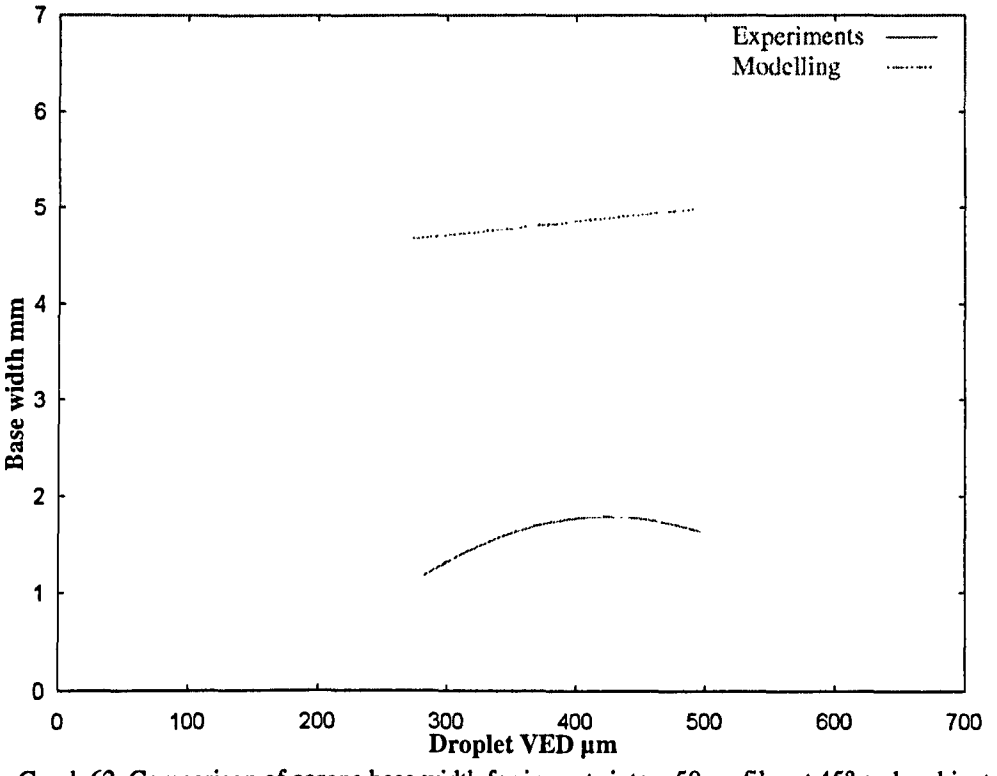

Graph 62. Comparison of corona base width for impacts into a 50µm film at 45° and ambient temperatures.

Graph 62 shows that, besides the difference of the values of results obtained through the simulations and the experiments, an increase can be seen in the values of the corona base width as the droplet VED increases. However the difference found between both cases is about 3 millimetres.

Corona height parameter comparison.

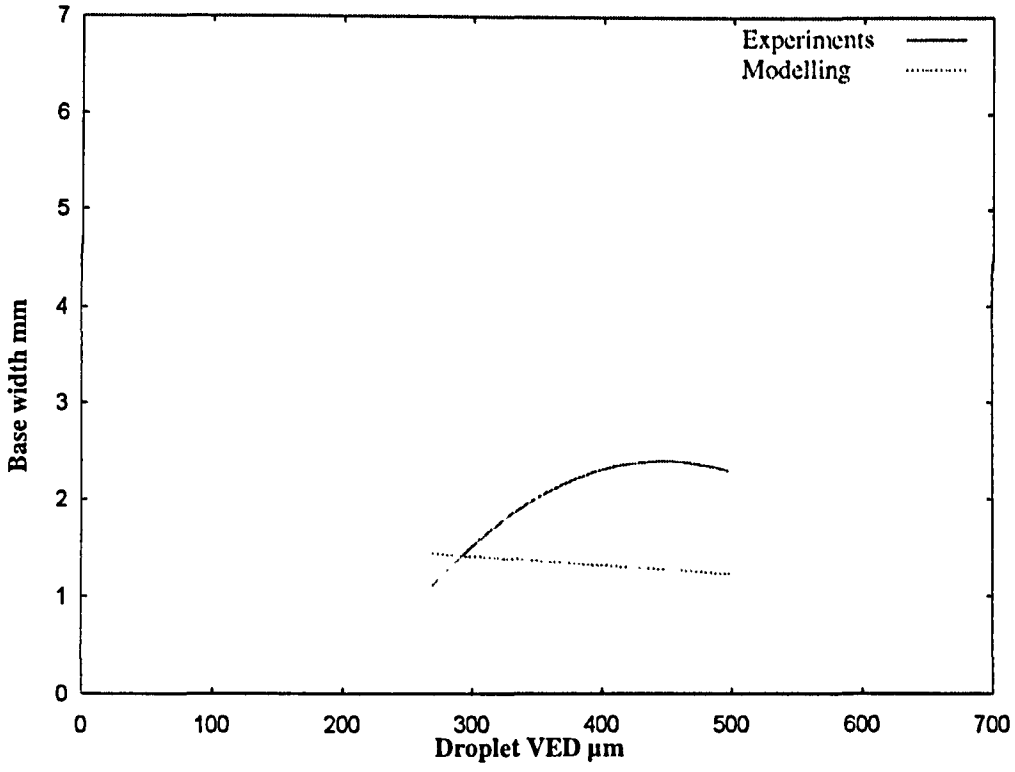

Graph 63. Comparison of corona height for impacts into a 50µm film at 45° and ambient temperatures.

The values for the corona height differ by as much as one millimetre. The higher results are obtained in the experiments especially for the biggest droplets. For the small droplets the results give similar values. However as the droplet size increases the values of this parameter decrease in the model but increases for the experiments.

Jets angle comparison for impacts at 45° into a 50μm water film.

Big angle comparison.

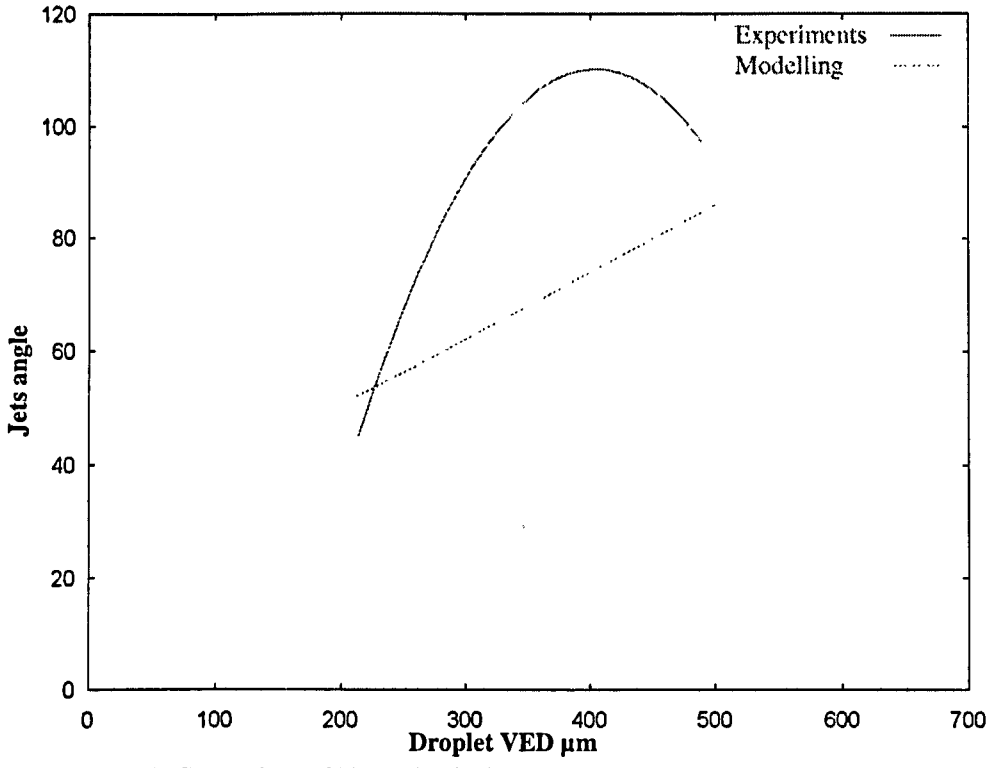

Graph 63. Comparison of big angles for impacts into a 50μm film at 45° and ambient temperatures.

Agreement can be seen between the experiments and the modelling for the impacts of small and big droplets. There is a significant disagreement for impacts made by 400m droplet size, although this observation could be a consequence of the low number of impacts recorded and the reliability of the experimental data.

Small angle comparison.

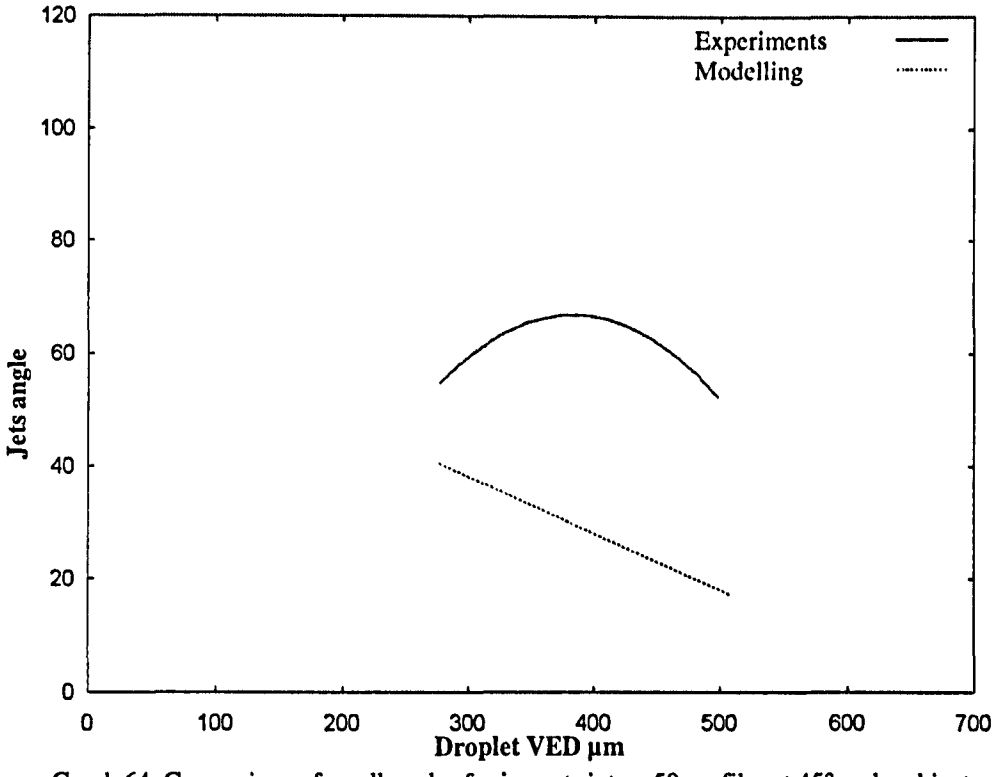

Graph 64. Comparison of small angles for impacts into a 50µm film at 45° and ambient temperatures.

Graph 64 shows that a decrease of the values for the "small" angle can be observed in the experiments and the simulations as the droplet size increases. The difference between the two cases goes from 10 degree for the small droplets impact to more than 20 for the biggest.

Jets velocity comparison for impacts at 45° into a 50μm water film and ambient temperatures.

Big jet velocity comparison.

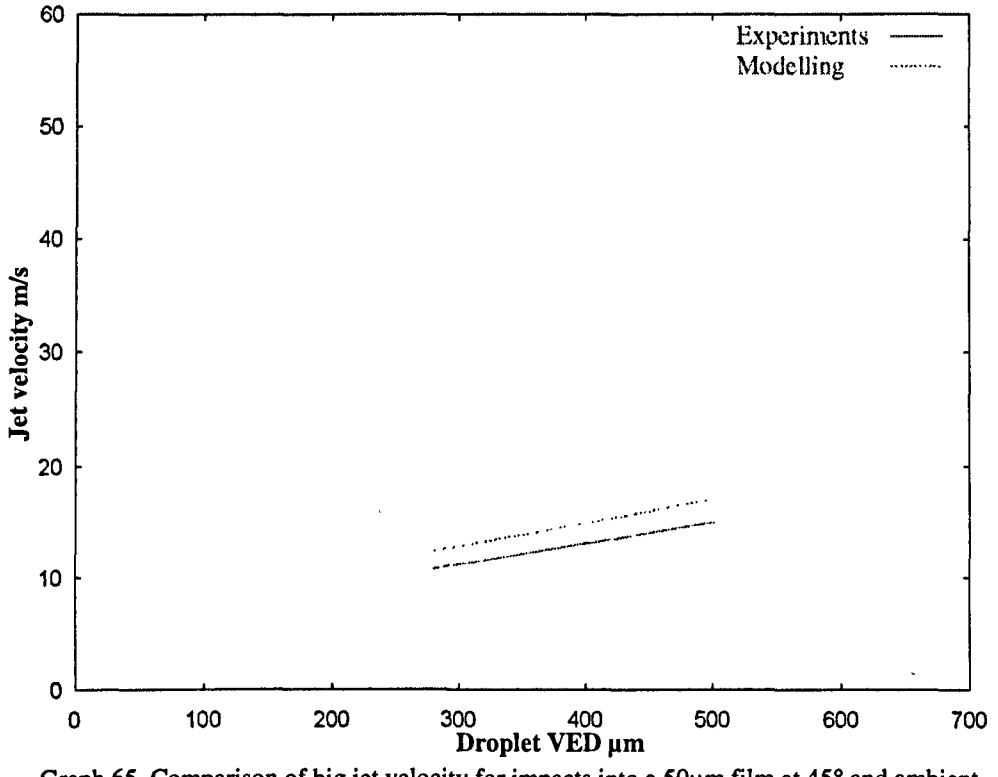

Graph 65. Comparison of big jet velocity for impacts into a 50μm film at 45° and ambient temperatures.

The similarity between both results shown in graph 65 is remarkable. In both cases there is an increase of the values for the velocity and in the same range of values. The difference is less than 5m/s.

Small jet velocity comparison.

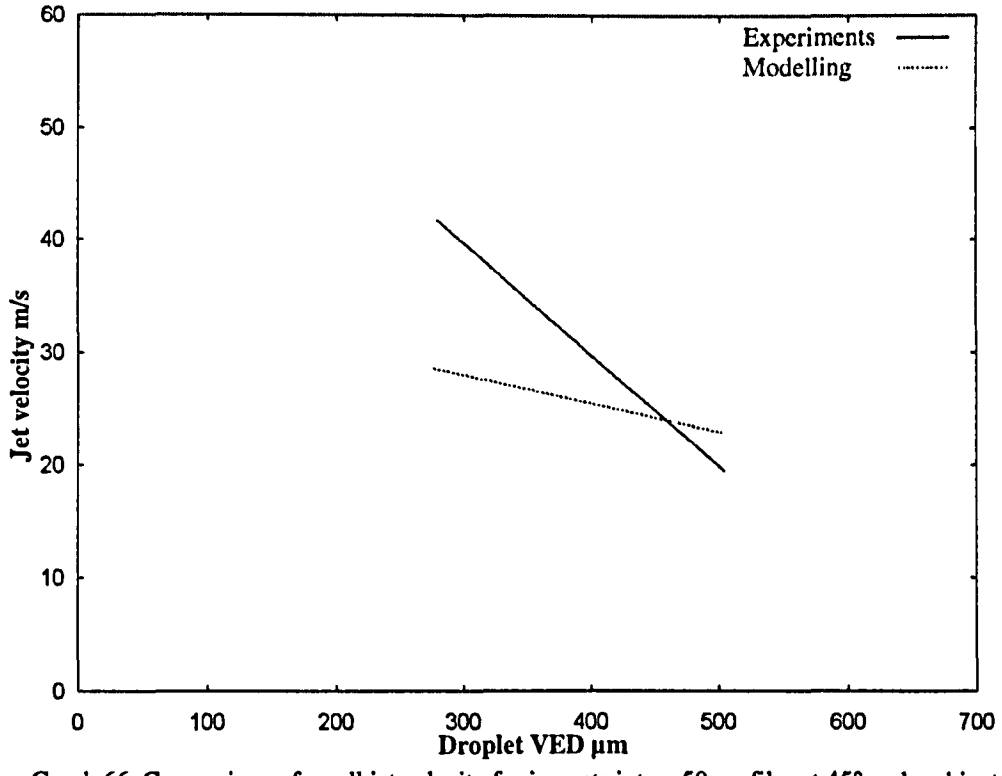

Graph 66. Comparison of small jet velocity for impacts into a 50µm film at 45° and ambient temperatures.

The velocity of the jet that forms the small angle with the water film decreases in the experiments and the simulations as the droplet VED increases. Although the agreement of the values is not as good as in the previous case, it can be seen that the most relevant differences are found for the impacts of the smallest droplets. The values of the velocity can differ by 10m/s, although this variation is reduced as the droplet size increases.

Corona parameters comparison for impacts at 20° into a 50μm water film.

The corona height and the corona top and base width are compared for impacts made at 20° considering the 50μm water film thicknesses.

Corona top width parameter comparison.

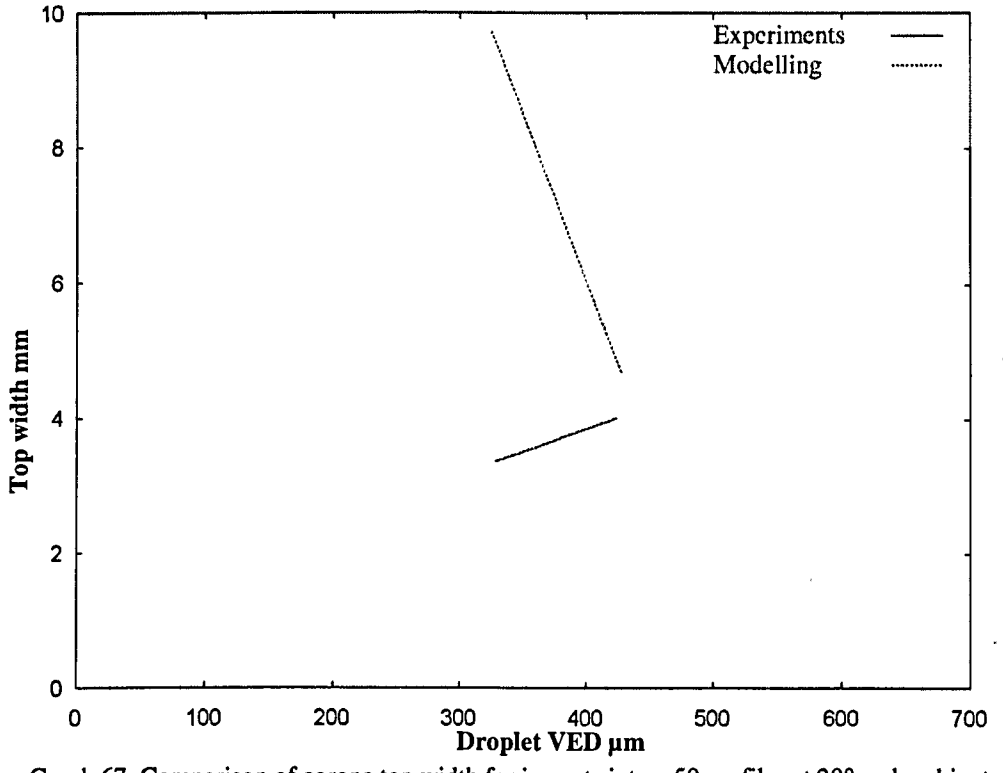

Graph 67. Comparison of corona top width for impacts into a 50μm film at 20° and ambient temperatures

The results shown in graph 67 give different tendencies and values for the evolution of the top width of the corona with the increase of the droplet VED. The most significant differences are for the smaller droplets and the best similarity is found for the bigger ones where there is a variation of one millimetre.

Corona base width parameter comparison.

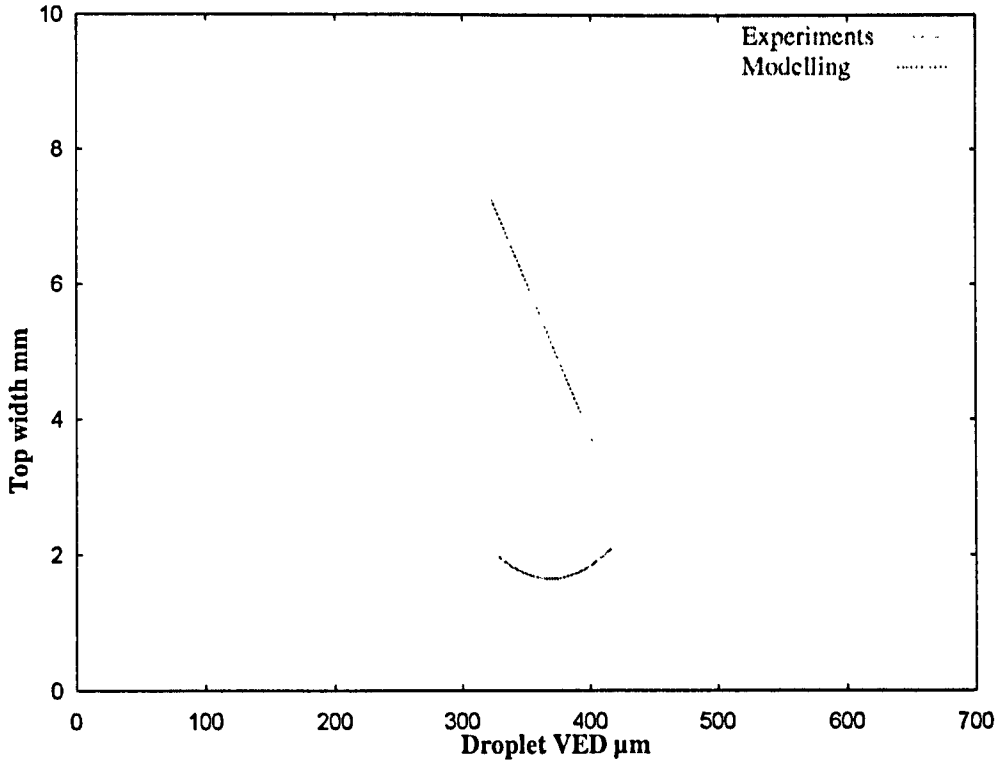

Graph 68. Comparison of corona base width for impacts into a 50µm film at 20° and ambient temperatures

As happened in the previous case, the results from the modelling decrease dramatically as the droplet size increases. Also the values for this parameter differ significantly with the results obtained from the experiments. This difference is found again mainly for the corona with impacts of the small droplets.

Corona height parameter comparison.

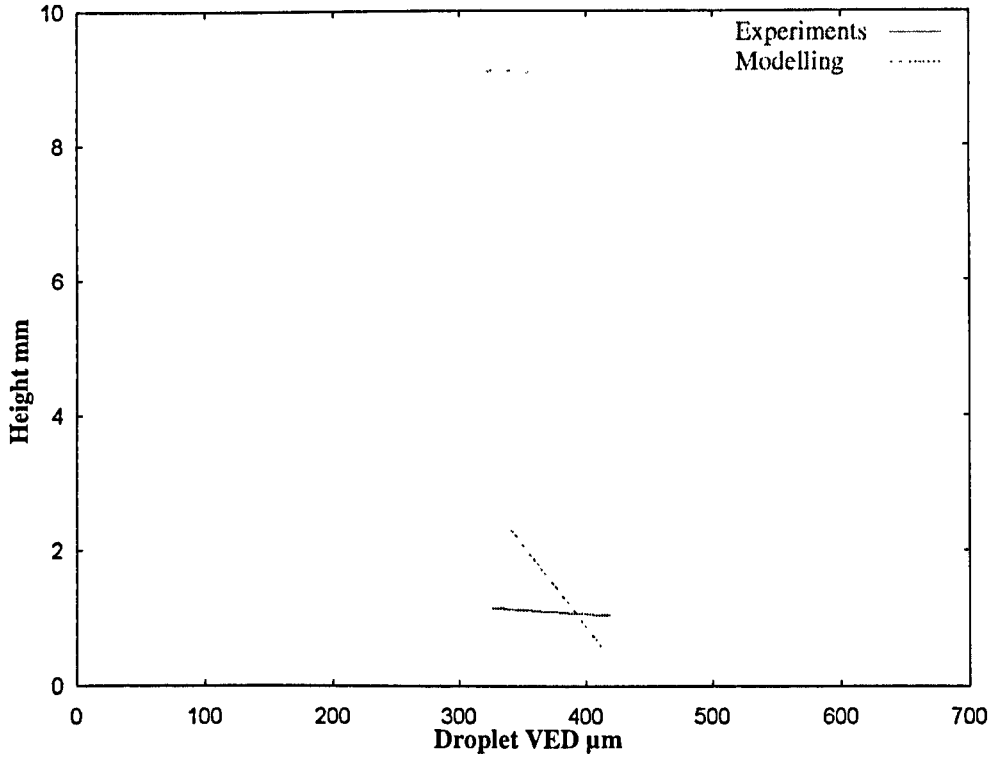

Graph 69. Comparison of corona height for impacts into a 50µm film at 20° and ambient temperatures

The results in graph 69 show a decrease of the values of the corona height as the droplet size increases. In this case the difference is low in comparison with the two previous parameters analysed.

The impacts made at 20° are the only ones found that show greater values for the height in the simulations compared with the experiments.

Jets angle comparison for impacts at 20° into a 50μm water film.

Big angle comparison.

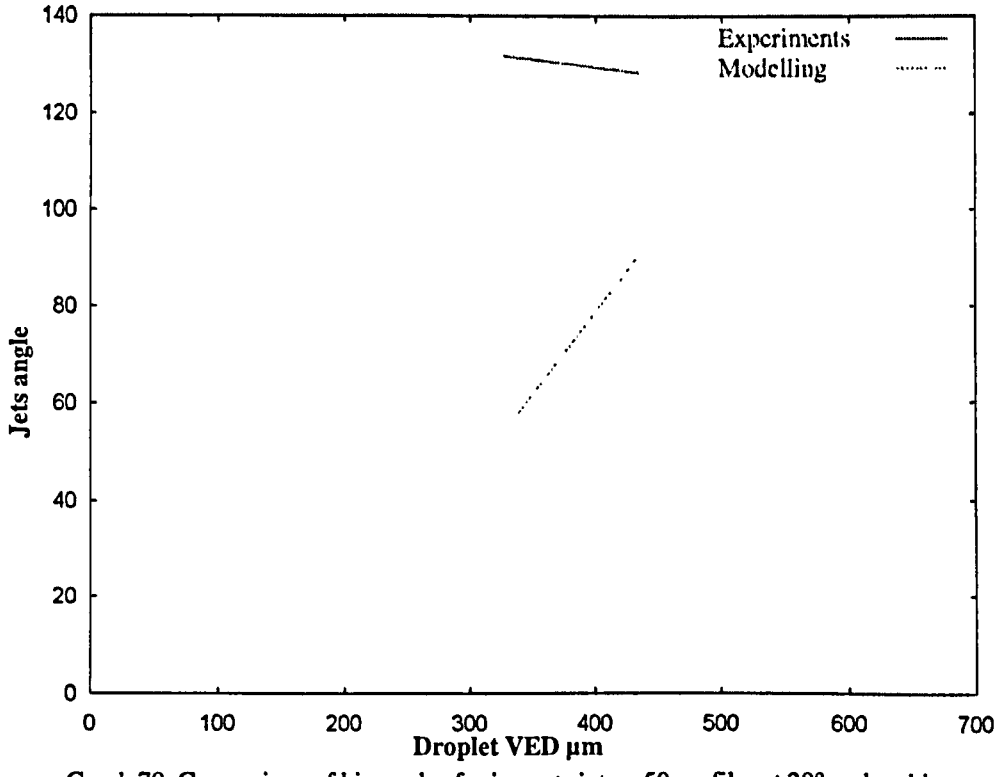

Graph 70. Comparison of big angles for impacts into a 50μm film at 20° and ambient temperatures.

The results shown in graph 70 give different tendency and values for the angles. The values for the experiments are much higher than the values of the simulations. This is in part because of the influence of the airflow which is not included in the model. As it was seen in figure 60 and illustrated in part in figure 105, the impact at small angles produced a corona whose right side forms an obtuse angle with the water film.

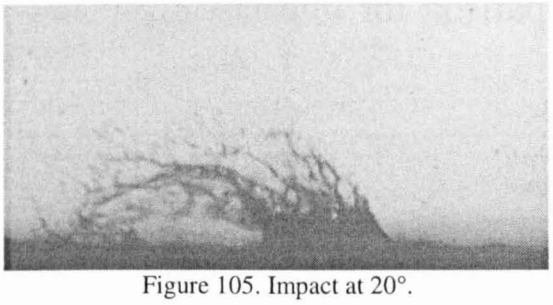

Figure 105. Impact at 20°.

Small angle comparison.

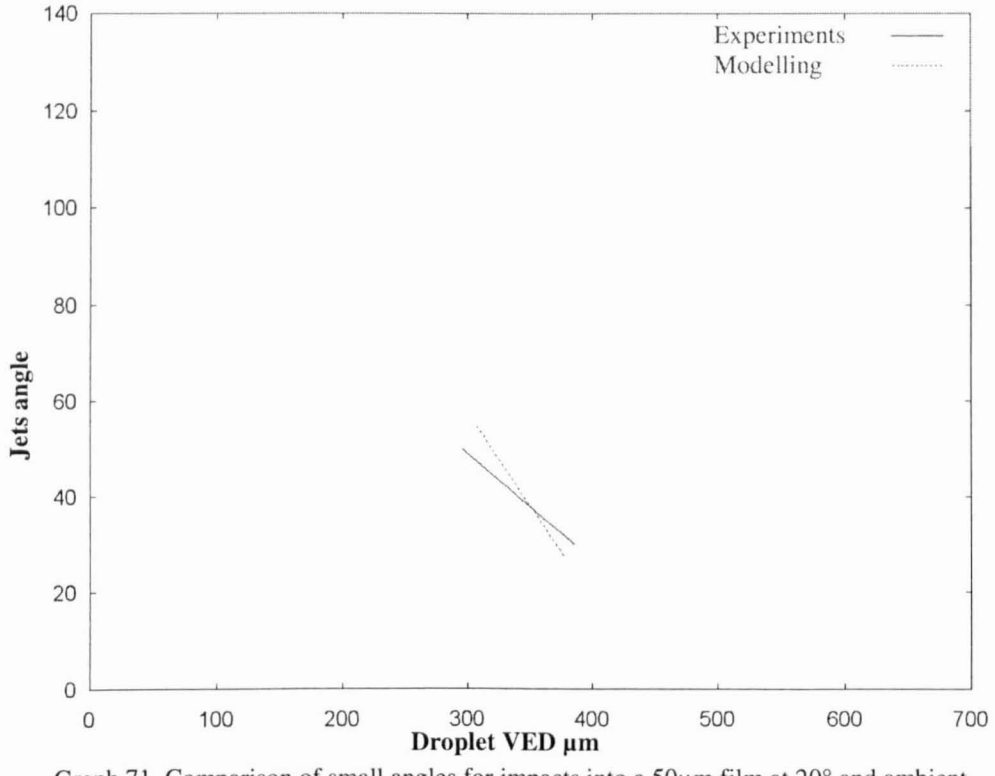

Graph 71. Comparison of small angles for impacts into a 50µm film at 20° and ambient temperatures.

The results show a good agreement between experiments and model. The values for the angles go from around 50° to 30°.

Jets velocity comparison for impacts at 20° into a 50μm water film and ambient temperatures.

Big jet velocity comparison.

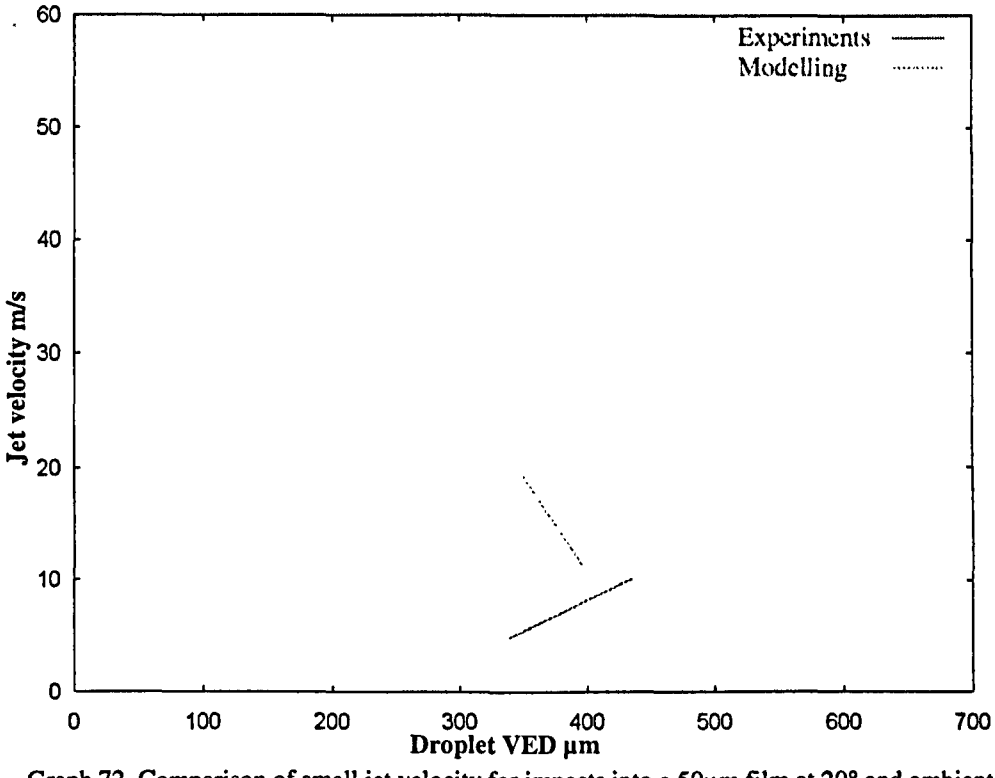

Graph 72. Comparison of small jet velocity for impacts into a 50μm film at 20° and ambient temperatures.

Graph 72 shows two different trend lines for the velocity calculation. As the results from the experiments increase, those from the simulation decrease. Also the values for the velocity of the jets are different and a discrepancy of 15m/s can be found for the small droplets, although this is reduced to 5m/s for the bigger droplets.

Small jet velocity comparison.

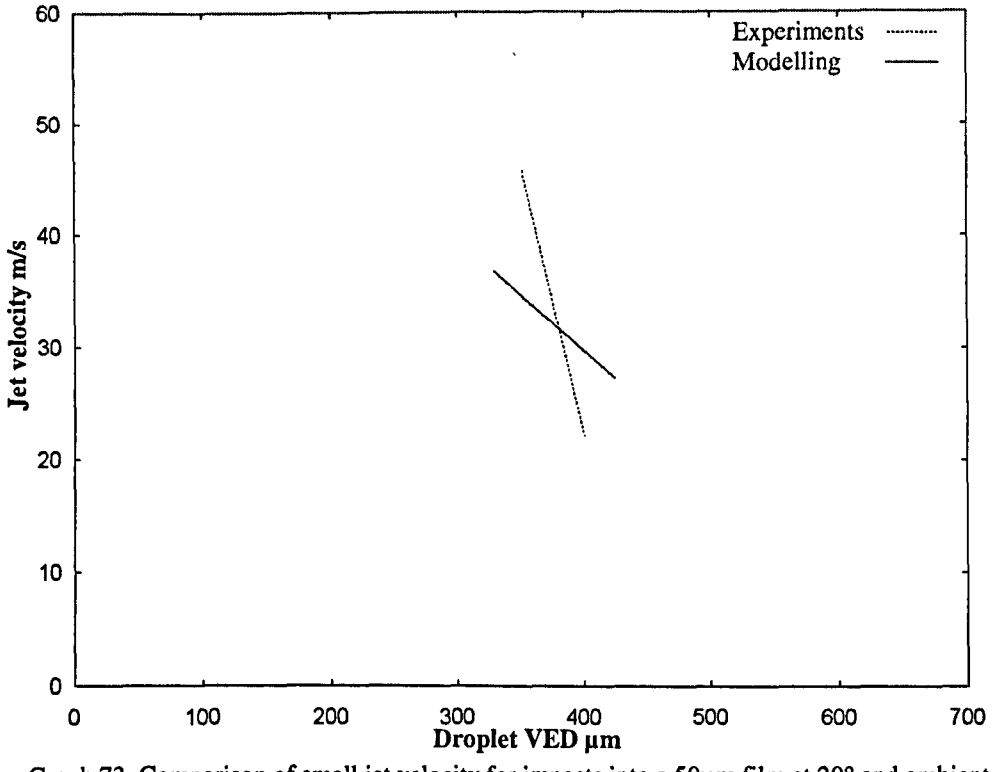

Graph 73. Comparison of small jet velocity for impacts into a 50µm film at 20° and ambient temperatures.

Graph 73 shows a decrease of the values of the velocity as the droplet size increases. In this case agreement is found between experiments and model and the differences are lower than 10m/s.

Summary of Results.

The project is divided in two different sections. One is experimental which includes the work in the Vertical Tunnel and analysis, understanding and classification of the results. The second is analytical, numerical and computational and includes the development of a numerical model based on an updated VOF method that simulates droplet impact into a water film. During this second section a code capable of comparison of the numerical results with the experiments was developed. The method also quantifies the heat transfer between droplet and water film, the temperature distribution during the splash and the fluid solidification and ice growth as the temperatures drops below the melting temperature.

A summary of the findings are presented.

Experiments.

Effect of droplet size and velocity of impact.

The increase of the droplet VED usually produces an increase of the corona size and the velocity of the jets. The variation of corona size and velocity is more sensitive to the variation of the droplet VED than to the variation of the velocity of impact. The increase of the droplet size also has a relevant importance in the evolution of the angles formed between the corona sides and the water film. It has been seen that, as the droplet size increases, there is an increase of the "big" angle and a decrease of the "small" angle.

The sizes and velocities of the satellite droplets also increase as the droplet VED increases.

However there are some particularities. Not always the parameters are scaled to the droplet VED. These exceptions were found in impacts made at 20° where the jet angles decrease slightly with the increase of the droplet size.

The velocity of impact has also a significant influence on some other parameters. This influence is more relevant in the velocity of the jets and the time that the coronas need to develop and to reach the maximum size. Thus, the higher the velocity of the impact, the higher the velocity of the jets.

There is a general increase of the velocity of the satellite droplets as the droplet impact speed increase.

Effect of water film thickness.

The variation of the water film thickness does not appear to make relevant differences in the size of the corona. However the angles that the corona sides form with the water film are more sensitive to this variable. Therefore the "small" angle is greater for impacts into a shallower water film. The velocity of the jets is also affected by the variation of the thickness. Thus there are found higher velocities for the coronas formed after impacts into the thicker layer.

A thinner water film also produces smaller satellite droplets, although the differences are not very significant. Impingements into the 150μm water film produce faster satellite droplets than impacts into the 50μm water layer.

Effect of temperature.

Regarding impacts made at super-cooled temperature it has been seen that the coronas formed during the splash are less sensitive to the droplet size and velocity variation. The impacts of the smallest droplets produce higher values for the corona parameters in the cold impacts.

The time for the corona collapse is affected by the super-cooled temperatures. This time is longer for the cold impacts than for those made at ambient temperatures.

The temperature also has some influence on the jets. It has been seen that the angles that they form do not change as much as those angles formed at warm impacts

due to the increase of the droplet size. The velocity of the big jets (or the right jet in the experiments) increases slightly for the colder impacts.

Super-cooled temperatures do not seem to affect the size of the satellite droplets. But it may increase the velocity of these tiny droplets, although the data is limited and variable.

Effect of the angle of impact.

The corona size is affected by the reduction of the angle of impact. As it has been seen, the height and base width decrease and the top width increases as the angle of impact decreases from 70° to 45° and 20°. The time for the corona formation and collapse is also reduced.

As the angle of impact decreases it is observed that the small angles formed by the corona sides decrease but the big angles increase. The decrease of the angle of impact also increases the velocity of the small jet velocities.

A little increase of the satellite droplet size is also found when the angle of impact is reduced. Thus, for impacts made at 45° and 20° bigger satellite droplets are observed than during the impacts made at 70°. The reduction of the angle of impact also seems to increase the speed of the satellite droplets.

Dry impacts.

The impacts on a dry target showed that no corona was formed but only satellite droplets that were ejected into the air.

The effect that a dry impact has on these satellite droplets is seen in their sizes. The smallest satellite droplets have been found during the impacts made on a dry target. Dry impacts did not show any clear tendency and due to the scatter of the values, the results were found to be in the same range as the previous cases.

Modelling.

Effect of droplet size and velocity of impact.

The increase of the size of the impacting droplet affects the size of the corona. In general it is observed that the three parameters measured increased with the droplet VED. The angles of the jet seem to be in general insensitive to the size variation. Only the right jet for impacts into the 50μm water film decrease as the droplet size increase. The jet velocities are influenced by the variation of the droplet VED. Thus, the bigger droplet, the higher velocity for the jet. The size of satellite droplets do not seem to be significantly affected by the increase of the droplet size.

It has not been observed that there is any significant change in the splash parameters as velocity of impact increases. Specifically the jet velocities and the satellite droplet velocities are not noticeably affected by the increase of the velocity of impact.

Effect of water film thickness.

The corona parameters are more sensitive to the increase of the droplet size during the impacts into the thin film. Also higher values for corona top and base width are found for impacts into the 50μm water film.

The jet angles and velocities are affected by the variation of the water film. Thus, for thinner film the angles decrease and the velocity increases.

The satellite droplet sizes and velocities increase slightly for the impacts into the thin film.

Effect of cold temperature.

The impacts simulated when super-cooled droplets where considered reflected no changes on corona sizes or jets angles. However it was observed that the velocities of the jets and satellite droplets were reduced dramatically.

Effect of angle of impact.

For smaller angles of impact, the values of the corona parameters decrease with the increase of the droplet VED. However those values are higher for the impacts at 45° and 20°, in particular the corona top width.

It can be observed that the jet angles also change as the angle of impact decreases. Thus the values that the small jet forms are lower and the angles that the big jet forms are higher as the angle of impact decreases. The jet velocities are also affected. It was seen that for small angles these velocities are higher, in particular the small jet.

The values for the satellite droplet sizes and velocities also increase for impacts at 45° and 20°.

Comparison Experiments-Modelling.

The computing code has been used to compare a number of impacts run in the Cranfield University High Speed Vertical Tunnel in order to observe the similarities and differences between experiments and simulation. The cases that have been run using the model are done under the same conditions that the cases run in the experiments. Also the same parameters have been considered. The model does not include airflow. The parameters such as viscosity, specific heat, thermal conductivity and surface tension are temperature dependent. Therefore two fluids are considered which initially have different values for these physical properties (droplet and water film). As the time increases, the value of these properties changes due to the change of the temperature.

It has been observed that the modelling agrees well quantitatively with corresponding experiments in respect to the velocity and initial trajectory of ejected water, in particular during the early stages of the splash when the corona is being formed. However as the splash evolves further, the experimental corona shape begins to differ significantly from the form of the simulated jets. This is thought to be in part due to the influence of the air movement.

The results show in general that the model works better for the 150μm film. For impacts into this water layer more agreement is found between model and experiments. There are however particular instances that show a significant difference, they are the corona height and the "small angle".

The impacts simulated into the 50μm film present in general more differences with the experiments, in particular for the size of the corona. However in most of the cases the values of the jet velocities and, in some runs, the jet angles are found to agree between the model and the experiments.

It is relevant that the values of the satellite droplets sizes are in the same range in the modelling and the experiments. It is also is noticed an increase of the satellite droplet velocities as the droplet VED increases which are also in the same range in both, model and experiment.

It is relevant that the most significant disparities are found for cases where the number of experimental and simulated impacts is low and, therefore, the trend lines are more likely to be affected by particular cases.

Temperature in the Corona.

Impacts of super-cooled and warm water droplets have been simulated in order to quantify the temperature of the ejected liquid as a function of the temperature of the incoming droplet and water layer present on the surface. The results show that the temperature of the water at the impact area is similar to the temperature of the

impacting droplet. Therefore, in the case of a super-cooled water droplet impact, the temperature is below freezing point.

An important difference between the super-cooled and warm impacts was found in the temperature of the water sheet that forms the corona. The impacts made at ambient temperature showed that the temperature of both jets was highly influenced by the temperature of the droplet unless the ratio between the water film thickness and the droplet VED is "big" and the velocity of impact low. The impacts of super-cooled droplets produce a different temperature distribution. It has been seen that the right jet, which contained a considerable amount of water from the droplet, was super-cooled.

Water Solidification.

The numerical method for fluid solidification made the model capable of simulating the very early stages of the ice growth during the impact of a super-cooled water droplet into a thin water film. Some rough ice was placed in the water film and, as the water temperature decreased below the melting temperature, the ice propagated through the liquid film. It was possible to observe that the temperature of the fluid decreased faster in the area of impact of the droplet, therefore the ice also grew faster in this zone.

The simulation results provide information about the heat transfer between a super-cooled droplet, a water film and the ice. Also the model provides information about the exact position of the ice-liquid boundary during the impact and finally about the splash into a water film which is being frozen.

CHAPTER 12. Conclusions

- The droplet impact in the experiments and simulation shows that, during the splashes, the size of the droplet has more effect on the corona formation than any other parameter considered. The velocity of impact has been seen to have a direct influence on the velocity of corona growth.
- It was observed that a thinner water film increases the velocity of the corona sides.
- Impacts at super-cooled temperatures produce splashes less sensitive to the variation of the droplet size and velocity of impact.
- Smaller angles of impact increase the angles formed by the "big" jet and decrease the angles formed by the "small" jet. The top width of the corona is the parameter more affected by the decrease of the angle of impact.
- Model and experiment agree in the previous points. However impacts into the 50μm water film show important differences between model and experiments. Therefore it can be affirmed that the model works better for droplet impact into thicker water films.
- The comparison between model and experiment reflects two main problems: First, a 3D experiment is compared with a 2D model. Second, the airflow is neglected in the model. Thus only early stages of the splash can be compared. The agreement is particularly good for bigger droplets.
- Some variability was found during the experiments. It is assumed that this is due to experimental variables which were not accounted for, e.g. turbulence in the air and waviness in the film. Also, in a number of cases, the measure of some of the parameters considered was found particularly hard due to the quality of the images recorded. This may have some influence in the final value obtained for the parameters in some cases.
- The simulation of SLD impact shows that, during the splash and corona formation, the impact area, the tip of the small jets and the satellite droplets ejected from it remain at super-cooled temperatures. It is relevant that the super-cooled water from the droplet is in direct contact with the bottom of the water film which simulates the critical surfaces of the aircraft

- The simulation of the early stages of ice formation shows that the ice set at the bottom of the water film has been seen to grow during the droplet impact. Also the temperature in the impact area is reduced dramatically as the droplet makes contact with the water film. Finally the splash does not form a corona. Instead, satellite droplets are ejected into the "air", as happens during the dry impacts in the experiments.

This investigation provides some general conclusions that might influence the design and certification of aircraft.

Regarding the droplet impact, it has been seen for first time how the splash is produced once the droplet impinges into a thin water film. During the experiments it has been reproduced the conditions under which the aircraft impact the droplets included the super-cooled temperatures that produces ice.

The results provide very complete information about the splash produced after the impact. Now it is possible to know how the corona is formed regarding parameters such as droplet size, velocity and angle of impact and temperature. Attending to these variables the splashes have been analysed and classified considering parameters including corona height, top width and base width, velocity of the corona rim, angles formed by the sides of the corona and satellite droplets size and velocity. All this work gives an accurate study of the consequences of the droplet impact made under icing conditions.

Numerically it has been possible to simulate those impacts made under the same conditions that the cases run during the experiments. Although the model reproduces the impacts in two dimensions, the result provide in several cases an accurate approximation to the experiments.

A numerical model has been also developed in order to investigate the heat transfer between the SLD and the warmer and thin water film. The results show the heat distribution in the corona as the splash is being developed. In general, the coldest temperatures remain in the impact zone where the water from the super-cooled is more plentiful. This area will be in direct contact with the target surface which

simulates the one of the most sensitive areas of the aircraft to icing. Also there has been found water at super-cooled temperatures in some of the satellite droplets that are released and in the jet which contains more water from the droplet during its formation.

The last goal achieved is the development of an initial computational solidification model that simulates the early stages of the ice growth in the water film covering the surface. Although the method should be improved in the future in order to get more accurate results, the model is capable to reproduce the building up of the ice as the temperature decreases in the water film during the super-cooled droplet impact.

ALL MISSING PAGES ARE BLANK IN ORIGINAL

Problems and Recommendations for Future.

During this project different problems have been sorted out and some others still remain unsolved. Also new questions have come up. This final section lists and comments these new difficulties and issues.

Experiments.

The results obtained for the different parameters provided good and helpful information about the corona formation during the splash. However there are some gaps that could be usefully filled. Due to the relatively low number of impacts recorded for some combinations of parameters, there are a number of comparisons which could not be done. Therefore it would be beneficial to start to carry out experiments considering impacts of big size droplets at high speed. But also it is necessary to make more impacts into the 50μm thickness water film, especially impacts at high speed. The same should be done for impacts at super-cooled temperatures. In the case of impacts at 45 and 20° more experiments should be also carried out but in these cases for the whole range of droplets VED and velocities.

Modelling.

Comparison with experiments.

The computational code agrees well with part of the experiments. However it is limited as the airflow is not included and also that the model works in 2D. Therefore for long time-steps the experimental corona shape begins to differ significantly from the form of the simulated jets. It could be useful if the model turns into 3D and includes airflow.

In order to more easily achieve a three dimensional computational code and to get second order accuracy (instead of first order as at present), it would be useful to adapt the code to the PLIC method.

Solidification.

The freezing model presents different problems that should be considered carefully. It has been found that the connection between the vertexes of the segments simulating the ice-fluid interface in the cell, sometimes fails. It has been seen that some time-steps later the problem might be sorted out automatically, however this does not always happens. The problem is that this may cause the calculation of the pressure in the neighbouring cells with fluid to fail. Therefore, the velocity is going to be affected producing instabilities and future errors which may affect the convergence.

The velocity calculation in the cells containing ice and liquid may also cause some problems. As it was explained, the fluid velocity in these kinds of cells was related to the velocity of the ice growth and it was pointing in the direction of the normal exterior vector. However it should be considered that, if the cell is over the melting temperature the ice recedes and the velocity should act in the opposite direction to the normal exterior vector. This does not currently occur.

The temperature calculation between ice and fluid and the ice growth rate seem to agree with the theory. However this is untested.

It could also be interesting to refine the freezing model to consider the nucleation of freezing away from the ice layer-water interface.

Appendix:

Solution of the Solidification Method Equations.

This appendix shows a work done together with Professor Frank Smith from University College, London and explains how the equations for the calculation of the temperature of the fluid close to the ice and the advance of the ice-liquid interface are obtained. These terms were represented by equations (9) and (10) in chapter "a numerical method for fluid solidification".

$$\hat{T}(\hat{z},\hat{t}) = \hat{T}_{\infty} + (\hat{T}_m - \hat{T}_{\infty})\left[1 - 4.5 \cdot \frac{\hat{z} - \hat{h}_0}{\sqrt{k'\hat{t}}}\right], \tag{9}$$

$$\hat{h}(\hat{t}) = \hat{h}_0 + 9.027 \cdot S^{-1}\sqrt{k'\hat{t}}\,. \tag{10}$$

The starting point to obtain these expressions was the system of equations representing the original problem:

$$\hat{T}^S = \hat{T}_m \qquad \text{On solid, } \hat{z} < \hat{h}(0) \tag{1}$$

$$\hat{T}^l_{\hat{t}} = k'\hat{T}^l_{\hat{z}\hat{z}} \qquad \text{On liquid, } \hat{z} > \hat{h}\ (0) \tag{2}$$

$$\hat{T}^l = \hat{T}^S = \hat{T}_m$$
$$\rho^S L \frac{\partial \hat{h}}{\partial \hat{t}} = -k^l_T \hat{T}^l_{\hat{z}} \qquad \text{On } \hat{z} = \hat{h}\ (0) \tag{3}$$

This was also previously shown in chapter "a numerical method for fluid solidification". Remember that $\hat{T}_m$ is the melting temperature, $\hat{T}^S$ the temperature in the solid and $\hat{T}^l$ the temperature on the liquid. L is the latent heat, k_T is the thermal conductivity and $\frac{\partial \hat{h}}{\partial \hat{t}}$ the advance on time of the ice-liquid interface.

Calculation of the Temperature.

In order to solve this system of equations, (1), (2) and (3) were desdimensionalisated. Thus put

$$\hat{T}^l = \hat{T}_\infty + \left(\hat{T}_m - \hat{T}_\infty\right)\cdot\theta, \tag{4}$$

$$\hat{t} = \left(\frac{\hat{h}_0^2}{k^l}\right)t, \tag{4a}$$

$$\hat{z} = \hat{h}_0 z, \tag{4b}$$

$$\hat{h} = \hat{h}_0 h. \tag{4c}$$

Remember that the symbol ^ referred to the dimensional variable, θ to the non-dimensional form of the temperature and T_∞ denotes the temperature of the droplet or the layer as explained before.

Applying (1), (2) and (3) to (4) and considering (4a), (4b), and (4c) the non-dimensional problem to be solved is:

$$\frac{\partial\theta}{\partial t} = \frac{\partial^2\theta}{\partial z^2} \tag{5a}$$

with:

$$\begin{aligned} \theta &= 1 && \text{at } z = h(t), \\ \frac{\partial\theta}{\partial z} &= -S\frac{dh}{dt} && \text{at } z = h(t). \\ \theta &\to 0 && \text{as } z \to \infty. \end{aligned} \tag{5b}$$

The initial conditions at $t = 0^+$ are $h(0) = 1$ and

$$\begin{aligned} \theta\big|_{t=0^+} &= 1 && \text{for } 0 \le z \le 1, \\ \theta\big|_{t=0^+} &= T_1(z) && \text{for } 1 \le z < \alpha, \\ \theta\big|_{t=0^+} &= 0 && \text{for } z > \alpha. \end{aligned} \tag{5c}$$

Remember that S is the Stefan Number and is defined by:

$$S \equiv \frac{L\rho^l k^l}{k_T^l\left(\hat{T}_m - \hat{T}_\infty\right)} \tag{6}$$

Denoting c^l the specific heat of the liquid ($c^l = k_T^l / \rho^l k^l$), the Stefan number (eq. 6) can also be written as follows

$$S \equiv \frac{L\rho^l k^l}{k_T^l(\hat{T}_m - \hat{T}_\infty)} = \frac{L}{c^l(\hat{T}_m - \hat{T}_\infty)} \tag{6a}$$

Once the non-dimensional problem is planted, (5a) is solved taken into account the fixed conditions and assuming that Stefan Number is large. This is acceptable due to the values found for this dimensionless number are up to more than 600.

Consider:

$$\theta(z,t) = F(\eta) \qquad \text{with } \eta = \frac{z-1}{t^{\frac{1}{2}}} \text{ of O(1)} \tag{7}$$

Substituting in (5a):

$$\theta_t = \theta_{zz} \Leftrightarrow F'' + \frac{\eta}{2}F' = 0 \Leftrightarrow \frac{F''}{F'} = -\frac{\eta}{2} \Leftrightarrow \left[\ln F'\right]' = -\frac{\eta}{2} \Leftrightarrow$$

$$\Leftrightarrow \ln F' = -\frac{\eta^2}{4} + C_1 \Leftrightarrow F' = C_1 e^{\left(\frac{-\eta^2}{4}\right)} \Leftrightarrow F = C_1 \int_0^\eta e^{\left(\frac{-\hat{\eta}^2}{4}\right)} d\hat{\eta} + C_2 \qquad \forall C_1, C_2 \in \Re$$

Therefore

$$\theta_t = \theta_{zz} \Leftrightarrow F = C_1 \int_0^\eta e^{\left(\frac{-\hat{\eta}^2}{4}\right)} d\hat{\eta} + C_2 \;\; \forall C_1, C_2 \in \Re \tag{8}$$

Constants C_1 and C_2 have to be calculated in order to get the final expression for F and subsequently, for θ.

For $t \sim 1$

$$h \sim 1 + S^{-1}h_1 + \ldots$$
$$\theta = 0(1) + \ldots \tag{9}$$

From (5b) we know $\theta(z, t) = 1$ if $z = h(t)$, but regarding (9) and attending the leading order it can be taken: $h \sim 1$. Therefore $z = h(t) = 1$ and then, regarding (7) $\eta = 0$. Thus it is obtained the condition $F(0) = \theta(1, t) = 1$.

Then, applying this condition in (8) the value for C_2 is found.

$$F(0) = C_2 = 1 \tag{10}$$

Hence

$$\theta_t = \theta_{zz} \Leftrightarrow F = C_1 \int_0^{\eta} e^{\left(\frac{-\hat{\eta}^2}{4}\right)} d\hat{\eta} + 1 \; \forall C_1 \in \Re \tag{11}$$

In order to get the final expression of F, C_1 has to be determined. To achieve this (5b) is used again. One of the conditions says:

$$\lim_{z \to \infty} \theta(z,t) = 0 \tag{12}$$

Therefore

$$\lim_{z \to \infty} \theta(z,t) = 0 \Leftrightarrow \lim_{z \to \infty} F(\eta) = 0 \Leftrightarrow \lim_{z \to \infty} C_1 \int_0^{\eta} e^{\left(\frac{-\hat{\eta}^2}{4}\right)} d\hat{\eta} + 1 = 0 \tag{13}$$

Then

$$C_1 = \frac{-1}{\int_0^{\infty} e^{\left(\frac{-\hat{\eta}^2}{4}\right)} d\hat{\eta}} = -4.51 \tag{14}$$

Thus

$$F(\eta)=-\frac{\int_0^{\eta} e^{\left(\frac{-\hat{\eta}^2}{4}\right)}d\hat{\eta}}{\int_0^{\infty} e^{\left(\frac{-\hat{\eta}^2}{4}\right)}d\hat{\eta}}+1=-4.51\int_0^{\eta} e^{\left(\frac{-\hat{\eta}^2}{4}\right)}d\hat{\eta}+1 \qquad (15)$$

In the other hand, where $z-1$ is O(1) then η is small, hence

$$F(\eta)\approx -4.51\eta+1+O(\eta^3) \qquad (16)$$

From (7) and substituting

$$F(\eta)=\theta(z,t)\approx -4.51\frac{z-1}{t^{\frac{1}{2}}}+1+O\left(\left(\frac{z-1}{t^{\frac{1}{2}}}\right)^3\right) \qquad (17)$$

Then (4) can be determined once (17) is dimensionalised. In order to get this, conditions (4a), (4b) and (4c) are applied. Taken into account the definitions given for t, h and z the dimensional form of (17) established. Thus expression (9) is obtained.

$$\hat{T}(\hat{z},\hat{t})=\hat{T}_{\infty}+(\hat{T}_m-\hat{T}_{\infty})\left[1-4.5\cdot\frac{\hat{z}-\hat{h}_0}{\sqrt{k'\hat{t}}}\right], \qquad (9)$$

Advance of the Ice-liquid Interface.

Once the expression for the temperature calculation is determined the equation that gives the advance of the ice as the melting temperature T_m is reached in the cells is obtained.

Condition (9) gave an approximation for $h(t)$ and (4b) was a boundary condition. In particular it is interesting in this case

$$\frac{\partial\theta}{\partial z}=-S\frac{dh}{dt} \qquad \text{at } z=h(t). \qquad (5b)$$

Therefore if (9) gave $h \sim 1 + S^{-1}h_1+\ldots$ substituting in (5b) it is obtained

$$\frac{\partial \theta}{\partial z} = -\frac{dh_1}{dt}. \tag{18}$$

From (17) we find

$$\frac{\partial \theta}{\partial z} = -4.5t^{-\frac{1}{2}}. \tag{19}$$

Then

$$4.5t^{-\frac{1}{2}} = \frac{dh_1}{dt}. \tag{20}$$

Integrating

$$h_1 = 4.5\int t^{-\frac{1}{2}}dt = 4.5\cdot 2\cdot t^{\frac{1}{2}} + C = 9\cdot t^{\frac{1}{2}} + C \tag{21}$$

and because as initial condition it was set that at $t = 0^+$ are $h(0) = 1$, then

$$h(0) \approx 1 + S^{-1}h_1(0) = 1 \Rightarrow h_1(0) = C = 0. \tag{22}$$

Thus

$$h(t) = 1 + 9\cdot S^{-1}\cdot t^{\frac{1}{2}}. \tag{23}$$

In order to find the dimensional form, conditions (4a), (4b) and (4c) are used and finally the expression for the ice-liquid interface is as follows

$$\hat{h}(\hat{t}) = \hat{h}_0 + 9\cdot S^{-1}\sqrt{k'\hat{t}} \tag{24}$$

Acknowledgements.

Thanks to

David Hammond for the work he has done, his dedication, his patience and explanations,
Frank Smith from UCL for making everything very understandable, for his tranquillity and for trust in me since I "dropped" the first time in his office,
Richard Purvis from UEA for his unconditional help and wise ideas and advises,
GKN Aerospace Services for the support through the Faraday Partnership for Industrial Mathematics, managed by the Smith Institute, and in particular David Allwright,
Roger Gent from QinetiQ for pointing the important issues in every meeting,
Dean Miller from NASA Glenn for his help during the experiments, his organisation and explanations,
Jason Tan from Wichita State University for the explanations and help,
Paul Spooner from UK CAA for the support,
The Turbomachinery group students in Cranfield for the help always when I needed, in particular Robin and Adam,
All those in the Rainbow Room who made long working days easier and
The Cranfield University Library staff, Jane Slaughter from the Computing Centre and the technicians, and in particular to Brian.

Quisiera agradecer también a

Guillermo Curbera de la Facultad de Matemáticas de Sevilla por su incondicional esfuerzo,
Enrique Fernández Cara, Tomás Chacón y Rosa Echevarría de la Facultad de Matemáticas de Sevilla por no dudar en prestarme toda la ayuda a su alcance cuando lo necesité,
Jesús por su comprensión, apoyo y ánimo,

Mi familia por estar siempre ahí.

Especialmente quiero dar las gracias a Leti. Por todo y en todo momento.

Thanks all, gracias a todos.

References.

H.E. Addy, Jr. Ice Accretion and Icing Effects for Modern Aerofoils. *NASA/ TP-2000-210031.*

Aerospace America. *AIAA Atmospheric and Space Environments Technical Committee.* December 2005.

Al-Khalil. Numerical Simulation of an aircraft Anti-Icing System Incorporating a Rivulet model for the Runback Water. *Ph.D. Dissertation, Univ. Toledo. Toledo.* OH, June 1991.

O. Benchikh, D. Fournier, A.C. Boccara and J. Teixeira. Photothermal Measurement of the Thermal Conductivity of Super-cooled Water. *Journal of Physics (Paris)* (1985), *vol* 46, *pp* 727-731.

A.Q. Chapleo *et al.* The Effect of Glaze Icing on Wing Aerodynamics and Aircraft Lateral Stability. *AIAA* 1994-0812

S.H. Davis. Theory of Solidification. *Cambridge University Press.* 2001.

A. Feo, F. Rogles and M. Urdiales. The Measurement of Water Film Thicknesses on Airfoils in Heavy Rain Conditions using Conductance Sensors. *AGARD report CP 496,* 1991.

R. W. Gent, J. M. Ford, R. J. Moser and D. Miller. Results from Super-Cooled Large Droplet Mass Loss Test in the ACT Luton Icing Wind Tunnel. *AIAA 2003-389.*

D. Gueyffier, J. Li, A. Nadim, R. Scardovelli and S. Zaleski. Volume of Fluid Interface Tracking with Smoothed Surface Stress Methods for Three Dimensional Flows. *Journal of Computational Physics* (1999), *vol.* 152, *pp.* 423-456.

J. Hallett. The Temperature Dependence of the Viscosity of Super-cooled Water. *Proceedings of Physical Society* (1963), *vol.* 82, *pp* 1046-1050.

D. Hammond. Investigation into Super cooled Large Droplet Splashing Final Report. Commissioned by the CAA (contract 623). March 2005.

D.Hammond, M.Quero, D.Miller, R.Purvis, O.McGregor and J.Tan. Analysis and Experimental Aspects of the Impact of Super-cooled Water Droplets into Thin Water Layers. *AIAA*-2005-0077.

F.H. Harlow, J.E. Welch. Numerical Calculation of Time-Dependent Viscous Incompressible Flow of Fluid with Free Surface. *The Physics of Fluids* (1965), *vol.* 8, *number* 12, *pp.* 2182-2189.

E. C. Hastings and L. M. Weinstein. Preliminary Indications of Water Film Distribution on an Aerofoil in a Water Spray. *NASA technical memo number 85796,* 1984.

C.W. Hirt and B.D. Nichols. Volume of Fluid (VOF) Method for the Dynamics of Free Boundaries. *Journal of Computational Physics* (1981), *vol.* 39, *pp.* 201-225.

Hoffmann. On the state of knowledge meteorologically causing icing of aircrafts in clouds, *ESA-TT*-861.

S.D. Howison, J.R. Ockendon, J.M. Oliver, R. Purvis and F.T. Smith. Droplet Impact on a Thin Fluid Layer. *Journal of Fluid Mechanics* (2004).

C. Josserand and S. Zaleski. Drop Impact on a Thin Layer. *The Physics of Fluids* (2003), *vol.* 15, *pp.* 1650-1657.

J. M. Kay and R. M. Nedderman. An introduction to Fluids Mechanics and Heat Transfer. *Cambridge University Press.*

J. Li. Calcul d'Interface Affine par Morceaux (Piecewise Linear Interface Calculation). *CR Academie Sciences de Paris, Sér. IIb* (1995), *vol.* 320, *pp.* 391-396.

Liu and Liu. SMOOTHED PARTICLE HYDRODYNAMICS. A Meshfree Particle Method. *World Scientific Publishing.* 2003.

G. Luxfford. Ph.D. Thesis. Cranfield University. March 2005.

O. G. McGregor and R. P. Dalton. Development of an Ultrasonic Probe to Measure Water Film Thickness. *QinetiQ report.* QinetiQ/04/01010, 2004, pp 28.

D. Miller. SLD Technology Roadmap. *IPHWG- SLD Specialists Meeting.* Cleveland OH (U.S.) 21st March 2000.

Morency *et al.* Anti icing System Simulation Using CANICE. *Journal of Aircraft, Vol.* 36, *No* 6.

B. D. Nichols, C. W. Hirt and R. S. Hotchkiss. SOLA-VOF: A Solution Algorithm for Transient Fluid Flow with Multiple Free Boundaries. *UOCILA*-8355.

S. Pearson. The Cranfield University Icing Facilities. *Cranfield University.* 2005.

M. Politovich. Aircraft Icing Caused by Large Super cooled Droplets. *Journal of Applied Meteorology. Vol.* 28, *pp* 856-868.

R.Purvis and F.Smith. Large Droplet Impact on Water Layers. *AIAA*-2004-0414.

A. Saito, S. Okawa and D. Shimamoto. Research on a Thermal Conductivity Measurement of Super-cooled water. *Proceedings of 5th Symposium on Thermal Engineering and Science for Cold Regions.* 19-22 May 1996. Ottawa, Canada.

R. Scardovelli and Stéphane Zaleski. Direct Numerical Simulation of Free-Surface and Interfacial Flow. *Annual Review of Fluid Mechanics* (1999), *vol* 31, *pp.* 567-603.

J. Tan. Draft Report. Design of a Vertical Tunnel for Large Droplet Dynamic Studies. *College of Engineering. National Institute for Aviation Research.* Wichita State University. U.S.A. October 2002.

S. T. Thoroddsen. The Ejecta Sheet Generated by the Impact of a Drop. *Journal of Fluid Mechanics* (2002), *vol.* 451, *pp.* 371-381.

M.D. Torrey, L.D. Cloutman, R.C. Mjolsness and C.W. Hirt. NASA-VOF2D: A Computer Program for Incompressible Flows with Free Surface. *LA*-10612-*MS. UC*-32. December 1985.

Trinh *et al.* Measurement of the density, sound velocity, surface tension and viscosity of freely suspended super cooled liquids. *Twelfth Symposium on Thermophysical Properties* (1994), June 19-24.

D.A. Weiss and A.L. Yarin. Single Drop Impact onto Liquid Films: Neck Distorsion, Jetting, Tiny Bubble Entrainment and Crown Formation. *Journal of Fluid Mechanics* (1999), *vol.* 385, *pp.* 229-254.